

Evolved Chiral Hamiltonians at the Three-Body Level and Beyond



Vom Fachbereich Physik
der Technischen Universität Darmstadt

zur Erlangung des akademischen Grades
eines Doktors der Naturwissenschaften
(Dr. rer. nat.)

genehmigte Dissertation von
M.Sc. Angelo Calci
aus Kassel

Darmstadt 2014
D17

Referent:	Prof. Dr. Robert Roth
Korreferent:	Prof. Dr. Jochen Wambach
Tag der Einreichung:	17. Juni 2014
Tag der Prüfung:	14. Juli 2014

Abstract

Based on the fundamental symmetries of QCD, chiral effective field theory (EFT) provides two- (NN), three- (3N), four- (4N), and many-nucleon interactions in a consistent and systematic scheme. Recent developments to construct chiral NN+3N interactions at different chiral orders and regularizations enable exciting nuclear structure investigations as well as a quantification of the fundamental uncertainties resulting from the chiral expansion and regularization.

We present the complete toolchain to employ the present and future chiral NN, 3N, and 4N interactions in nuclear structure calculations and emphasize technical developments in the three- and four-body space, such as the similarity renormalization group (SRG), the frequency conversion, and the transformation to the JT -coupled scheme. We study the predictions of the chiral NN+3N interactions in ab initio nuclear structure calculations with the importance-truncated no-core shell model and coupled-cluster approach. We demonstrate that the inclusion of chiral 3N forces improves the overall agreement with experiment for excitation energies of p-shell nuclei and it qualitatively reproduces the systematics of nuclear binding energies throughout the nuclear chart up to heavy tin isotopes. In this context it is necessary to introduce truncations in the three-body model space and we carefully analyze their impact and confirm the reliability of the reported results.

The SRG evolution induces many-nucleon forces that generally cannot be included in the calculations and constitute a major limitation for the applicability of SRG-evolved chiral forces. We study the origin and effect of the induced many-nucleon forces and propose a modification of the interaction, which suppresses the induced beyond-3N forces. This enables applications of the chiral interactions far beyond the mid-p shell. Furthermore, we test alternative formulations of SRG generators aiming to prevent the induced many-body forces from the outset. The extension of the SRG evolution and matrix-element treatment to the four-body space allows for an explicit inclusion of induced and initial 4N forces. We discuss the truncations and limitations in the four-body space and present first ab initio nuclear structure calculations for p-shell nuclei with induced 4N forces.

By changing the parameters of the local 3N force we perform a comprehensive sensitivity analysis for nuclear spectra in the p shell that provides constraints for the construction of chiral interactions. Moreover, we identify certain correlations that prevent an accurate description of the experimental results by an adjustments of the local 3N force at $N^2\text{LO}$. We report first results obtained with a next-generation NN+3N interaction at $N^3\text{LO}$ and compare the spectra obtained with several chiral interactions at different chiral orders, varying the regulator function and cutoff. These studies present a first step towards a systematic uncertainty quantification for the chiral forces and we show that p-shell spectroscopy is a sensitive diagnostic for chiral 3N interactions.

Zusammenfassung

Basierend auf den fundamentalen Symmetrien der QCD ermöglicht die chirale effective Feldtheorie (EFT) einen konsistenten und systematischen Zugang zu Zwei- (NN), Drei- (3N), Vier- (4N) und Mehrteilchen Wechselwirkungen. Die aktuellen Entwicklungen von chiralen NN+3N Wechselwirkungen für verschiedene chirale Ordnungen und Regularisierungen ermöglichen eine Vielzahl von Kernstrukturuntersuchungen und erlauben die Bestimmung der fundamentalen Unsicherheit die aus der chiralen Ordnungsentwicklung und Regularisierung stammen.

Wir erarbeiten die Techniken um die heutigen sowie die zukünftigen chiralen NN, 3N und 4N Wechselwirkungen in Kernstrukturrechnungen zu verwenden und setzen einen besonderen Schwerpunkt auf die Innovationen im Drei- und Vierteilchen Raum zu denen die Similarity Renormalization Group (SRG), die Frequenzkonversion und die Transformation zum JT -gekoppelten Schema gehören. Wir untersuchen die Vorhersagen der chiralen NN+3N Wechselwirkungen in ab initio Kernstrukturrechnungen mit dem Importance-Truncated No-Core Schalen Modell und der Coupled-Cluster Methode. Es wird demonstriert, dass das Einbinden von chiralen 3N Kräften die experimentelle Übereinstimmung von Anregungsenergien in der p-Schale insgesamt verbessert. Zudem erlauben die 3N Kräfte eine qualitative Reproduktion der Grundzustandsenergie-Systematik über einen weiten Bereich der Nuklidkarte hinweg, bis hin zu den schweren Zinn-Isotopen. In diesem Zusammenhang ist es nötig Trunkierungen des Dreiteilchen-Modellraumes einzuführen. Wir analysieren den Einfluss dieser Trunkierungen und bestätigen die Zuverlässigkeit der Ergebnisse, die in dieser Arbeit präsentiert werden.

Die SRG-Evolution induziert 4N Kräfte, die im Allgemeinen nicht in Vielteilchenrechnungen verwendet werden können. Die induzierten Kräfte stellen die Hauptursache dar für die Beschränkung des Anwendungsbereiches der SRG-evolierten chiralen Wechselwirkungen. Wir untersuchen den Ursprung und den Effekt der induzierten Vielteilchenkräfte und stellen eine Modifikation der Wechselwirkung vor, welche die induzierten Kräfte unterdrückt. Diese Modifikation ermöglicht eine Anwendung der chiralen Wechselwirkungen weit über die Kerne der mittleren p-Schale hinaus. Des Weiteren untersuchen wir alternative Konstruktionen des SRG Generators mit Hinblick auf eine Vermeidung der induzierten Vielteilchenkräfte. Die Erweiterung der SRG Evolution und der Matrixelement-Behandlung auf den Vierteilchenraum erlauben eine explizite Verwendung der induzierten und genuinen 4N Kräfte. Wir diskutieren die Trunkierungen und Grenzen der Entwicklungen im Vierteilchenraum und präsentieren die ersten ab initio Kernstrukturrechnungen für Kerne der p-Schale mit induzierten 4N Kräften.

Mittels einer Variation der Parameter in der lokalen 3N Kraft betreiben wir eine ausführliche Sensitivitätsanalyse der Spektren von p-Schalen Kernen. Aus dieser Analyse werden wichtige Hinweise für die Konstruktion der chiralen Wechselwirkungen gewonnen. Zudem identifizieren wir Korrelationen für bestimmte Observablen gegenüber Variationen in der 3N Kraft. Die

Korrelationen verhindern eine quantitative Beschreibung der experimentellen Daten durch eine Anpassung der lokalen 3N Kraft bis $N^2\text{LO}$. Schließlich präsentieren wir die ersten Resultate mit der nächsten Generation von chiralen NN+3N Wechselwirkungen die konsistent bis $N^3\text{LO}$ entwickelt werden und vergleichen Spektren für verschiedenen chiralen Wechselwirkungen mit unterschiedlichen Ordnungen und Cutoffs. Diese Studien stellen einen ersten Schritt hin zu einer systematischen Fehleranalyse dar. Insbesondere wird gezeigt, dass die p-Schalen Spektroskopie hervorragend geeignet ist um Sensitivitäten bezüglich der chiralen 3N Wechselwirkungen zu diagnostizieren.

Contents

Introduction	1
1 Chiral Effective Field Theory	5
1.1 Chiral Symmetry and Perturbation Theory	5
1.2 Regularization, Renormalization and Parameter Fit	8
1.3 Present Chiral NN+3N Interactions	10
1.3.1 Chiral NN Interactions	11
1.3.2 Chiral 3N Interactions at N ² LO	13
1.3.3 NN+3N Interactions Combinations	16
1.4 Next-Generation Chiral NN+3N Interactions	17
2 Ab Initio Many-Body Methods	21
2.1 The No-Core Shell Model	22
2.2 Importance Truncated No-Core Shell Model	25
2.3 Coupled-Cluster Approach	34
3 Momentum and HO Basis Sets	39
3.1 The Jacobi Basis	40
3.1.1 Two-Body Basis	41
3.1.2 Three-Body HO Basis and Antisymmetrization	42
3.1.3 Four-Body HO Basis and Antisymmetrization	45
3.2 Single-Particle Scheme vs. Jacobi basis	48
3.2.1 Transformation to <i>JT</i> -Coupled Scheme in Three-Body Space	50
3.2.2 Transformation to <i>JT</i> -Coupled Scheme in Four-Body Space	53
3.2.3 Decoupling and Storage Scheme	56
3.3 The Normal-Ordering Approach	59
3.4 Simplistic Particle-Rank Reduction	62
3.5 Partial-Wave Decomposed Jacobi-Momentum Basis	62
3.5.1 Transformation to the Jacobi-HO Basis	64
3.5.2 Basis Conventions for Practical Applications	67

4	Similarity Renormalization Group	71
4.1	Concept	72
4.2	Cluster Decomposition	74
4.3	Types of Evolved Hamiltonians	75
4.4	Evolution in HO Representation	76
4.5	Evolution in Two-Body Space	79
4.6	Evolution in Three-Body Space	80
4.6.1	Chiral Interactions Evolved in the Triton Channel	80
4.6.2	Subtraction Procedure	82
4.6.3	Frequency Conversion	83
4.7	SRG Evolution in Four-Body Space	85
4.7.1	Chiral Interactions Evolved in the ${}^4\text{He}$ Channel	85
4.7.2	Subtraction Procedure	92
4.7.3	Frequency Conversion	94
5	Role of the SRG Model Space and Frequency Conversion	97
5.1	Sensitivity to the SRG Model Space	98
5.2	The Frequency-Conversion Approach	101
5.3	SRG Space for Medium-Mass and Heavy Nuclei	103
6	SRG-Induced Many-Nucleon Contributions	109
6.1	Ground-State and Excitation Energies up to the p Shell	109
6.2	Origin and Suppression of Induced 4N Contributions	114
6.3	Alternative SRG Generators	118
6.3.1	Exclusion of Initial 3N Contributions	118
6.3.2	Restriction of Range	121
6.4	Inclusion of Induced 4N Forces	125
6.4.1	SRG-Space and Subtraction-Scheme Dependence	126
6.4.2	The Frequency-Conversion Approach	131
6.4.3	Final Results	133
7	NN+3N forces in Medium-Mass and Heavy Nuclei	141

7.1	Normal-Ordering Approximation	142
7.2	Towards Heavy Nuclei with Coupled Cluster	147
8	Sensitivity Analysis and Spectroscopy with Chiral Interactions	153
8.1	Sensitivity Analysis of Local 3N Interaction	153
8.2	Comparison of Present Chiral NN+3N Interactions	161
8.2.1	Spectroscopy of p-Shell Nuclei	162
8.2.2	Ground-State Energies and Induced Many-Nucleon Force	168
9	Next-Generation Chiral Interactions	171
10	Conclusion and Outlook	175
A	Notation and Conventions	179
B	Publications	183

Introduction

The theoretical description of the atomic nucleus is an outstanding problem that connects several physical disciplines ranging from microscopic elementary particles to macroscopic astrophysical objects. The interaction among the nucleons is dominated by the strong force and its determination is an important aspect of nuclear theory.

According to the standard model, the strong interaction is described by quantum chromodynamics (QCD) with quarks and gluon as fundamental degrees of freedom. In general, nuclear structure phenomena are dominated by low energies and QCD becomes non-perturbative in this regime, which so far impedes a direct derivation of the nuclear interaction from the underlying theory. Inspired by the meson-exchange theory proposed by Yukawa [1], phenomenological high-precision interactions, such as the Argonne V18 [2] and CD-Bonn [3] potentials, have been developed. The experimental discrepancies observed in nuclear structure application with these interactions indicate the importance of many-nucleon interactions beyond the two-body level [4–6] and reveal the necessity for a consistent scheme to construct the nuclear interactions.

Thus, Weinberg formulated an effective theory for the low-energy regime using nucleons and pions as explicit degrees of freedom. Rooted in the fundamental symmetries of QCD, chiral effective field theory (EFT) [7] allows to derive nucleon-nucleon (NN), three-nucleon (3N), four-nucleon (4N), and many-nucleon interactions in a consistent and systematically improvable scheme. The rapid developments of chiral NN [8–11] and 3N interactions [12–14] in recent years open great opportunities for nuclear structure theory to target the wealth of nuclear observables with interactions rooted in QCD.

Moreover, the conceptual and computational progress of the past decade enables us to tackle the nuclear structure problem for an increasing number of nuclei with *ab initio* methods. Starting from a realistic interaction these methods solve the many-body problem in a controlled and systematically improvable manner and obtain the exact solution within the estimated uncertainties.

Generally, realistic interactions such as the chiral interactions cause short-range and tensor correlations among the nucleons. Most many-body methods that rely on a matrix representation of the Hamiltonian require enormously large model spaces to adequately describe these correlations. To soften the interaction and to accelerate the convergence with respect to the model space different unitary transformations have been developed, such as the similarity renormalization group (SRG) [15–17] and the unitary correlation operator method (UCOM) [18]. For some time these transformations have been performed at the two-body level and many-body

calculations were restricted to NN interactions. Moreover, both transformations are known to induce sizable beyond-NN contributions that could not be included.

The extension of the SRG evolution to the three-body space [19–21] and the innovations for the computational treatment of three-body matrix elements allow for applications of chiral NN+3N interactions to several many-body methods. It is now possible to study a multitude of systems and observables, such as nuclear spectroscopy [20, 22, 23], nuclear reactions [24], hypernuclei [25], and neutron drops [26]. Furthermore, the improvements of the coupled-cluster (CC) methods [27–30], the self-consistent Green’s function methods [31–33], and the in-medium similarity renormalization group (IM-SRG) [34–36] allow to assess nuclei far beyond the p and sd shell in ab initio calculations.

However, medium-mass and heavy nuclei pose tremendous challenges regarding the truncations of the 3N interactions and the three-body SRG evolution, which need to be addressed for reliable applications. An unsolved problem are SRG-induced many-body contributions beyond the three-body level that generally are omitted due to computational reasons. These induced contributions can have sizable effects depending on the nucleus and observable and constitute a major limitation for the application to heavier nuclei. Therefore, it is necessary to prevent, suppress, or include these induced beyond-3N contributions.

The inclusion of beyond-3N forces are also of particular interest in view of the current efforts to derive the chiral force at next-to-next-to-next-to-leading order (N^3LO). At N^3LO 4N forces appear that need to be included to obtain a fully consistent interaction. In addition to the present chiral NN+3N forces a variety of chiral interactions up to the four-body level will be available in the future that, e.g., use improved fit and regularization procedures, include contributions from higher chiral orders, or use the Δ resonance as an explicit degree of freedom [37].

Due to the exciting progress in nuclear structure theory we are approaching a stage, where a systematic quantification of theoretical uncertainties of the chiral interactions becomes mandatory. Hence, future chiral interactions need to be constructed at different chiral orders for a sequence of cutoffs, to estimate the uncertainties due to the regularization and the truncation of the chiral order.

In this context it is necessary to work out techniques to efficiently employ the present and future chiral NN+3N+4N interactions in ab initio many-body methods in order to confront the predictions of chiral EFT for a variety of nuclear observables with experiment. From these studies one can also identify sensitivities of selected observables, which provide constraints for the construction of chiral interactions.

This thesis is organized as follows: In Sec. 1 the basic concept of chiral EFT is discussed and currently available chiral NN and 3N interactions at N^2LO and N^3LO are introduced.

The differences regarding the parameter fit procedure, the chiral order, and the regularization are emphasized. In Sec. 2 the ab initio many-body methods used in this work are discussed. The benefits and limitations of the no-core shell model (NCSM) and the importance-truncated NCSM are described and the basic concept of the coupled-cluster approach, which is applied for the medium-mass and heavy nuclei is presented. The different momentum and HO basis sets in the two-, three-, and four-body space are explained in Sec. 3. The treatment of the interaction matrix elements from the momentum representation through the Jacobi-HO representation to the JT -coupled scheme in the three- and four-body space is discussed, such that a fully self-consistent toolchain emerges to employ the present and future chiral NN, 3N, and 4N interactions in nuclear structure theory. The SRG evolution is introduced in Sec. 4. The formal aspects are discussed and the effects of the SRG evolution in the three- and four-body Jacobi-HO representation are illustrated. Also important technical aspects are studied, such as the subtraction procedure, the model-space truncation of the SRG evolution, and the frequency conversion. The accuracy of the three-body SRG evolution is verified in Sec. 5. We demonstrate the challenges regarding the SRG evolution with increasing mass number and that the frequency conversion enables an efficient and reliable application up to heavy nuclei. The effects and the origin of SRG-induced many-body contributions are discussed in Sec. 6. A suppression of the induced beyond-3N contributions via a modification of the chiral Hamiltonian is presented and alternative generators are investigated. For the first time, the induced 4N contributions are explicitly included in ab initio nuclear structure calculations in the p-shell. The developments regarding the treatment of the NN+3N interactions to access the medium-mass and heavy nuclei in ab initio calculations are outlined in Sec. 7. The nuclear binding energies up to the heavy tin isotopes are studied and the effect of omitted many-body contributions beyond the three-body level is discussed. An application of the chiral NN+3N interactions to nuclear spectroscopy is presented in Sec. 8. The sensitivity to chiral 3N contributions is analyzed and the spectra for the present chiral interactions are compared, providing a first step towards a systematic uncertainty quantification of the chiral forces. The uncertainty quantification is continued in Sec. 9, where the impact of the truncation of the chiral order is probed by presenting first nuclear structure results with the next-generation chiral NN+3N interaction at N³LO. Finally, the results of this work are summarized in Sec. 9 and an outlook on future developments is provided.

1 Chiral Effective Field Theory

Within the Standard Model of particle physics the underlying theory for the strong interaction is quantum chromodynamics (QCD). According to this theory, the fundamental degrees of freedom are quarks and gluons. Unfortunately, in the low-energy regime of nuclear structure physics, QCD becomes non-perturbative due to the large coupling constant of the strong interaction. Therefore, a direct derivation of nuclear forces from QCD is not yet possible (see Ref. [38] for a recent attempt). In 1979 Weinberg applied the concept of effective field theory (EFT) to low-energy QCD [7]. By this pioneering work, the idea of Yukawa [1] to describe the nuclear interactions using pions and nucleons as degrees of freedom, has been combined with the use of the fundamental symmetries of QCD. Thus, chiral EFT allows for an analysis of nuclear systems at low energies in a systematic and improvable manner, based on the fundamental symmetries of QCD. In this section we give an overview of the basic concepts of chiral EFT and present different chiral nucleon-nucleon (NN) and three-nucleon (3N) potentials that are presently available.

1.1 Chiral Symmetry and Perturbation Theory

The foundation of chiral EFT are the fundamental symmetries of low-energy QCD. In particular, the spontaneously broken chiral symmetry is an essential ingredient for the formulation of chiral EFT. For instance, massless particles exhibit an exact chiral symmetry, as a consequence such particles with spin and momentum either parallel (right-handed) or anti-parallel (left-handed) are completely decoupled and cannot be transformed into each other. In the following we focus on the QCD Lagrangian in the two-flavor case using the light up (u) and down (d) quarks that build the nucleons [39],

$$\mathcal{L}_{\text{QCD}} = \bar{q}(i\gamma_\mu D^\mu - \mathcal{M})q - \frac{1}{4}G_{\mu\nu}^a G_a^{\mu\nu}, \quad (1)$$

with the gauge-covariant derivative

$$D_\mu = \partial_\mu - ig\frac{\lambda_a}{2}A_\mu^a, \quad (2)$$

where λ_a are the $\text{SU}(3)_{\text{color}}$ Gell-Mann matrices and q the quark field vectors. Furthermore, g is the strong coupling constant, $G_{\mu\nu}^a$ are the gluon field-strength tensors, A_μ^a are the gluon fields, and the diagonal quark-mass matrix is given by $\mathcal{M} = \text{diag}(m_{\mu,\nu})$.

Since the two lightest quarks are almost massless ($m_u = (2.5 \pm 0.8) \text{ MeV}/c^2$, $m_d = (5 \pm 0.9) \text{ MeV}/c^2$) [40], compared to the hadronic scale of $1 \text{ GeV}/c^2$, the Lagrangian in the two-flavor case (1) is approximately invariant under independent global flavor rotations of the left- and right-handed quark fields. The corresponding symmetry group $SU(2)_L \times SU(2)_R$ is referred to as the $SU(2)$ chiral group [41, 42]. By virtue of Noether's theorem there are six conserved currents, which can be expressed in terms of vector- and axial-vector currents. The conserved vector currents are manifest in the mass degeneracy of the isospin multiplets, which is explicitly broken to a small extent due to the non-vanishing u and d quark masses. While the QCD Lagrangian is invariant under the axial-vector transformations, the ground state has not the corresponding symmetry property, hence, the axial-vector subgroup of the chiral symmetry group is spontaneously broken. Evidences for this spontaneous symmetry breaking can be found in the hadron spectrum, where one does not observe degenerate masses for hadrons with identical quantum numbers except for opposite parity. These mass-degenerated hadron partners would be predicted from the axial-vector symmetry. Another strong indication is the existence of the unnaturally (in comparison with other hadrons) light pseudoscalar mesons. These mesons, also known as pions, can be identified as the three Nambu-Goldstone bosons of the spontaneous chiral-symmetry breakdown. Goldstone's theorem [43, 44] predicts massless bosons for the vacuum excitations, that are caused by spontaneously broken symmetries. The fact that pions do not have vanishing masses is an indication for the slight explicit breaking of chiral symmetry due to non-vanishing quark masses. Note, that the discussion above can be extended to further hadrons by including the strange quark s , with the corresponding chiral symmetry group $SU(3)$ rather than $SU(2)$. Due to the larger mass of the s quark ($m_s = (101 \pm 25) \text{ MeV}$) [40] compared to the u and d quarks, chiral symmetry is only valid to a lesser extent and the additional five Nambu-Goldstone bosons, namely the kaons and the eta meson, have a larger mass than the pions [45].

After the introduction of the spontaneously broken chiral symmetry (see [46, 47] for more detailed discussions), we discuss the idea of chiral perturbation theory (ChPT). While the strong interaction between colored objects is weak at short distances or high momenta ("asymptotic freedom") [48], it is strong at large distances or low momenta, leading to the confinement of quarks into colorless hadrons. Therefore, QCD is highly non-perturbative at low energies, where nuclear physics resides. In addition, the nuclear force corresponds to a residual color interaction similar to the van-der-Waals force between neutral atoms, which complicates the description in terms of quarks and gluons [49]. Fortunately, there is a conspicuous separation of scales, when considering the lightest mesons, i.e., the pions predicted by the spontaneous chiral symmetry breaking. The pion mass $m_\pi \approx 140 \text{ MeV}/c^2$ is much smaller than the mass of other vector mesons like $m_\rho \approx 770 \text{ MeV}/c^2$ or $m_\omega \approx 782 \text{ MeV}/c^2$ [50].

Thus, one can develop an effective theory at low energies using pions and nucleons as relevant degrees of freedom, where the pion mass sets the soft scale Q , and the rho mass sets the hard

scale, also known as the chiral symmetry breaking scale. A perturbative scheme can be applied to the theory by an expansion in terms of $\left(\frac{Q}{\Lambda_\chi}\right)^\nu$, where the power ν is the corresponding expansion order. This scheme is also known as chiral perturbation theory (ChPT) and we summarize the basic concept of the chiral EFT by making use of this scheme. According to Steven Weinberg one has to write down the most general Lagrangian consistent with the symmetries and symmetry breakings of low-energy QCD [7, 51] using pions and nucleons as effective degrees of freedom. The effective chiral Lagrangian includes the following contributions

$$\mathcal{L}_{\text{eff}} = \mathcal{L}_{\pi\pi} + \mathcal{L}_{\pi N} + \mathcal{L}_{NN} \dots, \quad (3)$$

where the ellipsis corresponds to terms involving two nucleons plus pions and three or more nucleons, with and without pions.

One can organize the contributions to the chiral Lagrangian in terms of increasing values of the parameter $\Delta = d + n/2 - 2$, where d is the number of derivatives or pion-mass insertions and n is the number of nucleon fields. The terms of the Lagrangian in Eq. (3) necessary to derive nuclear forces up to $\nu = 4$ are given by ¹

$$\mathcal{L}^{\Delta=0} = \mathcal{L}_{\pi\pi}^{(2)} + \mathcal{L}_{\pi N}^{(1)} + \mathcal{L}_{NN}^{(0)} \quad (4)$$

$$\mathcal{L}^{\Delta=1} = \mathcal{L}_{\pi N}^{(2)} + \mathcal{L}_{NN}^{(1)} \quad (5)$$

$$\mathcal{L}^{\Delta=2} = \mathcal{L}_{\pi\pi}^{(4)} + \mathcal{L}_{\pi N}^{(3)} + \mathcal{L}_{NN}^{(2)} + \dots \quad (6)$$

$$\mathcal{L}^{\Delta=4} = \mathcal{L}_{NN}^{(4)} + \dots, \quad (7)$$

where the superscript in parentheses correspond to the number of derivatives or pion-mass insertions d . As example one can consider the leading order term of the NN Lagrangian

$$\mathcal{L}_{NN}^{(0)} = -\frac{1}{2}c_S \bar{N}N \bar{N}N - \frac{1}{2}c_T (\bar{N}\vec{\sigma}N) \cdot (\bar{N}\vec{\sigma}N), \quad (8)$$

where the nucleon fields are represented by N and $\vec{\sigma}$ denotes the spin operator. The unknown constants c_S and c_T are discussed in Sec. 1.2.

Finally, Weinberg designed an organizational scheme, defining the importance or order ν of the appearing contributions [7, 51] (see also [47] for a comprehensive presentation of the chiral EFT approach). In Fig. 1.1 the diagrammatic contribution for the chiral NN, 3N, and 4N forces are illustrated for the chiral orders up to $\nu = 4$.

For an irreducible diagram that involves A nucleons (see Fig. 1.1), the chiral order ν is determined by the so-called ‘‘power counting’’ [52]

$$\nu = -4 + 2A + 2L + \sum_i \Delta_i \quad \text{with} \quad \Delta_i = d_i + \frac{n_i}{2} - 2, \quad (9)$$

¹The quoted Lagrangians are written in the heavy baryon formalism (see [47] for a more detailed description).

where the sum runs over all vertices i contained in the diagram, L is the number of loops, d_i is the number of derivatives or pion-mass insertions and n_i is the number of nucleon fields at the vertex i . The terms in the Lagrangian are related to the vertices of the nuclear force diagrams in Fig. 1.1 and can be used for the derivation of the nuclear potential.

For $\nu = 0$, that means at leading order (LO), the NN force is defined by the static one-pion exchange diagram, as well as a two-nucleon contact diagram with a small-dot ($\Delta = 0$) vertex. The related Lagrangian $\mathcal{L}_{NN}^{(0)}$ in Eq. (8) leads to the following contact potential in momentum representation

$$V_{ct}^{(0)}(\vec{\Pi}', \vec{\Pi}) = c_S + c_T \vec{\sigma}_1 \cdot \vec{\sigma}_2, \quad (10)$$

where $\vec{\Pi}'$ and $\vec{\Pi}$ are the initial and final relative momenta and $\vec{\sigma}_i$ denotes the spin of the particle i . For $\nu = 1$, all contributions vanish due to parity and time-reversal invariance. At next-to-leading order (NLO) with $\nu = 2$, besides diagrams including pion exchanges such as the two-pion exchange term, which occurs for the first time, there are seven contact terms. The next-to-next-to-leading order (N²LO, $\nu = 3$) contains a rich NN structure and, in addition, also 3N forces, whose effects in nuclear structure are investigated in detail in this work. Furthermore, the next chiral order, i.e., the next-to-next-to-next-to-leading order (N³LO) does not only contain a large number of NN and 3N contributions, but also four-nucleon (4N) contributions appear for the first time.

An important practical point of the chiral expansion is the finite number of diagrams at given order ν . The next order provides a rough estimate of the missing contributions. Thus, the chiral forces, in principle, can be calculated to any desired accuracy by increasing the order [47]. It is worth mentioning that to the systematically improvable character of chiral EFT, also allows to generate NN, 3N, and many-nucleon forces in a consistent scheme [53].

1.2 Regularization, Renormalization and Parameter Fit

Chiral EFT is constructed through a low-momentum expansion and is valid only at low energies, where nuclear structure processes are expected to take place. In fact, to avoid infinities, e.g., when solving the Lippmann-Schwinger equation, it is necessary to suppress high-momentum contributions in the chiral potential by introducing certain regularizations, e.g., by multiplying the potential with a regulator function [47]. There are different choices for the regular function, as discussed in Sec. 1.3. Besides variations in the details, generally one uses an exponential regulator function of the form

$$f(Q, \Lambda) = \exp\left[-\left(\frac{Q}{\Lambda}\right)^{2n}\right], \quad (11)$$

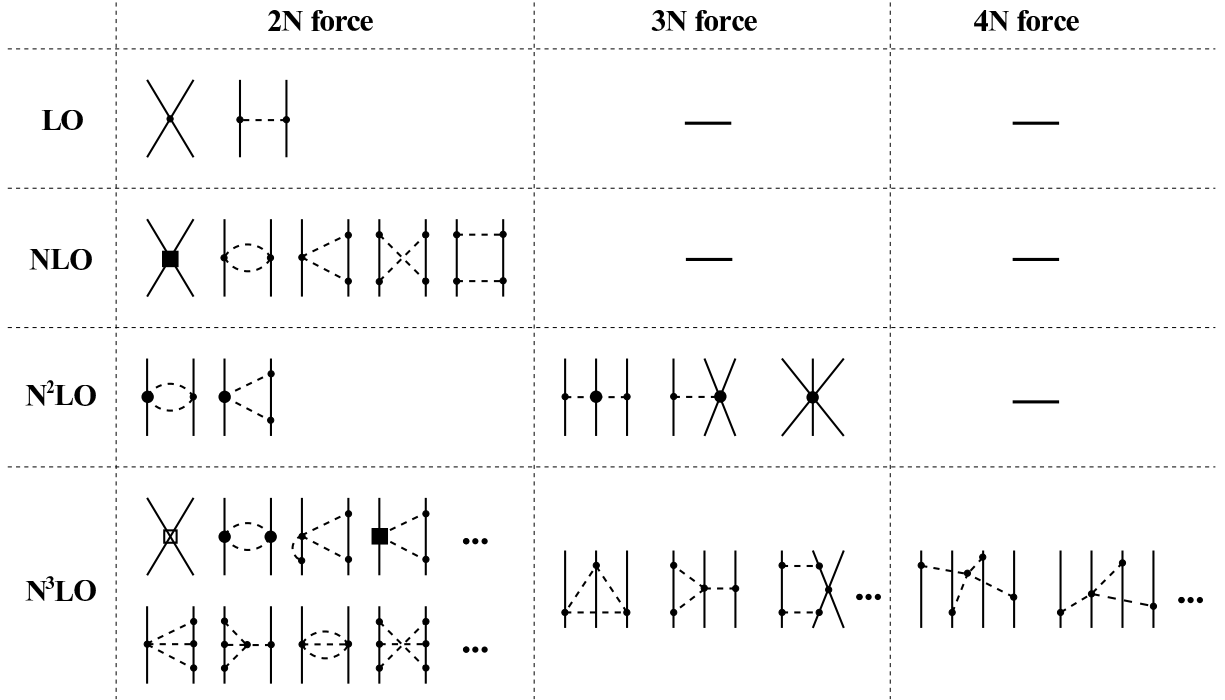


Figure 1.1 *Hierarchy of nuclear forces in chiral EFT [54]*: The interaction diagrams up to N³LO arranged by the particle rank of the interaction. Dashed lines represent pions and the solid lines nucleons. Small dots, large solid dots, solid squares and open squares denote vertices with $\Delta = 0, 1, 2$ and 4, respectively.

with the chiral cutoff momentum Λ , a quantity Q related to the nucleon momentum, and the integer n large enough to ensure that the regulator introduces only contributions beyond the given chiral order, i.e., $n \geq 3$ for an interaction at N³LO. Ideally, the theory should not depend on the applied regulator or cutoff, Weinberg's implicit assumption was that the incorporated contact terms (also called counterterms) can be used to renormalize the theory and remove dependencies on the regularization and cutoff [52]. Renormalizable quantum-field theories, such as the quantum electrodynamics, have essentially one set of prescriptions that take care of the renormalization through all orders. In contrast, chiral EFT is renormalized order by order, such that its parameters, the low-energy constants (LECs), need to be readjusted when increasing the chiral order.

Naively, the perfect renormalization should provide stable results even when taking the cutoff to infinity. Investigations along these lines [55–58] have shown that the existing counterterms are not sufficient to allow for the application of cutoff parameters considerably larger than the chiral breakdown scale. A possible solution for this problem can be found in [59], where an alternative to the Weinberg power-counting scheme is discussed. In this scheme many-body calculations are performed using the LO potential, while the subleading orders are added perturbatively in a distorted wave Born approximation. So far, there are some disadvantages of this approach, which might prevent the production of accurate interactions for nuclear few- and

many-body problems [47]. First of all, this scheme uses more counterterms, which reduces the predictive power. Secondly, this scheme will presumably show a slower convergence with respect to the chiral order, and most importantly it is expected that the interaction will incorporate an unnaturally large tensor contribution, that could prevent reliable applications [47].

Throughout this thesis we investigate interactions obtained within the Weinberg power counting scheme and stick to the philosophy of Lepage [60], by using momentum cutoffs between 300 and 700 MeV/c, large enough to keep the physical relevant content of the interaction, but not beyond the validity of the EFT, corresponding to the chiral breakdown scale $\Lambda_\chi \approx 1$ GeV/c. Having defined the power-counting scheme, the regularization, and the cutoff, we are left with the determination of the LECs, that are the free parameters of the chiral EFT. Commonly the parameters of the NN interaction are determined in two-body systems by using scattering phase shifts and deuteron properties for the fit procedure, while the new LECs appearing in the 3N interactions are typically fitted to three- and four-body systems, as discussed in Sec. 1.3. It is crucial to note that the LECs, in particular those of the contact terms, are used to renormalize the theory and, in addition, to account for the effects of omitted degrees of freedom, e.g., heavier meson exchanges, as well as contributions from subleading chiral orders. In principle the LECs can be quantified from lattice QCD calculations (see [61] for a recent review), but there are still open issues and the calculations are computationally demanding. Therefore, the practicable chiral NN and 3N interactions presented in Sec. 1.3 are obtained from fitting the LECs to experiment.

1.3 Present Chiral NN+3N Interactions

In the following we introduce the available chiral NN and 3N interactions by discussing the chiral order, the LECs, and the regularization procedure that determine the forces. We introduce the NN and 3N forces separately and present the commonly used NN+3N combinations in Sec. 1.3.3, but in principle there are also other combinations, which could be constructed from the NN and 3N potentials. Since the LECs of the 3N interactions depend on the NN interaction the parameters of the 3N forces are presented in context of the underlying NN force in Sec. 1.3.3. In this work we perform a comprehensive investigation of the 3N-force parameters, while using fixed NN potentials introduced in Sec. 1.3.1. There are several reasons for this: First of all, this work concentrates on the efficient application and investigation of chiral 3N forces in nuclear structure calculations. Secondly, the chiral 3N force effects are rather unknown beyond the lightest systems, since these forces became available over the recent years only. Moreover, apart from the influence of the NN force, the 3N interactions at N²LO only depend on the regularization, and two new LECs, while the NN force at N³LO contains 26 LECs from the contact terms (two of them are charge dependent) and eight LECs originating from the π N vertices [8]. Thus, refitting the parameters of the 3N force is straightforward and can be iterated

multiple times, but it is a highly demanding procedure for the NN force and to some extent still an open issue. Nevertheless, for a complete investigation of the chiral NN+3N interaction also variations of the NN force parameters are desirable and efforts for improvements towards a systematic fit procedure are under way [11].

1.3.1 Chiral NN Interactions

In this section we briefly present the chiral NN interactions used in this work. We summarize the regularization and LEC fit procedure as well as important properties of the interactions.

Standard NN Interaction at N³LO. The most commonly used NN interaction in nuclear structure physics is the Idaho NN interaction by Entem and Machleidt [8], obtained at N³LO. For this potential a regulator function of the following form is used

$$f(\Lambda, \Pi, \Pi') = \exp \left[- \left(\frac{\Pi}{\Lambda} \right)^{2n} - \left(\frac{\Pi'}{\Lambda} \right)^{2n} \right], \quad (12)$$

where Π and Π' denote the magnitude of the initial and final relative momentum, respectively. A Taylor series expansion of this regulator

$$f(\Lambda, \Pi, \Pi') = 1 - \left[- \left(\frac{\Pi}{\Lambda} \right)^{2n} - \left(\frac{\Pi'}{\Lambda} \right)^{2n} \right] + \dots, \quad (13)$$

indicates that the exponential regulator produces only contributions of higher chiral order, as long as n is chosen appropriately large. For the regularization of this interaction at N³LO, that we refer to as our “*standard*” NN interaction, the power is used rather flexible with the constraints $n \geq 3$ at LO and $n \geq 2$ at NLO and higher chiral orders, such that the regulator generates exclusively contributions beyond the order N³LO ($\nu = 4$).

Finally, the LECs have to be fit. Besides eight LECs, the pion-exchange contributions depend on the axial-vector coupling and the pion-decay constant, which are chosen to be $g_A = 1.29$ and $f_\pi = 92.4 \text{ MeV}$, respectively. Since five of these LECs do not have a large effect on NN systems [8], they are determined by πN scattering data [62, 63]. The remaining three LECs c_1, c_3, c_4 of the pion-exchange contributions, together with the 26 LECs of the contact terms that are fitted to neutron-proton (np) and proton-proton (pp) data below 290 MeV, obtaining $c_1 = -0.81 \text{ GeV}^{-1}$, $c_3 = -3.20 \text{ GeV}^{-1}$, $c_4 = 5.40 \text{ GeV}^{-1}$ [8].² The resulting χ^2/datum is 1.10 for the np data and 1.50 for the pp data up to 290 MeV [8]. The accuracy for the reproduction of the NN data is comparable to one of so-called phenomenological high-precision NN potentials, such as the Argonne V18 [2] or the CD-Bonn [3] potential.

²In comparison one obtains $c_1 = -0.81 \text{ GeV}^{-1}$, $c_3 = -4.69 \text{ GeV}^{-1}$, $c_4 = 3.40 \text{ GeV}^{-1}$ from a fit to πN scattering data [62].

Epelbaum NN Interactions at N²LO and N³LO. The NN interactions by Epelbaum, Glöckle, and Meißner are obtained at N²LO [9] and at N³LO [10], and we refer to this interaction as “Epelbaum” NN interaction. For both chiral orders the exponential regulator (12) as for the Idaho NN interaction is used, but with a fixed power $n = 3$. In addition to the exponential regularization also a so-called spectral-function regularization (SFR) of the two-pion exchange (2PE) contributions is applied to remove the corresponding short-distance contributions [9, 64]. To this purpose one uses the momentum-dependent components $W(q)$ of the 2PE potential, which can be treated separately for the isoscalar and isovector central, spin-spin and tensor contributions and represents this function $W(q)$ by a continuous superposition of Yukawa functions

$$W(q) = \frac{2}{\pi} \int_{2m_\pi}^{\infty} d\mu \mu \frac{\sigma(\mu)}{\mu^2 + q^2}, \quad (14)$$

with the momentum transfer $q = |\vec{q}| = |\vec{p}' - \vec{p}|$, where \vec{p} and \vec{p}' are the initial and final momenta of the nucleon and $\sigma(\mu)$ is the spectral function, which contains the whole dynamics of the 2PE contribution [64]. The SFR suppresses the contributions of large μ via a sharp cutoff $\hat{\Lambda}$ using a Heaviside function

$$\sigma(\mu) \mapsto \theta(\hat{\Lambda} - \mu)\sigma(\mu). \quad (15)$$

This additional cutoff regulates the short-distance contributions of the 2PE term, leading to improved convergence with respect to the chiral order [9, 64]. The LECs $c_1 = -0.81 \text{ GeV}^{-1}$ and $c_4 = 3.40 \text{ GeV}^{-1}$ is fitted to πN scattering data [62], while $c_3 = -3.4 \text{ GeV}^{-1}$ is chosen consistently with NN phase shifts and is at the lower side of the result obtained in Ref. [62]. For a more detailed discussion of the fit procedure see Refs. [9] and [10].³

In Ref. [9] it has been found, that a cutoff momentum of $\Lambda = 650 \text{ MeV}/c$ is already rather close to its critical value, such that one encounters spurious deeply-bound states for larger cutoff momenta. Note that additionally the values of various LECs start to strongly vary for cutoffs in the range and beyond this critical value. The Epelbaum NN interactions at both chiral orders applied in this work are constructed for five different cutoff combinations, with $\Lambda = 450 \dots 600 \text{ MeV}/c$, while $\hat{\Lambda}$ is varied independently in the range $500 \dots 700 \text{ MeV}/c$, allowing for investigations of the effect of the regularization in nuclear structure calculations and, thus, to draw conclusions about the theoretical uncertainties originating from the interaction.

The resulting NN interactions at N²LO have a χ^2/datum at the order of 10 for the np-scattering data up to 290 MeV, while the pp data is reproduced with even less accuracy [9] and are not as precise as the description of the scattering data for the Idaho NN interaction. Increasing the chiral order to N³LO improves this description and leads to an accurate NN potential [10].

³In addition to the regularization and fit procedure, the Epelbaum NN interactions differ from the standard NN interaction by the treatment of relativistic corrections. See Ref. [45] and references therein.

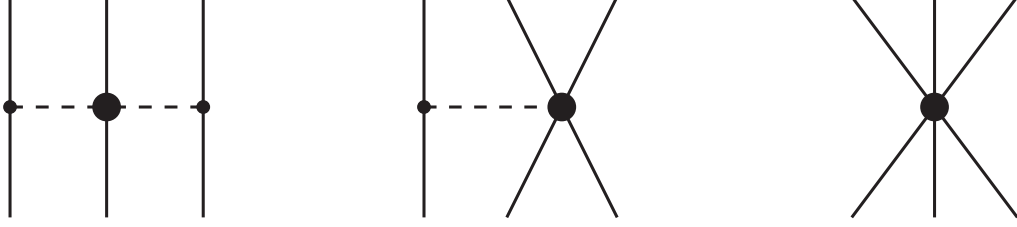


Figure 1.2 $3N$ forces at N^2LO [47]: The diagram on the left corresponds to the two-pion exchange terms depending on the LECs c_1, c_3, c_4 , in the middle we see the one-pion exchange plus two-nucleon contact term depending on c_D and on the right the three-nucleon contact term, which depends on c_E , is depicted. The vertices are defined as in Fig. 1.1.

POUNDER NN Interaction at N^2LO . The optimized chiral NN interaction by Ekström et. al [11] is obtained at N^2LO and is a recent example for the necessity of an optimized systematic LEC fit. The fits have been performed with the Practical Optimization Using No Derivatives (for Squares) algorithm (POUNDER) [65] to optimize the values of pion-nucleon (πN) couplings c_1, c_3, c_4 , as well as the 11 contact parameters to describe the experimental phase shifts from the Nijmegen partial-wave analysis [66]. We refer to this interaction as “POUNDER” NN interaction. For the regularization an exponential regulator (12) with power $n = 3$, cutoff $\Lambda = 500 \text{ MeV}/c$ and an additional SFR with $\hat{\Lambda} = 700 \text{ MeV}/c$, as for the Epelbaum interactions is used. The χ^2/datum are considerably improved compared to the Epelbaum interactions at N^2LO . For the description of the np data up to 290 MeV a χ^2/datum of around 3 is achieved. From these fits the LECs of the 2PE 3N force are determined as $c_1 = -0.92 \text{ GeV}^{-1}$, $c_3 = -3.89 \text{ GeV}^{-1}$, and $c_4 = 4.31 \text{ GeV}^{-1}$ [11].

1.3.2 Chiral 3N Interactions at N^2LO

Since one of the major purposes of this thesis is the inclusion and investigation of the 3N forces initially obtained at N^2LO (the expressions are derived in [67]), we concentrate on the corresponding diagrams, depicted in Fig. 1.2. The 2PE term, which is related to the Fujita-Miyazawa term [68], contains the long-range part of the 3N force. The corresponding potential in a momentum basis representation is given by [12, 69]

$$V_{2PE}^{3N}(\vec{q}_1, \vec{q}_2, \vec{q}_3) = \left(\frac{g_A}{2f_\pi} \right)^2 \frac{1}{2} \sum_{i \neq j \neq k} \frac{(\vec{\sigma}_i \cdot \vec{q}_i)(\vec{\sigma}_j \cdot \vec{q}_j)}{(q_i^2 + m_\pi^2)(q_j^2 + m_\pi^2)} F_{ijk}^{\alpha\beta} \tau_i^\alpha \tau_j^\beta, \quad (16)$$

with

$$F_{ijk}^{\alpha\beta} = \delta^{\alpha\beta} \left[-\frac{4c_1 m_\pi^2}{f_\pi^2} + \frac{2c_3}{f_\pi^2} \vec{q}_i \cdot \vec{q}_j \right] + \frac{c_4}{f_\pi^2} \varepsilon^{\alpha\beta\gamma} \tau_k^\gamma \vec{\sigma}_k \cdot [\vec{q}_i \times \vec{q}_j], \quad (17)$$

the one-pion exchange (1PE) plus two nucleon contact potential can be written as

$$V_{1PE}^{3N}(\vec{q}_1, \vec{q}_2, \vec{q}_3) = -c_D \frac{g_A}{8f_\pi^4 \Lambda_\chi} \sum_{i \neq j \neq k} \frac{\vec{\sigma}_j \cdot \vec{q}_j}{\vec{q}_j^2 + m_\pi^2} (\vec{\tau}_i \cdot \vec{\tau}_j) (\vec{\sigma}_i \cdot \vec{q}_j), \quad (18)$$

and the three-nucleon contact (ct) interaction reads

$$V_{ct}^{3N}(\vec{q}_1, \vec{q}_2, \vec{q}_3) = c_E \frac{1}{2f_\pi \Lambda_\chi} \sum_{j \neq k} (\vec{\tau}_j \cdot \vec{\tau}_k). \quad (19)$$

Here we use the momentum transfer $\vec{q}_i = \vec{p}'_i - \vec{p}_i$, where \vec{p}_i and \vec{p}'_i are the initial and final momenta of the nucleon i , respectively, and $\vec{\sigma}_i$ denotes the spin and $\vec{\tau}_i$ the isospin of nucleon i . The Latin letters $i, j, k \in \{1, 2, 3\}$ indicate the index of the nucleon, while Greek letters correspond to the isospin components. Further, g_A is the axial-vector coupling, and f_π the pion decay constant. The LECs c_i for $i = 1, 3, 4$ correspond to the 2PE term and already appear in the NN interactions and are fixed by NN systems, while c_D and c_E , the LECs of the 1PE and three-nucleon contact term, respectively, occur exclusively in the 3N force and have to be fit to $A \geq 3$ systems.

After these general considerations of the operator structure, we now introduce the presently available chiral 3N interactions at N^2LO and briefly discuss the numerical evaluation of the interaction matrix elements, which are required for nuclear structure calculations as well as the regularization.

Local 3N Interactions at N^2LO . The “standard” 3N interaction, extensively used in this work as well as by the nuclear structure community in general, has been introduced by Navrátil in Ref. [13]. Besides the specific choice of the physical constants, i.e., $g_A = 1.29$, $f_\pi = 92.4$ MeV, and $\Lambda_\chi = 700$ MeV/c the interaction is characterized by the regularization procedure. As in the two-body case the 3N interaction matrix elements in a certain momentum representation $\langle V^{3N} \rangle$ (see Sec. 3.5) are regularized by multiplying the regulator functions

$$\langle V^{3N} \rangle \longrightarrow F(q_2, \Lambda_{3N}) \langle V^{3N} \rangle F(q_3, \Lambda_{3N}), \quad \text{with} \quad F(q, \Lambda_{3N}) = \exp\left[-\left(\frac{q}{\Lambda_{3N}}\right)^{2n}\right], \quad (20)$$

where $n = 2$ is being used. The quantities q_2 and q_3 are the magnitudes of the momentum transfer of the second and third nucleon, respectively. The momentum transfer is defined by

$$\begin{aligned} \vec{q}_2 &= \vec{p}'_2 - \vec{p}_2, \\ \vec{q}_3 &= \vec{p}'_3 - \vec{p}_3, \end{aligned} \quad (21)$$

where \vec{p} and \vec{p}' correspond to the bra (final) and ket (initial) state of the matrix element, respectively. Note, the regulator function can be easily expressed as function of the Jacobi momenta by using relation (49) introduced in Sec. 3.1. Due to the special choice of the regulator

the spatial locality of the operator structure is maintained. The local character of the regularized 3N interaction has advantages for certain few- and many-body approaches, depending on the applied basis representation. For the application in this thesis we rely on the harmonic-oscillator (HO) representation of the potential (see Sec. 3.1.2), such that we do not exploit the locality explicitly. However, the locality is utilized to derive the analytical expression of the 3N interaction matrix elements in Ref. [13] and allows for an efficient numerical evaluation, which is performed by Petr Navrátil’s MANYEFF code [70]. Hence, we have access to the 3N interaction contributions in the Jacobi-HO representation for very large model spaces, without introducing additional truncations regarding the angular-momenta of the partial waves. These matrix elements are the starting point for the studies of the 3N force effects in this work.

Non-Local 3N Interactions at N²LO. Another chiral 3N interaction at N²LO, that is commonly applied to few-body [12] and neutron-matter [71–73] calculations, but rather untested in nuclear structure calculations, is developed by Epelbaum and collaborators [12]. Besides a slightly distinct value for the axial-vector coupling of $g_A = 1.26$, the major difference to the previous chiral 3N interaction is the regularization. As before the interaction matrix elements are multiplied by a regulator function [12]

$$\langle V^{3N} \rangle \longrightarrow f(\pi_1, \pi_2, \Lambda_{3N}) \langle V^{3N} \rangle f(\pi'_1, \pi'_2, \Lambda_{3N}), \quad (22)$$

explicitly defined in terms of the Jacobi momenta $\vec{\pi}_1$ and $\vec{\pi}_2$ (see Sec. 3.1)

$$f(\pi_1, \pi_2, \Lambda_{3N}) = \exp\left[-\left(\frac{\pi_1^2 + \pi_2^2}{(2\Lambda_{3N})^2}\right)^n\right]. \quad (23)$$

Throughout this work we choose the exponent to be $n = 3$ as in Ref. [42, 74], while also different values have been employed in the literature (e.g., see Ref. [12]). The explicit Jacobi momentum dependence of the regulator (23) destroys the spatial locality of the operator structure and yields a non-local 3N potential. In contrast to the local “standard” 3N interaction of the previous section, the unregularized Cartesian momentum-space operators are evaluated in the partial-wave decomposed momentum representation. The regularization is performed subsequently at essentially no additional cost, allowing for a flexible adjustment of the regulator function. Eventually, we transform the regularized partial-wave decomposed momentum matrix elements into the Jacobi-HO representation. The transformation has been derived and implemented in this thesis and is described in Sec. 3.5.

The numerical calculation of the partial-wave decomposed momentum 3N matrix elements is carried out in an automatized approach proposed by Skibiński et. al [75], called automatized partial-wave decomposition (aPWD), that can be utilized independently of the underlying operator structure, and, in principle, enables the evaluation of the 3N interaction matrix elements at N³LO in a similar manner. The generality of this approach is accompanied with enormous

computational effort. Although the aPWD uses massive parallelization, without exploiting certain properties of the operator structures, e.g., the locality in coordinate space, it requires a five-dimensional integration for the evaluation of each matrix element. Due to the sheer number of required partial-wave decomposed matrix elements this method is restricted to low partial waves. In particular, when aiming at the 3N interaction at N³LO (see Sec. 1.4), where the additional operator structures complicate the evaluation of the integrand, the computational demands of the aPWD become even more severe and there are ongoing efforts within the LENPIC collaboration [76] to generate these matrix elements.

1.3.3 NN+3N Interactions Combinations

Different combinations of the potentials introduced in the previous section define the NN+3N Hamiltonians studied in this work. For all interactions the $c_i = c_1, c_3, c_4$ values are adopted from the NN interaction, while c_D and c_E are fit to $A = 3, 4$ systems. We start with the “standard” chiral NN+3N interactions, where we combine the Idaho NN interaction at N³LO with cutoff momentum 500 MeV/c with the local 3N interaction at N²LO. For the standard three-body cutoff $\Lambda_{3N} = 500$ MeV/c the LECs c_D and c_E are obtained by a fit to the average ground-state energy of ³H and ³He, as well as to the β -decay half-life of ³H [77].

In addition, we introduce NN+3N interactions with a reduced three-body cutoff, where we maintain the Idaho NN interaction with the $\Lambda = 500$ MeV/c cutoff momentum. The c_D value is fixed in order to reproduce the triton β -decay half-life that is rather insensitive to the three-body cutoff. The c_E is fit to the ⁴He ground-state energy of -28.30 MeV with an uncertainty below 10 keV, utilizing the no-core shell model (NCSM) (see Tab. 1.1). Note, that these interactions slightly underbind the triton ground state. A fit to the triton binding energy would lead to a slight overbinding in ⁴He that increases perceptibly with the mass number.

Since the NN and 3N interactions are obtained at different chiral orders, these interactions are inconsistent from the point of view of chiral EFT. Owing to the different regulator functions for the NN and 3N interactions it is questionable if the well established NN+3N interaction with $\Lambda_{3N} = 500$ MeV/c is “more” consistent than the interactions with the reduced cutoff. Moreover, we stress that the reduced cutoff interactions, which are discussed in this thesis, are very successful in applications beyond the mid-p shell (see Sec. 6 and 7).

In the middle of Tab. 1.1 we list the parameters of the NN+3N interaction at N²LO, that we refer to as the “POUNDERs” interactions. The optimized NN interaction is combined with the local 3N potentials.⁴ As for the standard interaction c_D is fit to the triton β -decay half-life, and for $\Lambda_{3N} = 500$ MeV/c we adjust c_E to the $A = 3$ ground-state energies, while for the reduced cutoff $\Lambda_{3N} = 400$ MeV/c it is fit to the ⁴He ground-state energy [78]. Note that the NN+3N

⁴Note, there is no established combination of the POUNDERs NN interaction with a certain 3N force and, in principle, one can also combine this NN potential with the non-local 3N forces.

interaction with the larger Λ_{3N} slightly overbinds the ${}^4\text{He}$ ground state by less than 200 keV.

The third type of NN+3N interactions is summarized on the bottom of Tab. 1.1, where the Epelbaum NN potentials are combined with the non-local 3N potentials consistently at $N^2\text{LO}$. In the following we refer to them as “Epelbaum” interactions. The fits for the five cutoff combinations have been performed to the coherent neutron-deuteron scattering length b_{nd} and the triton ground-state energy [42, 79]. For the cutoff combination (600/500) MeV/c a rather large value for c_D is obtained. This might indicate that $\Lambda = 600$ MeV/c is already too close to the critical value, where spurious bound states violate the naturalness of the LECs. We probe if this might affect spectra of p-shell nuclei in Sec. 8.2.

We do not use the last interaction combination of the Epelbaum NN+3N potential, but list the parameter in the table for completeness. While the standard interactions, also with the reduced three-body cutoffs, are used in various investigations throughout this work, the POUNDerS as well as the Epelbaum interactions are investigated in Sec. 8.2.

In principle, one can construct other combinations, e.g., the Idaho NN plus non-local 3N interaction, that have been applied in [80]. Such a combination might be of particular interest, because the Idaho NN potential at $N^3\text{LO}$ provides a high-precision description of the NN data and has proven to be successful in nuclear structure calculations. Furthermore, the regularization of the non-local 3N interactions uses a consistent regulator function. Nevertheless, the standard NN+3N interaction seems to provide results, that show better experimental agreement for mid-p-shell nuclei [13, 80, 81] and we restrict ourselves to the interactions presented in Tab. 1.1.

1.4 Next-Generation Chiral NN+3N Interactions

The techniques developed in this thesis allow for an efficient application of the present chiral NN+3N interactions, as well as upcoming new interactions to nuclear structure calculations. An important example are the consistent NN+3N interaction at $N^3\text{LO}$, by combining the Epelbaum NN interaction with the 3N interactions that are recently generated within the LENPIC collaboration, by an improved matrix-element evaluation approach [82]. This approach performs the partial-wave decomposition efficiently utilizing properties of the operator structures, e.g., the locality in coordinate space. The regularization and antisymmetrization are performed afterwards during the transformation to HO representation as discussed in Sec. 3.5.

The chiral 3N interaction at $N^3\text{LO}$ is much more complex than the one at $N^2\text{LO}$. In addition to the subleading contributions of the two-pion exchange topology, there are further long-range contributions such as the two-pion-one-pion exchange topology and so-called ring diagrams [83]. Moreover, also relativistic corrections and short-range contributions appear, such as the one-pion-exchange-contact and the two-pion-exchange-contact topology [84]. Besides the non-local relativistic corrections, we add these contributions to the 3N interaction at $N^2\text{LO}$. Note that

standard interactions						
NN at N ³ LO	local 3N at N ² LO					
Λ [MeV/c]	Λ_{3N} [MeV/c]	c_1 [GeV ⁻¹]	c_3 [GeV ⁻¹]	c_4 [GeV ⁻¹]	c_D	c_E
500	500	-0.81	-3.2	+5.4	-0.2	-0.205
500	450	-0.81	-3.2	+5.4	-0.2	-0.016
500	400	-0.81	-3.2	+5.4	-0.2	+0.098
500	350	-0.81	-3.2	+5.4	-0.2	+0.205

POUNDERs interactions						
NN at N ² LO	local 3N at N ² LO					
$(\Lambda/\hat{\Lambda})$ [MeV/c]	Λ_{3N} [MeV/c]	c_1 [GeV ⁻¹]	c_3 [GeV ⁻¹]	c_4 [GeV ⁻¹]	c_D	c_E
(500/700)	500	-0.9186	-3.8887	+4.3103	-0.39	-0.398
(500/700)	400	-0.9186	-3.8887	+4.3103	-0.40	-0.2812

Epelbaum interactions						
NN at N ² LO	non-local 3N at N ² LO					
$(\Lambda/\hat{\Lambda})$ [MeV/c]	(Λ_{3N}) [MeV/c]	c_1 [GeV ⁻¹]	c_3 [GeV ⁻¹]	c_4 [GeV ⁻¹]	c_D	c_E
(450/500)	450	-0.81	-3.40	+3.40	-0.14	-0.319
(600/500)	600	-0.81	-3.40	+3.40	-4.71	-2.124
(550/600)	550	-0.81	-3.40	+3.40	-0.45	-0.798
(450/700)	450	-0.81	-3.40	+3.40	-2.43	-0.113
(600/700)	600	-0.81	-3.40	+3.40	-2.00	-1.074

Table 1.1 *Parameter for the chiral 3N interaction at N²LO:*

Summarized are the three-body LECs and cutoffs for the NN+3N interactions used in this work. The upper table lists the parameters of the local 3N interaction, that are combined with the Idaho NN interaction at N³LO with cutoff momentum of 500 MeV/c. Besides the standard NN+3N interaction ($\Lambda_{3N} = 500$ MeV/c) we introduce modifications of this interactions with reduced three-body cutoffs. The middle table shows the combined POUNDERs potentials of the optimized NN plus local 3N interactions and the lower table lists the parameters of the Epelbaum interactions, where the NN interaction by Epelbaum, Glöckle, and Meißner is combined with the non-local 3N interaction for five different cutoff combinations. See text for further information.

next-generation Epelbaum interaction						
NN at N ³ LO	non-local 3N at N ³ LO					
($\Lambda/\tilde{\Lambda}$) [MeV/c]	(Λ_{3N}) [MeV/c]	\tilde{c}_1 [GeV ⁻¹]	\tilde{c}_3 [GeV ⁻¹]	\tilde{c}_4 [GeV ⁻¹]	c_D	c_E
(450/500)	450	-0.94	-2.51	+2.51	-13.442	+0.206

Table 1.2 *Parameters for the next-generation chiral 3N interaction at N³LO:*

In this table the LECs and cutoffs for the non-local 3N interactions that are combined with the NN by Epelbaum, Glöckle, and Meißner at N³LO with a cutoff combination of (450/500) MeV/c are listed [14].

no additional LECs appear at N³LO. The subleading two-pion exchange contributions, can be partially absorbed by a shift of the c_i values [75, 83, 85]

$$\begin{aligned}
 \tilde{c}_1 &= c_1 - \frac{g_A^2 m_\pi}{64\pi f_\pi^2}, \\
 \tilde{c}_3 &= c_3 + \frac{g_A^4 m_\pi}{16\pi f_\pi^2}, \\
 \tilde{c}_4 &= c_4 - \frac{g_A^4 m_\pi}{16\pi f_\pi^2},
 \end{aligned} \tag{24}$$

where we adopt c_1 , c_3 , and c_4 from the NN potential [10]. Furthermore, the two-pion-exchange-contact topology depends on the LEC $c_T = -0.45 \text{ GeV}^{-1}$, that already appears in the NN contact potential (10), and is fixed by NN data [10]. Thus, we are left with the determination of c_D and c_E that are fit to the triton ground-state energy and the neutron-deuteron doublet scattering length a_{nd} [14]. The relevant parameters of the NN+3N interaction are summarized in Tab. 1.2.

In Sec. 9 we show the first application of the consistent NN+3N interaction at N³LO in nuclear structure calculations for the p-shell nuclei, which provides an outlook of future applications and, in addition, allows for a systematic estimation of the convergence with respect to the chiral order. In this context it is worthwhile to mention that there are still open issues especially regarding the LECs fit of the NN interaction that can influence the 3N force effects. The NN data are not as precisely described as by the standard interaction, which could be the reason for the rather large c_D value necessary to reproduce $A = 3$ observables. Due to the large number of LECs in the NN sector, the present fit procedure needs to be improved. A first step towards a more systematic fit procedure has been demonstrated in [11] for the POUNDerS interaction at N²LO and it is an open question if the procedure can be extended to the N³LO terms in the near future. Such a systematic fit procedure is important regarding the further developments of chiral interactions including the Δ -excitation of the nucleon as an explicit degree of freedom. While the Δ degree of freedom is implicitly considered for the presented chiral interactions via the LECs fit, the so-called Δ -full theory [37] provides a promising approach to improve the

predictive power of the chiral EFT and the convergence with respect to the chiral order. The techniques presented in this work enable the efficient application of such interactions in the future. However, a consistent inclusion of the Δ will also change the NN sector, which requires a reassessment of the LEC fit to the NN data. At the moment such a fit is very time- and man-power consuming.

Thus, for the intermediate term a combination of the Idaho NN potential and the non-local 3N interaction at N³LO could be promising from a practical point of view and would only require a fit of c_D and c_E . However, the long-term goal is to test the chiral NN+3N interaction, with respect to the fundamental EFT quantities, i.e., by a variation of the chiral order and the cutoff consistently for the NN and 3N sector, which among other things requires the generation of several high-accuracy NN interactions.

Finally, it is important to note that at N³LO also chiral 4N forces appear (see Fig.1.1). This means, fully consistent future interactions at this chiral order require the treatment of irreducible 4N interactions. In this work we present the necessary techniques to apply irreducible 4N to nuclear structure calculations, which can be also used for the application of chiral 4N forces.

2 Ab Initio Many-Body Methods

Ab initio many-body methods are of particular importance for nuclear structure and reaction theory. On the one hand, they are indispensable for the investigation of nuclear interaction properties with controlled uncertainties, on the other hand, they allow to assess the quality of approximative approaches and to identify new ab initio candidates, which incorporate physically justified and systematically improvable approximations.

In this section we introduce the ab initio many-body methods that are used in this work. We discuss the concept as well as the application range of these methods, and point out approximations or truncations that are applied during the solution of the many-body eigenvalue problem

$$\mathbf{H}_{\text{int}} |\Psi^{(m)}\rangle = E_m |\Psi^{(m)}\rangle, \quad (25)$$

where $\mathbf{H}_{\text{int}} = \mathbf{T}_{\text{int}} + \mathbf{V}$ is the many-body Hamilton operator, decomposed of the intrinsic kinetic energy $\mathbf{T}_{\text{int}} = \mathbf{T} - \mathbf{T}_{\text{cm}}$ and the nuclear interaction $\mathbf{V} = \mathbf{V}_{\text{NN}} + \mathbf{V}_{\text{3N}} + \mathbf{V}_{\text{4N}} + \dots$, both acting exclusively on the intrinsic part.⁵ The m -th eigenstate is denoted by $|\Psi^{(m)}\rangle$ and the corresponding energy eigenvalue by E_m .

The no-core shell model (NCSM) [70,81,86–89] together with the Green’s function Monte Carlo (GFMC) method [90–92] are famous examples of exact ab initio methods that can solve the many-body eigenvalue problem (25) with quantified and systematic improvable uncertainties. During the past years the NCSM-type methods have been improved towards the description of heavier mass systems. A crucial example is the importance truncated no-core shell model (IT-NCSM). This method bridges the gap in the application range between the aforementioned exact methods and novel ab initio methods, such as the coupled-cluster (CC) method [27–30,93–95], the self-consistent Green’s function methods [31–33], or the in-medium similarity renormalization group (IM-SRG) [34–36].

We start with an introduction of the NCSM in Sec. 2.1 and continue with its extension, namely the IT-NCSM in Sec. 2.2, which is mainly used in this work. Finally we briefly discuss the concept of the coupled-cluster method in Sec. 2.3, which is used for the investigation of heavier nuclei.

⁵Since we are interested on relative or intrinsic properties of the nuclei, we use \mathbf{H}_{int} as the Hamiltonian. Note that the relative part is often referred as intrinsic part and has to be distinguished from the phrase “intrinsic” used in context of, e.g., deformations in mean-field calculations.

2.1 The No-Core Shell Model

The no-core shell model (NCSM) is a special configuration interaction (CI) approach, which is successfully used to solve the many-body eigenvalue problem exactly. For this purpose the NCSM represents the eigenvalue problem (25) in a finite many-body model space, spanned by HO eigenstates $|\Phi_\nu\rangle$ or short HO states.

Due to the special structure of the NCSM model space the HO many-body basis can be constructed in particle coordinates as well as in relative coordinates, also called Jacobi coordinates (see Sec. 3.1). A basis formulation in the latter coordinates has the advantage that the center-of-mass degrees of freedom are separated from the outset. Hence, center-of-mass contaminations are avoided elegantly by the basis choice. Unfortunately, NCSM calculations using antisymmetrized Jacobi bases are generally not feasible for particle numbers larger than $A \approx 7$ (see Sec. 3.1.2 and 3.1.3), i.e., we are typically reliant on a formulation of the many-body basis in single-particle coordinates. In this case the many-body HO states are Slater determinants composed of single-particle HO states. Such many-body states are known as m -scheme states (see Sec. 3.2). In the following we introduce the definition of the NCSM model space that is as beneficial as simple and characterizes the method. The model-space truncation is determined by the so-called unperturbed excitation energy $N_{\max}\hbar\Omega$. The quantity N_{\max} corresponds to the maximal number of HO excitation quanta with respect to the unperturbed Slater determinant required to create a certain basis state $|\Phi_\nu\rangle$. We illustrate this quantity by an example of an ^{16}O basis configuration in Fig. 2.1. The unperturbed Slater determinant is given by the configuration, where the protons and neutrons occupy the lowest HO orbits. Starting from this configuration one can construct HO basis states by exciting nucleons to orbits with a larger single-particle HO energy quantum number e . The NCSM model space for a given N_{\max} is spanned by all HO configurations whose total excitation energy is smaller or equal N_{\max} , i.e.,

$$\sum_{i=1}^A \Delta e_i \leq N_{\max}, \quad (26)$$

where Δe_i corresponds to the number of HO excitation quanta of the nucleon i . As an example we consider the configuration in Fig. 2.1, where a proton is excited by one $\hbar\Omega$ ($\Delta e = 1$) and a neutron by three $\hbar\Omega$ ($\Delta e = 3$) while the remaining nucleons are not excited ($\Delta e = 0$), thus, this basis state is included in all NCSM model spaces with $N_{\max} \geq 4$. We can represent the eigenvalue problem (25) in the NCSM model space and end up with a finite matrix-eigenvalue problem, which can be solved by taking advantage of the sparse Hamilton matrix using the Lanczos diagonalization algorithm. As a result we obtain the eigenenergies of the lowest energy eigenstates, as well as the expansion coefficients $C_\nu^{(m)}$ in the HO basis $|\Phi_\nu\rangle$ that define the

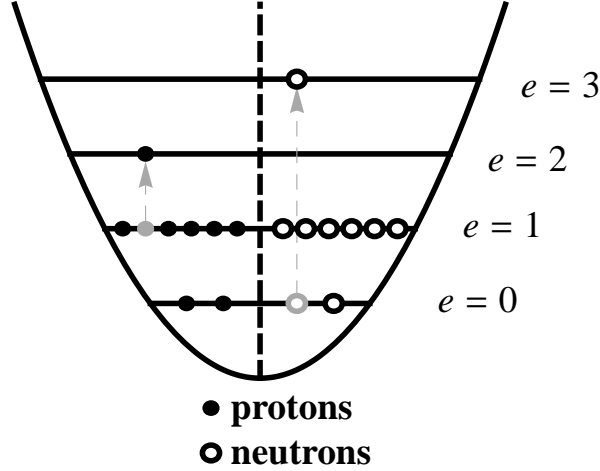


Figure 2.1 *Illustration of the unperturbed excitation energy in the NCSM:* The figure shows a schematic representation of a HO many-body basis configuration for an ^{16}O nucleus. The protons (solid circles) and the neutrons (open circles) occupy the single particle HO shells defined by the energy quantum number e . The illustrated configuration is constructed by a total $4\hbar\Omega$ excitation with respect to the unperturbed ground state and is, thus, contained in all NCSM model spaces with $N_{\max} \geq 4$.

eigenstates

$$|\Psi^{(m)}\rangle = \sum_{\nu} C_{\nu}^{(m)} |\Phi_{\nu}\rangle. \quad (27)$$

We can determine any nuclear observable from the eigenstates by evaluating expectation values or matrix elements between different eigenstates, e.g., in case of transition operators. With increasing N_{\max} the observables converge towards the exact result of the eigenvalue problem that is obtained for $N_{\max} \rightarrow \infty$. To obtain the converged result with NCSM calculations in finite model spaces one uses an extrapolation of the calculated observable for an N_{\max} sequence. Especially in case of absolute eigenenergies the NCSM has the advantage that the Raleigh-Ritz variational principle holds [96]. One of the most important benefits of the NCSM results from the definition of the model space in combination with the HO basis choice. This combination is the reason for the fact that the model space can be equivalently formulated in single-particle or Jacobi coordinates and allows for a factorization of the eigenstates into a center-of-mass part $|\Psi^{(m)}\rangle_{\text{cm}}$ and a relative part $|\Psi^{(m)}\rangle_{\text{int}}$

$$|\Psi^{(m)}\rangle = |\Psi^{(m)}\rangle_{\text{cm}} \otimes |\Psi^{(m)}\rangle_{\text{int}}. \quad (28)$$

As mentioned above by using Jacobi coordinates the center-of-mass degree of freedom can be neglected from the outset, while it is necessary to apply an intermediate step to get rid of center-of-mass excitation when using single-particle coordinates. To suppress the center-

of-mass excitations one adds the Lawson term $\mathbf{H}_{\text{cm}} - \frac{3}{2}\hbar\Omega$ to the Hamiltonian [97], where $\mathbf{H}_{\text{cm}} = \mathbf{T}_{\text{cm}} + \frac{Am_N\Omega^2\mathbf{R}_{\text{cm}}^2}{2}$ corresponds to the center-of-mass HO Hamilton operator of an A -body system, with the HO frequency Ω and the averaged nucleon mass m_N . The latter is used in the following in good approximation for the proton and neutron mass. In practice the eigenvalue problem for the extended Hamiltonian is solved

$$\mathbf{H} = \mathbf{T}_{\text{int}} + \mathbf{V} + \beta\left\{\mathbf{H}_{\text{cm}} - \frac{3}{2}\hbar\Omega\right\}. \quad (29)$$

By increasing the factor β , eigenstates with excited center-of-mass part are shifted to higher energies, such that the energetically lowest eigenstates, which we obtain from the diagonalization, have a center-of-mass contribution in the HO ground state. Therefore, observables obtained in an NCSM calculations do not contain center-of-mass contaminations.

A further advantage of the NCSM formalism becomes obvious when applying modern nuclear potentials, which contain NN, 3N and might even contain 4N interactions. The majority of the present many-body methods need substantial conceptual and technical developments to include 3N forces approach (as the case for IM-SRG [35, 36], Gor'kov-Green's function [32, 33], and CC [28–30, 98, 99] applications). However, NCSM-type approaches have the natural ability to include 3N, 4N and even higher-order forces, with only moderately increasing computational costs. Due to the higher-order interactions the NCSM A -body Hamilton matrix becomes more dense or, stated differently, there are more non-vanishing matrix elements. Thus, the matrix diagonalized by the Lanczos algorithm is less sparse provoking increased computational demands [100].

The sheer number of three-body m -scheme matrix elements sets a severe limit to the accessible model-space sizes. For NCSM calculations of mid-p-shell nuclei with $N_{\text{max}} = 8$ about 33 GB are required to store the 3N interaction matrix elements in single precision [101]. A recent key development for the inclusion of 3N interactions and even of 4N contributions in large model spaces, is the storage of the interaction matrix elements in the so-called JT -coupled scheme, which be discuss in detail in Sec. 3.2. Using this scheme the required storage for the 3N interaction matrix in the aforementioned case reduces to 0.4 GB. The interaction matrix elements stored in the JT -coupled scheme are decoupled on-the-fly during the many-body calculation into the m -scheme. The latter basis representation is ideal to construct the A -body Hamilton matrix utilizing Slater rules [102, 103]. A high performance application of the NCSM approach can be found in Ref. [104] porting the on-the-fly decoupling procedure to accelerator cards.

Having emphasized the advantages of the NCSM we now concentrate on the limitations of this method. The main drawback is the factorial growth of the many-body model-space dimension with particle number A and truncation parameter N_{max} . Today's implementations of the NCSM are able to handle model-space dimensions of $10^9 - 10^{10}$ taking advantage of massive

parallelization. For instance an NCSM calculation of ^{16}O with $N_{\text{max}} = 8$ corresponds to a model-space dimension of about 10^9 . As discussed in the next section such a calculation is not yet sufficiently converged with respect to N_{max} to perform reliable extrapolations to infinite model spaces. Therefore, the NCSM is limited to nuclei in the p-shell. Furthermore, the HO basis is not suited to describe long-range properties, e.g., halo structures, as well as cluster structures, which would require unfeasible large N_{max} for accurate calculations [105].

To overcome the limitation inherent in the HO basis, in particular to extend the NCSM to the long-range physics, alternatives to the standard HO basis are under investigation. Examples are the Coulomb Sturmian basis [106–108], which is obtained from the solution of a Sturm-Liouville problem associated with the Coulomb potential and retains the exponential asymptotics of the Coulomb problem. A further attempt to improve the convergence properties of the NCSM by modifying the underlying HO basis has been also performed as part of this thesis. We generalized the HO basis as proposed by Rowe [109] and applied the basis sets to nuclear structure calculations. Unfortunately, the approach failed, due to the complicated structure of the intrinsic kinetic-energy matrix elements in the generalized HO basis. Thus, we do not present the details of this approach, but refer the interested reader to related Bachelor theses [110, 111]. In addition to these strategies there are approaches that extend the HO model space of the NCSM by long-range basis states, e.g, scattering states used in the NCSM combined with the resonating group method (NCSM/RGM) [24, 112, 113] or the NCSM with continuum (NCSMC) [114, 115]. See Ref. [116] for a detailed discussion of the inclusion of 3N forces in both approaches.

Despite the limited application range of the NCSM, which we address in the next section, it constitutes an indispensable foundation for a broad range of nuclear structure physics. This is due to the fact that the NCSM obtains the exact solution of the intrinsic eigenvalue problem, which can be used as benchmark for approximations concerning many-body methods and the interaction treatment, which is necessary to tackle atomic nuclei significantly beyond the application range of the NCSM.

2.2 Importance Truncated No-Core Shell Model

As discussed in the previous section the NCSM is limited to light nuclei in the p-shell, due to the rapid combinatorial growth of the model space. The importance truncated no-core shell model (IT-NCSM) [21, 117, 118] provides an extension of the NCSM increasing the application range to larger N_{max} and, hence, to larger particle numbers, while keeping all the advantages of the conventional NCSM. The global truncation of the many-body model space, determined by N_{max} , does not account for specific properties of the Hamiltonian or the targeted states. The basic idea of the IT-NCSM is to impose an additional adaptive, physics guided, state and interaction specific truncation that reduces the growth of the model space.

We target at a small number M of eigenstates $|\Psi^{(m)}\rangle$ with $m = 1, \dots, M$ for a certain N_{\max} . The exact result obtained in a conventional NCSM calculation can be expressed by representing the eigenstates in the many-body basis $|\Phi_\nu\rangle$

$$|\Psi^{(m)}\rangle = \sum_{\nu} C_{\nu}^{(m)} |\Phi_{\nu}\rangle. \quad (30)$$

In this expansion a large number of basis states contribute with very small or even vanishing amplitudes $C_{\nu}^{(m)}$. Those basis states have a minor impact on the result and can be treated, e.g., in a perturbative scheme or via other a posteriori approaches that we discuss in the following. By defining an appropriate importance truncation (IT), we aim at the identification and omission of these basis states a priori in order to reduce the model space to the physically relevant states.

We focus initially on the general concept of this method and discuss the practical benefits and limitation subsequently. A more detailed description of the importance selection used in this work is published in Ref. [118]. In addition a realization of a slightly different implementation can be found in Ref. [119]. The starting point of the IT-NCSM are approximations of the targeted states, the so-called reference states $|\Psi_{\text{ref}}^{(m)}\rangle$, that are typically determined by previous NCSM calculations in a feasible model space \mathcal{M}_{ref} . The reference states $|\Psi_{\text{ref}}^{(m)}\rangle$ carry the quantum numbers of the targeted states and are determined by a superposition of the many-body basis states $|\Phi_{\nu}\rangle$, that span the reference space \mathcal{M}_{ref}

$$|\Psi_{\text{ref}}^{(m)}\rangle = \sum_{|\Phi_{\nu}\rangle \in \mathcal{M}_{\text{ref}}} C_{\text{ref},\nu}^{(m)} |\Phi_{\nu}\rangle. \quad (31)$$

Guided by first-order multiconfigurational perturbation theory the reference states are used to define the importance measures

$$\kappa_{\nu}^{(m)} = -\frac{\langle \Phi_{\nu} | \mathbf{H} | \Psi_{\text{ref}}^{(m)} \rangle}{\Delta\varepsilon_{\nu}}, \quad (32)$$

which estimate the importance of the basis states $|\Phi_{\nu}\rangle$ contributing to the targeted state indicated by the superscript m . Here \mathbf{H} corresponds to the Hamiltonian of the NCSM calculation including the Lawson term as discussed in Sec. 2.1, and $\Delta\varepsilon_{\nu}$ is chosen to be the excitation energy of $|\Phi_{\nu}\rangle$ with respect to the unperturbed HO Slater determinant [21, 117, 118]. The reference space \mathcal{M}_{ref} is extended by those basis states $|\Phi_{\nu}\rangle \notin \mathcal{M}_{\text{ref}}$ that fulfill the condition $|\kappa_{\nu}^{(m)}| \geq \kappa_{\min}$ for at least one m , where κ_{\min} denotes a certain importance threshold. A solution of the eigenvalue problem in this extended model space, the so-called importance-truncated model space, yields a new set of reference states, which provide an improved approximation of the targeted states. As evident from (32), the additional truncation of the model space parametrized by κ_{\min} , contains information of the Hamiltonian and the targeted states, carried by the reference states, combined with the structure of the individual basis states. Note, that the importance

measure in (32) originates from the first-order perturbative state correction and, hence, not only aims at a description of the energy, but of the eigenstate in general, i.e., it aims at an optimal description of all observables. In principle, the idea of importance selection, pioneered in quantum chemistry in the 1970s [120, 121], can be applied to other CI methods as well. In nuclear structure theory it is almost exclusively applied in combination with the NCSM. There are different possibilities to embed the IT into general CI-type calculations (see [118] for a detailed overview). See also [122] for a recent application of the IT procedure to the nuclear shell-model approach.

In the context of NCSM calculations one aims at a sequence of N_{\max} values for the extrapolation of the observable to infinite model spaces. Therefore, a sequential scheme, where one increases N_{\max} in steps of 2 to the next-larger same-parity NCSM space, emerges to be most appropriate. For the explanation of the sequential scheme we again consider the eigenstates obtained from the full NCSM in an N_{\max} space. These states define the reference states $|\Psi_{\text{ref}}^{(m)}\rangle$ used for the construction of the importance-truncated ($N_{\max} + 2$) model space. In order to reduce the computational cost of evaluating the importance measure, we apply an additional truncation, defined by the so-called reference threshold C_{\min} . That is we do not keep the full reference space, but only those basis states, that correspond to amplitudes with $|C_{\nu}^{(m)}| \geq C_{\min}$ for at least one reference state. Hence, the reference states are defined as the normalized projection of the eigenstates onto the C_{\min} -truncated reference space. Eventually, basis states contained in the ($N_{\max} + 2$) model space, but not in the reference space, are probed during the importance selection to construct the importance-truncated model space. The eigenstates for the next iteration are obtained by diagonalizing the Hamiltonian in this model space via the Lanczos algorithm.

Typically we start with a full NCSM calculation for $N_{\max} = 4$ or 6 and increase the model space via the sequential scheme described above. It is important to point out that in the limit $(\kappa_{\min}, C_{\min}) \rightarrow 0$ we recover the full NCSM result. As we show in the following the applied reference truncation C_{\min} has only minor effects on the results, while it is crucial to perform a $\kappa_{\min} \rightarrow 0$ extrapolation. For this purpose we economically generate a sequence of importance thresholds κ_{\min} by constructing the importance-truncated model space first for the smallest κ_{\min} , i.e., the largest model space. Based on this model space we obtain the next smaller model space by omitting the basis states incompatible with the next larger κ_{\min} and so on.

Although the amplitudes in the eigenstates might be small for the discarded basis states, due to their large number they can lead to non-negligible contributions to observables. There are two established options to include these effects. The simplest possibility to account for the contributions of the discarded basis states on the eigenenergies is through a second-order perturbation correction. During the importance-selection procedure we can evaluate the second-order energy corrections to the m -th eigenstate caused by the individual basis states $|\Phi_{\nu}\rangle$ that

have been discarded

$$\xi_\nu^{(m)} = -\frac{|\langle \Phi_\nu | \mathbf{H} | \Psi_{\text{ref}}^{(m)} \rangle|^2}{\Delta \varepsilon_\nu}. \quad (33)$$

The sum of these second-order energy contributions $\xi_\nu^{(m)}$ can be used to estimate the energy contribution of the excluded states $\Delta_{\text{exclu}}^{(m)}$. This correction can be calculated during the importance selection at essentially no additional cost and can be added a posteriori to the energy eigenvalue $E_{\text{eval}}^{(m)}(\kappa_{\text{min}})$. Here $E_{\text{eval}}^{(m)}(\kappa_{\text{min}})$ corresponds to the energy eigenvalue of the m -th eigenstate obtained via a diagonalization of the Hamiltonian in the importance-truncated model space for a certain κ_{min} . Unfortunately, an analogous correction for other observables can generally not be obtained by such a simple approach. The second more general and superior option to include the effect of discarded basis states is to calculate the observables for a sequence of thresholds and extrapolate to $(\kappa_{\text{min}}, C_{\text{min}}) \rightarrow 0$ to recover the full NCSM result.

We use Fig. 2.2 to illustrate the usual extrapolation protocol. In panel (a) and (c) the ground-state energy of ^{16}O obtained in an importance-truncated model space for $N_{\text{max}} = 8$ and 10, respectively, is plotted as function of the importance threshold κ_{min} . The different curves correspond to the reference thresholds $C_{\text{min}} = 1 \times 10^{-4}$ (blue circles), 2×10^{-4} (red diamonds), 3×10^{-4} (green triangles), and 5×10^{-4} (violet boxes). In all calculations shown in this section the standard chiral NN interaction at N³LO by Entem and Machleidt [8] is used, which is evolved by the Similarity Renormalization Group (SRG) at the two-body level to a flow parameter $\alpha = 0.04 \text{ fm}^4$ (see Sec. 4 for a detailed discussion of the SRG). The calculations are performed with a HO frequency of $\hbar\Omega = 20 \text{ MeV}$. All results were obtained by starting with a reference state from a full NCSM calculation in an $N_{\text{max}} = 4$ space and applying the sequential scheme described above. As evident from Fig. 2.2(a) and (c) for practical applications we can choose C_{min} small enough such that it essentially does not affect the results. Typically a value of $C_{\text{min}} = 2 \times 10^{-4}$ is used throughout this work.

Hence, we are left with the extrapolation $\kappa_{\text{min}} \rightarrow 0$. In practice we generate a sequence of about 8 importance thresholds in the range of $\kappa_{\text{min}} = 3 \times 10^{-5}$ to 10×10^{-5} . The energy eigenvalues decrease smoothly and monotonically for increasing κ_{min} . The latter is due to the variational principle that holds also for the importance-truncated model spaces. Other observables generally show a smooth behavior with respect to κ_{min} as well, but they do not necessarily exhibit a monotonic dependence. The extrapolations indicated by the gray lines are obtained by a fit of the full data set with a polynomial, typically of the order $n = 3$. Note that the only additional uncertainty compared to the NCSM is caused by this extrapolation, thus, it is important to control and quantify this systematic uncertainty. To this end we perform additional extrapolations using the full data set with polynomials of order $(n - 1)$ and $(n + 1)$, as well as extrapolations with order n , where we omit the data points for the lowest and two lowest κ_{min} values. The extrapolation uncertainty of this protocol is indicated by the error band

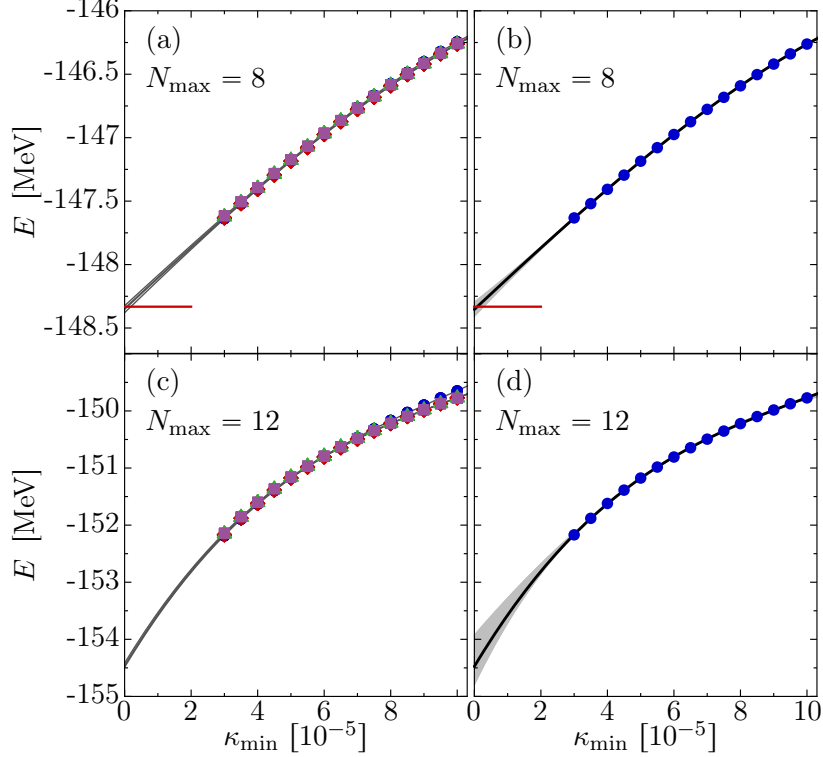


Figure 2.2 *Threshold dependence and extrapolation for ground-state energies of ^{16}O* : Shown are the ground-state energies as function of the importance threshold κ_{\min} for IT-NCSM calculations using the standard NN interaction, SRG evolved at the two-body level to $\alpha = 0.04 \text{ fm}^4$ at $\hbar\Omega = 20 \text{ MeV}$ for $N_{\max} = 8$ (upper panels) and $N_{\max} = 12$ (lower panels). In panel (a) and (c) the energies correspond to different $C_{\min} = 1 \times 10^{-4}$ (●), 2×10^{-4} (◆), 3×10^{-4} (▲), and 5×10^{-4} (■). Panel (b) and (d) illustrate the simple threshold extrapolation for $C_{\min} = 2 \times 10^{-4}$ using a third-order polynomial with uncertainty bands derived from the extrapolation protocol described in the text. The red bars correspond to the full NCSM result calculated with the ANTOINE code [123]. Results are published in [21].

in Fig. 2.2 (b) and (d). The upper panels show the IT-NCSM results for $N_{\max} = 8$. For this model space full NCSM calculations are feasible using the highly optimized ANTOINE code [123] and the results are indicated by the red bars. Figure 2.2 (b) illustrates the agreement of the extrapolated IT-NCSM result and the full NCSM result within the small extrapolation errors. For the $N_{\max} = 12$ calculations plotted in the lower panels, the extrapolation uncertainties increase, but are still well under control. Note that for such large model spaces full NCSM calculations are not feasible.

In order to reduce the uncertainties of the energy eigenvalues further one can take advantage of the fact that the energy contribution of the excluded states $\Delta_{\text{exclu}}^{(m)}(\kappa_{\min})$, obtained from second-order perturbation theory, vanishes for $\kappa_{\min} \rightarrow 0$. Therefore, we can construct a family

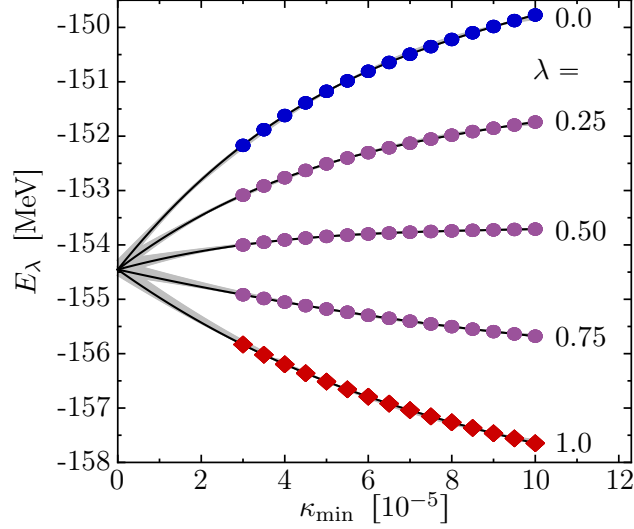


Figure 2.3 *Simultaneous threshold extrapolation for the ground-state energy of ^{16}O* : The curves correspond to the improved energies (34) for different λ values. The results have been achieved for $N_{\max} = 12$ and $C_{\min} = 2 \times 10^{-4}$. The interaction and remaining parameters are chosen as in Fig. 2.2. Results are published in [21].

of improved energy curves

$$E_{\lambda}^{(m)}(\kappa_{\min}) = E_{\text{eval}}^{(m)}(\kappa_{\min}) + \lambda \Delta_{\text{exclu}}^{(m)}(\kappa_{\min}), \quad (34)$$

with an auxiliary control parameter λ . Per definition all curves converge to the full NCSM energy for the limit $\kappa_{\min} \rightarrow 0$. We use this property as constraint for the simultaneous fit of the curves for a set of λ parameters. As an example for this approach Fig. 2.3 shows the energies E_{λ} of the ^{16}O ground state with the same parameters as in Fig. 2.2(d) for five λ values as function of the importance threshold κ_{\min} . The extrapolation error is determined again through a variation of the polynomial order by ± 1 and omitting the lowest or the two lowest κ_{\min} data points. In addition to this we perform extrapolations omitting the curve with the largest (red squares) or lowest (blue circles) λ . Typically the λ parameters are chosen such that the $E_{\lambda}^{(m)}(\kappa_{\min})$ curves exhibit an approximately symmetrical appearance, which stabilizes the extrapolation significantly. In practical applications throughout this work we typically follow the simpler extrapolation protocol illustrated in Fig. 2.2(d) and if necessary we use the constrained simultaneous fit procedure to stabilize the extrapolation.

In the following we show further examples of IT-NCSM calculations using the simpler extrapolation, varying the nucleus and the observables. In Fig. 2.4 IT-NCSM energies of ^{12}C are shown as function of κ_{\min} for the ground-state energy (a), the excitation energy of the first 2^+ state (b), the angular momentum of the ground state (c) and the expectation value E_{cm} of the Lawson term (d) to estimate the center-of-mass contamination. We utilize the same NN

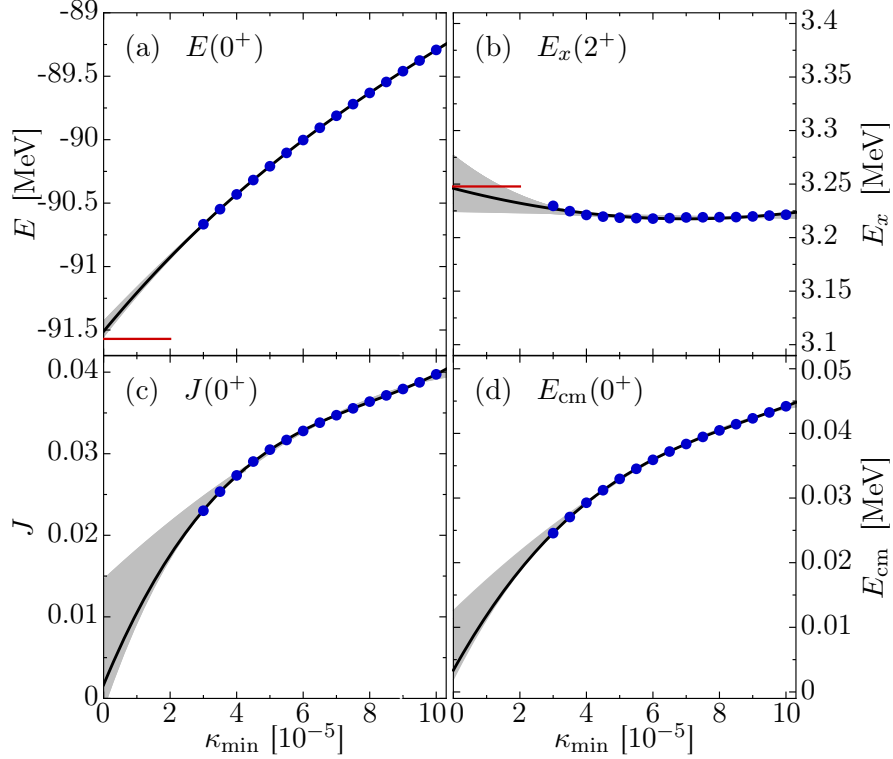


Figure 2.4 *Threshold dependence in ^{12}C* : Illustrated are the ground-state energy (a), the angular momentum (c), and the expectation value of the Lawson term (d), as well as the excitation energy of the first excited 2^+ state (b). The IT-NCSM calculations are carried out for $N_{\max} = 8$, $\hbar\omega = 20$ MeV, $C_{\min} = 2 \times 10^{-4}$ and the same interaction as in Fig. 2.2. The red bars mark the full NCSM results obtained with the ANTOINE code [123]. Results are published in [21].

Hamiltonian as above, SRG evolved to $\alpha = 0.04 \text{ fm}^4$. The IT-NCSM calculations have been performed for $N_{\max} = 8$, $\hbar\Omega = 20 \text{ MeV}$ and $C_{\min} = 2 \times 10^{-4}$. The ground-state energy of ^{12}C is again a smooth, monotonic curve as function of κ_{\min} and the full NCSM result (red bars) are reproduced rather precise, although the NCSM result is located at the lower edge of the error band obtained from the extrapolation protocol. The excitation energy of the first excited 2^+ state is almost constant with respect to the importance threshold, yielding an extrapolation error of about 50 keV. This indicates that for the plotted κ_{\min} range the excluded basis states contribute to the same amount to the absolute energy of the ground and first-excited 2^+ state. The angular momentum J for the ground state, i.e., the 0^+ state, is not a good quantum number for finite κ_{\min} but can be reproduced very accurately when extrapolating to $\kappa_{\min} \rightarrow 0$. Further, we can investigate the center-of-mass contamination by, e.g., calculating the expectation value of the Lawson term E_{cm} introduced in Sec. 2.1. For a full NCSM calculation E_{cm} vanishes up to numerical noise. From panel (d), where the mentioned expectation value for the ground state of ^{12}C is depicted, we observe that IT-NCSM results for finite κ_{\min} show a noticeable center-of-mass contaminations, which almost vanishes when extrapolating to $\kappa_{\min} \rightarrow 0$. Thus,

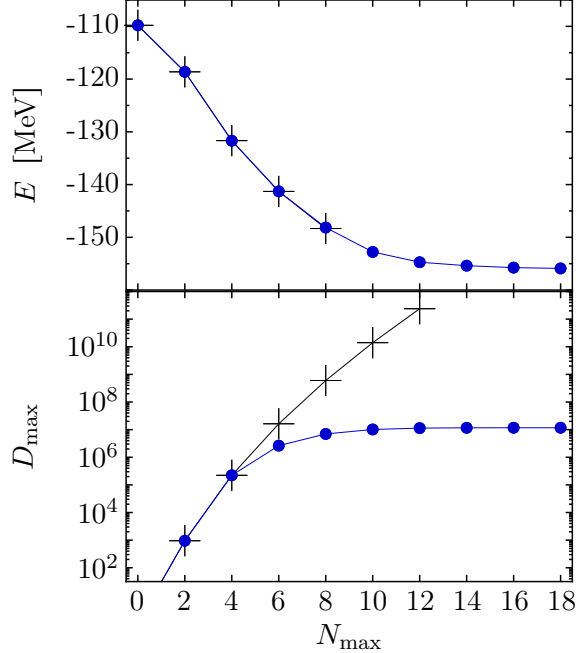


Figure 2.5 *Ground-state energy and model-space dimensions for ^{16}O* : Illustrated are the ground-state energies (upper panel) and the corresponding model-space dimensions (lower panel) for the IT-NCSM (●) and the full NCSM (+) calculations as function of N_{\max} . The interaction and remaining parameters are chosen as in Fig. 2.4. The error bars for the IT-NCSM energies resulting from the importance extrapolation are covered by the plot symbols. Results are published in [21].

the final threshold extrapolated IT-NCSM results are essentially not affected by center-of-mass contaminations.

Eventually, we elucidate the major advantage of the IT-NCSM, namely the reduction of the dimension of the many-body model space. In the upper panel of Fig. 2.5 we compare the ground-state energy of ^{16}O as function of N_{\max} , for the same NN interaction and HO frequency as in the previous figures of this section, obtained with the IT-NCSM (blue circles) and the full NCSM (black crosses). The NCSM calculations are performed with the ANTOINE code [123] and the IT-NCSM results are obtained using the simple extrapolation protocol described above. For the model spaces feasible with the NCSM, i.e., $N_{\max} \leq 8$, both results agree to within 200 keV, illustrating the excellent agreement of the IT-NCSM with the full NCSM. In addition the IT procedure allows to extend the model space up to $N_{\max} = 18$, far beyond the application range of the NCSM. The reason is illustrated in the lower panel of Fig. 2.5, where we plot the model-space dimensions used during the Lanczos diagonalization for the IT-NCSM (blue circle) and the NCSM (black crosses) as function of N_{\max} . The IT model spaces are constructed with an importance threshold $\kappa_{\min} = 3 \times 10^{-5}$, which corresponds to the largest IT model space used for the calculation of the ground-state energies in the upper panel. Note that the IT-NCSM typically starts with reference states from a full $N_{\max} = 4$ NCSM calculation to construct the

IT $N_{\max} = 6$ model space, i.e., both methods are identical for $N_{\max} \leq 4$ in this case. While the model-space dimension of the NCSM increases dramatically with N_{\max} , it saturates for the IT case, yielding a reduction of the model-space dimension by more than two orders of magnitude. From the saturation we conclude that the majority of the new basis states for large N_{\max} have small or vanishing importance measures when targeting the ground state. This agrees with the fact that the ground-state energy is approximately converged for $N_{\max} = 12$. However, the results beyond the NCSM application range ($N_{\max} > 8$) are essential to perform accurate extrapolations with respect to the N_{\max} .

Finally, we consider the limitations of the IT-NCSM. From the model-space dimension analysis in Fig. 2.5 one could get the impression that the larger N_{\max} calculations can be performed with constant effort. This is true for the Lanczos diagonalization, but the computing time required for the importance selection increases considerably owing to the large number of importance measures that have to be evaluated. The IT-NCSM has proven to have the capability of calculating eigenenergies as well as other observables on the same footing [21]. The pattern of observables with respect to the IT threshold is generally smooth and can be extrapolated to the full NCSM space with high accuracy. However, we stress that there are observables that depend substantial on basis states with a small importance measure or show a pattern less suited for the extrapolation protocol used in this work. Examples are the quadrupole moments or B(E2) transition strength,⁶ which generally have a larger relative extrapolation error than the observables shown in this section [21].

Furthermore, the extrapolation procedure becomes less accurate when using too large HO frequencies, because the contributions to the eigenstates are distributed over the full NCSM model space for such inappropriate HO frequencies [21]. See Ref. [119] for an investigation of the κ_{\min} extrapolation for different HO frequencies. In these cases it might be necessary to extend the typically κ_{\min} range to lower values in order to obtain the desired accuracy of the extrapolation. To sum up, the importance-truncation technique in combination with the threshold extrapolation, enables the IT-NCSM to reproduce the results of the full NCSM and keeping its advantages, namely: the variational principle holds, the center-of-contamination approximately vanishes, other observables can be obtained from the calculated eigenstates, 3N and higher-order interactions can be included in this method with moderate effort. The IT extends the application range to larger model spaces and particle numbers, i.e., nuclei in the p- and lower sd-shell become accessible, entering an interesting regime of nuclear physics. Furthermore, the IT-NCSM bridges the gap between light nuclei accessible with exact methods, such as the NCSM and the medium-mass and heavy nuclei that are the terrain of approximative methods such as the CC or IM-SRG approach. Therefore, this method is crucial to investigate the uncertainty

⁶The results shown in this work are achieved by using chiral interactions softened by the Similarity Renormalization Group. A reliable investigation of other observables than the eigenenergies requires a corresponding unitary transformation of the operators. We mainly concentrate on eigenenergies in this work, but refer the interested reader to [124, 125] for recent applications of the unitary transformation of observables.

of approximative approaches and represents the central many-body method in this work.

2.3 Coupled-Cluster Approach

To study the impact of chiral NN and 3N interactions for heavier nuclei far beyond the p and sd shell we utilize the ab initio single-reference coupled-cluster (CC) approach to compute ground-state energies for closed-shell nuclei. In the following, we briefly outline the formal concept of CC theory and refer to Ref. [99] for a detailed description. The CC approach elegantly assesses the energy E of the A -particle ground state $|\Psi\rangle$ by solving the many-body eigenvalue problem

$$\mathbf{H}_{\text{int}}|\Psi\rangle = E|\Psi\rangle, \quad (35)$$

using an exponential ansatz [126, 127]

$$|\Psi\rangle = e^{\mathbf{T}}|\Phi_{\text{ref}}\rangle, \quad (36)$$

where the same Hamiltonian \mathbf{H}_{int} as in Eq. (25) is used and $|\Phi_{\text{ref}}\rangle$ is a single-reference determinant that approximates the ground state. The cluster operator

$$\mathbf{T} = \sum_{n=1}^A \mathbf{T}_n, \quad (37)$$

is a particle-hole excitation operator and its many-body components

$$\mathbf{T}_n = \left(\frac{1}{n!}\right)^2 \sum_{\substack{\nu_1 \dots \nu_n \\ \mu_1 \dots \mu_n}} t_{\nu_1 \dots \nu_n}^{\mu_1 \dots \mu_n} \mathbf{a}_{\mu_1}^\dagger \dots \mathbf{a}_{\mu_n}^\dagger \mathbf{a}_{\nu_n} \dots \mathbf{a}_{\nu_1}, \quad (38)$$

depend on the coefficients $t_{\nu_1 \dots \nu_n}^{\mu_1 \dots \mu_n}$ also called cluster amplitudes and comprise n pairs of creation and annihilation operators, which are defined with respect to the reference state. The indices ν_1, ν_2, \dots denote single-particle state occupied in $|\Phi_{\text{ref}}\rangle$ and μ_1, μ_2, \dots denote single-particle state unoccupied in $|\Phi_{\text{ref}}\rangle$, such that the creation and annihilation operators are in normal-ordered form (see Sec. 3.3).

Expanding the operator $e^{\mathbf{T}}$ in a Taylor series using the expression of the cluster operator (37), yields

$$\begin{aligned} e^{\mathbf{T}} &= \mathbb{1} + \mathbf{T}_1 + \mathbf{T}_2 + \dots \\ &+ \frac{1}{2!}\mathbf{T}_1^2 + \mathbf{T}_1\mathbf{T}_2 + \frac{1}{2!}\mathbf{T}_2^2 + \dots \\ &+ \frac{1}{3!}\mathbf{T}_1^3 + \frac{1}{2!}\mathbf{T}_1^2\mathbf{T}_2 + \frac{1}{2!}\mathbf{T}_1\mathbf{T}_2^2 + \frac{1}{3!}\mathbf{T}_2^3 + \dots \\ &\vdots \end{aligned} \quad (39)$$

where the dots correspond to contributions including either products of more than three cluster-operator components or \mathbf{T}_m operators with $m \geq 3$. In this work we report results with the CC approach using the Hartree-Fock state as the reference state. This single Slater determinant is unable to describe short-range and tensor correlations [128], e.g., induced by the chiral interactions. Due to the application of the operator in Eq. (39) to the reference state, the eigenstate $|\Psi\rangle$ contains multiple excitations that allow to account for these correlations. Contributions to the eigenstate of the form $\mathbf{T}_m |\Phi_{\text{ref}}\rangle$ are called connected-cluster contributions while contributions including products of the cluster operators components are called disconnected-cluster contributions. The latter are a direct consequence of the exponential ansatz for the eigenstate and are responsible for the extensivity of the CC eigenstate [94]. Because of the \mathbf{T}_1 components the CC methods are relatively insensitive to the choice of the reference state, since the operator $e^{\mathbf{T}_1}$ transforms the reference state to another Slater determinant [129].

To derive the CC equations that need to be solved to obtain the ground-state energy it is convenient to decompose the ground-state energy E into the reference energy $E_{\text{ref}} = \langle \Phi_{\text{ref}} | \mathbf{H}_{\text{int}} | \Phi_{\text{ref}} \rangle$ and the CC correlation energy ΔE

$$E = E_{\text{ref}} + \Delta E \quad (40)$$

and to subtract the E_{ref} from the Schrödinger equation (35), yielding the eigenvalue problem

$$\mathbf{H}_N |\Phi_{\text{ref}}\rangle = \Delta E |\Phi_{\text{ref}}\rangle \quad \text{with} \quad \mathbf{H}_N = \mathbf{H}_{\text{int}} - E_{\text{ref}}. \quad (41)$$

Moreover, one multiplies both sides of this equation by $e^{-\mathbf{T}}$ from the left to obtain the connected-cluster form of the Schrödinger equation [130, 131]

$$\overline{\mathbf{H}}_N |\Phi_{\text{ref}}\rangle = \Delta E |\Phi_{\text{ref}}\rangle, \quad (42)$$

where $\overline{\mathbf{H}}_N = e^{-\mathbf{T}} \mathbf{H}_N e^{\mathbf{T}}$ is the similarity-transformed Hamiltonian. Finally, both sides of Eq. (42) are projected on the reference state $|\Phi_{\text{ref}}\rangle$ and on the excited states

$$|\Phi_{\nu_1 \dots \nu_n}^{\mu_1 \dots \mu_n}\rangle = \mathbf{a}_{\mu_1}^\dagger \dots \mathbf{a}_{\mu_n}^\dagger \mathbf{a}_{\nu_n} \dots \mathbf{a}_{\nu_1} |\Phi_{\text{ref}}\rangle, \quad (43)$$

which are obtained by applying particle-hole excitations to the reference state.

These projections yield the CC equations [28, 130, 131], i.e., the correlation energy formula

$$\Delta E = \langle \Phi_{\text{ref}} | \overline{\mathbf{H}}_N | \Phi_{\text{ref}} \rangle \quad (44)$$

and the non-linear system of explicitly connected and energy-independent equations

$$\langle \Phi_{\nu_1 \dots \nu_n}^{\mu_1 \dots \mu_n} | \overline{\mathbf{H}}_N | \Phi_{\text{ref}} \rangle = 0, \quad \text{with} \quad \nu_1 < \dots < \nu_n, \quad \mu_1 < \dots < \mu_n, \quad (45)$$

for $n = 1 \dots A$. The solution of the system of equations (45) determines the cluster amplitudes $t_{\nu_1 \dots \nu_n}^{\mu_1 \dots \mu_n}$ and thus the eigenstate $|\Psi\rangle$. Furthermore, the amplitudes can be inserted in Eq. (44) to obtain the correlation energy ΔE and thus the ground-state energy E .

Since the exponential ansatz in Eq. (36) allows to consider all configurations that appear in a full CI approach, the CC solution for the ground state is equivalent to the full CI approach. For practical reasons, this exact CC approach is limited to small few-body problems and applications to heavier systems require a truncations of the cluster operator \mathbf{T} . Generally, one truncates the many-body expansion for T in Eq. (37) at a certain excitation component \mathbf{T}_m (cluster truncation). Commonly used is the coupled-cluster method with singles and doubles excitations (CCSD) [28,93–95,132,133], where the excitation components \mathbf{T}_1 and \mathbf{T}_2 are considered. In quantum chemistry an excellent approximation to the exact result is usually achieved by the coupled-cluster method with singles, doubles, and triples excitations (CCSDT), including additionally the \mathbf{T}_3 components. However, an iterative solution of the system of equations (45) causes high computational cost, when including the \mathbf{T}_3 excitations. Therefore, in this work we apply the CCSD method and add corrections to the CCSD energy originating from the dominant triples contributions, using the Λ CCSD(T) method [28–30,93–95] as well as the left-eigenstate completely renormalized coupled-cluster method with singles, doubles and non-iterative triples excitations [30,134,135], CR-CC(2,3) for short. The systematic uncertainties of the ground-state energies due to the cluster truncation can be estimated by the energy corrections of the triples contributions.

Note that the derivation of the final expressions for the CC energy and amplitude equations that are used in practical implementations is a conceptual demanding task. Moreover, the final form of the equation depends on the Hamiltonian used in the calculations. This becomes evident when one utilizes the Baker-Campbell-Hausdorff expansion to derive the following expression for the similarity-transformed Hamiltonian [28,94]

$$\overline{\mathbf{H}}_N = \mathbf{H}_N + \sum_{n=1}^{n_{\max}} \frac{1}{n!} \underbrace{[\dots [\mathbf{H}_N, \mathbf{T}], \dots, \mathbf{T}]}_{n \text{ times}}. \quad (46)$$

Using Wicks’s theorem one can show that only those terms in the nested commutators $[\dots [\mathbf{H}_N, \mathbf{T}], \dots, \mathbf{T}]$ provide non-vanishing contributions that involve contractions between $\overline{\mathbf{H}}_N$ and one or more components of \mathbf{T} , yielding

$$\overline{\mathbf{H}}_N = \sum_{n=0}^{n_{\max}} \frac{1}{n!} (\mathbf{H}_N \mathbf{T}^n)_C, \quad (47)$$

where the subscript C indicates that \mathbf{H}_N is contracted with at least one of the following \mathbf{T} operators. This restricts the maximum power of the \mathbf{T} operators and simplifies the CC equations. Nevertheless, the form of \mathbf{H}_N depends on n_{\max} that is determined by the maximal

particle-rank of the interaction in the Hamiltonian, i.e., $n_{\max}=4$ for an NN interaction, $n_{\max}=6$ for a 3N interaction and so on. Without conceptual changes the CC approaches developed for NN interactions can include effects of 3N interactions by reducing the particle-rank of the interaction via the normal-ordering approximation, discussed in Sec. 3.3. However, to employ 3N interactions explicitly one requires formal extensions [28–30,98,99] that complicate the CC equations and increase the computational costs of the calculations.

Nevertheless, the CC approach constitutes an elegant ab initio many-body approach allowing for an efficient computation of the ground-state energies for closed-shell nuclei far beyond the p and sd shell using a many-body model space truncation defined by the maximum single-particle energy e_{\max} . In particular due to the spherical formulation of the CC equations (see Ref. [99] for a detailed description) one can reach much larger model spaces than with the NCSM and IT-NCSM approaches, such that, in general, all 3N interaction matrix elements required for the CC model spaces cannot be provided. Thus, it is important to study the sensitivity of the CC results to the truncation of the 3N contributions.

3 Momentum and HO Basis Sets

An important objective when dealing with quantum-mechanical problems both, algebraically and numerically is the choice of an adequate basis that, e.g., exploits the symmetries of the involved operators and allows to define model spaces with tractable dimensions that cover the relevant physics. The harmonic-oscillator (HO) basis has been successfully established in a wide range of nuclear structure physics and is commonly used in different many-body methods in this field, such as the NCSM, IT-NCSM, CC, IM-SRG, Gor'kov-Green's function, etc. The harmonic oscillator provides a complete and discrete basis of localized wave functions that depend on the HO frequency $\hbar\Omega$ or equivalently the oscillator length a . These parameters can be adjusted to improve the description of finite systems or can be varied to study the sufficiency of the model space. Although the HO basis is not suited to describe all aspects relevant for nuclear structure physics, such as short-range correlations, cluster-structures, long-range properties, or continuum effects, it provides an excellent starting point for further developments.

Throughout this section we introduce and discuss the basis sets and basis transformations that are used in our toolchain to perform nuclear structure calculations. The major focus is on the introduction of the HO basis sets used for the inclusion of 3N and 4N contributions and the presentation of the corresponding basis transformations. We highlight the advantages and disadvantages of the different basis sets that justify their application for certain tasks in the toolchain used to carry out nuclear structure calculations.

In order to motivate the basis sets and basis transformations that are presented in the following, we briefly summarize the different strategies to include the chiral 3N and 4N contributions into nuclear structure calculations: The standard procedure using the HO basis for the inclusion of these interactions is to perform the unitary similarity renormalization group (SRG) transformation (see Sec. 4) in the Jacobi-HO basis, followed by a basis transformation into the so-called JT -coupled scheme. In case of the (IT-)NCSM we perform the final decoupling to the m -scheme on-the-fly during the many-body calculations. The procedures for the inclusion of the 3N and 4N contributions are similar, even though the treatment of the latter requires extensions of all the discussed steps to the four-body space and, thus, several novel developments and optimizations.

In addition, it is possible to simplify the treatment of the 3N and 4N interactions by introducing approximations that reduce the particle rank of the interaction. Throughout this work such approximations are applied via a normal-ordering (NO) approximation to reduce contributions

of the 3N interaction to interactions with lower particle ranks.

Eventually, we concentrate on the partial-wave decomposed Jacobi-momentum basis, which is the starting point for the non-local chiral 3N interactions (see Sec. 1.3 and 1.4). We discuss the basis transformation from the three-body momentum basis to the HO basis in order to feed these interactions into the efficient HO toolchain that is presented throughout this work.

3.1 The Jacobi Basis

The first basis set we discuss corresponds to the HO eigenstates defined with respect to Jacobi coordinates. These coordinates allow to disentangle the relative from the center-of-mass motion, which allows for a direct investigation of the intrinsic structure of the nucleus. There are different choices for these coordinates. In this work we use the definition also applied in Refs. [13, 70] for the spatial Jacobi coordinates

$$\begin{aligned}\vec{\xi}_0 &= \sqrt{\frac{1}{A}}[\vec{r}_1 + \vec{r}_2 + \cdots + \vec{r}_A], \\ \vec{\xi}_n &= \sqrt{\frac{n}{n+1}}\left[\frac{1}{n}(\vec{r}_1 + \vec{r}_2 + \cdots + \vec{r}_n) - \vec{r}_{n+1}\right],\end{aligned}\tag{48}$$

and for the Jacobi momenta

$$\begin{aligned}\vec{\pi}_0 &= \sqrt{\frac{1}{A}}[\vec{p}_1 + \vec{p}_2 + \cdots + \vec{p}_A], \\ \vec{\pi}_n &= \sqrt{\frac{n}{n+1}}\left[\frac{1}{n}(\vec{p}_1 + \vec{p}_2 + \cdots + \vec{p}_n) - \vec{p}_{n+1}\right].\end{aligned}\tag{49}$$

where \vec{r}_i and \vec{p}_i correspond to the single-particle coordinates and momenta of the i -th particle, respectively. The coordinates $\vec{\xi}_0$ and $\vec{\pi}_0$ are proportional to the center-of-mass coordinates of the A -body system. The Jacobi coordinates $\vec{\xi}_n$ and $\vec{\pi}_n$ with $n = 1, 2, \dots, (A - 1)$ describe the relative motion of the A -body system. Apart from prefactors $\vec{\xi}_n$ is defined as the distance of the $(n + 1)$ -th particle to the center-of-mass of the first n particles, and analogous for $\vec{\pi}_n$.

In the following we utilize basis sets defined with respect to Jacobi and single-particle coordinates in various relations and transformations. To distinguish between the underlying coordinate systems we use numeric indices for quantities defined with respect to Jacobi coordinates and latin indices for the ones defined with respect to single-particle coordinates. With this

convention the Jacobi coordinates relevant for the relative motion read

$$\begin{aligned}
 \vec{\xi}_1 &= \sqrt{\frac{1}{2}}[\vec{r}_a - \vec{r}_b], \\
 \vec{\xi}_2 &= \sqrt{\frac{2}{3}}\left[\frac{1}{2}(\vec{r}_a + \vec{r}_b) - \vec{r}_c\right], \\
 \vec{\xi}_3 &= \sqrt{\frac{3}{4}}\left[\frac{1}{3}(\vec{r}_a + \vec{r}_b + \vec{r}_c) - \vec{r}_d\right], \\
 &\vdots
 \end{aligned} \tag{50}$$

and

$$\begin{aligned}
 \vec{\pi}_1 &= \sqrt{\frac{1}{2}}[\vec{p}_a - \vec{p}_b], \\
 \vec{\pi}_2 &= \sqrt{\frac{2}{3}}\left[\frac{1}{2}(\vec{p}_a + \vec{p}_b) - \vec{p}_c\right], \\
 \vec{\pi}_3 &= \sqrt{\frac{3}{4}}\left[\frac{1}{3}(\vec{p}_a + \vec{p}_b + \vec{p}_c) - \vec{p}_d\right], \\
 &\vdots
 \end{aligned} \tag{51}$$

3.1.1 Two-Body Basis

We start with the two-body basis states as the simplest example for Jacobi-HO states and define the notation used later on.

In the two-body space there are the antisymmetric HO eigenstates

$$|N_{\text{cm}(2)}L_{\text{cm}(2)}M_{L_{\text{cm}(2)}}\rangle \otimes |N_1; (L_1S_1)J_1M_{J_1}; T_1M_{T_1}\rangle_a, \tag{52}$$

where N_1, L_1 are the radial and orbital angular-momentum quantum numbers, defined with respect to the Jacobi coordinate $\vec{\xi}_1$. The coupled spin and isospin are denoted by S_1 and T_1 , respectively, with the isospin projection M_{T_1} . The angular-momentum quantum number of the relative part and its projection are denoted by J_1 and M_{J_1} . Further, $N_{\text{cm}(2)}, L_{\text{cm}(2)}$, and $M_{L_{\text{cm}(2)}}$ correspond to the center-of-mass coordinate $\vec{\xi}_0$ and define the center-of-mass part of the two-body HO basis state. The subscript a of the relative state indicates its antisymmetry with respect to particle exchanges, i.e., its quantum numbers fulfill the condition $(-1)^{L_1+S_1+T_1} = 1$. The center-of-mass part is symmetric under particle exchanges by definition, such that the complete state in Eq. (52) is antisymmetric. Note, that we use upper-case letters for the quantum number to indicate their dependence on more than one particle, while we use lower-case letters for single-particle quantum numbers. The subscript $\text{cm}(n)$ indicates that the quantity is defined with respect to the center-of-mass coordinate of the n -body system. As

mentioned before, quantities with numeric indices correspond to Jacobi coordinates and those with latin indices to single-particle coordinates. Note, there are quantities that correspond to both coordinate systems. For example the single-particle spins s_a and s_b couple to S_{ab} , which is equivalent to S_1 .⁷ The HO basis in Eq. (52) is used, e.g., for the SRG evolution in the two-space (see Sec. 4) and is transformed via a Talmi-Moshinsky transformation [128, 136, 137] to the m -scheme or to the so-called JT -coupled scheme (see Ref. [138] for a detailed derivation of the transformation).

In analogy to the antisymmetric Jacobi-HO states in the three- and four-body space that are introduced in Sec. 3.1.2 and 3.1.3, respectively, one can also introduce the following short-hand notation for the relative part of the two-body states

$$|E_1 i_1 J_1 T_1 \rangle_a = |N_1; (L_1 S_1) J_1; T_1 \rangle_a, \quad (53)$$

with the energy quantum number $E_1 = 2N_1 + L_1$ and the collective index $i_1 = \{L_1, S_1, T_1\}$. Note that we omit the projection quantum numbers for brevity.

Another common two-body Jacobi basis is the antisymmetric partial-wave decomposed momentum basis

$$|\pi_1; (L_1 S_1) J_1; T_1 \rangle_a, \quad (54)$$

where we omit the center-of-mass part for brevity. The quantity π_1 corresponds to the absolute value of the first Jacobi momentum. This basis is applied, e.g., to perform the SRG transformation of the chiral NN interaction in the two-space, which is used in the many-body Hamiltonian (see Sec. 4.5) and is partially utilized in the derivation of the frequency conversion formula (see Sec. 5). The transformation of the momentum basis to the HO basis is discussed for the more complicated three-body case in Sec. 3.5.

3.1.2 Three-Body HO Basis and Antisymmetrization

The construction of antisymmetric three-body Jacobi-HO states can be performed by utilizing the antisymmetrization technique discussed in the following. We begin with the Jacobi-HO states

$$|N_{\text{cm}(3)} L_{\text{cm}(3)} \rangle \otimes |N_1 N_2; [(L_1 S_1) J_1, (L_2 \frac{1}{2}) J_2] J_{12}; (T_1 \frac{1}{2}) T_{12} \rangle_{a_1}, \quad (55)$$

⁷We emphasize that it is crucial to distinguish between the angular momentum, spin, and isospin operators that can couple with each other in the corresponding Hilbert spaces, and the quantum numbers that are associated with this operators. Nevertheless, we refer, e.g., to the ‘‘coupling of two quantum numbers’’ and point out that this is only a short-hand formulation for the coupling of the corresponding operators.

that are only partially antisymmetric with respect to the exchange of the first two particles, which correspond to the first Jacobi coordinate, indicated by the index a_1 of the state, i.e., $(-1)^{L_1+S_1+T_1} = 1$ holds. We suppress the projection quantum numbers for brevity and utilize the notation introduced in Sec. 3.1.1, e.g., the quantum number J_{12} correspond to the coupled relative angular momentum of the three-body state that are defined with respect to the Jacobi coordinates $\vec{\xi}_1$ and $\vec{\xi}_2$. The total isospin and its projection is denoted by T_{12} and $M_{T_{12}}$, respectively. Since we are considering nucleons the single-particle spin and isospin quantum numbers are equal to $\frac{1}{2}$. The total HO energy quantum number of the three-body state is defined by $E_{abc} = E_{\text{cm}(3)} + E_{12}$, with the center-of-mass contribution $E_{\text{cm}(3)} = 2N_{\text{cm}(3)} + L_{\text{cm}(3)}$ and the relative energy quantum number $E_{12} = (2N_1 + L_1) + (2N_2 + L_2)$. We omit the center-of-mass part and concentrate on the relative part

$$|N_1 N_2; \alpha_{12}\rangle_{a_1} = |N_1 N_2; [(L_1 S_1) J_1, (L_2 \frac{1}{2}) J_2] J_{12}; (T_1 \frac{1}{2}) T_{12}\rangle_{a_1}, \quad (56)$$

where we suppress the projection quantum numbers $M_{J_{12}}$ and $M_{T_{12}}$ for brevity and introduce a short-hand notation using the collective index $\alpha_{12} = \{L_1, S_1, J_1, L_2, J_2, J_{12}, T_1, T_{12}\}$ for the angular momentum, spin and isospin quantum numbers that define the partial waves.

Since we describe fermionic systems it is necessary to antisymmetrize this basis. In case of the two-body Jacobi-HO basis this can be achieved by allowing only certain combinations of quantum numbers. Unfortunately, an analogous relation does not exist for the three-body Jacobi-HO states. Thus, one could obtain a completely antisymmetric state, e.g., by applying the antisymmetrization operator \mathcal{A} . For the m -scheme such a procedure reduces the number of basis states in a certain model space due to the fact that permutations of single-particles only differ by a trivial factor and can be omitted. However, it is generally not possible to identify such permutation relations for Jacobi basis states. Therefore, we apply a more sophisticated approach that leads to an antisymmetric and orthonormal basis: We represent the antisymmetrizer \mathcal{A} in the partially antisymmetric Jacobi-HO basis of Eq. (56) and diagonalize the corresponding matrix to obtain the eigenstates of this operator. The antisymmetrizer matrix elements vanish for different energy E_{12} , angular momentum J_{12} , and isospin T_{12} quantum numbers in the bra and ket states, such that the diagonalization can be performed for each $(E_{12} J_{12} T_{12})$ -block separately. To obtain the corresponding matrix elements we exploit the partial antisymmetry of our basis yielding

$${}_{a_1} \langle N_1 N_2; \alpha_{12} | \mathcal{A} | N'_1 N'_2; \alpha'_{12} \rangle_{a_1} = {}_{a_1} \langle N_1 N_2; \alpha_{12} | \frac{1}{3} (\mathbb{1} - 2 \mathcal{T}_{bc}) | N'_1 N'_2; \alpha'_{12} \rangle_{a_1}, \quad (57)$$

with the transposition operator \mathcal{T}_{bc} of particle b and c . The matrix elements of the transposition

operator are given by [70]

$$\begin{aligned}
 & {}_{a_1}\langle N_1 N_2; [(L_1 S_1) J_1, (L_2 \frac{1}{2}) J_2] J_{12}; (T_1 \frac{1}{2}) T_{12} | \mathcal{T}_{bc} \\
 & \quad \times | N'_1 N'_2; [(L'_1 S'_1) J'_1, (L'_2 \frac{1}{2}) J'_2] J_{12}; (T'_1 \frac{1}{2}) T_{12} \rangle_{a_1} \\
 & = \sum_{L_{12} S_{12}} \sum_{L'_{12} S'_{12}} \sum_{M_{L_{12}} M_{S_{12}}} \sum_{M'_{L_{12}} M'_{S_{12}}} \hat{J}_1 \hat{J}'_1 \hat{L}_{12} \hat{L}'_{12} \hat{S}_{12} \hat{S}'_{12} \hat{J}_2 \hat{J}'_2 \hat{S}_1 \hat{S}'_1 \hat{T}_1 \hat{T}'_1 (-1)^{T_1 + T'_1 + S_1 + S'_1} \\
 & \quad \times \delta_{S_{12}, S'_{12}} \delta_{M_{S_{12}}, M'_{S_{12}}} \delta_{T_{12}, T'_{12}} \delta_{L_{12}, L'_{12}} \delta_{M_{L_{12}}, M'_{L_{12}}} \delta_{(2N_1 + L_1 + 2N_2 + L_2), (2N'_1 + L'_1 + 2N'_2 + L'_2)} \quad (58) \\
 & \quad \times \left\{ \begin{array}{ccc} L_1 & S_1 & J_1 \\ L_2 & \frac{1}{2} & J_2 \\ L_{12} & S_{12} & J_{12} \end{array} \right\} \left\{ \begin{array}{ccc} L'_1 & S'_1 & J'_1 \\ L'_2 & \frac{1}{2} & J'_2 \\ L'_{12} & S'_{12} & J'_{12} \end{array} \right\} \left(\begin{array}{cc|c} L_{12} & S_{12} & J_{12} \\ M_{L_{12}} & M_{S_{12}} & M_{J_{12}} \end{array} \right) \left(\begin{array}{cc|c} L'_{12} & S'_{12} & J'_{12} \\ M'_{L_{12}} & M'_{S_{12}} & M'_{J_{12}} \end{array} \right) \\
 & \quad \times \left\{ \begin{array}{ccc} \frac{1}{2} & \frac{1}{2} & T_1 \\ \frac{1}{2} & T'_{12} & T'_1 \end{array} \right\} \left\{ \begin{array}{ccc} \frac{1}{2} & \frac{1}{2} & S_1 \\ \frac{1}{2} & S'_{12} & S'_1 \end{array} \right\} \langle\langle N_1 L_1, N_2 L_2; L_{12} | N'_1 L'_1, N'_2 L'_2 \rangle\rangle_{\frac{1}{3}},
 \end{aligned}$$

with the short hand $\hat{x} = \sqrt{2x + 1}$. For the derivation of this formula (see Refs. [138, 139] for details) several angular-momentum recouplings are necessary, yielding the $6j$ - and $9j$ -symbols. Moreover, the transposition changes the underlying coordinate system in one state, which generates the harmonic-oscillator brackets (HOBs) $\langle\langle \dots; \dots \rangle\rangle_{\frac{1}{3}}$ [137, 140–142]. Note, the HOBs used in this work correspond to the definition in Ref. [140], an alternative formulation that differs by a phase can be found, e.g., in Ref. [142].

From the diagonalization of the antisymmetrizer matrix we obtain the antisymmetric eigenstates that correspond to the eigenvalue (-1) . These eigenstates can be expressed as a superposition of the partial-antisymmetric states as

$$|E_{12} i_{12} J_{12} T_{12}\rangle_a = \sum_{N'_1 N'_2 \alpha'_{12}} \delta_{(2N'_1 + L'_1 + 2N'_2 + L'_2), E_{12}} \delta_{J'_{12}, J_{12}} \delta_{T'_{12}, T_{12}} C_{N'_1 N'_2 \alpha'_{12}}^{i_{12}} |N_1 N_2; \alpha_{12}\rangle, \quad (59)$$

where the states $|E_{12} i_{12} J_{12} T_{12}\rangle_a$ correspond to the relative part of the antisymmetric Jacobi-HO states and $C_{N'_1 N'_2 \alpha'_{12}}^{i_{12}}$ are the expansion coefficients, also referred to as ‘‘coefficients of fractional parentage’’ (CFPs) [70]. The index i_{12} is not a physical quantum number, but enumerates the antisymmetric states. The choice of the antisymmetric Jacobi basis states, i.e., the choice of the CFPs, is not unique. In fact there are arbitrarily many possibilities to choose an orthonormal basis that spans the antisymmetric space. The specific values of the CFPs are defined by the diagonalization procedure and the physical content of a numerical matrix element in the antisymmetric Jacobi-HO representation is only defined with respect to the underlying CFPs.

The starting point for the inclusion of $3N$ interactions in the HO basis is a representation of the interaction in the antisymmetric Jacobi-HO basis

$${}_a \langle E_{12} i_{12} J_{12} T_{12} | \mathbf{V} | E'_{12} i'_{12} J_{12} T_{12} \rangle_a, \quad (60)$$

which are only nonvanishing for equal angular momentum J_{12} , isospin T_{12} and parity π of the bra and ket states, yielding a separation of the interaction matrix into $(J_{12}^\pi T_{12})$ -blocks. Note that the parity is defined by the orbital angular momenta $\pi = (-1)^{L_1+L_2}$ and thus is related to the energy quantum number $E_{12} = 2N_1 + L_1 + 2N_2 + L_2$ via $\pi = (-1)^{E_{12}}$, where we exploited that $(-1)^{2N_1+2N_2}$ is equivalent to 1. The matrix elements of the local standard 3N interaction (see Sec 1.3.2) and the corresponding CFPs are evaluated with Petr Navrátil's MANYEFF code [70].

The introduction of the antisymmetric Jacobi-HO basis reduces the number of interaction matrix elements by one order of magnitude compared to the partial antisymmetric basis. The antisymmetrization procedure discussed above is generally not applicable to continuous basis sets, such as the momentum basis. Further, advantages and disadvantages of the Jacobi-HO basis in comparison to other three-body bases are discussed in Sec. 3.2 and 3.5, where we introduce the HO single-particle schemes and the partial-wave decomposed Jacobi-momentum basis, respectively.

3.1.3 Four-Body HO Basis and Antisymmetrization

For the construction of the four-body Jacobi-HO basis we adopt the strategy of Ref. [70]: One arrives at the A -body Jacobi-HO state via an extension of the antisymmetric $(A-1)$ -body state and performs the subsequent antisymmetrization as presented in Sec. 3.1.2.

We start with a partial-antisymmetric four-body Jacobi-HO basis

$$|N_{\text{cm}(4)}L_{\text{cm}(4)}\rangle \otimes |E_{12}i_{12}N_3; [J_{12}, (L_3\frac{1}{2})J_3]J_{123}; (T_{12}\frac{1}{2})T_{123}\rangle_{a_{12}}, \quad (61)$$

where we omit the projection quantum numbers $M_{L_{\text{cm}(4)}}$, $M_{J_{123}}$, and $M_{T_{123}}$ for brevity. The state in Eq. (61) is an extension of the antisymmetric three-body state of Eq. (59) by the quantum numbers N_3, L_3, J_3 corresponding to the Jacobi coordinate $\vec{\xi}_3$ and the spin and isospin of the fourth particle, which couple with the quantities of the three-body state to the angular momentum J_{123} and isospin T_{123} . The symmetric center-of-mass part of the four-body state is omitted in the following, for the same reasons as in the previous section. The total HO energy quantum number of the four-body state is given by $E_{abcd} = E_{\text{cm}(4)} + E_{123}$, with the center-of-mass contribution $E_{\text{cm}(4)} = 2N_{\text{cm}(4)} + L_{\text{cm}(4)}$ and the relative-energy quantum number $E_{123} = E_{12} + 2N_3 + L_3$.

For brevity we introduce the short hand

$$|E_{12}i_{12}N_3; \alpha_{123}\rangle_{a_{12}} = |E_{12}i_{12}N_3; [J_{12}, (L_3\frac{1}{2})J_3]J_{123}; (T_{12}\frac{1}{2})T_{123}\rangle_{a_{12}}, \quad (62)$$

with the collective index $\alpha_{123} = \{J_{12}, L_3, J_3, J_{123}, T_{12}, T_{123}\}$. Note, that the partial-wave information is partially contained in the index i_{12} , such that the states are defined with respect to

the three-body CFPs.

The basis state in Eq. (61) is only antisymmetric with respect to the exchange of the first three particles. The full antisymmetrization is performed analogously as for the three-body case. We represent the antisymmetrizer \mathcal{A} using the basis states of Eq. (61). By exploiting the partial antisymmetry of the basis we obtain

$$\begin{aligned}
 {}_{a_{12}}\langle E_{12}i_{12}N_3; \alpha_{123} | \mathcal{A} | E'_{12}i'_{12}N'_3; \alpha'_{123} \rangle_{a_{12}} = \\
 {}_{a_{12}}\langle E_{12}i_{12}N_3; \alpha_{123} | \frac{1}{4}(\mathbb{1} - 3\mathcal{T}_{cd}) | E'_{12}i'_{12}N'_3; \alpha'_{123} \rangle_{a_{12}} .
 \end{aligned} \tag{63}$$

The nonvanishing matrix elements of the transposition operator \mathcal{T}_{cd} can be calculated by [143]

$$\begin{aligned}
 & {}_{a_{12}}\langle E_{12}i_{12}N_3; [J_{12}, (L_3\frac{1}{2})J_3]J_{123}; (T_{12}\frac{1}{2})T_{123} | \frac{1}{4}(\mathbb{1} - 3\mathcal{T}_{cd}) \\
 & \quad \times | E'_{12}i'_{12}N'_3; [J'_{12}, (L'_3\frac{1}{2})J'_3]J_{123}; (T'_{12}\frac{1}{2})T_{123} \rangle_{a_{12}} \\
 & = \sum_{N_1N_2} \sum_{\alpha} \sum_{N'_2L'_2J'_2} \sum_{i_{12}i'_{12}} \sum_{L_{23}K} (-1)^{T_{12}+T'_{12}+L_2+L'_2+J_2+J'_2} \hat{J}_{12}\hat{J}_2\hat{J}_3\hat{T}_{12}\hat{J}'_{12}\hat{J}'_2\hat{J}'_3\hat{L}'_2\hat{K}^2 \\
 & \quad \times C_{N_1N_2\alpha_{12}}^{i_{12}} C_{N_1N'_2\alpha'_{12}}^{i'_{12}} \begin{Bmatrix} J_1 & J_2 & J_{12} \\ J'_2 & K & J_3 \\ J'_{12} & J'_3 & J_{123} \end{Bmatrix} \begin{Bmatrix} L'_2 & L_3 & K \\ J_3 & J'_2 & \frac{1}{2} \end{Bmatrix} \begin{Bmatrix} L_2 & L'_3 & K \\ J'_3 & J_2 & \frac{1}{2} \end{Bmatrix} \\
 & \quad \times \begin{Bmatrix} L_3 & L'_2 & K \\ L'_3 & L_2 & L_{23} \end{Bmatrix} \begin{Bmatrix} \frac{1}{2} & T_{123} & T_{12} \\ \frac{1}{2} & T_1 & T'_{12} \end{Bmatrix} \langle\langle N'_2L'_2, N'_3L'_3; L_{23} | N_2L_2, N_3L_3 \rangle\rangle_{\frac{1}{8}},
 \end{aligned} \tag{64}$$

with the collective index $\tilde{\alpha}'_{12} = \{L_1, S_1, J_1, T_1, L'_2, J'_2\}$. The intermediate angular momenta L_{23} and K result from the angular momentum-recouplings, and the HOBs $\langle\langle \dots \rangle\rangle_{\frac{1}{8}}$ appear due to the coordinate transformation caused by the transposition operator (see Ref. [144] for a derivation of the formula). The calculation of the antisymmetrizer eigenstates with eigenvalue (-1) yields the four-body CFPs that determine the antisymmetric four-body Jacobi-HO basis states

$$\begin{aligned}
 |E_{123}i_{123}J_{123}T_{123}\rangle_a = \sum_{E'_{12}N'_3} \sum_{i'_{12}\alpha'_{123}} \delta_{(E'_{12}+2N'_3+L'_3), E_{123}} \delta_{J'_{123}, J_{123}} \delta_{T'_{123}, T_{123}} \\
 \times \tilde{C}_{E'_{12}N'_3\alpha'_{123}}^{i'_{12}i_{123}} |E'_{12}i'_{12}N'_3; \alpha'_{123}\rangle_{a_{12}} .
 \end{aligned} \tag{65}$$

The four-body CFPs $\tilde{C}_{E'_{12}N'_3\alpha'_{123}}^{i'_{12}i_{123}}$ depend on the diagonalization algorithm of the antisymmetrizer matrix in the three- and four-body space, such that the physical content of the antisymmetric Jacobi state $|E_{123}i_{123}J_{123}T_{123}\rangle_a$ is defined by the choice of the three- and four-body CFPs. As in the three-body case the index i_{123} enumerates the antisymmetric basis states. The interaction matrix elements represented in the basis states of Eq. (65) separate into blocks of equal angular momentum J_{123} , isospin T_{123} , and parity $\pi = (-1)^{E_{123}}$ in the bra and ket states.

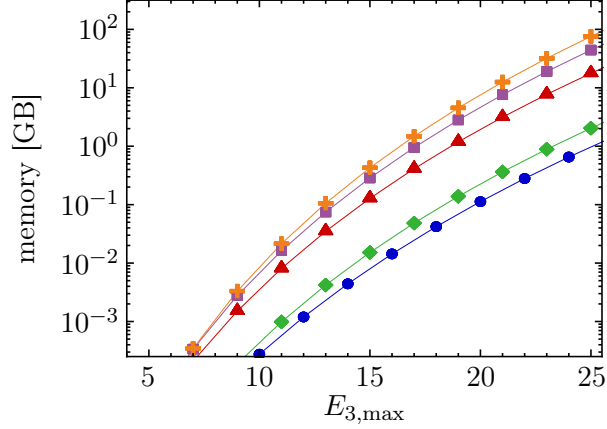


Figure 3.1 *Number of $4N$ interaction matrix elements in the four-body Jacobi-HO basis:* Illustrated are the memory needs in GB to store the interaction matrix in the four-body Jacobi-HO basis with single precision as function of the maximum energy quantum number $E_{4,\max}$. The curves correspond to the $(J_{123}^{\pi} T_{123})$ -blocks: 0^+0 (●), 0^-1 (◆), 1^-1 (▲), 2^-1 (■), and 3^-1 (⊕).

Note, that the explicit consideration of the antisymmetry reduces the number of matrix elements by a factor of almost 16 compared to the partial antisymmetric basis of Eq. (61). Nevertheless, in comparison to the three-body case the number of four-body matrix elements grows more rapidly with the energy quantum number E_{123} and the angular momentum J_{123} .

We focus on the limitations that appear when performing calculations, e.g., the SRG transformation in the Jacobi-HO basis representation. In Fig. 3.1 we illustrate the memory needed to store interaction matrix elements for different $(J_{123}^{\pi} T_{123})$ -blocks as function of the model-space truncation denoted by the maximum energy quantum number $E_{4,\max}$. We show the memory needs for the (0^+0) -block (blue circles), corresponding to the ^4He channel as well as for those channels corresponding to $T_{123} = 1$ and negative parity, which are the largest channels using an odd $E_{4,\max}$ truncation for given $J_{123} = 0$ (green diamonds), 1 (red triangles), 2 (violet boxes), and 3 (orange crosses).

Due to combinatorial reasons for the isospin coupling the number of matrix elements for $T_{123} = 1$ channels are considerably larger than for $T_{123} = 0$ or 2 channels. In particular, raising of the angular momentum from $J_{123} = 0$ to $J_{123} = 1$ increases the number of matrix elements dramatically by about one order of magnitude. Although, the growth with J_{123} tends to slow down for the higher angular momenta we are confronted with huge model-space dimensions for rather small values of $E_{4,\max}$ compared to the energy quantum numbers used in the three-body space (see Sec. 5). In Sec. 6.4 we investigate which partial waves can be treated accurately and whether these partial waves capture the relevant physics.

To summarize, the separation of the center-of-mass degree of freedom and the possibility to exploit the antisymmetry of the discrete basis, utilizing the CFPs, makes the Jacobi-HO basis

an optimal candidate for the treatment of the 4N contributions. However, the major limitation is the large number of interaction matrix elements in the four-body space.

Moreover, the antisymmetrization procedure becomes challenging for larger model spaces. This is due to the increasing number of antisymmetrizer matrix elements that have to be evaluated by means of Eq. (64), which requires careful optimizations, precaching of several computing-intensive objects and utilizing, e.g., BLAS routines to perform efficient matrix-matrix and matrix-vector multiplications. Further, the subsequent diagonalization requires the storage of the dense antisymmetrizer matrix, which becomes an additional obstacle with increasing model-space size.

3.2 Single-Particle Scheme vs. Jacobi basis

In the previous section we discussed the Jacobi-HO basis including its advantages concerning the omission of the center-of-mass part from the outset. Nonetheless, since we are interested in the description of A -nucleon systems, e.g., with NCSM-type approaches, it is necessary to solve the nuclear eigenvalue problem in the A -body space. Formally one can construct an A -body Jacobi basis by an extension of the $(A - 1)$ -body basis, but the antisymmetrization becomes computational too demanding for $A \geq 7$ [70]. Thus, it is necessary to transform the interaction matrix elements to the single-particle scheme to embed them into the A -body space and to solve the eigenvalue problem. The antisymmetrized product states of ls -coupled single-particle HO states, the so-called m -scheme, can be converted from the two-, three-, or four-body basis to the A -body basis simply by using Slater rules [102, 103]. Thus, we aim at a representation of the interaction in the m -scheme to perform, e.g., NCSM-type calculations.

To simplify the discussion, we concentrate on the inclusion of 3N interactions via their representation in three-body space, but stress that this procedure is analogous for the four-body case. The m -scheme states in the three-body space are defined as

$$|abc\rangle_a = |n_a l_a j_a m_{j_a} m_{t_a}; n_b l_b j_b m_{j_b} m_{t_b}; n_c l_c j_c m_{j_c} m_{t_c}\rangle_a, \quad (66)$$

where $a = \{n_a l_a j_a m_{j_a} m_{t_a}\}$ is a short-hand for the single-particle quantum numbers. Utilizing this basis one can exploit the Hermiticity and the particle-exchange symmetry of the interaction, as well as the symmetries corresponding to time-reversal, rotation, and the charge.

The major disadvantage of the m -scheme is the large number of non-vanishing matrix elements necessary to represent the interaction, which becomes problematic for applications of 3N forces beyond mid-p-shell nuclei. Therefore, we develop an intermediate step, namely, the transformation from the Jacobi-HO representation into the JT -coupled scheme (see Sec. 3.2.1)

$$|\tilde{a}\tilde{b}\tilde{c}; J_{ab}J_{abc}; T_{ab}T_{abc}\rangle_a = |n_a l_a n_b l_b n_c l_c; [(j_a j_b)J_{ab}, j_c]J_{abc}; [(\frac{1}{2} \frac{1}{2})T_{ab}, \frac{1}{2}]T_{abc}\rangle_a, \quad (67)$$

where we suppress the projection quantum numbers $M_{J_{abc}}$ and $M_{T_{abc}}$ for brevity and introduce the short hand $\tilde{a} = \{n_a, l_a, j_a\}$ that collect the radial and angular momentum single-particle quantum numbers. This basis is obtained from the m -scheme by coupling the angular momenta and isospins of the first two particles and subsequently coupling the resulting quantities (J_{ab}, T_{ab}) to those of the third particle. In the JT -coupled scheme one can exploit that the interaction does not connect different angular momenta J_{abc} and isospins T_{abc} in the bra and ket states, which reduces the number of non-vanishing matrix elements by more than two orders of magnitude compared to the m -scheme representation. This becomes evident from Fig. 3.2, where the memory required to store the 3N interaction elements is plotted for the different HO basis sets as function of the maximum three-body energy quantum number $E_{3,\max}$. We point out that in practice the time-reversal symmetry is not exploited to reduce the number of non-vanishing matrix elements. In order to be comparable with Ref. [101] the m -scheme storage demands in the figure are reduced by a factor of 2 exploiting this symmetry. Furthermore, the figure illustrates the storage demands of the T -coefficients, that are necessary for the transformation of the Jacobi basis into the single-particle schemes (see Sec. 3.2.1). For the storage demands in the plot the basic symmetries of the 3N interaction are exploited and the quantities are assumed to be stored in single precision. The JT -coupled scheme provides a compromise between the enormous memory needs in the m -scheme and the large recompute costs in the Jacobi basis. Thus, the storage of the 3N interaction in the JT -coupled scheme is the key to perform reliable (IT-)NCSM calculations for $N_{\max} > 8$ for p- and lower sd-shell nuclei including 3N forces. The NCSM calculations of mid-p-shell nuclei for $N_{\max} = 8$ requires 3N matrix elements up to $E_{3,\max} = 11$. These 3N matrix elements require 33GB in the m -scheme representation [101]. This is at the borderline of current supercomputers, while one only needs 0.4GB in the JT -coupled scheme representation, which is typically even manageable on commercial laptops. In practice we perform the decoupling to the m -scheme on the fly during the NCSM-type calculation, using an efficient storage scheme explained in Sec. 3.2.3.

So far we focused on NCSM-type calculations to motivate the transformation to a single-particle scheme and, in particular, to utilize the JT -coupled scheme for storing the interaction matrix elements. It is worth mentioning that the JT -coupled scheme provides important advantages for a number of other approaches and many-body methods as well. For instance, the normal-ordering approach discussed in Sec. 3.3 can be formulated directly in the JT -coupled scheme, avoiding the m -scheme completely. The moderate memory footprint in combination with the simplicity of the decoupling procedure leads to the adoption in various many-body methods [28, 29, 32, 35, 36, 101, 145]. By analogous developments also the inclusion of 4N interactions becomes feasible, e.g., in the (IT-)NCSM. The necessary ingredients to derive and store the three- and four-body interaction matrix elements in the JT -coupled scheme, are discussed in the following.

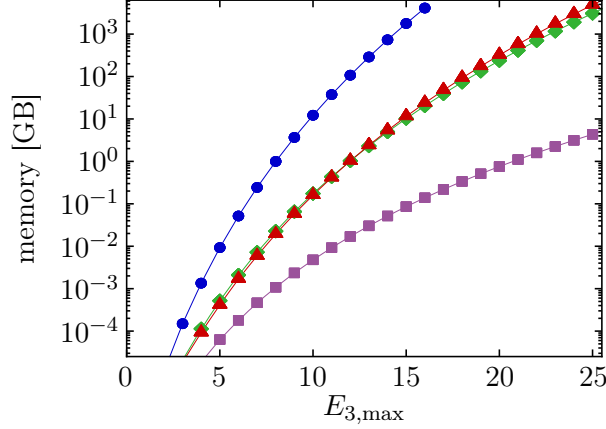


Figure 3.2 *Required memory in the three-body basis*: Illustrated is the memory in GB required to store 3N interaction matrix in the representation of the four-body Jacobi-HO basis (\blacklozenge), the JT -coupled scheme (\blacktriangle), and the m -scheme (\bullet), as well as the storage demand for the T -coefficients (\blacksquare). The storage demand is plotted as function of the maximum three-body energy quantum number $E_{3,\max}$. All quantities are assumed to be single-precision floating point numbers.

3.2.1 Transformation to JT -Coupled Scheme in Three-Body Space

In this section we summarize the formal steps to derive the transformation of the interaction matrix elements in the three-body Jacobi-HO representation (59) to the JT -coupled scheme (67), and discuss the computational limits of the transformation. We refer the reader to Ref. [138] for a comprehensive derivation of the transformation formula.

The starting point are the interaction matrix elements in the antisymmetric Jacobi-HO basis (60). We aim at the transformation to a single-particle scheme, hence, we need to include the center-of-mass part, yielding

$$\begin{aligned} & {}_a\langle E_{12}i_{12}J_{12}T_{12}; N_{\text{cm}(3)}L_{\text{cm}(3)}; J_{abc} | \mathbf{V} | E'_{12}i'_{12}J'_{12}T'_{12}; N'_{\text{cm}(3)}L'_{\text{cm}(3)}; J'_{abc} \rangle_a \\ & = \delta_{N_{\text{cm}(3)}, N'_{\text{cm}(3)}} \delta_{L_{\text{cm}(3)}, L'_{\text{cm}(3)}} \delta_{J_{abc}, J'_{abc}} {}_a\langle E_{12}i_{12}J_{12}T_{12} | \mathbf{V} | E'_{12}i'_{12}J'_{12}T'_{12} \rangle_a, \end{aligned} \quad (68)$$

where we couple the angular momentum of the relative part J_{12} with the orbital angular momentum of the center-of-mass part $L_{\text{cm}(3)}$ to the total angular momentum J_{abc}

$$|E_{12}i_{12}J_{12}T_{12}; N_{\text{cm}(3)}L_{\text{cm}(3)}; J_{abc}\rangle_a = \{ |E_{12}i_{12}J_{12}T_{12}\rangle_a \otimes |N_{\text{cm}(3)}L_{\text{cm}(3)}\rangle \}^{J_{abc}}. \quad (69)$$

With help of the CFPs we express these antisymmetric states as superposition of the partial

antisymmetric Jacobi-HO states (56). The corresponding overlap reads

$$\begin{aligned} & a_1 \langle N_1 N_2; \alpha_{12}; N_{\text{cm}(3)} L_{\text{cm}(3)}; J_{abc} | E'_{12} i'_{12} J'_{12} T'_{12}; N'_{\text{cm}(3)} L'_{\text{cm}(3)}; J'_{abc} \rangle_a \\ & = \delta_{(2N_1+L_1+2N_2+L_2), E'_{12}} \delta_{J_{12}, J'_{12}} \delta_{T_{12}, T'_{12}} \delta_{N_{\text{cm}(3)}, N'_{\text{cm}(3)}} \delta_{L_{\text{cm}(3)}, L'_{\text{cm}(3)}} \delta_{J_{abc}, J'_{abc}} C_{N_1 N_2 \alpha_{12}}^{i'_{12}}, \end{aligned} \quad (70)$$

with

$$|N_1 N_2; \alpha_{12}; N_{\text{cm}(3)} L_{\text{cm}(3)}; J_{abc} \rangle_{a_1} = \{ |N_1 N_2; \alpha_{12} \rangle_{a_1} \otimes |N_{\text{cm}(3)} L_{\text{cm}(3)} \rangle \}^{J_{abc}}. \quad (71)$$

As before all projection quantum numbers are suppressed in this section for brevity. The central component of the transformation consist of a coordinate-system change, which can be achieved by evaluating the overlap of the partial-antisymmetric Jacobi-HO state (71) with the non-antisymmetrized JT -coupled state $|\tilde{a}\tilde{b}\tilde{c}; J_{ab} J_{abc}; T_{ab} T_{abc} \rangle$ that defines the so-called T -coefficient

$$\begin{aligned} & T_{N_1 N_2 \alpha_{12} N_{\text{cm}(3)} L_{\text{cm}(3)}}^{\tilde{a}\tilde{b}\tilde{c} J_{ab} J_{abc}} = T_{N_1 L_1 S_1 J_1 N_2 L_2 S_2 J_2 J_{12} N_{\text{cm}(3)} L_{\text{cm}(3)}}^{n_a l_a j_a n_b l_b j_b n_c l_c j_c J_{ab} J_{abc}} \\ & = a_1 \langle N_1 N_2; \alpha_{12}; N_{\text{cm}(3)} L_{\text{cm}(3)}; J_{abc} | \tilde{a}\tilde{b}\tilde{c}; J_{ab} J_{abc}; T_{ab} T_{abc} \rangle. \end{aligned} \quad (72)$$

The overlap is non-vanishing only for equal total angular momentum J_{abc} in both states, as well as for $T_1 = T_{ab}$ and $T_{12} = T$. Besides there is no further dependence on the isospin quantum numbers. As discussed in Ref. [80] this overlap can be derived by multiple angular-momentum recouplings that are necessary to perform the Talmi-Moshinsky transformations, which change the coordinate system. The analytic form is given by

$$\begin{aligned} & T_{N_1 L_1 S_1 J_1 N_2 L_2 S_2 J_2 J_{12} N_{\text{cm}(3)} L_{\text{cm}(3)}}^{n_a l_a j_a n_b l_b j_b n_c l_c j_c J_{ab} J_{abc}} \\ & = \sum_{N_{\text{cm}(2)} L_{\text{cm}(2)}} \sum_{L_{ab} L_{12} S_{12}} \sum_K \delta_{(2n_a+l_a+2n_b+l_b+2n_c+l_c), (2N_{\text{cm}(3)}+L_{\text{cm}(3)}+2N_1+L_1+2N_2+L_2)} \\ & \times (-1)^{l_c+K+L_{ab}+L+S_{12}+L_1+J_{abc}} \hat{j}_a \hat{j}_b \hat{j}_c \hat{J}_{ab} \hat{J}_{abc} \hat{J}_1 \hat{J}_2 \hat{S}_1 \hat{S}_{12} \hat{L}_{12} \hat{L}_{ab} \hat{L}_{abc} \hat{L}_{12}^2 \hat{L}_{\text{cm}(2)}^2 \hat{K}^2 \\ & \times \langle \langle N_{\text{cm}(2)} L_{\text{cm}(2)}, N_1 L_1; L_{ab} | n_b l_b, n_a l_a \rangle \rangle_1 \\ & \times \langle \langle N_{\text{cm}(3)} L_{\text{cm}(3)}, N_2 L_2; K | N_{\text{cm}(2)} L_{\text{cm}(2)}, n_c l_c \rangle \rangle_2 \\ & \times \begin{Bmatrix} l_a & l_b & L_{ab} \\ \frac{1}{2} & \frac{1}{2} & S_1 \\ j_a & j_b & J_{ab} \end{Bmatrix} \begin{Bmatrix} L_{ab} & l_c & L_{abc} \\ S_1 & \frac{1}{2} & S_{12} \\ J_{ab} & j_c & J_{abc} \end{Bmatrix} \begin{Bmatrix} L_1 & L_2 & L_{12} \\ S_1 & S_2 & S_{12} \\ J_1 & J_2 & J_{12} \end{Bmatrix} \\ & \times \begin{Bmatrix} l_c & L_{\text{cm}(2)} & K \\ L_1 & L_{abc} & L_{ab} \end{Bmatrix} \begin{Bmatrix} L_{\text{cm}(3)} & L_2 & K \\ L_1 & L_{abc} & L_{12} \end{Bmatrix} \begin{Bmatrix} L_{\text{cm}(3)} & L_{12} & L \\ S_{12} & J_{abc} & J_{12} \end{Bmatrix}, \end{aligned} \quad (73)$$

with the short hand $\hat{x} = \sqrt{2x+1}$. The summation over $N_{\text{cm}(2)}$ can be eliminated by using the energy-conservation property of the first HOB, i.e., $2N_{\text{cm}(2)} + L_{\text{cm}(2)} + 2N_1 + L_1 = 2n_b + l_b + 2n_a + l_a$.

Note, that for the derivation of the T -coefficient we used a non-antisymmetric JT -coupled state, thus, we express the final antisymmetric matrix element in terms of this state

$$\begin{aligned} & {}_a\langle\tilde{a}\tilde{b}\tilde{c}; J_{ab}J_{abc}; T_{ab}T_{abc} | \mathbf{V} | \tilde{a}'\tilde{b}'\tilde{c}'; J'_{ab}J_{abc}; T'_{ab}T_{abc}\rangle_a \\ & = 3! \langle\tilde{a}\tilde{b}\tilde{c}; J_{ab}J_{abc}; T_{ab}T_{abc} | \mathcal{A}\mathbf{V}\mathcal{A} | \tilde{a}'\tilde{b}'\tilde{c}'; J'_{ab}J_{abc}; T'_{ab}T_{abc}\rangle, \end{aligned} \quad (74)$$

where the factor $3!$ is due to the fact that the antisymmetrizer \mathcal{A} is a projection operator. For completeness we mention that the non-antisymmetric JT -coupled states are orthogonal but not normalized while the antisymmetric state are orthonormal. However, since we typically decouple those states to the orthonormal m -scheme, this does not affect the subsequent calculations.

The antisymmetrizer can be expressed by the antisymmetric Jacobi-HO basis (69) as

$$\begin{aligned} \mathcal{A} & = \sum_{E_{12}i_{12}} \sum_{J_{12}T_{12}} \sum_{N_{\text{cm}(3)}L_{\text{cm}(3)}} \sum_{J_{abc}} \\ & |E_{12}i_{12}J_{12}T_{12}; N_{\text{cm}(3)}L_{\text{cm}(3)}; J_{abc}\rangle_{aa} \langle E_{12}i_{12}J_{12}T_{12}; N_{\text{cm}(3)}L_{\text{cm}(3)}; J_{abc} |. \end{aligned} \quad (75)$$

Plugging this into Eq. (74) and inserting a unity in the partial-antisymmetric Jacobi-HO basis representation (69) yields the final expression containing the CFPs (70) and the T -coefficients (73)

$$\begin{aligned} & {}_a\langle\tilde{a}\tilde{b}\tilde{c}; J_{ab}J_{abc}; T_{ab}T_{abc} | \mathbf{V} | \tilde{a}'\tilde{b}'\tilde{c}'; J'_{ab}J_{abc}; T'_{ab}T_{abc}\rangle_a \\ & = 3! \sum_{N_1N_2\alpha_{12}} \sum_{N'_1N'_2\alpha'_{12}} \sum_{N_{\text{cm}(3)}L_{\text{cm}(3)}} \sum_{i_{12}i'_{12}} \delta_{T_{ab},T_1} \delta_{T'_{ab},T'_1} \delta_{T_{abc},T_{12}} \delta_{T'_{abc},T'_{12}} \delta_{J_{12},J'_{12}} \\ & \times T_{N_1N_2\alpha_{12}N_{\text{cm}(3)}L_{\text{cm}(3)}}^{\tilde{a}\tilde{b}\tilde{c}J_{ab}J_{abc}} T_{N'_1N'_2\alpha'_{12}N_{\text{cm}(3)}L_{\text{cm}(3)}}^{\tilde{a}'\tilde{b}'\tilde{c}'J'_{ab}J_{abc}} C_{N_1N_2\alpha_{12}}^{i_{12}} C_{N'_1N'_2\alpha'_{12}}^{i'_{12}} \\ & \times {}_a\langle E_{12}i_{12}J_{12}T_{12} | \mathbf{V} | E'_{12}i'_{12}J_{12}T_{12}\rangle_a. \end{aligned} \quad (76)$$

The transformation of the three-body interaction matrix elements is computationally demanding. In practice we precompute the T -coefficients and store them in memory, in order to circumvent multiple evaluations of these complicated objects. The sheer number of T -coefficients causes limitations due to computing time and memory demands. The number of T -coefficients that need to be evaluated is comparable to the number of the matrix elements in the JT -coupled scheme (see Fig. 3.2). Due to optimized caching of the relevant intermediates and a separation of the transformation to multiple nodes, we are able to provide $3N$ interactions up to $E_{3,\text{max}} \approx 16$. The use of BLAS routines for the matrix multiplications enables us to calculate a $3N$ matrix element set for $E_{3,\text{max}} = 14$ on a single node in about one hour. Further information about technical details can be also found in Ref. [21].

3.2.2 Transformation to JT -Coupled Scheme in Four-Body Space

The transformation from the Jacobi-HO to the JT -coupled scheme in the four-body space can be performed following analogous steps as for the three-body space. However, the derivation of the transformation formula is more complex and requires a considerably larger number of angular-momentum recouplings and also additional Talmi-Moshinsky transformations to change the underlying coordinate system. First we introduce the JT -coupled basis states

$$\begin{aligned} & |\tilde{a}\tilde{b}\tilde{c}\tilde{d}; J_{ab}J_{abc}J_{abcd}; T_{ab}T_{abc}T_{abcd}\rangle_a \\ &= |n_a l_a n_b l_b n_c l_c n_d l_d; \{[(j_a j_b) J_{ab}, j_c] J_{abc}, j_d\} J_{abcd}; \{[(\frac{1}{2} \frac{1}{2}) T_{ab}, \frac{1}{2}] T_{abc}, \frac{1}{2}\} T_{abcd}\rangle_a, \end{aligned} \quad (77)$$

where the coupled angular momentum of the first three particles J_{abc} couples with the angular momentum of the fourth particle j_d to J_{abcd} and analogously for the isospin. As before we suppress the projection quantum number for brevity.

A complete derivation of the transformation formula can be found in Ref. [144]. In the following we quote the result, emphasizing the differences to the three-body case and discussing the limitations of the transformation. Performing similar steps as in the three-body case yields the formula

$$\begin{aligned} & {}_a\langle\tilde{a}\tilde{b}\tilde{c}\tilde{d}; J_{ab}J_{abc}J_{abcd}; T_{ab}T_{abc}T_{abcd} | \mathbf{V} | \tilde{a}'\tilde{b}'\tilde{c}'\tilde{d}'; J'_{ab}J'_{abc}J_{abcd}; T'_{ab}T'_{abc}T_{abcd}\rangle_a \\ &= 4! \sum_{N_{\text{cm}(4)} L_{\text{cm}(4)}} \sum_{J_{123} T_{123}} \sum_{E_{123} i_{123}} \sum_{E'_{123} i'_{123}} \\ &\times \tilde{T}_{E_{123} i_{123} J_{123} N_{\text{cm}(4)} L_{\text{cm}(4)}}^{\tilde{a}\tilde{b}\tilde{c}\tilde{d} J_{ab} J_{abc} J_{abcd} T_{ab} T_{abc} T_{abcd}} \tilde{T}_{E'_{123} i'_{123} J_{123} N_{\text{cm}(4)} L_{\text{cm}(4)}}^{\tilde{a}'\tilde{b}'\tilde{c}'\tilde{d}' J'_{ab} J'_{abc} J_{abcd} T'_{ab} T'_{abc} T_{abcd}} \\ &\times {}_a\langle E_{123} i_{123} J_{123} T_{123} | \mathbf{V} | E'_{123} i'_{123} J_{123} T_{123}\rangle_a. \end{aligned} \quad (78)$$

The interaction matrix elements in the JT -coupled scheme only connect bra and ket states with equal angular momentum J_{abcd} , isospin T_{abcd} , and projection quantum numbers $M_{J_{abcd}}$ and $M_{T_{abcd}}$. The latter are suppressed for brevity. Also the parity $\pi = (-1)^{E_{abcd}}$ is conserved, which is determined by the total energy quantum number $E_{abcd} = 2n_a + l_a + \dots + 2n_d + l_d$. In Eq. (78) we introduce a somewhat different definition of the T -coefficient compared to the three-body case and we come to the reason for this later on. The four-body T -coefficient corresponds to an overlap that contains the antisymmetric Jacobi-HO state (80), rather than the partial-antisymmetric Jacobi-HO state (61), and is defined by

$$\begin{aligned} & \tilde{T}_{E_{123} i_{123} J_{123} N_{\text{cm}(4)} L_{\text{cm}(4)}}^{\tilde{a}\tilde{b}\tilde{c}\tilde{d} J_{ab} J_{abc} J_{abcd} T_{ab} T_{abc} T_{abcd}} \\ &= \frac{1}{\sqrt{4!}} {}_a\langle E_{123} i_{123} J_{123} T_{123}; N_{\text{cm}(4)} L_{\text{cm}(4)}; J_{abcd} | \tilde{a}\tilde{b}\tilde{c}\tilde{d}; J_{ab} J_{abc} J_{abcd}; T_{ab} T_{abc} T_{abcd}\rangle, \end{aligned} \quad (79)$$

where the relative part of the Jacobi state is augmented by the center-of-mass part

$$\begin{aligned}
 & |E_{123}i_{123}J_{123}T_{123}; N_{\text{cm}(4)}L_{\text{cm}(4)}; J_{abcd}\rangle_a \\
 & = \{ |N_{\text{cm}(4)}L_{\text{cm}(4)}\rangle \otimes |E_{123}i_{123}J_{123}T_{123}\rangle_a \}^{J_{abcd}}.
 \end{aligned} \tag{80}$$

For the derivation of these overlaps we perform the analogous steps as in the previous section, namely, we calculate the overlap of the non-antisymmetrized JT -coupled state with the four-body Jacobi-HO state that is only antisymmetric with respect to the exchange of the first two particles. The latter state reads

$$\begin{aligned}
 & \{ |N_{\text{cm}(4)}L_{\text{cm}(4)}\rangle \otimes |N_1N_2N_3; \{[(L_1\frac{1}{2})J_1, (L_2\frac{1}{2})J_2]J_{12}, (L_3\frac{1}{2})J_3\}J_{123}; [(T_1\frac{1}{2})T_{12}, \frac{1}{2}]T_{123}\rangle_{a_1} \}^{J_{abcd}} \\
 & = |N_1N_2N_3; \alpha_{12} \tilde{\alpha}_{123}; N_{\text{cm}(4)}L_{\text{cm}(4)}; J_{abcd}\rangle_{a_1}
 \end{aligned} \tag{81}$$

with $\alpha_{12} = \{L_1, S_1, J_1, L_2, J_2, J_{12}, T_1, T_{12}\}$ and $\tilde{\alpha}_{123} = \{L_3, J_3, J_{123}, T_{123}\}$. By inserting the antisymmetrizer in the Jacobi-HO basis representation and using the overlap

$$\begin{aligned}
 & {}_{a_1}\langle N_1N_2N_3; \alpha_{12} \tilde{\alpha}_{123}; N_{\text{cm}(4)}L_{\text{cm}(4)}; J_{abcd} | E'_{123}i'_{123}J'_{123}T'_{123}; N'_{\text{cm}(4)}L'_{\text{cm}(4)}; J'_{abcd}\rangle_a \\
 & = \sum_{E_{12}i_{12}} C_{N_1N_2\alpha_{12}}^{i_{12}} \tilde{C}_{E_{12}N_3\alpha_{123}}^{i'_{12}i_{123}} \delta_{(2N_1+L_1+2N_2+L_2), E_{12}} \delta_{(2N_1+L_1+2N_2+L_2+2N_3+L_3), E'_{123}} \\
 & \quad \times \delta_{J_{123}, J'_{123}} \delta_{T_{123}, T'_{123}} \delta_{J_{abcd}, J'_{abcd}} \delta_{N_{\text{cm}(4)}, N'_{\text{cm}(4)}} \delta_{L_{\text{cm}(4)}, L'_{\text{cm}(4)}}
 \end{aligned} \tag{82}$$

one can evaluate the T -coefficient and obtains

$$\begin{aligned}
 & \tilde{T}_{E_{123} i_{123}}^{\tilde{a} \tilde{b} \tilde{c} \tilde{d}} J_{ab} J_{abc} J_{abcd} T_{ab} T_{abc} T_{abcd} \\
 &= \sum_{N_1 N_2} \sum_{\alpha_{12}} \sum_{E_{12} i_{12} N_3} \sum_{\alpha_{123}} \sum_{L_{ab}} \sum_{K P} \sum_{Q R} \sum_{N_{\text{cm}(2)} L_{\text{cm}(2)}} \sum_{N_{\text{cm}(3)} L_{\text{cm}(3)}} \\
 & \times \hat{j}_a \hat{j}_b \hat{j}_c \hat{j}_d \hat{L}_{ab}^2 \hat{S}_{ab} \hat{J}_{ab} \hat{J}_{abc} \hat{K}^2 \hat{P}^2 \hat{Q}^2 \hat{R}^2 \hat{J}_1 \hat{J}_2 \hat{J}_3 \hat{J}_{12} \hat{J}_{123} \\
 & \times (-1)^{1+J_{ab}+J_{abc}+J_{abcd}+L_{\text{cm}(2)}+L_{\text{cm}(3)}+L_{\text{cm}(4)}+L_1+S_1+J_1+J_2+J_3+J_{12}} \\
 & \times \langle\langle N_{\text{cm}(2)} L_{\text{cm}(2)}, N_1 L_1; L_{ab} | n_a l_a, n_b l_b \rangle\rangle_1 \\
 & \times \langle\langle N_{\text{cm}(3)} L_{\text{cm}(3)}, N_2 L_2; K | N_{\text{cm}(2)} L_{\text{cm}(2)}, n_c l_c \rangle\rangle_2 \\
 & \times \langle\langle N_{\text{cm}(4)} L_{\text{cm}(4)}, N_3 L_3; Q | N_{\text{cm}(3)} L_{\text{cm}(3)}, n_d l_d \rangle\rangle_3 \tag{83} \\
 & \times \begin{Bmatrix} l_a & \frac{1}{2} & j_a \\ l_b & \frac{1}{2} & j_b \\ L_{ab} & S_1 & J_{ab} \end{Bmatrix} \begin{Bmatrix} L_{\text{cm}(2)} & J_1 & J_{ab} \\ l_c & \frac{1}{2} & j_c \\ K & P & J_{abc} \end{Bmatrix} \begin{Bmatrix} L_{\text{cm}(3)} & J_{12} & J_{abc} \\ l_d & \frac{1}{2} & j_d \\ Q & R & J_{abcd} \end{Bmatrix} \\
 & \times \begin{Bmatrix} \text{cm}(2) & L_1 & L_{ab} \\ S_1 & J_{ab} & J_1 \end{Bmatrix} \begin{Bmatrix} \text{cm}(3) & L_2 & K \\ P & J_{abc} & J_{12} \end{Bmatrix} \begin{Bmatrix} \text{cm}(4) & L_3 & Q \\ R & J_{abcd} & J_{123} \end{Bmatrix} \\
 & \times \begin{Bmatrix} L_2 & \frac{1}{2} & J_2 \\ J_1 & J_{12} & P \end{Bmatrix} \begin{Bmatrix} L_3 & \frac{1}{2} & J_3 \\ J_{12} & J_{123} & R \end{Bmatrix} C_{N_1 N_2 \alpha_{12}}^{i_{12}} \tilde{C}_{E_{12} N_3 \alpha_{123}}^{i_{12} i_{123}},
 \end{aligned}$$

with $\alpha_{123} = \{L_3, J_3, J_{12}, J_{123}, T_{12}, T_{123}\}$. Note, the sums over the isospin quantum numbers T_1 , T_{12} , and T_{123} can be eliminated by the conditions $T_1 = T_{ab}$, $T_{12} = T_{abc}$, and $T_{123} = T_{abcd}$. In this formula the $6j$ - and $9j$ -symbols result from various angular momentum recouplings in order to obtain the appropriate coupling order for the Talmi-Moshinsky transformations that result the HOBs. The computation of the JT -coupled matrix elements (78) and, in particular, of the required T -coefficients (83) is a formidable task. The experience and technical developments from the three-body transformation are utilized and extended to facilitate the transformation for model spaces required in the many-body calculations of Sec. 6.4.

An important detail is the slightly different definition of the four-body T -coefficients compared to the three-body case. Due to the fact that the number of antisymmetric four-body Jacobi-HO states (65) in a certain model space is about a factor of 4 smaller than for the partial-antisymmetric states (61) (antisymmetric with respect to the exchange of the first three particles) and even a factor 12 smaller than for the states (81) (antisymmetric with respect to the exchange of the first two particles), the memory needs of these coefficients are considerably reduced. A similar definition could be also introduced for the three-body case to reduce the memory demands during the transformation. The four-body model space is typically truncated by the maximum total-energy quantum number $E_{4,\text{max}}$. In Fig. 3.3 we illustrate the memory required to store the interaction matrix elements in the Jacobi basis (violet squares), the JT -coupled scheme (red triangles) and the m -scheme (blue circles). The matrix elements are

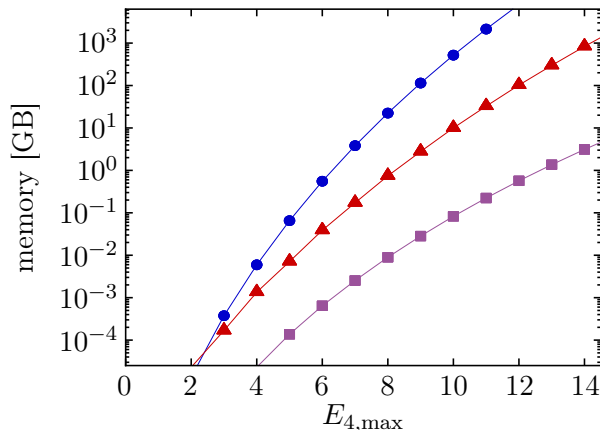


Figure 3.3 *Required memory in the four-body basis*: Illustrated is the memory in GB required to store the $4N$ interaction matrix in the representation of the four-body Jacobi-HO basis (■), the JT -coupled scheme (▲), and the m -scheme (●). The storage demand is plotted as function of the maximum four-body energy quantum number $E_{4,\max}$, all matrix elements are assumed to be single-precision floating point numbers.

assumed to be stored in single precision and the considered symmetries correspond to the ones in the three-body case. We observe an equal pattern as in Fig. 3.2, the memory demands in JT -coupled scheme provides a compromise between the recompute demands in the Jacobi basis and the memory demands in the m -scheme. Obviously, the growth of the number of matrix elements is even more dramatic than in the three-body case, limiting us to model space with smaller $E_{4,\max}$. However, due to optimizations concerning the implementation of the transformation we can provide $4N$ interaction matrix elements up to $E_{4,\max} \approx 10$ and we investigate in Sec. 6.4 if such model spaces are sufficient to cover the relevant physics of the $4N$ contributions.

3.2.3 Decoupling and Storage Scheme

As illustrated in Fig. 3.2 and 3.3 the JT -coupled scheme reduces the storage demands by about two orders of magnitude compared to the m -scheme. However, several many-body methods, such as NCSM-type approaches, rely on the m -scheme representation, since it enables an efficient transformation to the A -body space via Slater rules [102, 103]. The precomputation of the $3N$ contributions in the JT -coupled scheme in combination with a fast on-the-fly decoupling during the many-body calculations, provides an optimal compromise between increasing disk-I/O and computational demands. In this section we discuss the storage scheme that enables an efficient and cache optimized decoupling to the m -scheme.

The decoupling can be performed via summations over the coupled quantities of the JT -coupled scheme using several Clebsch-Gordon coefficients, yielding the three-body m -scheme matrix

elements

$$\begin{aligned}
 {}_a\langle abc | \mathbf{V} | a'b'c' \rangle_a &= \sum_{J_{ab}J'_{ab}} \sum_{T_{ab}T'_{ab}} \sum_{J_{abc}T_{abc}} \\
 &\times {}_a\langle \tilde{a}\tilde{b}\tilde{c}; J_{ab}J_{abc}; T_{ab}T_{abc} | \mathbf{V} | \tilde{a}'\tilde{b}'\tilde{c}'; J'_{ab}J_{abc}; T'_{ab}T_{abc} \rangle_a \\
 &\times \begin{pmatrix} j_a & j_b & | & J_{ab} \\ m_a & m_b & | & M_{J_{ab}} \end{pmatrix} \begin{pmatrix} J_{ab} & j_c & | & J_{abc} \\ M_{J_{ab}} & m_{j_c} & | & M_{J_{abc}} \end{pmatrix} \begin{pmatrix} \frac{1}{2} & \frac{1}{2} & | & T_{ab} \\ m_{t_a} & m_{t_b} & | & M_{T_{ab}} \end{pmatrix} \begin{pmatrix} T_{ab} & \frac{1}{2} & | & T_{abc} \\ M_{T_{ab}} & m_{t_c} & | & M_{T_{abc}} \end{pmatrix} \\
 &\times \begin{pmatrix} j'_a & j'_b & | & J'_{ab} \\ m'_{j_a} & m'_{j_b} & | & M'_{J_{ab}} \end{pmatrix} \begin{pmatrix} J'_{ab} & j'_c & | & J_{abc} \\ M'_{J_{ab}} & m'_{j_c} & | & M_{J_{abc}} \end{pmatrix} \begin{pmatrix} \frac{1}{2} & \frac{1}{2} & | & T'_{ab} \\ m'_{t_a} & m'_{t_b} & | & M'_{T_{ab}} \end{pmatrix} \begin{pmatrix} T'_{ab} & \frac{1}{2} & | & T_{abc} \\ M'_{T_{ab}} & m'_{t_c} & | & M_{T_{abc}} \end{pmatrix}, \tag{84}
 \end{aligned}$$

and analogously the four-body matrix elements

$$\begin{aligned}
 {}_a\langle abcd | \mathbf{V} | a'b'c'd' \rangle_a &= \sum_{J_{ab}J'_{ab}} \sum_{J_{abc}J'_{abc}} \sum_{T_{ab}T'_{ab}} \sum_{T_{abc}T'_{abc}} \sum_{J_{abcd}T_{abcd}} \\
 &\times {}_a\langle \tilde{a}\tilde{b}\tilde{c}\tilde{d}; J_{ab}J_{abc}J_{abcd}; T_{ab}T_{abc}T_{abcd} | \mathbf{V} | \tilde{a}'\tilde{b}'\tilde{c}'\tilde{d}'; J'_{ab}J'_{abc}J_{abcd}; T'_{ab}T'_{abc}T_{abcd} \rangle_a \\
 &\times \begin{pmatrix} j_a & j_b & | & J_{ab} \\ m_a & m_b & | & M_{J_{ab}} \end{pmatrix} \begin{pmatrix} J_{ab} & j_c & | & J_{abc} \\ M_{J_{ab}} & m_{j_c} & | & M_{J_{abc}} \end{pmatrix} \begin{pmatrix} J_{abc} & j_d & | & J_{abcd} \\ M_{J_{abc}} & m_{j_d} & | & M_{J_{abcd}} \end{pmatrix} \\
 &\times \begin{pmatrix} \frac{1}{2} & \frac{1}{2} & | & T_{ab} \\ m_{t_a} & m_{t_b} & | & M_{T_{ab}} \end{pmatrix} \begin{pmatrix} T_{ab} & \frac{1}{2} & | & T_{abc} \\ M_{T_{ab}} & m_{t_c} & | & M_{T_{abc}} \end{pmatrix} \begin{pmatrix} T_{abc} & \frac{1}{2} & | & T_{abcd} \\ M_{T_{abc}} & m_{t_d} & | & M_{T_{abcd}} \end{pmatrix} \\
 &\times \begin{pmatrix} j'_a & j'_b & | & J'_{ab} \\ m'_{j_a} & m'_{j_b} & | & M'_{J_{ab}} \end{pmatrix} \begin{pmatrix} J'_{ab} & j'_c & | & J'_{abc} \\ M'_{J_{ab}} & m'_{j_c} & | & M'_{J_{abc}} \end{pmatrix} \begin{pmatrix} J'_{abc} & j'_d & | & J_{abcd} \\ M'_{J_{abc}} & m'_{j_d} & | & M_{J_{abcd}} \end{pmatrix} \\
 &\times \begin{pmatrix} \frac{1}{2} & \frac{1}{2} & | & T'_{ab} \\ m'_{t_a} & m'_{t_b} & | & M'_{T_{ab}} \end{pmatrix} \begin{pmatrix} T'_{ab} & \frac{1}{2} & | & T'_{abc} \\ M'_{T_{ab}} & m'_{t_c} & | & M'_{T_{abc}} \end{pmatrix} \begin{pmatrix} T'_{abc} & \frac{1}{2} & | & T_{abcd} \\ M'_{T_{abc}} & m'_{t_d} & | & M_{T_{abcd}} \end{pmatrix}. \tag{85}
 \end{aligned}$$

Note, the projection quantum numbers of the coupled quantities are determined by the single-particle projection quantum numbers, e.g., $m_{t_a} + m_{t_b} = M_{T_{ab}}$ and so forth. Although the decoupling formulas are rather simple, they have to be evaluated many times due to the huge number of required m -scheme matrix elements during the many-body calculation. Therefore, an efficient decoupling procedure based on a cache-optimized storage scheme is crucial.

The JT -coupled three- and four-body matrix elements are stored in an one-dimensional array, without quantum numbers. The position of the matrix elements is specified by a fixed loop order for all quantum numbers of the JT -coupled matrix elements. In the following we discuss the loop order in the three-body space [21] and stress that it is used in an analogous manner in the four-body space.

The order of the matrix elements is illustrated by the loops of the pseudo code in Fig. 3.4. The six outer loops are defined by the quantum numbers of the single-particle orbitals $\tilde{a}, \tilde{b}, \tilde{c}, \tilde{a}', \tilde{b}'$, and \tilde{c}' with $\tilde{a} = \{n_a, l_a, j_a\}$ and exploit parity conservation, Hermiticity, and the antisymmetry

outer loops:

```

for(  $\tilde{a} = 0; \tilde{a} \leq \tilde{a}_{\max}; \tilde{a} ++$ )
  for(  $\tilde{b} = 0; \tilde{b} \leq \tilde{b}_{\max}; \tilde{b} ++$ )
    for(  $\tilde{c} = 0; \tilde{c} \leq \tilde{c}_{\max}; \tilde{c} ++$ )
      for(  $\tilde{a}' = 0; \tilde{a}' \leq \tilde{a}'_{\max}; \tilde{a}' ++$ )
        for(  $\tilde{b}' = 0; \tilde{b}' \leq \tilde{b}'_{\max}; \tilde{b}' ++$ )
          for(  $\tilde{c}' = 0; \tilde{c}' \leq \tilde{c}'_{\max}; \tilde{c}' ++$ )

```

inner loops:

```

for(  $J_{ab} = |j_a - j_b|; J_{ab} \leq (j_a + j_b); J_{ab} ++$ )
  for(  $J_{ab} = |j_a - j_b|; J_{ab} \leq (j_a + j_b); J_{ab} ++$ )
    for(  $J'_{ab} = |j'_a - j'_b|; J'_{ab} \leq (j'_a + j'_b); J'_{ab} ++$ )
      for(  $J_{abc} = \text{MAX}[|J_{ab} - j_c|, |J'_{ab} - j'_c|]; J_{abc} \leq \text{MIN}[(J_{ab} + j_c), (J'_{ab} + j'_c)]; J_{abc} ++$ )
        for(  $T_{ab} = 0; T_{ab} \leq 1; T_{ab} ++$ )
          for(  $T'_{ab} = 0; T'_{ab} \leq 1; T'_{ab} ++$ )
            for(  $T_{abc} = \frac{1}{2}; T_{abc} \leq \text{MIN}[(T_{ab} + \frac{1}{2}), (T'_{ab} + \frac{1}{2})]; T_{abc} ++$ ),

```

Figure 3.4 *Storage order of 3N interaction matrix elements in the JT-coupled scheme:* The pseudo code illustrates the loop order to store and access the 3N interaction matrix elements in the JT-coupled scheme.

of the interaction matrix elements with respect to particle exchange. The six inner loops correspond to the coupled quantum numbers $J_{ab}, J'_{ab}, J_{abc}, T_{ab}, T'_{ab}$, and T_{abc} . These loops are constrained by the triangular conditions and do not exploit the antisymmetry constraints for the matrix elements with identical single-particle orbitals to keep a fixed inner segment. It is worth noting that the loop order specified by the pseudo code above is chosen such that the six inner loops correspond to the coupled quantum numbers we sum over in the decoupling procedure (84). Thus, the decoupling requires only a contiguous segment of the JT-coupled storage vector, whose position is defined by the orbital quantum numbers. Moreover, there are only five combinations for the inner-most sums over the isospin, such that these loops can be rolled-out manually. Due to the cache-optimized order and the simplicity of the evaluation the decoupling routine is an excellent candidate for porting it to accelerator cards (see Ref. [104] for a successful application).

The decoupling procedure in the four-body space uses a similar storage scheme with eight outer loops over the orbital quantum numbers $\tilde{a}, \tilde{b}, \tilde{c}, \tilde{d}, \tilde{a}', \tilde{b}', \tilde{c}'$, and \tilde{d}' and ten inner loops over the coupled quantum numbers $J_{ab}, J'_{ab}, J_{abc}, J'_{abc}, J_{abcd}, T_{ab}, T'_{ab}, T_{abc}, T'_{abc}$, and T_{abcd} . Besides, the increased complexity due to the extension by an additional particle, the formal aspects of the decoupling procedure in the three- and four-body space are rather the same. The optimized

storage scheme presented in this section is of great importance for an efficient application of 3N and 4N contributions, in particular, for those many-body methods that rely on a representation of the Hamiltonian in the m -scheme.

3.3 The Normal-Ordering Approach

For several many-body methods the explicit inclusion of 3N and 4N interactions lead to formal and computational efforts that are disproportionated. Thus, we introduce an approximative scheme to convert the relevant physical content to a lower particle rank. To this purpose we utilize the normal-ordering (NO) approach, which is a standard technique in quantum many-body physics. For the following discussion we restrict ourselves to the approximative inclusion of the 3N contributions, whose quality is investigated in Sec. 7.1. The NO transformation of the 4N contributions can be formulated in a straight-forward manner to apply 4N contributions to various many-body methods that can handle three- or even just two-body contributions. So far we include the 4N interactions explicitly and have also developed a rather simplistic approximation to construct an effective 3N interaction from the 4N force, which is briefly discussed in Sec. 3.4.

We concentrate on the single-reference NO approach throughout this work that is in general limited to closed-shell nuclei, but the NO approach can be also formulated with respect to multi-reference states as discussed in Ref. [146]. This formulation extends the application range to ground and excited states of open-shell systems.

Using creation and annihilation operators \mathbf{a}_ν^\dagger and \mathbf{a}_ν , for the single-particle states $|\nu\rangle$ defined with respect to the trivial zero-body vacuum state $|0\rangle$, one can express a 3N operator in second quantization

$$\mathbf{V}_{3N} = \frac{1}{36} \sum_{\substack{\nu_1 \nu_2 \nu_3 \\ \mu_1 \mu_2 \mu_3}} V_{\mu_1 \mu_2 \mu_3}^{\nu_1 \nu_2 \nu_3} \mathbf{A}_{\mu_1 \mu_2 \mu_3}^{\nu_1 \nu_2 \nu_3}, \quad (86)$$

with the antisymmetrized matrix elements $V_{\mu_1 \mu_2 \mu_3}^{\nu_1 \nu_2 \nu_3} = {}_a \langle \nu_1 \nu_2 \nu_3 | \mathbf{V}_{3N} | \mu_1 \mu_2 \mu_3 \rangle_a$ and the short hand $\mathbf{A}_{\mu_1 \mu_2 \mu_3}^{\nu_1 \nu_2 \nu_3} = \mathbf{a}_{\nu_1}^\dagger \mathbf{a}_{\nu_2}^\dagger \mathbf{a}_{\nu_3}^\dagger \mathbf{a}_{\mu_3} \mathbf{a}_{\mu_2} \mathbf{a}_{\mu_1}$ for products of creation and annihilation operators. Since all creation operators are to the left of the annihilation operators, the 3N operator on the right-hand side of Eq. (86) is expressed in the normal-ordered form with respect to the trivial vacuum (vacuum NO). Instead of the trivial vacuum state $|0\rangle$ one can also use a single Slater determinant $|\Phi_{\text{ref}}\rangle = \prod_\alpha \mathbf{a}_\alpha^\dagger |0\rangle$ made up of A single-particle states to define the creation and annihilation operators as particle or hole operators that are rearranged in the normal-ordered form (reference NO).

In the following, we use the index α to label occupied single-particle states in the reference state $|\Phi_{\text{ref}}\rangle$, also called hole states and β for the unoccupied ones referred as particle states.

Further we can define $\mathbf{a}_\alpha^\dagger, \mathbf{a}_\beta$ as quasi-particle annihilators, since they act on the reference state like annihilators on the vacuum state, i.e.,

$$\mathbf{a}_\alpha^\dagger |\Phi_{\text{ref}}\rangle = 0 \quad (87)$$

$$\mathbf{a}_\beta |\Phi_{\text{ref}}\rangle = 0. \quad (88)$$

The quasi-particle annihilators $\mathbf{a}_\alpha^\dagger, \mathbf{a}_\beta$ annihilate a hole state or a particle state, respectively. Accordingly, we define $\mathbf{a}_\beta^\dagger, \mathbf{a}_\alpha$ as quasi-particle creators that create a particle or a hole state, respectively. The 3N interaction can be expressed in normal-ordered form with respect to the reference state $|\Phi_{\text{ref}}\rangle$ by rearranging the quasi-particle creators to the left of the quasi-particle annihilators in all products of operators. Using Wick's theorem we obtain [145]

$$\mathbf{V}_{3N} = W + \sum_{\substack{\nu_1 \\ \mu_1}} W_{\mu_1}^{\nu_1} \tilde{\mathbf{A}}_{\mu_1}^{\nu_1} + \frac{1}{4} \sum_{\substack{\nu_1 \nu_2 \\ \mu_1 \mu_2}} W_{\mu_1 \mu_2}^{\nu_1 \nu_2} \tilde{\mathbf{A}}_{\mu_1 \mu_2}^{\nu_1 \nu_2} + \frac{1}{36} \sum_{\substack{\nu_1 \nu_2 \nu_3 \\ \mu_1 \mu_2 \mu_3}} W_{\mu_1 \mu_2 \mu_3}^{\nu_1 \nu_2 \nu_3} \tilde{\mathbf{A}}_{\mu_1 \mu_2 \mu_3}^{\nu_1 \nu_2 \nu_3}, \quad (89)$$

where $\tilde{\mathbf{A}}_{\mu_1 \mu_2 \dots}^{\nu_1 \nu_2 \dots}$ is a short hand for the normal-ordered product with respect to the reference state. Further, we use $W = \frac{1}{6} \sum_{\alpha_1 \alpha_2 \alpha_3} V_{\alpha_1 \alpha_2 \alpha_3}^{\alpha_1 \alpha_2 \alpha_3}$ as the matrix elements for the zero-body term, $W_{\mu_1}^{\nu_1} = \frac{1}{2} \sum_{\alpha_2 \alpha_3} V_{\mu_1 \alpha_2 \alpha_3}^{\nu_1 \alpha_2 \alpha_3}$ for the one-body term, $W_{\mu_1 \mu_2}^{\nu_1 \nu_2} = \sum_{\alpha_3} V_{\mu_1 \mu_2 \alpha_3}^{\nu_1 \nu_2 \alpha_3}$ for the two-body term, and $W_{\mu_1 \mu_2 \mu_3}^{\nu_1 \nu_2 \nu_3} = V_{\mu_1 \mu_2 \mu_3}^{\nu_1 \nu_2 \nu_3}$ for the three-body term. Note, that the indices α_i label the occupied single-particle states in the reference state $|\Phi_{\text{ref}}\rangle$. Apparently, the 3N interaction in the vacuum representation consists of zero-, one-, two-, and three-body operators in the NO representation. Note, the NO transformation is an identity and the right-hand-sides in Eqs. (86) and (89) are equivalent. As an important property, the NO of an m -body operator with respect to a certain reference state generally yields an expression with non-vanishing operators up to the m -body level, but not beyond. The transformation back to the vacuum representation leads to a cancellation of the lower particle-rank operators and we end up with the initial m -body operator in the vacuum representation.

Neglecting the operators beyond the n -body level in the NO expression (with $n < m$) and rearranging the operators to vacuum NO representation only yields non-vanishing operator contributions up to the n -body level. This truncation we call the normal-ordered n -body (NO n B) approximation. Of particular interest in the following is the NO2B approximation of the 3N interaction, where we neglect the normal-ordered three-body operators on the right-hand-side of (89)

$$\mathbf{V}_{3N} \approx \mathbf{V}_{3N}^{(\text{NO2B})} = W + \sum_{\substack{\nu_1 \\ \mu_1}} W_{\mu_1}^{\nu_1} \tilde{\mathbf{A}}_{\mu_1}^{\nu_1} + \frac{1}{4} \sum_{\substack{\nu_1 \nu_2 \\ \mu_1 \mu_2}} W_{\mu_1 \mu_2}^{\nu_1 \nu_2} \tilde{\mathbf{A}}_{\mu_1 \mu_2}^{\nu_1 \nu_2}. \quad (90)$$

Rearranging this expression to the vacuum NO representation yields [147]

$$\mathbf{V}_{3N}^{(\text{NO2B})} = W - \sum_{\substack{\nu_1 \\ \mu_1}} W_{\mu_1}^{\nu_1} \mathbf{A}_{\mu_1}^{\nu_1} + \frac{1}{4} \sum_{\substack{\nu_1 \nu_2 \\ \mu_1 \mu_2}} W_{\mu_1 \mu_2}^{\nu_1 \nu_2} \mathbf{A}_{\mu_1 \mu_2}^{\nu_1 \nu_2}, \quad (91)$$

where $W_{\mu_1 \dots}^{\nu_1 \dots}$ are defined as in the NO representation and the creation and annihilation operators are vacuum normal-ordered. The NO2B approximation is based on the fact that we shift information from the 3N interaction to lower particle ranks, using information about the targeted system. Thus, we can apply the relevant 3N effects in many-body methods that treat the interactions only up to the two-body level. The information about the system is included using a reference state that approximates the targeted state. For the ground state of a closed-shell nucleus one can use, e.g., the unperturbed HO Slater determinant or the ground state of a Hartree-Fock calculation. The latter provides typically a better approximation suggesting a more accurate NO procedure. The NO approximation is benchmarked in Sec. 7.1.

As an important application of the NO approximation we utilize it to include 3N contributions up to larger maximum energy quantum numbers $E_{3,\text{max}}$. In the NO2B approximation for instance, the $W_{\mu_1 \dots}^{\nu_1 \dots}$ symbols incorporate at least one sum over the single-particle states occupied in the reference state, which reduces the number of required 3N matrix elements significantly. By performing the transformation from the m -scheme to the JT -coupled scheme, as discussed in Sec. 3.2.1, in combination with the NO approach, we can avoid saving the 3N matrix elements to disk and reduces the number of required 3N matrix elements that have to be calculated. This combination allows to include the information about 3N matrix element up to $E_{3,\text{max}} \approx 20$. For this approach it is necessary to determine the targeted state and to calculate the corresponding reference state a priori to perform the NO2B approximation. In practice we perform the normal-ordered JT -coupling for a sequence of closed-shell nuclei, where we obtain the reference states from Hartree-Fock calculations. Due to this we have to calculate each JT -coupled matrix element only once and add its contribution to the normal-ordered interaction for the different reference states. It is worth noticing, that the Hartree-Fock calculation is performed with the explicit 3N interactions, generally limited to a lower $E_{3,\text{max}}$, e.g., of 14. Thus, the reference state does not contain information of 3N contributions with higher energy quantum numbers, which contribute during the normal-ordered JT -coupling. To overcome this inconsistency one can embed the NO into an iterative scheme using the resulting normal-ordered interaction, which contains the high-energy 3N interaction information, to obtain an improved reference state in a subsequent Hartree-Fock calculation. The procedure can be iterated until convergence is reached. For a detailed description and benchmark of the iterative normal-ordered JT -coupling, see Refs. [99, 116].

3.4 Simplistic Particle-Rank Reduction

Inspired by the concept of the NO approximation discussed in the previous section, one can develop a simplistic approximation to include the 4N interaction by a summation over the quantum numbers of the fourth particle yielding an effective 3N interaction. For this approach one transforms the four-body Jacobi basis to a hybrid basis that is a product state of the antisymmetric three-body Jacobi basis (including the center-of-mass part) and a single-particle HO state describing the fourth particle, which can be achieved by using the Talmi-Moshinsky transformation. Eventually, we sum over the quantum numbers of the fourth particle. The summation is constrained to the single-particle states that occupy the unperturbed Slater determinant, which provides the reference state for the target nucleus. Moreover, we introduce some rather rough approximations, e.g., concerning the center-of-mass part, to transform the 4N interaction from the four-body Jacobi-HO representation to an effective 3N interaction in the three-body Jacobi-HO representation that can be treated with the three-body techniques developed in this work.

For the derivation and details of this summation see Ref. [144]. Although, this procedure contains rough approximations whose effects need to be studied, it can be used to obtain a quick estimate of the general trend of the 4N interaction effects.

However, the transformation of the 4N interaction matrix elements to the JT -coupled scheme is well under control for the applications of this work (see Sec. 6.4). Thus, we stick to the explicit inclusion of the 4N contributions as presented in Sec. 3.2.2 and refer to Ref. [144] for an application of this approximative inclusion. The concept of this approach might be relevant nevertheless, since it enables us to access very large model spaces that are far beyond the reach of the exact transformation to the single-particle scheme. The formulas for the simplistic particle-rank reduction have been derived and implemented in the three- and four-body space and can be revisited if certain approaches or observables show evidence for the need of high-energy interaction contributions.

3.5 Partial-Wave Decomposed Jacobi-Momentum Basis

After focusing on the HO basis sets in three- and four-body space, we discuss a momentum basis in three-body space. The partial-wave decomposed Jacobi-momentum basis is of particular interest since it is used to calculate the chiral 3N interactions produced by the LENPIC collaboration [76]. The present non-local 3N force at $N^2\text{LO}$ (see Sec. 1.3.2) and the next-generation 3N force at $N^3\text{LO}$ (see Sec. 1.4), which we refer as the Epelbaum 3N interactions, are represented in the following basis

$$|\Pi_1\Pi_2; \alpha_{12}\rangle_{a_1} = |\Pi_1\Pi_2; [(L_1 S_1)J_1, (L_2 \frac{1}{2})J_2]J_{12}; (T_1 \frac{1}{2})T_{12}\rangle_{a_1}, \quad (92)$$

where we omit the center-of-mass part and the projection quantum numbers for brevity and introduced a short hand with the collective index $\alpha_{12} = \{L_1, S_1, J_1, L_2, J_2, J_{12}, T_1, T_{12}\}$. The coupling order is the same as for the Jacobi-HO basis (56) and exhibits the same partial antisymmetry under exchange of the first two particles. Thus, the angular part can be treated as in the HO case. The difference is the radial part that is parametrized by the absolute values of the Jacobi momenta. Note, that the Jacobi-momentum states in Eq. (92) are defined with respect to the Jacobi momenta used, e.g., in Ref. [148]

$$\begin{aligned}\vec{\Pi}_1 &= \frac{1}{2}[\vec{p}_a - \vec{p}_b], \\ \vec{\Pi}_2 &= \frac{2}{3}[\vec{p}_c - \frac{1}{2}(\vec{p}_a + \vec{p}_b)],\end{aligned}\tag{93}$$

which differ from the previous Jacobi momenta of Eq. (92) by a factor and are related by

$$\begin{aligned}\vec{\pi}_1 &= \sqrt{2}\vec{\Pi}_1, \\ \vec{\pi}_2 &= -\sqrt{\frac{3}{2}}\vec{\Pi}_2.\end{aligned}\tag{94}$$

We come back to this difference in Sec. 3.5.1. The 3N interaction matrix elements in the Jacobi momentum representation read

$${}_{a_1}\langle \Pi_1 \Pi_2; \alpha_{12} | \mathbf{V} | \Pi'_1 \Pi'_2; \tilde{\alpha}'_{12} \rangle_{a_1},\tag{95}$$

with $\tilde{\alpha}'_{12} = \{L'_1, S'_1, J'_1, L'_2, J'_2, J'_{12}, T'_1, T'_{12}\}$. The matrix elements are only partially antisymmetric and need to be antisymmetrized explicitly. As explained before this continuous basis does not allow to use the antisymmetrization procedure discussed for the Jacobi-HO basis (see Sec. 3.1.2), such that the model-space dimension for the completely antisymmetric representation is not reduced. Due to the large model-space dimension one has to omit partial waves with large angular momenta, which is physically motivated when aiming at low-energy properties. However, the antisymmetrization of the partial-wave decomposed momentum basis couples the interaction matrix elements to the omitted partial waves, which causes truncation errors [149].⁸

The 3N interaction matrix is discretized on a four-dimensional momentum grid typically using 8 – 14 grid points for each dimension. An advantage of the Jacobi-momentum representation is the possibility to recover physical information that is lost by the discretization via an interpolation on the four-dimensional grid. However, one needs to investigate the reliability of the interpolation, in particular for large angular momenta where the matrix elements show rather strong oscillations as function of the momenta. We typically use Akima splines [150] with periodic boundary conditions for the interpolation and verify the numerical accuracy by a

⁸In the following we perform the transformation of these Jacobi-momentum matrix elements into the Jacobi-HO basis representation. Thus, the truncation errors of the antisymmetrization can be avoided by performing it in the HO basis.

variation of the initial and interpolated grid point numbers. The momentum representation is an appropriate choice for nuclear- or neutron-matter calculations [71, 151], but when aiming at the structure of nuclei one requires basis sets that appropriately describe finite systems, such as the HO basis.

To apply the non-local Epelbaum 3N interactions to nuclear structure calculations we perform the transformation of the partial-wave decomposed momentum interaction matrix elements to the Jacobi-HO representation. In the following sections we derive the transformation formula and emphasize the different conventions used for the two basis sets as well as the consequences, which need to be considered for a subsequent application of the HO machinery.

3.5.1 Transformation to the Jacobi-HO Basis

In the following we discuss the transformation of the 3N interaction matrix elements from the partial-wave decomposed Jacobi-momentum representation (92) to the antisymmetric Jacobi-HO representation (59). We concentrate on the derivation of the transformation formula, assuming the interaction represented in the Jacobi-momentum basis using the same coordinates and conventions as in the HO case

$${}_{a_1}\langle \pi_1 \pi_2; \alpha_{12} | \mathbf{V} | \pi'_1 \pi'_2; \tilde{\alpha}_{12} \rangle_{a_1}, \quad (96)$$

where the Jacobi momenta correspond to those introduced in Sec. 3.1 and with the collective indices $\alpha_{12} = \{L_1, S_1, J_1, L_2, J_2, J_{12}, T_1, T_{12}\}$ and $\tilde{\alpha}_{12} = \{L'_1, S'_1, J'_1, L'_2, J'_2, J_{12}, T'_1, T_{12}\}$.

We start with the HO state and expand it in the momentum basis. Because the transformation exclusively concerns the spatial part we first separate it from the spin part by decoupling the angular momenta and omit isopin part (which is already separated) for brevity

$$\begin{aligned} |N_1 N_2; \alpha_{12}\rangle_{a_1} &= |N_1 N_2; [(L_1 S_1) J_1, (L_2 \frac{1}{2}) J_2] J_{12} M_{J_{12}}\rangle_{a_1} \\ &= \sum_{M_{J_1} M_{J_2}} \sum_{M_{L_1} M_{L_2}} \sum_{M_{S_1} M_{S_2}} \\ &\quad \times \begin{pmatrix} J_1 & J_2 & | & J_{12} \\ M_{J_1} & M_{J_2} & | & M_{J_{12}} \end{pmatrix} \begin{pmatrix} L_1 & S_1 & | & J_1 \\ M_{L_1} & M_{S_1} & | & M_{J_1} \end{pmatrix} \begin{pmatrix} L_2 & \frac{1}{2} & | & J_2 \\ M_{L_2} & M_{S_2} & | & M_{J_2} \end{pmatrix} \\ &\quad \times \{ |N_1 L_1 M_{L_1}\rangle \otimes |N_2 L_2 M_{L_2}\rangle \otimes |S_1 M_{S_1}\rangle \otimes |\frac{1}{2} M_{S_2}\rangle \}_{a_1}. \end{aligned} \quad (97)$$

The Jacobi-HO state on the right-hand side is a product state of the spatial and spin components, which are defined with respect to the Jacobi coordinates. The product state allows us to focus on a general HO state, which we transform to the momentum basis. Note, that the partial antisymmetry is only defined for the complete Jacobi-HO state including the spin and isopin part. However, the partial antisymmetry is realized by allowing only certain combinations of quantum numbers that fulfill $(-1)^{L_1+S_1+T_1} = 1$. This means the partial antisymmetry

is ensured by the choice of the states $|N_1 N_2; \alpha_{12}\rangle_{a_1}$ and does not require further consideration. Expressing the HO states by the momentum states, yields

$$\begin{aligned} |NLM_L\rangle &= \int d^3\pi |\vec{\pi}\rangle\langle\vec{\pi}|NLM_L\rangle \\ &= \int d\pi \pi^2 \int d\Omega \langle\vec{\pi}|NLM_L\rangle |\vec{\pi}\rangle, \end{aligned} \quad (98)$$

where the angles are parametrized by Ω . The overlap in Eq. (98) corresponds to the HO wave function in momentum space

$$\langle\vec{\pi}|NLM_L\rangle = \Psi_{NLM_L}(\vec{\pi}) = R_{NL}(\pi)Y_{LM_L}(\Omega), \quad (99)$$

where $Y_{LM_L}(\Omega)$ are the spherical harmonics and $R_{NL}(\pi)$ describes the radial part defined as

$$R_{NL}(\pi) = (-1)^N \sqrt{\frac{2(N!) \left(\frac{a}{\hbar}\right)^3}{\Gamma(N+L+\frac{3}{2})}} \left(\pi\frac{a}{\hbar}\right)^L e^{-\frac{1}{2}\left(\pi\frac{a}{\hbar}\right)^2} \mathcal{L}_N^{L+1/2}\left(\left(\pi\frac{a}{\hbar}\right)^2\right), \quad (100)$$

with the HO length a and the generalized or associated Laguerre polynomials $\mathcal{L}_N^{L+1/2}\left(\left(\pi\frac{a}{\hbar}\right)^2\right)$. The phase $(-1)^N$ results from the convention we use for the basis definition. The relation to the partial-wave decomposed momentum basis is given by

$$\begin{aligned} |\vec{\pi}\rangle &= \sum_{LM_L} \int d\pi' (\pi')^2 |\pi'LM_L\rangle\langle\pi'LM_L|\vec{\pi}\rangle \quad \text{with} \quad \langle\pi'LM_L|\vec{\pi}\rangle = \frac{\delta(\pi' - \pi)}{\pi'\pi} Y_{LM_L}^*(\Omega) \\ &= \sum_{LM_L} Y_{LM_L}^*(\Omega) |\pi LM_L\rangle, \end{aligned} \quad (101)$$

with the complex conjugate of the spherical harmonics. From the above relations the HO state can be expressed as

$$\begin{aligned} |NLM_L\rangle &= \sum_{L'M'_L} \int d\pi \pi^2 R_{NL}(\pi) |\pi LM_L\rangle \int d\Omega Y_{LM_L}(\Omega) Y_{L'M'_L}^*(\Omega) \\ &= \int d\pi \pi^2 R_{NL}(\pi) |\pi LM_L\rangle, \end{aligned} \quad (102)$$

where we use the orthonormality relation of the spherical harmonics.

We come back to the three-body Jacobi basis in Eq. (97) and utilize the general transformation

formula (102) combined with a coupling of the angular momenta, yielding

$$\begin{aligned}
 |N_1 N_2; \alpha_{12}\rangle_{a_1} = & \sum_{M_{J_1} M_{J_2}} \sum_{M_{L_1} M_{L_2}} \sum_{M_{S_1} M_{S_2}} \sum_{L'_1 L'_2} \sum_{J'_1 J'_2} \sum_{J'_{12}} \sum_{M'_{L_1} M'_{L_2}} \sum_{M'_{J_1} M'_{J_2} M'_{J_{12}}} \\
 & \times \begin{pmatrix} J_1 & J_2 & | & J_{12} \\ M_{J_1} & M_{J_2} & | & M_{J_{12}} \end{pmatrix} \begin{pmatrix} L_1 & S_1 & | & J_1 \\ M_{L_1} & M_{S_1} & | & M_{J_1} \end{pmatrix} \begin{pmatrix} L_2 & \frac{1}{2} & | & J_2 \\ M_{L_2} & M_{S_2} & | & M_{J_2} \end{pmatrix} \\
 & \times \begin{pmatrix} J'_1 & J'_2 & | & J'_{12} \\ M'_{J_1} & M'_{J_2} & | & M'_{J_{12}} \end{pmatrix} \begin{pmatrix} L'_1 & S'_1 & | & J'_1 \\ M'_{L_1} & M'_{S_1} & | & M'_{J_1} \end{pmatrix} \begin{pmatrix} L'_2 & \frac{1}{2} & | & J'_2 \\ M'_{L_2} & M'_{S_2} & | & M'_{J_2} \end{pmatrix} \quad (103) \\
 & \times \int d\pi_1 \pi_1^2 \int d\pi_2 \pi_2^2 R_{N_1 L_1}(\pi_1) R_{N_2 L_2}(\pi_2) \\
 & \times \int d\Omega_1 \int d\Omega_2 Y_{L_1 M_{L_1}}(\Omega_1) Y_{L'_1 M'_{L_1}}^*(\Omega_1) Y_{L_2 M_{L_2}}(\Omega_2) Y_{L'_2 M'_{L_2}}^*(\Omega_2) \\
 & \times |\pi_1 \pi_2; [(L'_1 S_1) J'_1, (L'_2 \frac{1}{2}) J'_2] J'_{12} M'_{J_{12}}\rangle_{a_1}.
 \end{aligned}$$

Exploiting the orthonormality relation of the Clebsch-Gordan coefficients and the spherical harmonics in the appropriate order, leads to

$$\begin{aligned}
 |N_1 N_2; \alpha_{12}\rangle_{a_1} = & \int d\pi_1 \pi_1^2 \int d\pi_2 \pi_2^2 R_{N_1 L_1}(\pi_1) R_{N_2 L_2}(\pi_2) \\
 & \times |\pi_1 \pi_2; [(L_1 S_1) J_1, (L_2 \frac{1}{2}) J_2] J_{12} M_{J_{12}}\rangle_{a_1}, \quad (104)
 \end{aligned}$$

such that we arrive at the final formula for the transformation of the 3N interaction matrix elements to the partial antisymmetrized Jacobi-HO basis

$$\begin{aligned}
 & {}_{a_1} \langle N_1 N_2; \alpha_{12} | \mathbf{V} | N'_1 N'_2; \tilde{\alpha}'_{12} \rangle_{a_1} \\
 & = \int d\pi_1 \pi_1^2 \int d\pi_2 \pi_2^2 R_{N_1 L_1}(\pi_1) R_{N_2 L_2}(\pi_2) \\
 & \times \int d\pi'_1 (\pi'_1)^2 \int d\pi'_2 (\pi'_2)^2 R_{N'_1 L'_1}^*(\pi'_1) R_{N'_2 L'_2}^*(\pi'_2) \\
 & \times {}_{a_1} \langle \pi_1 \pi_2; \alpha_{12} | \mathbf{V} | \pi'_1 \pi'_2; \tilde{\alpha}'_{12} \rangle_{a_1}. \quad (105)
 \end{aligned}$$

This transformation can be evaluated by interpolating the interaction matrix elements on the discrete four-dimensional momentum grid and calculating the radial wave functions explicitly to perform the integrals.

The momentum input matrix elements are unregularized and we regularize them by a multiplication with the regulator function

$$\begin{aligned}
 & {}_{a_1} \langle \pi_1 \pi_2; \alpha_{12} | \mathbf{V} | \pi'_1 \pi'_2; \tilde{\alpha}'_{12} \rangle_{a_1} \rightarrow \\
 & f(\pi_1, \pi_2, \Lambda_{3N}) {}_{a_1} \langle \pi_1 \pi_2; \alpha_{12} | \mathbf{V} | \pi'_1 \pi'_2; \tilde{\alpha}'_{12} \rangle_{a_1} f(\pi'_1, \pi'_2, \Lambda_{3N}), \quad (106)
 \end{aligned}$$

with

$$f(\pi_1, \pi_2, \Lambda_{3N}) = e^{-\left(\frac{\pi_1^2 + \pi_2^2}{(\sqrt{2}\Lambda_{3N})^2}\right)^{2n}} = e^{-\left(\frac{4\Pi_1^2 + 3\Pi_2^2}{(2\Lambda_{3N})^2}\right)^{2n}} = \tilde{f}(\Pi_1, \Pi_2, \Lambda_{3N}), \quad (107)$$

where we also quote the regulator function for the other choice of the Jacobi momenta of Eq. (93). For the 3N interactions at N²LO and N³LO used in this work we set $n = 3$.

Finally, the interaction matrix elements are antisymmetrized in the HO basis via the procedure discussed in Sec. 3.1.2

$$\begin{aligned} & {}_a \langle E_{12} i_{12} J_{12} T_{12} | \mathbf{V} | E'_{12} i'_{12} J_{12} T_{12} \rangle_a \\ &= \sum_{N_1 N_2 \alpha_{12}} \sum_{N'_1 N'_2} \sum_{L'_1 S'_1 J'_1 T'_1} \sum_{L'_2 J'_2} \delta_{E_{12}, (2N_1 + L_1 + 2N_2 + L_2)} \delta_{E'_{12}, (2N'_1 + L'_1 + 2N'_2 + L'_2)} \\ & \times C_{N_1 N_2 \alpha_{12}}^{i_{12}} C_{N'_1 N'_2 \tilde{\alpha}'_{12}}^{i'_{12}} {}_{a_1} \langle N_1 N_2; \alpha_{12} | \mathbf{V} | N'_1 N'_2; \tilde{\alpha}'_{12} \rangle_{a_1}. \end{aligned} \quad (108)$$

Due to the large number of matrix elements in the HO and momentum representation a careful pre-calculation of several quantities and an optimized ordering of the summations and integrations is required to perform an efficient transformation.

3.5.2 Basis Conventions for Practical Applications

An important issue that has to be addressed meticulously are the different conventions for the HO and momentum basis sets. As described in Sec. 1.3.2 and 1.4 the momentum interaction matrix elements are produced in a large collaboration named LENPIC and there are different formats used, depending on the production procedure. Therefore, the matrix elements either represent the pure 3N interaction operator \mathbf{V}_{3N} or the operators $\mathbf{V}_{3N}(\mathbb{1} + \mathbf{P})$ or $(\mathbb{1} + \mathbf{P})\mathbf{V}_{3N}(\mathbb{1} + \mathbf{P})$, with the permutation operator $\mathbf{P} = \mathcal{T}_{ac} \mathcal{T}_{ab} + \mathcal{T}_{bc} \mathcal{T}_{ab}$, which is equivalent to $(-2\mathcal{T}_{bc})$ when acting on the partial-antisymmetrized states and $\frac{1}{3}(\mathbb{1} + \mathbf{P})$ is equivalent to the antisymmetrizer \mathcal{A} . Because we perform the antisymmetrization in the HO basis the only difference between the potential inputs $\{\mathbf{V}_{3N}, \mathbf{V}_{3N}(\mathbb{1} + \mathbf{P}), (\mathbb{1} + \mathbf{P})\mathbf{V}_{3N}(\mathbb{1} + \mathbf{P})\}$ is a factor $\{1, \frac{1}{3}, \frac{1}{9}\}$, respectively, in the transformation formula of the previous section.

A further factor results from the fact that the provided momentum matrix elements are expressed in units of $[\text{fm}^5]$, while we require them in units of $[\text{MeV fm}^6]$ to obtain the HO matrix elements in units $[\text{MeV}]$. Thus, we have to multiply the momentum matrix elements with an additional factor $\hbar c$.

It is worth noticing that the overlap of the orthonormalized momentum and HO basis is determined only up to an arbitrary complex phase. The convention we use in this work is defined by Eqs. (98) and (100). It turns out that the convention used for the production of the momentum matrix elements differs by a complex orbital angular-momentum dependent phase, such that the matrix elements in Eq. (105) need to be multiplied by a phase $i^{L_1 + L'_1 - L_2 - L'_2}$, which in total

is real due to the equal parity of the bra and ket states.

Finally, we consider a rather tedious factor that results from the different definitions of the Jacobi momenta. To derive this factor we assume two momentum basis sets $|\vec{\pi}\rangle$ and $|\vec{\Pi}\rangle$, where the momenta $\vec{\pi} = g\vec{\Pi}$ are related by a real factor g . The two basis sets fulfill the completeness relations

$$\int d^3\pi |\vec{\pi}\rangle\langle\vec{\pi}| = \mathbb{1} = \int d^3\Pi |\vec{\Pi}\rangle\langle\vec{\Pi}|, \quad (109)$$

and we obtain

$$\begin{aligned} |\vec{\pi}\rangle &= \int d^3\Pi |\vec{\Pi}\rangle\langle\vec{\Pi}|\vec{\pi}\rangle, \\ |\vec{\Pi}\rangle &= \int d^3\pi |\vec{\pi}\rangle\langle\vec{\pi}|\vec{\Pi}\rangle, \end{aligned} \quad (110)$$

with $\langle\vec{\Pi}|\vec{\pi}\rangle = \delta^3(\vec{\Pi} - \frac{\vec{\pi}}{g})$ and $\langle\vec{\pi}|\vec{\Pi}\rangle = \delta^3(\vec{\pi} - g\vec{\Pi}) = |g|^3\delta^3(\vec{\Pi} - \frac{\vec{\pi}}{g})$. Our aim is to find the relation between the partial-wave decomposed state with respect to the Jacobi momentum $\vec{\pi}$ and $\vec{\Pi}$, i.e., $|\pi LM_L\rangle$ and $|\Pi LM_L\rangle$, respectively

$$\begin{aligned} |\pi LM_L\rangle &= \int d^3\pi' |\vec{\pi}'\rangle\langle\vec{\pi}'|\pi LM_L\rangle = \int d\Omega_\pi |\vec{\pi}\rangle Y_{LM_L}(\Omega_\pi) \\ &= \int d^3\Pi' \int d\Omega_\pi \langle\vec{\Pi}'|\vec{\pi}\rangle Y_{LM_L}(\Omega_\pi) |\vec{\Pi}'\rangle \\ &= \int d^3\Pi' \int d\Omega_\pi \delta^3\left(\vec{\Pi}' - \frac{\vec{\pi}}{g}\right) Y_{LM_L}(\Omega_\pi) |\vec{\Pi}'\rangle \\ &= \sum_{L'M'_L} \int d\Pi'' \Pi''^2 \int d^3\Pi' \int d\Omega_\pi \delta^3\left(\vec{\Pi}' - \frac{\vec{\pi}}{g}\right) \\ &\quad \times Y_{LM_L}(\Omega_\pi) \langle\Pi'' L'M'_L|\vec{\Pi}'\rangle |\Pi'' L'M'_L\rangle \\ &= \sum_{L'M'_L} \int d^3\Pi' \int d\Omega_\pi \delta^3\left(\vec{\Pi}' - \frac{\vec{\pi}}{g}\right) Y_{LM_L}(\Omega_\pi) Y_{L'M'_L}^*(\Omega'_{\Pi}) |\Pi' L'M'_L\rangle, \end{aligned} \quad (111)$$

where we use $\langle\vec{\Pi}|\vec{\pi}\rangle = \delta^3(\vec{\Pi} - \frac{\vec{\pi}}{g})$ and the overlaps between the momentum state $|\vec{\Pi}\rangle$ and the partial-wave decomposed momentum state $|\Pi LM_L\rangle$ introduced in Sec. 3.5.1. Evaluating the integral over the three-dimensional Dirac-delta function $\int d^3\Pi' \delta^3(\vec{\Pi}' - \frac{\vec{\pi}}{g})$ causes the momentum vector conversion $\vec{\Pi}' \rightarrow \frac{\vec{\pi}}{g} \equiv \vec{\Pi}$. If $\vec{\Pi}$ and $\vec{\pi}$ are antiparallel, i.e., $\frac{g}{|g|} = -1$, the spherical harmonics produces a phase $(-1)^{L'}$, while the phase is $(+1)$ for parallel momentum vectors.

Therefore, we obtain the phase $\left(\frac{g}{|g|}\right)^{L'}$ from the spherical harmonics, yielding

$$\begin{aligned}
 |\pi LM_L\rangle &= \sum_{L'M'_L} \left(\frac{g}{|g|}\right)^{L'} |\Pi L' M'_L\rangle \int d\Omega_\pi Y_{LM_L}(\Omega_\pi) Y_{L'M'_L}^*(\Omega_\pi) \\
 &= \sum_{L'M'_L} \left(\frac{g}{|g|}\right)^{L'} |\Pi L' M'_L\rangle \delta_{L',L} \delta_{M'_L,M_L} \\
 &= \left(\frac{g}{|g|}\right)^L |\Pi LM_L\rangle.
 \end{aligned} \tag{112}$$

The analogous calculation can be performed for the bra state, which is identical with the exception that the overlap $\langle\tilde{\pi}|\tilde{\Pi}\rangle = |g|^3 \delta^3(\tilde{\Pi} - \frac{\tilde{\pi}}{g})$ leads to an additional factor $|g|^3$

$$\langle\pi LM_L| = |g|^3 \left(\frac{g}{|g|}\right)^L \langle\Pi LM_L|. \tag{113}$$

In summary, owing to the two definitions of the Jacobi momenta related by Eq. (94) we gain additional factors when transforming from one momentum-basis set to the other. Because of the different absolute values of the Jacobi momenta we need to multiply the momentum-interaction matrix elements in (105) by a factor $|\sqrt{2}(-\sqrt{\frac{3}{2}})|^3 = 3\sqrt{3}$. The sign change for the second Jacobi momentum leads to an additional phase $(-1)^{L'_1+L_1}$. Although this section discusses rather technical details, it is indispensable for the application of an interaction to be aware of the different conventions, in particular because they are only partially documented in general. The formulas and conventions described in this thesis provide the required knowledge to apply the non-local Epelbaum 3N forces with the HO machinery to nuclear structure calculations. The final formula to regularize, antisymmetrize, and transform the Epelbaum 3N matrix elements in the partial-wave decomposed momentum representation to the Jacobi-HO representation reads

$$\begin{aligned}
 &{}_a \langle E_{12} i_{12} J_{12} T_{12} | \mathbf{V} | E'_{12} i'_{12} J'_{12} T'_{12} \rangle_a \\
 &= 3\sqrt{3} \hbar c \sum_{N_1 N_2 \alpha_{12}} \sum_{N'_1 N'_2} \sum_{L'_1 S'_1 J'_1 T'_1} \sum_{L'_2 J'_2} i^{L_1+L'_1-L_2-L'_2} (-1)^{L'_1+L_1} \\
 &\quad \times \delta_{E_{12},(2N_1+L_1+2N_2+L_2)} \delta_{E'_{12},(2N'_1+L'_1+2N'_2+L'_2)} C_{N_1 N_2 \alpha_{12}}^{i_{12}} C_{N'_1 N'_2 \alpha'_{12}}^{i'_{12}} \\
 &\quad \times \int d\Pi_1 \Pi_1^2 \int d\Pi_2 \Pi_2^2 R_{N_1 L_1}(\Pi_1) R_{N_2 L_2}(\Pi_2) \\
 &\quad \times \int d\Pi'_1 (\Pi'_1)^2 \int d\Pi'_2 (\Pi'_2)^2 R_{N'_1 L'_1}^*(\Pi'_1) R_{N'_2 L'_2}^*(\Pi'_2) \\
 &\quad \times \tilde{f}(\Pi_1, \Pi_2, \Lambda_{3N}) \tilde{f}(\Pi'_1, \Pi'_2, \Lambda_{3N}) \\
 &\quad \times {}_{a_1} \langle \Pi_1 \Pi_2; \alpha_{12} | \mathbf{V} | \Pi'_1 \Pi'_2; \alpha'_{12} \rangle_{a_1}.
 \end{aligned} \tag{114}$$

4 Similarity Renormalization Group

Compared to phenomenological high-precision interactions, such as the Argonne V18 [2] and the CD-Bonn [3] potential, the chiral interactions (see Sec. 1) are already quite soft owing to the regularization that suppresses high-momentum contributions. Nevertheless, using the bare chiral interactions, i.e., without subsequent transformations, most many-body methods cannot achieve converged results beyond the lightest systems. Therefore, additional transformations are desirable to soften the chiral interactions further.

The unitary correlation operator method (UCOM) [18] provides one possibility to soften the interaction via a unitary transformation. Also the V_{lowk} renormalization group method [152–154] is commonly used to produce a low-momentum NN force that is sufficiently soft. So far the UCOM and V_{lowk} formalism are restricted to the NN sector and cannot be applied in the three-body space to also consider 3N contributions, which we investigate in this work. The Okubo-Lee-Suzuki similarity transformation [155, 156] decouples a specific many-body model space from the so-called excluded space and is applicable for 3N contributions as well. However, the similarity transformed Hamiltonian depends on the model space and the nucleus. As a consequence the variational character of NCSM-type approaches is destroyed. For these reasons we use the similarity renormalization group (SRG) [15–17, 19] that provides model-space and nucleus independent softened interactions and allows for the application in two-, three-, and even four-body space. We refer the reader to Ref. [157] for a current review of renormalization group methods in nuclear physics.

In the following we present the formal aspects of the SRG transformation to soften the chiral NN+3N interactions and focus on its implementation in the harmonic-oscillator (HO) basis up to the four-body level. In particular, we discuss the formal and technical truncations and present possible improvements of these limitations. The effects of the truncations of the SRG evolution as well as the developed improvements are investigated in many-body calculations in Sec. 5 and 6.

4.1 Concept

Throughout this work we use the SRG to perform a continuous unitary transformation of the Hamiltonian \mathbf{H}

$$\mathbf{H}_\alpha = \mathbf{U}_\alpha^\dagger \mathbf{H} \mathbf{U}_\alpha, \quad (115)$$

with the initial condition

$$\mathbf{H}_{\alpha=0} = \mathbf{H}, \quad \mathbf{U}_{\alpha=0} = \mathbb{1}. \quad (116)$$

An appropriate choice for the unitary operator \mathbf{U}_α softens the interaction and enables us to handle tensor- and short-range correlations in tractable HO model spaces.

The derivative of Eq. (115) with respect to the continuous parameter α leads to a first-order differential equation

$$\frac{d}{d\alpha} \mathbf{H}_\alpha = [\boldsymbol{\eta}_\alpha, \mathbf{H}_\alpha], \quad (117)$$

where the dynamic generator $\boldsymbol{\eta}_\alpha$ is connected to the unitary operator \mathbf{U}_α through

$$\boldsymbol{\eta}_\alpha = -\mathbf{U}_\alpha^\dagger \frac{d}{d\alpha} \mathbf{U}_\alpha = -\boldsymbol{\eta}_\alpha^\dagger. \quad (118)$$

Instead of defining the SRG transformation directly by specifying the unitary operator \mathbf{U}_α , which is non-trivial, we use an appropriate choice of the dynamic generator to decouple the low- and high-energy/momentum contributions, in order to accelerate the convergence of the many-body calculations. Having defined the generator we can perform the SRG transformation by evolving the Hamiltonian via the flow equation (117) up to a certain value of the flow parameter α . The SRG-transformed operators are indicated by the flow-parameter index. In this work we essentially use the canonical choice for the generator that is also used in the majority of nuclear structure applications

$$\boldsymbol{\eta}_\alpha = \left(2\frac{\mu}{\hbar^2}\right)^2 [\mathbf{T}_{\text{int}}, \mathbf{H}_\alpha], \quad (119)$$

with the intrinsic kinetic-energy operator $\mathbf{T}_{\text{int}} = \mathbf{T} - \mathbf{T}_{\text{cm}}$. We assume equal proton and neutron masses, such that the reduced nucleon mass is given by $\mu = \frac{m_N}{2}$, with the nucleon mass m_N . The intrinsic kinetic-energy operator for equal proton and neutron masses is defined as

$$\mathbf{T}_{\text{int}} = \frac{1}{A\mu} \sum_{i<j} \vec{\mathbf{q}}_{ij}^2, \quad (120)$$

with the relative-momentum operator $\vec{\mathbf{q}}_{ij} = \frac{\vec{\mathbf{p}}_i - \vec{\mathbf{p}}_j}{2}$ and the particle number A . The operator in

Eq. (120) is diagonal in a momentum and partial-wave decomposed momentum representation and exhibits a band-diagonal structure in the HO representation (see Fig. 4.2 and 4.4). For the canonical generator a diagonal form of the Hamiltonian in the momentum representation leads to a vanishing commutator in (119) and provides a fix point of the flow equation. We illustrate in the following that the generator decouples the low- and high-energy components of the interaction causing a flow of the Hamiltonian in the HO basis representation towards a band-diagonal form, which leads to an accelerated convergence in the many-body calculations. The units of the flow parameter are defined via the prefactor in the generator (119) as $[\text{fm}^4]$. For this specific generator it is reasonable to associate the flow parameter with a momentum scale, using the relation $\lambda_{\text{SRG}} = \alpha^{-1/4}$ as often done in the literature [158, 159].

When aiming at observables other than binding and excitation energies it is formally necessary to transform the corresponding operators as well

$$\mathbf{O}_\alpha = \mathbf{U}_\alpha^\dagger \mathbf{O} \mathbf{U}_\alpha, \quad (121)$$

which can be achieved by evaluating \mathbf{U}_α directly or by solving the flow equation

$$\frac{d}{d\alpha} \mathbf{O}_\alpha = [\eta_\alpha, \mathbf{O}_\alpha]. \quad (122)$$

Because the generator we use contains the evolved Hamiltonian, the flow equations for the operator \mathbf{O}_α and the Hamiltonian \mathbf{H}_α need to be evolved simultaneously. We refer to [124, 125] for a recent application and stress that there is work in progress to perform the SRG transformation of observables.

The SRG requires the solution of a first-order differential operator equation. Due to the simplicity of the evolution the SRG can be implemented in three-body space and even beyond. A further important advantage is the inherent flexibility of this unitary transformation, since the only formal constraint on the generator is its anti-Hermiticity to ensure the unitarity of the transformation. A variety of SRG generators have been studied in different physics contexts [159, 160].

An example is the so-called in-medium SRG (IM-SRG) [34–36], which uses the SRG evolution in a normal-ordered form to decouple a certain reference state, that approximates the ground state, from all particle-hole excitations. Once the reference state is completely decoupled its energy expectation value provides the ground-state energy of a nucleus. The embedded normal-ordering approximation represents the major systematic error of this approach, that is well under control for the chiral interactions that have been initially softened with the “free-space” SRG discussed above. Therefore, the IM-SRG provides an elegant ab initio method that, in addition, can be extended to the use of a multi-reference state (multi-reference IM-SRG) [36] enabling studies of open-shell systems.

However, in terms of the "free-space" SRG it is difficult to take advantage of the formal flexibility by choosing an alternative generator that improves the properties of the SRG evolution for our purposes. See for instance Sec. 6.3 for attempts to find alternative generators.

4.2 Cluster Decomposition

The equations in the formal discussions in Sec. 4.1 are operator relations in A -body Hilbert space or even a Fock space. When aiming at a numerical solution of the flow equation (117), we have to express the operators in a certain basis representation. Owing to computational reasons we generally cannot perform the evolution in an A -body space, but we have to restrict ourselves to space with smaller particle numbers. This limitation causes one of the most challenging problems in context of the SRG transformation, because during the evolution irreducible contributions beyond the particle rank of the initial Hamiltonian are induced. This becomes clear when considering the right-hand side of the flow equation (117). Because the generator we use is at least a two-body operator, the commutator with the Hamiltonian increases the particle rank of the evolved Hamiltonian in each evolution step. Thus, induced contributions up to the A -body rank are produced, even if one starts with a two-body Hamiltonian. The SRG-evolved Hamiltonian can be decomposed into contributions with different particle ranks (cluster decomposition) [18,21,161]

$$\mathbf{H}_\alpha = \mathbf{H}_\alpha^{[1]} + \mathbf{H}_\alpha^{[2]} + \mathbf{H}_\alpha^{[3]} + \mathbf{H}_\alpha^{[4]} + \dots + \mathbf{H}_\alpha^{[A]}, \quad (123)$$

where the subscript α indicates that the operator is SRG evolved and the superscript indicates the irreducible particle rank of the operator, i.e., $\mathbf{H}_\alpha^{[k]}$ is an irreducible k -body operator that can be expressed in second quantization as

$$\mathbf{H}_\alpha^{[k]} = \frac{1}{(k!)^2} \sum_{\mu_1, \dots, \mu_k} \sum_{\nu_1, \dots, \nu_k} a \langle \mu_1 \dots \mu_k | \mathbf{H}_\alpha^{[k]} | \nu_1 \dots \nu_k \rangle_a \mathbf{a}_{\mu_1}^\dagger \dots \mathbf{a}_{\mu_k}^\dagger \mathbf{a}_{\nu_k} \dots \mathbf{a}_{\nu_1}. \quad (124)$$

For instance, we assume a Hamiltonian containing an initial NN+3N interaction

$$\begin{aligned} \mathbf{H} = \mathbf{T}_{\text{int}} + \mathbf{V}_{\text{NN}}^{[2]} + \mathbf{V}_{\text{3N}}^{[3]} \xrightarrow{\text{SRG}} \mathbf{H}_\alpha = \mathbf{T}_{\text{int}} + \mathbf{V}_{\text{NN},\alpha}^{[2]} + \left(\mathbf{V}_{\text{NN},\alpha}^{[3]} + \mathbf{V}_{\text{3N},\alpha}^{[3]} \right) \\ + \left(\mathbf{V}_{\text{NN},\alpha}^{[4]} + \mathbf{V}_{\text{3N},\alpha}^{[4]} \right) + \dots, \end{aligned} \quad (125)$$

where the induced irreducible k -body contributions of the intrinsic kinetic energy (with $k \geq 2$) are absorbed in the $\mathbf{V}_{\text{NN}}^{[k]}$ operators. With this definition exclusively the interaction is changed by the SRG, while the intrinsic kinetic-energy operator remains the initial one.

The special treatment of the intrinsic kinetic-energy operator in the cluster decomposition often leads to confusion. Therefore, we want to elucidate this issue further. We first consider the SRG transformation of the total kinetic-energy operator $\mathbf{T} = \mathbf{T}_{\text{int}} + \mathbf{T}_{\text{cm}}$, which is an irreducible

Hamiltonians with initial NN interaction	
NN _{only}	evolution performed in two-body space: $\mathbf{H}_{\text{NN}_{\text{only}}} = \mathbf{T}_{\text{int}} + \mathbf{V}_{\text{NN},\alpha}^{[2]}$
NN+3N _{ind}	evolution performed in three-body space: $\mathbf{H}_{\text{NN}+3\text{N}_{\text{ind}}} = \mathbf{T}_{\text{int}} + \mathbf{V}_{\text{NN},\alpha}^{[2]} + \mathbf{V}_{\text{NN},\alpha}^{[3]}$
NN+3N _{ind} +4N _{ind}	evolution performed in four-body space: $\mathbf{H}_{\text{NN}+3\text{N}_{\text{ind}}+4\text{N}_{\text{ind}}} = \mathbf{T}_{\text{int}} + \mathbf{V}_{\text{NN},\alpha}^{[2]} + \mathbf{V}_{\text{NN},\alpha}^{[3]} + \mathbf{V}_{\text{NN},\alpha}^{[4]}$
Hamiltonians with initial NN+3N interaction	
NN+3N _{full}	evolution performed in three-body space: $\mathbf{H}_{\text{NN}+3\text{N}_{\text{full}}} = \mathbf{T}_{\text{int}} + \mathbf{V}_{\text{NN},\alpha}^{[2]} + \left(\mathbf{V}_{\text{NN},\alpha}^{[3]} + \mathbf{V}_{3\text{N},\alpha}^{[3]} \right)$
NN+3N _{full} +4N _{ind}	evolution performed in four-body space: $\mathbf{H}_{\text{NN}+3\text{N}_{\text{full}}+4\text{N}_{\text{ind}}} = \mathbf{T}_{\text{int}} + \mathbf{V}_{\text{NN},\alpha}^{[2]} + \left(\mathbf{V}_{\text{NN},\alpha}^{[3]} + \mathbf{V}_{3\text{N},\alpha}^{[3]} \right) + \left(\mathbf{V}_{\text{NN},\alpha}^{[4]} + \mathbf{V}_{3\text{N},\alpha}^{[4]} \right)$

Table 4.1 *SRG-evolved Hamiltonians*: We introduce the short-hand notation for the SRG-evolved Hamiltonians that can be constructed using an initial NN (upper table) or NN+3N (lower table) interaction and contain the induced contributions that can be included by an SRG evolution in the two-, three-, or four-body space.

one-body operator. This operator induces irreducible many-body contributions during the SRG evolution, while the irreducible one-body contribution remains unchanged

$$\mathbf{T}^{[1]} \xrightarrow{\text{SRG}} \mathbf{T}^{[1]} + \mathbf{T}_{\alpha}^{[2]} + \mathbf{T}_{\alpha}^{[3]} + \dots \quad (126)$$

For \mathbf{T}_{int} one cannot assign a unique irreducible particle rank. Although the momentum operators in Eq. (120) suggest \mathbf{T}_{int} to be an irreducible two-body operator, the dependence on the particle number A requires special attention when converting the matrix elements to higher particle-rank model spaces. The center-of-mass part of the kinetic-energy operator \mathbf{T}_{cm} commutes with \mathbf{T}_{int} as well as with the interaction. As a consequence, the SRG evolution has the same effect if one replaces the intrinsic kinetic-energy operator in Eq. (117) and (119) by the total kinetic-energy operator. However, for practical purposes we use \mathbf{T}_{int} in the SRG evolution and the absorption of the induced kinetic energy contributions into the transformed V_{NN} operators simplifies the practical evolution.

4.3 Types of Evolved Hamiltonians

In this work we present the techniques to perform the SRG evolution up to the four-body level. Starting either from an initial NN or NN+3N interaction we define the five Hamiltonians listed in Tab. 4.1 by successively including contributions of higher particle ranks. If we start with

an initial Hamiltonian using a chiral NN interaction, we can perform the SRG evolution in the m -body space with $2 \leq m \leq 4$, leading to the Hamiltonians in the upper table. During the evolution we omit the induced contributions beyond the m -body level, since they cannot be represented in the m -body space. The Hamiltonians with the initial NN+3N interaction (lower table) are obtained from an evolution in the three-, or four-body space. The canonical generator we use contains the Hamiltonian, hence, it slightly differs for the evolution of a Hamiltonian with an initial NN or NN+NN interaction. Therefore, the induced contributions originating from the NN interaction ($\mathbf{V}_{\text{NN},\alpha}^{[3]}, \mathbf{V}_{\text{NN},\alpha}^{[4]}$) in the upper and lower table are not the same, because they result from evolutions with different generators.

The SRG evolution is a unitary transformation and, therefore, the converged eigenvalues of the Hamiltonian have to be invariant during the evolution. Formally, the omission of induced many-body contributions violates the unitarity of the SRG and it is mandatory to verify the invariance of the observables during the evolution. We want to assess the effect of the induced contributions using the presented Hamiltonians and expect a sizable dependence of our observables on the flow parameter if the omitted contributions are relevant for their description. Thus, we utilize a variation of the flow parameter as diagnostic tool to assess the effect of the omitted many-body contributions when we perform the many-body calculations.

4.4 Evolution in HO Representation

As already mentioned, in order to perform numerical evolutions of the operator equations, it is necessary to express the operators in a certain basis representation. We typically perform the SRG evolution in the Jacobi-HO representation. The reasons for this are the separation of the center-of-mass part and the fact that the discrete orthonormal HO basis simplifies the evolution and, in addition, allows for an explicit reduction of the model-space dimension due to the antisymmetry of the basis. A more detailed discussion of the advantages and disadvantages of different basis sets can be found in Sec. 3. Note, that the three-body SRG evolution can be also performed in other basis representations, such as the partial-wave decomposed momentum-Jacobi basis [149] and the hyperspherical momentum basis [162]. However, so far only the SRG in the HO basis has been used to provide reliably evolved 3N interactions for nuclear structure calculations beyond the lightest nuclei.

Inserting the canonical generator (119) into the flow equation (117) and expanding the commutators yields

$$\frac{d}{d\alpha} H_\alpha = \left(2 \frac{\mu}{\hbar^2}\right)^2 (\mathbf{T}_{\text{int}} \mathbf{H}_\alpha \mathbf{H}_\alpha - 2 \mathbf{H}_\alpha \mathbf{T}_{\text{int}} \mathbf{H}_\alpha + \mathbf{H}_\alpha \mathbf{H}_\alpha \mathbf{T}_{\text{int}}). \quad (127)$$

As discussed in Sec. 3 one can perform the SRG evolution for each ($J^\pi T$)-channel separately,

when using the Jacobi-HO representation

$$\begin{aligned}
\frac{d}{d\alpha} \langle EiJT | \mathbf{H}_\alpha | E' i' JT \rangle &= \left(2 \frac{\mu}{\hbar^2}\right)^2 \sum_{E'' E'''}^{E_{\text{SRG}}} \sum_{i'' i'''} \\
&\left(\langle EiJT | \mathbf{T}_{\text{int}} | E'' i'' JT \rangle \langle E'' i'' JT | \mathbf{H}_\alpha | E''' i''' JT \rangle \langle E''' i''' JT | \mathbf{H}_\alpha | E' i' JT \rangle \right. \\
&- 2 \langle EiJT | \mathbf{H}_\alpha | E'' i'' JT \rangle \langle E'' i'' JT | \mathbf{T}_{\text{int}} | E''' i''' JT \rangle \langle E''' i''' JT | \mathbf{H}_\alpha | E' i' JT \rangle \\
&\left. + \langle EiJT | \mathbf{H}_\alpha | E'' i'' JT \rangle \langle E'' i'' JT | \mathbf{H}_\alpha | E''' i''' JT \rangle \langle E''' i''' JT | \mathbf{T}_{\text{int}} | E' i' JT \rangle \right), \tag{128}
\end{aligned}$$

where $|EiJT\rangle$ corresponds to an antisymmetric Jacobi-HO basis state in the two-, three-, or four-body space. Formally, the sums go to infinite energy quantum numbers, but in practice we have to restrict the sums to a finite maximum energy quantum number $E'', E''' \leq E_{\text{SRG}}$ which defines the model space of the SRG evolution or the SRG space for short. The basis representation leads to a system of coupled linear first-order differential equations for the Hamilton matrix elements. Note that all matrix elements in the SRG space of a $(J^\pi T)$ -channel need to be evolved simultaneously, since they appear on the right-hand side of Eq. (128). In finite model spaces this right-hand side corresponds to a three-fold matrix product that can be evaluated efficiently using optimized BLAS routines. The flow equation is typically solved using an embedded Runge-Kutta solver with an adaptive step-size control.

Once we evolved the flow equation in the m -body space, with $m = 2, 3, 4$, we obtain the evolved Hamiltonian in form of matrix elements in the Jacobi-HO representation that contain all irreducible contributions up to the m -body level. This Hamiltonian can be used directly to solve the eigenvalue problem of an m -particle nucleus. In general, we aim at the description of nuclei with $A > m$ nucleons, thus, it is necessary to obtain the irreducible contributions separately for their conversion to the A -body space. In the antisymmetrized Jacobi-HO representation this is achieved by subtracting the irreducible contributions with lower particle ranks. The latter are derived from an additional SRG evolution in a Jacobi-HO basis of lower particle rank.

After the SRG evolution in m -body space we typically subtract the intrinsic kinetic energy part. This allows us to concentrate on the irreducible interactions for the subtraction procedure as illustrated in Fig. 4.1.

For instance, we assume to start we an initial NN interaction and aim at the irreducible 4N contributions $\mathbf{V}_{\text{NN},\alpha}^{[4]}$, we evolve the Hamiltonian in the four-body Jacobi-HO space yielding the interactions $\mathbf{V}_{\text{NN},\alpha}^{[2]} + \mathbf{V}_{\text{NN},\alpha}^{[3]} + \mathbf{V}_{\text{NN},\alpha}^{[4]}$.⁹ Next, we perform the evolution to the same flow-parameter value α and in a consistent SRG space, in the two- and three-body space. The NN contributions $\mathbf{V}_{\text{NN},\alpha}^{[2]}$ can be obtained directly from the evolution in the two-body space and are converted to the three-body Jacobi-HO space. In the three-body space one can now subtract the

⁹The general subtraction procedure is independent of the initial interaction, because the initial NN and NN+3N interactions induce irreducible contributions to all particle ranks.

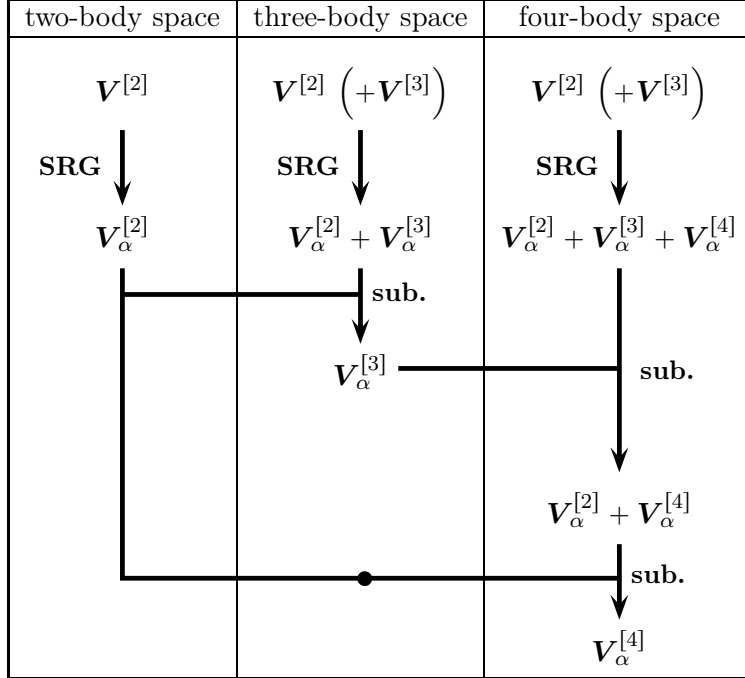


Figure 4.1 *Subtraction procedure in the two-, three-, and four-body space*: Illustrated are the irreducible interactions, resulting from the SRG evolution in the two-, three-, and four-body space and the subtractions performed to separate the irreducible contributions (see text for further description).

NN contribution from the interaction obtained from the three-body SRG evolution, yielding the irreducible 3N contributions $\mathbf{V}_{\text{NN},\alpha}^{[3]}$. Finally, one converts both 3N interaction matrix elements, of the NN and 3N contributions separately to the four-body Jacobi-HO basis and performs the subtraction from the matrix elements obtained from the four-body SRG evolution, yielding $\mathbf{V}_{\text{NN},\alpha}^{[4]}$.

Note, that owing to computational reasons and the construction of the antisymmetric Jacobi-HO basis it is advantageous to convert the irreducible NN contributions first to the three-body space and from this representation to the four-body space (indicated by the dot in Fig. 4.1), instead of converting them directly to the four-body space.

As mentioned before an important aspect is the consistency of the SRG space. For the subtraction procedure it is essential that the subtracted contributions correspond to those that appear during the SRG evolution in the higher particle-rank model spaces. Therefore, it is necessary to use a consistent generator and an equal flow-parameter value. Also an inconsistent choice of the SRG space can cause artifacts and we address this aspect in the following. The SRG space in the m -body Jacobi-HO representation is defined by the maximum energy quantum number E_{SRG} . This truncation depends on all m particles that contribute to the energy quantum number. Therefore, the SRG spaces cannot be chosen fully equivalent in the two-, three-, and

four-body space, by using the same E_{SRG} . In contrast to the single-particle space, where one could define the model space via a truncation of the single-particle basis,¹⁰ the Jacobi basis does not allow for the definition of a fully compatible model-space truncation for different particle ranks. For sufficiently large SRG spaces the slight differences in the model-space truncations are negligible, such that the SRG evolution and subtraction can be performed up to the desired accuracy. We come back to this aspect when we discuss the details of the subtractions in the three- (see Sec. 4.6.2) and, in particular, in the four-body space (see Sec. 4.7.2).

We present the typical SRG spaces for the different particle ranks in the following sections, where we discuss the technical aspects that need to be addressed for the individual SRG evolutions. For all applications in this section we use the standard chiral NN forces by Entem and Machleidt [8] and the 3N force by Navrátil [13] both with a cutoff of $\Lambda = 500 \text{ MeV}/c$.

4.5 Evolution in Two-Body Space

From a technical point of view the SRG evolution in the two-body space is simple and can be performed easily in the momentum [18] or the HO [163] representation. As mentioned before, to obtain converged NN contributions for the many-body calculations, we need rather large $E_{2,\text{SRG}} \approx 200$ [163], compared to those used in the three- and four-body space. The starting point for the initial NN interaction are matrix elements in the partial-wave decomposed Jacobi-momentum representation (54), thus, we typically perform the two-body SRG evolution in this representation on a sufficiently fine and large momentum grid. This avoids the transformation to the HO basis for the large model spaces, that would be required for the evolution in the HO basis. But, nevertheless we have to perform the two-body evolution in the HO basis for the subtraction procedure as described above. The Coulomb interaction and the isospin breaking are explicitly included in the two-body SRG evolution for the subsequent many-body calculations. However, we omit the Coulomb interaction and average over the isospin-projection quantum number for the ($T_1 = 1$) channels when we perform the SRG evolution for the subtraction procedure. This is because we do not consider the isospin breaking in the three- or four-body representation, since they are expected to produce minor corrections. This reduces the model-space dimensions, but does not allow to consider the effect of the induced 3N and many-nucleon contributions originating from the Coulomb interaction. These effects should be marginal as well because of the long-range character of the Coulomb force, what make it is rather insensitive to the SRG evolution [18]. We refer the interested reader to [18] for further details of the two-body SRG evolution, but since it is an already well established technique, we do not go into further details in this work.

¹⁰Although the single-particle basis formally allows for a consistent truncation of the model space for different particle ranks, such model spaces are of no practical use, since they lead to unfeasible large model-space dimensions to cover the physical relevant content.

4.6 Evolution in Three-Body Space

The implementation of the SRG evolution in three-body space is an essential ingredient for the application of evolved chiral interactions to nuclear structure calculations. The evolution in three-body space has been established over the recent years. In this section we illustrate its effect exemplarily for the triton and discuss technical ingredients for the application to A -body systems. Further, we explain the frequency-conversion approach that allows to provide accurately evolved chiral Hamiltonians for a large frequency range.

4.6.1 Chiral Interactions Evolved in the Triton Channel

We have already described the general purpose of the SRG evolution, to decouple low- and high-momentum/energy contributions and to accelerate the convergence of the many-body calculation. We investigate the effect of the SRG evolution by using the triton nucleus as an example. In Fig. 4.2 we illustrate the SRG evolution of the 3N matrix elements. Plotted are the absolute values of the intrinsic kinetic-energy matrix elements ${}_a\langle E_{12}i_{12}J_{12}T_{12} | \mathbf{T}_{\text{int}} | E'_{12}i'_{12}J_{12}T_{12} \rangle_a$, as well as of the interaction matrix elements ${}_a\langle E_{12}i_{12}J_{12}T_{12} | \mathbf{H}_\alpha - \mathbf{T}_{\text{int}} | E'_{12}i'_{12}J_{12}T_{12} \rangle_a$ in the antisymmetric Jacobi-HO representation for the triton channel ($J_{12}^\pi T_{12}$) = (1/2⁺1/2). We use the standard initial chiral NN+3N interaction and evolve it to typical flow-parameter values $\alpha = 0.04 \text{ fm}^4$ and 0.16 fm^4 . The initial interaction shows sizable off-diagonal contributions, corresponding to matrix elements between low- and high-energy HO eigenstates. The band-diagonal structure of the intrinsic kinetic-energy matrix represents a trivial fix point of the SRG evolution and, indeed, with increasing flow-parameter value α the off-diagonal contributions decouple, such that the interaction and accordingly the Hamiltonian is driven towards a band-diagonal form determined by the intrinsic kinetic-energy operator. Although, the detailed structure within the blocks of fixed energy quantum numbers E_{12} and E'_{12} (separated by the dark grid lines), depend on the specific choice of the coefficients of fractional parentage (CFPs), the suppression of the off-diagonal blocks is a general feature of the canonical SRG generator.

For the ($A = 3$) systems the subtraction procedure is not required and we can solve the eigenvalue problem by diagonalizing the Hamilton matrix in the antisymmetric Jacobi-HO basis. We truncate the model space at the maximum relative-energy quantum number $E_{3,\text{max}}$ such that the diagonalization corresponds to an NCSM calculation in a model space defined by $N_{\text{max}} = E_{3,\text{max}}$. In Fig. 4.3 the triton ground-state energy as function of the NCSM model space is illustrated. We use the bare standard NN+3N Hamiltonian (blue circles) and the corresponding evolved NN+3N_{full} Hamiltonians with $\alpha = 0.01 \text{ fm}^4$ (red diamonds), 0.04 fm^4 (green triangles), 0.16 fm^4 (violet boxes), and 0.64 fm^4 (light-blue stars). For the bare Hamiltonian rather large model spaces beyond $N_{\text{max}} = 20$ are required to achieve converged ground-state energies, while with increasing flow parameter the convergence with respect to the model-space size accelerates. In particular at the beginning of the evolution the acceleration effect is strong

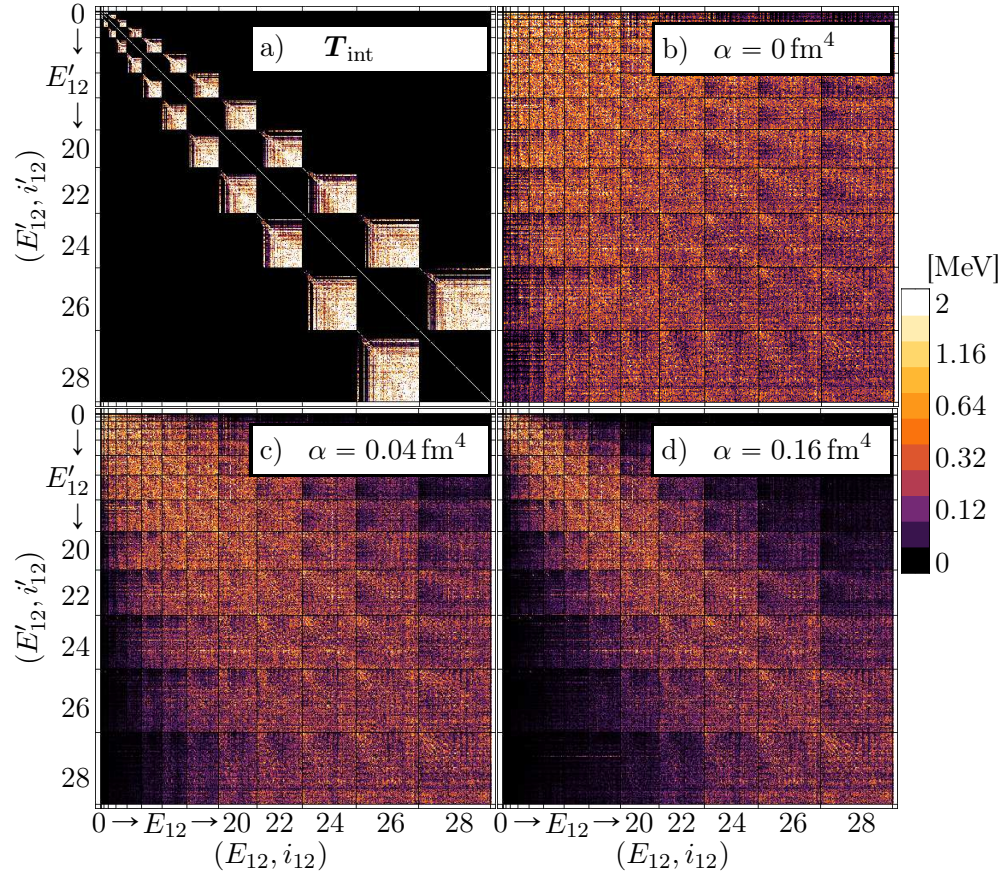


Figure 4.2 *Matrix elements in the antisymmetrized Jacobi-HO representation for the triton channel:* Plotted are the absolute values of the intrinsic kinetic-energy matrix elements (a), and of the interaction matrix elements for the flow parameter $\alpha = 0 \text{ fm}^4$ (b), 0.04 fm^4 (c) and 0.16 fm^4 (d). For the SRG evolution we used the standard chiral NN+3N interaction. Further, we used a HO frequency of $\hbar\Omega = 24 \text{ MeV}$ and an SRG space defined by $E_{3,\text{SRG}} = 40$. The dark grid lines separate blocks of fixed energy quantum numbers E_{12} and E'_{12} .

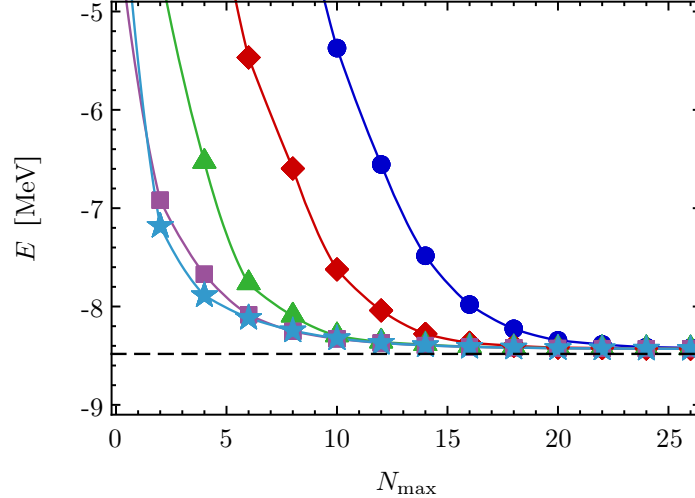


Figure 4.3 *Triton ground-state energy as function of the model space N_{max}* : The ground-state energies are obtained in an NCSM calculation using the initial NN+3N Hamiltonian as in Fig. 4.2. The SRG evolution has been performed in three-body space truncated by $E_{3,\text{SRG}} = 40$ up to the flow-parameter value $\alpha = 0 \text{ fm}^4$ (\bullet), 0.01 fm^4 (\blacklozenge), 0.04 fm^4 (\blacktriangle), 0.16 fm^4 (\blacksquare), and 0.64 fm^4 (\star), using $\hbar\Omega = 24 \text{ MeV}$. The dashed horizontal line correspond to the experimental value [164].

and starts to saturate for the largest flow-parameter values. The fact that all curves converge to the experimental value (dashed horizontal line), within an uncertainty of about 50 keV is not surprising. First of all we investigate an ($A = 3$) system, such that induced 4N contributions are not present and all curves must converge to the same result. Moreover, the standard initial chiral NN+3N interaction we use is fitted to the binding energies of ${}^3\text{He}$ and ${}^3\text{H}$.

It is important to note that heavier nuclear systems require the evolution of several three-body channels ($J_{12}^\pi T_{12}$), which increases the computational demands of the three-body SRG evolution. In contrast to previous applications of the SRG evolution in the Jacobi-HO basis [158] we have implemented a highly efficient transformation that, e.g., can evolve the triton channel to typical flow-parameter values in an SRG space of $E_{3,\text{SRG}} = 40$ in less than one hour on a single standard node.

4.6.2 Subtraction Procedure

When targeting nuclei with $A > 3$ in the many-body calculations it is necessary to separate the irreducible NN and 3N contributions, since they convert differently to the A -body space. The separate irreducible contributions can be constructed by using the subtraction procedure illustrated in Fig. 4.1. As mentioned before, it is crucial that the SRG evolutions are performed consistently in two- and three-body space. Specifying the SRG space via the maximum relative-energy quantum number E_{SRG} does not allow for a fully equivalent truncation in two- and three-body Jacobi-HO space. To demonstrate this problem, we consider an SRG space defined

by an even or odd energy truncation E_{SRG} of 20 and 21. We evolve the positive-parity triton channel $(J_{12}^{\pi}T_{12}) = (1/2^{+}1/2)$ and investigate the contributions from two-body channels with different parities used for the subtraction. Due to the positive parity of the triton channel the SRG evolution in three-body space is identical for $E_{3,\text{SRG}} = 20$ or 21, while the SRG evolution of the NN contributions with negative parity, which are required for the subtraction, are evolved either with $E_{2,\text{SRG}} = 19$ or 21, respectively.¹¹ As long as the high-energy NN contributions at the boundary of the SRG space have a sizable effect on the interaction matrix elements used in the many-body calculations, we will observe a dependence on the subtraction procedure. Since there is no unique choice we define several subtraction schemes and investigate the implications for the many-body results. In case of the three-body SRG evolution we generally choose the SRG space sufficiently large, so that the observables are independent of the subtraction scheme. For practical applications we use an even $E_{3,\text{SRG}}$ to specify the evolution of the three-body channels for both parities. The two-body SRG space used for the subtraction is truncated by the same even maximum energy quantum number, i.e., $E_{2,\text{SRG}} = E_{3,\text{SRG}}$.

4.6.3 Frequency Conversion

A seeming disadvantage of the SRG evolution in the HO representation is the explicit dependence of the SRG space on the HO frequency $\hbar\Omega$. Depending on the HO frequency SRG spaces with equal $E_{3,\text{SRG}}$ span different momentum or energy ranges, such that the SRG spaces for very small frequencies might not cover the relevant physics required in the many-body calculations. Furthermore, to investigate the frequency dependence in the many-body calculations, so far we have needed multiple SRG evolutions for the desired frequencies. To circumvent these disadvantages of the evolution in the HO representation we introduce the frequency-conversion approach. This approach takes advantage of the fact that the model space used for the SRG evolution (expressed in a Jacobi basis) is generally much larger than the one used for the many-body calculations (expressed in a single-particle scheme). The simple idea is to perform the SRG evolution for an adequate HO frequency $\hbar\Omega_{\text{SRG}}$ and transform the antisymmetric Jacobi-HO matrix elements of the interaction to the HO frequencies $\hbar\Omega$ required in the many-body calculations. The corresponding transformation formula reads

$$\begin{aligned}
 {}_a\langle E_{12}i_{12}J_{12}T_{12} | \mathbf{V}_{\alpha} | E'_{12}i'_{12}J_{12}T_{12} \rangle_a &= \sum_{\tilde{E}_{12}\tilde{E}'_{12}}^{E_{3,\text{SRG}}} \sum_{\tilde{i}_{12}\tilde{i}'_{12}} \\
 &\times {}_a\langle E_{12}i_{12}J_{12}T_{12} | \tilde{E}_{12}\tilde{i}_{12}J_{12}T_{12} \rangle_a {}_a\langle E'_{12}i'_{12}J_{12}T_{12} | \tilde{E}'_{12}\tilde{i}'_{12}J_{12}T_{12} \rangle_a \\
 &\times {}_a\langle \tilde{E}_{12}\tilde{i}_{12}J_{12}T_{12} | \mathbf{V}_{\alpha} | \tilde{E}'_{12}\tilde{i}'_{12}J_{12}T_{12} \rangle_a,
 \end{aligned} \tag{129}$$

¹¹For the negative-parity two-body channels the energy quantum numbers must be odd, such that an SRG space with $E_{2,\text{SRG}} = 20$ is identical to the one with $E_{2,\text{SRG}} = 19$.

where we denote the quantities that correspond to the HO frequency $\hbar\Omega_{\text{SRG}}$ by a tilde. The matrix elements on the left-hand side are represented in the Jacobi-HO basis with the frequency $\hbar\Omega$ and the matrix elements that appear on the right-hand side corresponds to the HO basis with $\hbar\Omega_{\text{SRG}}$. To derive this equation we inserted two unity operators and used the fact that the overlaps of the HO basis sets with different frequencies are only non-vanishing for equal parity and angular momentum J_{12}^π , and isospin T_{12} in the bra and ket states. We are left with the calculation of the overlaps ${}_a\langle E_{12}i_{12}J_{12}T_{12}|\tilde{E}_{12}\tilde{i}_{12}J_{12}T_{12}\rangle_a$. To derive the corresponding formula one can use a similar procedure as in Sec. 3.5.1, where the transformation of the Jacobi-HO basis to the partial-wave decomposed Jacobi-momentum basis is discussed. We first use the antisymmetrization relation (59) to express both states of the overlap as a superposition of the corresponding partial-antisymmetric states $|N_1N_2;\alpha_{12}\rangle_{a_1}$. Next we decouple the angular momenta as in Eq. (97), such that we can concentrate on the spatial part of the overlap $\langle NLM_L|\tilde{N}\tilde{L}\tilde{M}_L\rangle$, where the HO states are defined with respect to different frequencies. Expressing the HO overlap in the momentum representation yields

$$\begin{aligned}\langle NLM_L|\tilde{N}\tilde{L}\tilde{M}_L\rangle &= \int d\pi \pi^2 \int d\Omega R_{NL}^*(\pi) Y_{LM_L}^*(\Omega) R_{\tilde{N}\tilde{L}}(\pi) Y_{\tilde{L}\tilde{M}_L}(\Omega), \\ &= \delta_{L\tilde{L}}\delta_{M_L\tilde{M}_L} \int d\pi \pi^2 R_{NL}^*(\pi) R_{\tilde{N}\tilde{L}}(\pi),\end{aligned}\tag{130}$$

where we used the orthonormality relation of the spherical harmonics.

Finally, we couple the angular momenta, use several orthonormality relations of the Clebsch-Gordan coefficients, and antisymmetrize the states utilizing the CFPs yielding the formula

$$\begin{aligned}{}_a\langle E_{12}i_{12}J_{12}T_{12}|\tilde{E}_{12}\tilde{i}_{12}J_{12}T_{12}\rangle_a &= \sum_{N_1N_2} \sum_{\tilde{N}_1\tilde{N}_2} \sum_{\alpha_{12}} \\ &\times \delta_{E_{12},2N_1+L_1+2N_2+L_2} C_{N_1N_2\alpha_{12}}^{i_{12}} \int d\pi_1 \pi_1^2 R_{N_1L_1}^*(\pi_1) R_{\tilde{N}_1L_1}(\pi_1) \\ &\times \delta_{\tilde{E}_{12},2\tilde{N}_1+L_1+2\tilde{N}_2+L_2} C_{\tilde{N}_1\tilde{N}_2\alpha_{12}}^{\tilde{i}_{12}} \int d\pi_2 \pi_2^2 R_{\tilde{N}_2L_2}^*(\pi_2) R_{\tilde{N}_2L_2}(\pi_2).\end{aligned}\tag{131}$$

As indicated by the sums in (129) the frequency conversion is performed in the same finite model space that is used for the SRG evolution. Generally speaking, to perform an accurate conversion of the frequency the SRG space must cover those basis states $|\tilde{E}_{12}\tilde{i}_{12}J_{12}T_{12}\rangle_a$ that produce non-negligible overlaps with the basis states $|E_{12}i_{12}J_{12}T_{12}\rangle_a$ that are required for the many-body model space. For small frequency differences the overlap has a rather narrow band-diagonal structure, which broadens with the difference of the frequencies $\hbar\Omega$ and $\hbar\Omega_{\text{SRG}}$. In particular, for large frequency differences far-off diagonal overlaps can become relevant.

However, as the frequency conversion is performed after the SRG evolution the interaction already has a band-diagonal structure and the low- and high-energy basis states are decoupled. The frequency transformation in Eq. (129) only yields sizable contributions to the summation

on the right-hand side for interaction matrix elements with similar E_{12} and E'_{12} . The low-energy sector of the Jacobi-HO matrix-elements that enters the subsequent many-body calculations is thus typically not affected by the truncation of the model space used for the frequency conversion and we study the reliability of the approach in Sec. 5.

The simplicity of the transformation in Eq. (129) and (131) makes the frequency-conversion approach a useful tool to facilitate the SRG evolution procedure for multiple frequencies and enables the application of accurately evolved interactions for a large frequency range using tractable SRG spaces. As we discuss in Sec. 5 the frequency conversion is indispensable for many applications in nuclear structure physics and have been successfully applied in several publications [21, 28, 30].

4.7 SRG Evolution in Four-Body Space

In this work we demonstrate the importance of the SRG induced 4N interactions for nuclear structure applications beyond the mid-p-shell nuclei (see Sec. 6). The SRG evolution in the antisymmetric four-body Jacobi-HO representation is a useful tool to handle these induced contributions. All the techniques we highlight in this section are not tailored to special properties of the induced forces and can be used for the general inclusion of 4N interactions. This is of particular interest for the current efforts of the inclusion of an NN+3N interactions at N³LO by the LENPIC collaboration, since at the same chiral order initial 4N forces start to emerge and thus are required for a fully consistent N³LO Hamiltonian. In contrast to the established SRG evolution in three-body space, the four-body evolution has never been performed so far. The SRG evolution in the antisymmetric four-body Jacobi-HO representation provides unforeseen challenges in particular with respect to the rapidly increasing SRG space and we discuss the benefits, problems, and limitations for the application in nuclear structure calculations for p-shell nuclei in Sec. 6.4. In the following we present the inclusion of the induced 4N contributions using the ⁴He nucleus as an example. Further, we introduce several subtraction schemes that are used to investigate the dependence on the SRG-space truncation. Finally, we introduce the frequency-conversion approach in the four-body space.

4.7.1 Chiral Interactions Evolved in the ⁴He Channel

We start with the analog investigations of the SRG effect as in Sec. 4.6.1 for the three-body case. In Fig. 4.4 we illustrate the absolute values of the intrinsic-kinetic energy matrix elements (a) and the interaction matrix elements in the antisymmetric Jacobi-HO representation $|E_{123}i_{123}J_{123}T_{123}\rangle_a$ for the ⁴He channel ($J_{123}^\pi T_{123} = (0^+0)$). Plotted are the bare interaction matrix elements in Fig. 4.4(b) as well as the ones obtained from a four-body SRG evolution with $\alpha = 0.04 \text{ fm}^4$ (c) and 0.16 fm^4 (d). We start with the initial standard NN+3N interaction, using $\hbar\Omega = 24 \text{ MeV}$ and perform the evolution in an SRG space truncated at $E_{4,\text{SRG}} = 20$. As

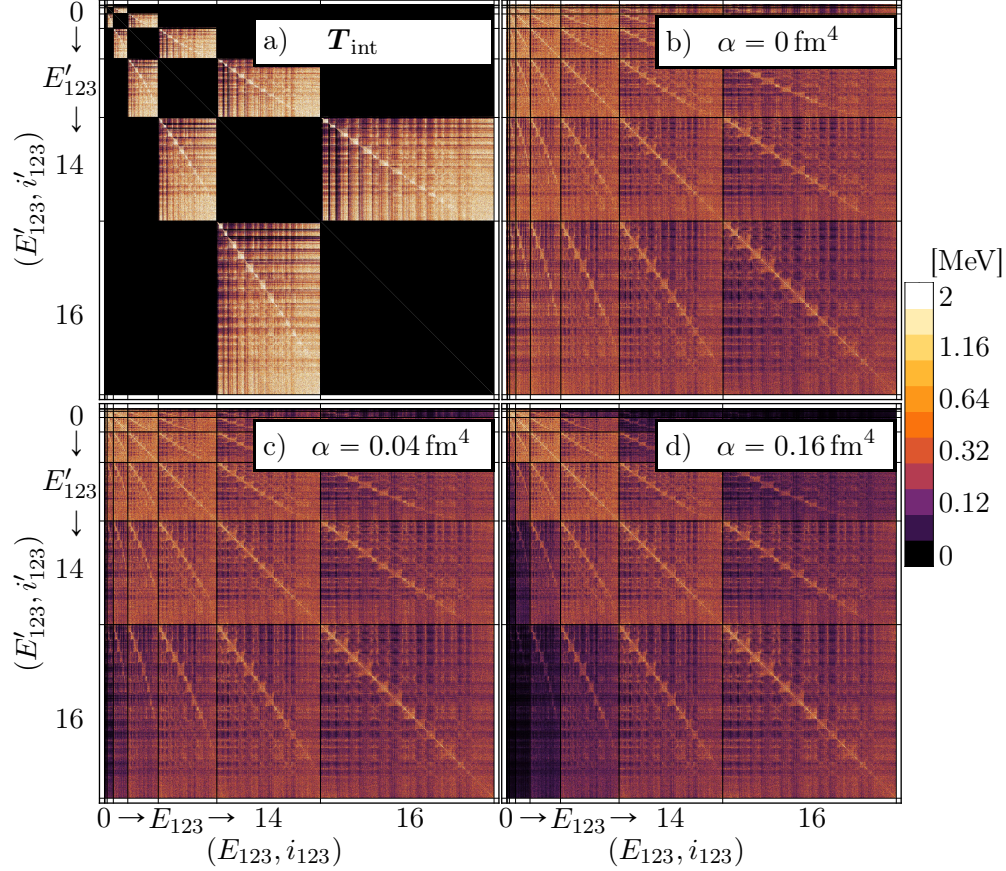


Figure 4.4 *Matrix elements in the antisymmetrized Jacobi-HO representation for the ${}^4\text{He}$ channel:* Plotted are the absolute values of the intrinsic kinetic-energy matrix elements (a), and of the interaction matrix elements for the flow parameter $\alpha = 0 \text{ fm}^4$ (b), 0.04 fm^4 (c) and 0.16 fm^4 (d). The SRG evolution is performed with the standard initial NN+3N interaction for $\hbar\Omega = 24 \text{ MeV}$ and an SRG space defined by $E_{4,\text{SRG}} = 20$. The dark grid lines separate blocks of fixed energy quantum numbers E_{123} and E'_{123} .

in the three-body case we observe a suppression of the off-diagonal interaction matrix elements driving the Hamiltonian to the pre-diagonal form determined by the intrinsic-kinetic energy matrix. The pre-diagonalization seems to be more pronounced in the three-body case but this is mainly due to the reduced range of energies in Fig. 4.4. Due to the large model-space dimensions in the four-body space we show only those matrix elements with $E_{123}, E'_{123} \leq 16$, while in the three-body case in Fig. 4.2 we display all matrix elements with $E_{12}, E'_{12} \leq 28$.

In Fig. 4.5 we examine the ${}^4\text{He}$ ground-state energy obtained in NCSM calculations plotted over the many-body model-space truncation N_{max} . The results are obtained with the initial NN+3N Hamiltonian (blue circles) as well as with the SRG-evolved NN+3N_{full}+4N_{ind} Hamiltonians for $\alpha = 0.01 \text{ fm}^4$ (red diamonds), 0.04 fm^4 (green triangles), 0.16 fm^4 (violet boxes), and 0.64 fm^4 (light blue stars). The Hamiltonian is evolved in the four-body Jacobi-HO representation with

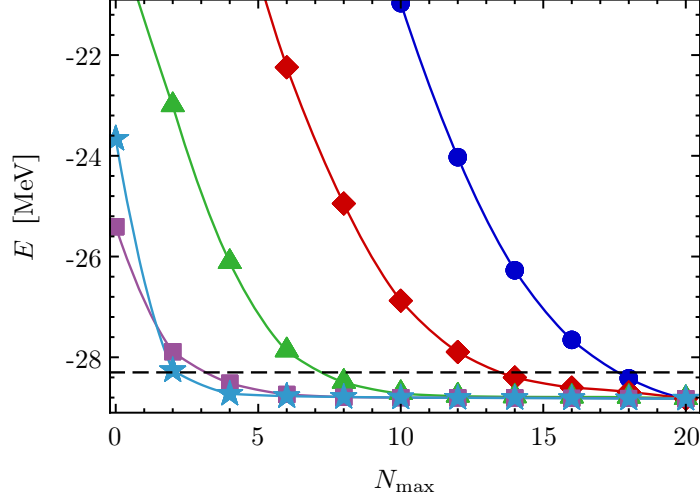


Figure 4.5 ${}^4\text{He}$ ground-state energy as function of the model space N_{\max} : The ground-state energies are obtained in an NCSM calculation using the standard NN+3N Hamiltonian without the Coulomb interaction. The SRG evolution has been performed in a four-body space truncated by $E_{4,\text{SRG}} = 20$ up to the flow-parameter value $\alpha = 0 \text{ fm}^4$ (●), 0.01 fm^4 (◆), 0.04 fm^4 (▲), 0.16 fm^4 (■), and 0.64 fm^4 (★), using $\hbar\Omega = 24 \text{ MeV}$. The dashed horizontal line correspond to the experimental value [164].

an SRG space of $E_{4,\text{SRG}} = 20$. Note, the SRG space corresponds to the $N_{\max} = 20$ model space of an NCSM calculation, which is performed by diagonalizing the Hamilton matrix in the Jacobi-HO representation. Therefore, by definition, the ground-state energies of all evolved Hamiltonians converge to the result of the bare interaction with $N_{\max} = 20$. As for the triton the convergence acceleration with respect to the model space caused by the SRG evolution is substantial. In particular, at the beginning of the evolution one achieves a strong convergence acceleration, while it tends to saturate for the largest studied flow parameters.

Note that the energy curve obtained with the bare Hamiltonian is not yet fully converged in the $N_{\max} = 20$ space. Thus we are missing relevant contribution during the SRG from the outset. After the SRG evolution this contributions cannot be considered via an N_{\max} extrapolation. To perform a reliable calculation for the ${}^4\text{He}$ ground-state energy it would be necessary to use much larger four-body SRG spaces. However, although the four-body SRG space cannot cover all relevant NN and 3N contributions, this model space might be large enough to treat the relevant induced 4N contributions and we investigate this issue in Sec. 6.4.

Therefore, a more sophisticated approach is to obtain the irreducible contributions from separate SRG evolutions in the two-, three-, and four-body space and to utilize the subtraction procedure illustrated in Fig. 4.1. This approach allows for the evolution of the NN and 3N contributions in much larger SRG spaces because we can use $E_{2,\text{SRG}} > E_{3,\text{SRG}} > E_{4,\text{SRG}}$. Note that repulsive Coulomb interaction is not included in the presented ${}^4\text{He}$ calculations leading to a sizable overbinding of the ground-state energy.

It is interesting to examine the induced 3N and 4N contributions that originate from the initial NN and NN+3N interactions. To this purpose Fig. 4.6 shows the ${}^4\text{He}$ ground-state energies, that have been obtained with the Hamiltonians denoted by NN_{only} (blue circles), $\text{NN}+3\text{N}_{\text{ind}}$ (red diamonds), and $\text{NN}+3\text{N}_{\text{ind}}+4\text{N}_{\text{ind}}$ (red open diamonds) starting from the initial NN interaction as well as the $\text{NN}+3\text{N}_{\text{full}}$ (green triangles) and $\text{NN}+3\text{N}_{\text{full}}+4\text{N}_{\text{ind}}$ (green open triangles), where we start with the initial NN+3N interaction. We perform the SRG evolution in two-, three-, and four-body space with an SRG space truncation of $E_{\text{SRG}} = 20$ for each evolution, such that the subtraction procedure is not required. The results are plotted over a large flow-parameter range, with the flow parameter doubling from $\alpha = 0.0025 \text{ fm}^4$ up to 1.28 fm^4 , which substantially exceeds the α range typically used in nuclear structure calculations. For those calculations with a particle number $A > 4$, we follow the philosophy to choose the flow parameter α as small as possible to avoid an increase of the induced many-body forces and to use α as large as necessary to achieve a sufficient convergence of the many-body calculations. Therefore, we typically use flow parameters in the range from $\alpha = 0.02$ to 0.16 fm^4 .

In the following, we demonstrate the emergence and, in particular, the inclusion of induced 4N forces. In Fig. 4.6 (a) we observe that the ground-state energy obtained with the NN_{only} Hamiltonian shows a strong dependence on the flow-parameter value. This indicates that the omitted induced contributions have a strong repulsive effect for the small α values, that turns into an attractive effect beyond the flow-parameter value $\alpha = 0.64 \text{ fm}^4$. The result of the initial NN interaction can be recovered for a large α range, when including the induced 3N contribution, i.e., using the $\text{NN}+3\text{N}_{\text{ind}}$ Hamiltonian. Furthermore, the inclusion of the initial 3N forces leads to an attraction and an improved description of the experimental value. Note that the omission of the Coulomb interaction leads to an overbinding of the calculated ground-state energy compared to experiment. When we include the induced 4N contributions we reproduce the ground-state energy of the bare NN and NN+3N Hamiltonians over the complete flow-parameter range. This confirms that all relevant contributions are included in the four-body space, such that the eigenvalues are invariant under the unitary SRG transformation. The discrepancies of the ground-state energies of the considered flow-parameter range are far below 1 keV, monitoring the numerical precision of the Hamilton matrix evolution.

In the following, we study the effect of the induced 4N contributions originating from the initial NN and NN+3N interaction by considering the deviations of the $\text{NN}+3\text{N}_{\text{ind}}$ and $\text{NN}+3\text{N}_{\text{full}}$ results from the result including the 4N contributions. We zoom in the corresponding regimes illustrated in Fig. 4.6 (b) and (c), respectively. The induced 4N forces show a rather complicated effect as function of the flow parameter. The induced 4N forces originating from the initial NN interaction in Fig. 4.6 (b) are slightly repulsive in the range of $\alpha = 0.0025 - 0.04 \text{ fm}^4$, leading to a local minimum for the curve with the $\text{NN}+3\text{N}_{\text{ind}}$ Hamiltonian and a maximal discrepancy of about 40 keV to the constant energy of the $\text{NN}+3\text{N}_{\text{ind}}+4\text{N}_{\text{ind}}$ Hamiltonian. Beyond the flow-parameter value $\alpha = 0.16 \text{ fm}^4$ the repulsive induced 4N forces cause a second minimum for the

curve with the $\text{NN}+3\text{N}_{\text{ind}}$ Hamiltonian of up to 370 keV.

When starting with an initial $\text{NN}+3\text{N}$ interaction in Fig. 4.6(c) the induced 4N forces are slightly repulsive for the range of $\alpha = 0.0025 - 0.08 \text{ fm}^4$ and their repulsion increases monotonically from about 25 keV to 70 keV, while it rapidly increases to more than 315 keV for the larger flow parameters and turns into an attraction for the largest studied flow-parameter value. Note, the discrepancy observed between the energies obtained with the $\text{NN}+3\text{N}_{\text{full}}$ and $\text{NN}+3\text{N}_{\text{full}}+4\text{N}_{\text{ind}}$ Hamiltonian are caused by a combination of the omitted induced 4N forces that originate from the initial NN as well as from the initial 3N interaction.

A similar investigation has been performed for the triton and ${}^4\text{He}$ using the NN_{only} , $\text{NN}+3\text{N}_{\text{ind}}$ and $\text{NN}+3\text{N}_{\text{full}}$ Hamiltonians in Ref. [163], i.e., without inclusion of the 4N contributions. Besides differences concerning the SRG spaces and the treatment of the isospin breaking, an alternative definition of the flow-parameter value is used. For comparison the equivalent results of Fig. 4.6 as function of the scale parameter $\lambda_{\text{SRG}} = \alpha^{-(1/4)}$ can be found in Fig. 4.7.

In summary, in the flow-parameter regime we typically use for nuclear structure calculations, i.e., $\alpha = 0.02 - 0.16 \text{ fm}^4$ ($\lambda_{\text{SRG}} \approx 1.58 - 2.66 \text{ fm}^{-1}$), the effect of the repulsive induced and attractive initial 3N forces to the ${}^4\text{He}$ ground-state energy are both of the order of 3 MeV and by coincidence almost cancel each other. The effect of the induced 4N forces are much smaller and lead to an attraction of less than 130 keV, indicating a hierarchy of the 3N and 4N forces. A small attractive 4N effect for the initial $\text{NN}+3\text{N}$ interaction already emerges at the very beginning of the SRG evolution and remains almost constant throughout our typical flow-parameter range. It would be difficult to identify such an effect of the induced 4N forces by a flow-parameter variation using SRG evolutions exclusively at the three-body level. Note, the effect of the 4N contributions for $\alpha \leq 0.02 \text{ fm}^4$ is almost negligible and based on the studies in this section we do not expect to miss sizable 4N effects by the flow-parameter variation used in practice. Nevertheless, it might be interesting to study the induced 4N forces by an explicit inclusion (or by determining the converged result of the bare Hamiltonian if possible) even for observables, where one finds a negligible flow-parameter dependence to confirm our assumption.

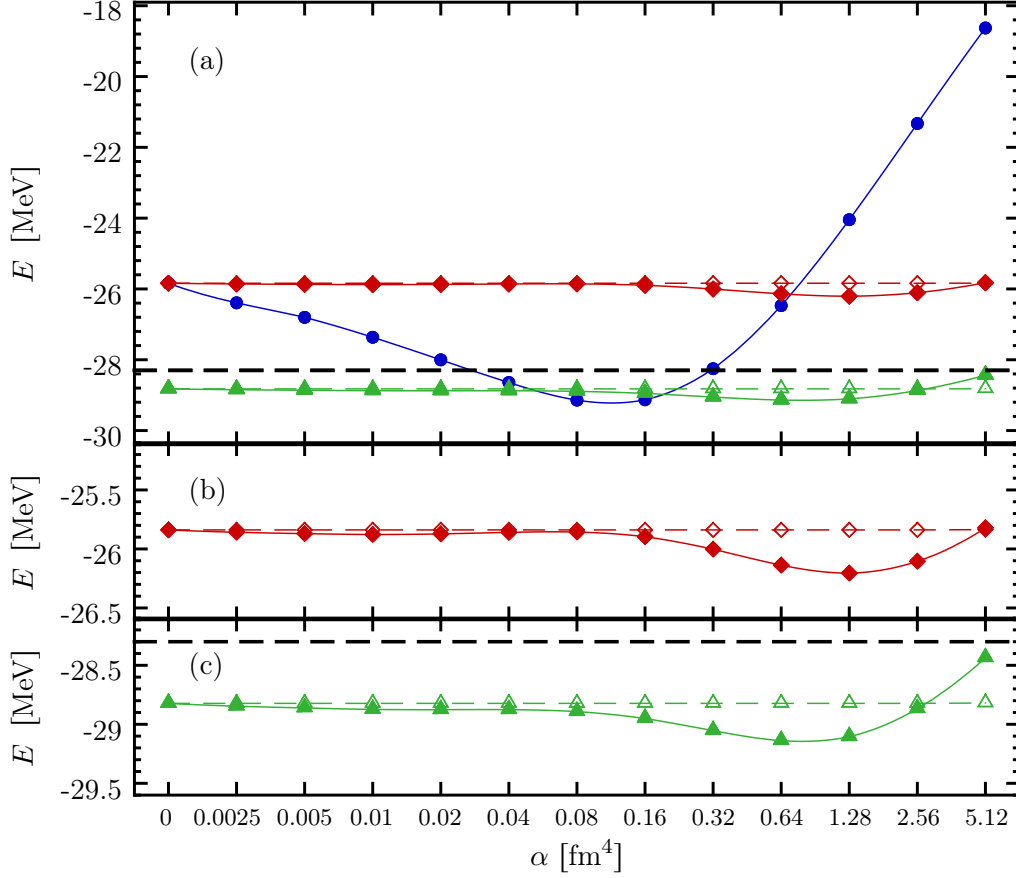


Figure 4.6 ${}^4\text{He}$ ground-state energy as function of the flow parameter α : Plotted is the ${}^4\text{He}$ ground-state energy obtained in an NCSM calculation for $N_{\text{max}} = 20$ using the SRG-evolved NN_{only} (\bullet), $\text{NN}+3\text{N}_{\text{ind}}$ (\blacklozenge), $\text{NN}+3\text{N}_{\text{ind}}+4\text{N}_{\text{ind}}$ (\diamond) Hamiltonians, where we start with the standard NN interaction, as well as the $\text{NN}+3\text{N}_{\text{full}}$ (\blacktriangle) and $\text{NN}+3\text{N}_{\text{full}}+4\text{N}_{\text{ind}}$ (\triangle) Hamiltonians, where we start with the standard NN+3N interaction. For all calculations the Coulomb interaction has been omitted and we have averaged over the isospin projection quantum numbers. In the lower two plots we emphasize the effect of the induced 4N contributions originating from the initial NN (b) and NN+3N (c) interaction using a diminished plot range. Further we used $\hbar\Omega = 24 \text{ MeV}$ and $E_{\text{SRG}} = 20$. The dashed horizontal line correspond to the experimental value [164]. Note that the flow-parameter value α is doubled for each tick on the abscissa. See text for further description.

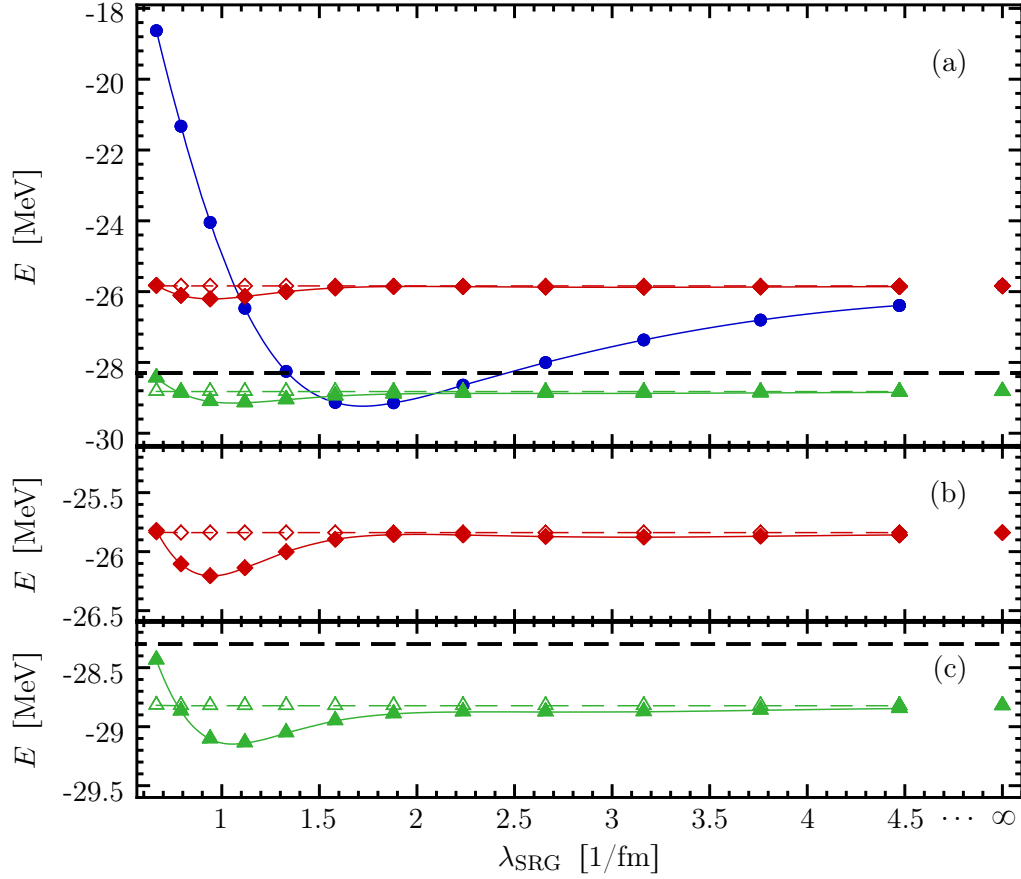


Figure 4.7 ${}^4\text{He}$ ground-state energy as function of the flow parameter λ_{SRG} : Illustrated are the same results as in Fig. 4.6, where the ground-state energy is plotted as function of $\lambda_{\text{SRG}} = \alpha^{-(1/4)}$ in order to provide a simpler comparison to the other flow-parameter convention commonly used in the nuclear structure community. The results of the bare Hamiltonian correspond to $\lambda_{\text{SRG}} = \infty$. The dashed horizontal line correspond to the experimental value [164].

4.7.2 Subtraction Procedure

In the previous section we have demonstrated how to include the relevant induced 4N contributions for the description of the ${}^4\text{He}$ ground-state energy. When aiming at many-body calculations for this nucleus or heavier nuclei that are converged with respect to the SRG space, it is necessary to perform the SRG evolutions in the two-, three-, and four-body space separately and utilize the subtraction procedure to obtain the corresponding irreducible contributions. We have discussed the incompatibility of the SRG spaces of different particle ranks with the truncation formulated in the Jacobi basis. Compared to the SRG in the three-body space the dimensions of the four-body model spaces increase dramatically with E_{SRG} , in particular, for the channels with an angular momentum $J_{123} > 0$ (see Sec. 3.1.3). Therefore, we are restricted to SRG spaces with $E_{4,\text{SRG}} < E_{3,\text{SRG}}$ and as we illustrate in Sec. 6.4 for nuclei in the p shell, the subtraction procedure can have sizable effects on the ground-state energy. For sufficiently large SRG spaces the nuclear observables are independent of the specific subtraction procedure. In order to validate that the SRG space is large enough we introduce several subtraction schemes and study their influence on the energies.

The subtractions are performed with the general procedure described in Fig. 4.1, while the schemes differ by an adjustment of the E_{SRG} truncation by typically (-1) or (-2) , according to the parity. In the following we use the notation $E_{n,\text{SRG}}^{(\pi)}$ for the SRG truncation, where the superscript denotes the parity of the channel with particle rank n and for general statements independent of the particle rank we skip the subscript n . For instance $E_{4,\text{SRG}}^{(+)}$ corresponds to the SRG space truncation of a four-body channel with positive parity.

It is important to note that the relative energy quantum numbers of the states corresponding to positive-parity channels are even, and odd for negative-parity channels. Thus SRG evolutions for positive-parity channels are identical for an even $E_{\text{SRG}}^{(+)}$ and an odd $E_{\text{SRG}}^{(+)} + 1$. Similarly evolutions of negative-parity channels are equivalent for an odd $E_{\text{SRG}}^{(-)}$ and an even $E_{\text{SRG}}^{(-)} + 1$. We now list the subtraction schemes, that successively increase in complexity.

SubA: This subtraction scheme is the simplest one and corresponds to the subtraction used in practice to obtain the irreducible 3N contributions (see Sec. 4.6.2). The SRG space for the four-body channels is defined by an even $E_{4,\text{SRG}}^{(+/-)}$ truncation for both parities and use this truncation also for the evolution in two- and three-body space, i.e., $E_{2,\text{SRG}}^{(+/-)} = E_{3,\text{SRG}}^{(+/-)} = E_{4,\text{SRG}}^{(+/-)}$, to obtain the contributions for the subtraction.

As illustrated for the three-body case, this scheme is not unique because the four-body channels with negative parity are effectively evolved using $E_{4,\text{SRG}}^{(-)} = E_{4,\text{SRG}}^{(+)} - 1$, while the subtracted positive-parity two- and three-body contributions are evolved for $E_{2,\text{SRG}}^{(+)} = E_{3,\text{SRG}}^{(+)} = E_{4,\text{SRG}}^{(-)}$. This means that we subtract contributions of model spaces that do not contribute during the

four-body evolution and one might adjust the $E_{4,\text{SRG}}^{(-)}$ for the negative parity channels, yielding the next subtraction scheme.

SubB: The SRG spaces for the four-body channels with positive and negative parity are defined by an even $E_{4,\text{SRG}}^{(+)}$ and an odd $E_{4,\text{SRG}}^{(-)} = E_{4,\text{SRG}}^{(+)} + 1$ truncation.¹² Further, the same truncation as in the four-body space is used for the evolution of the subtracted contributions, i.e., for positive-parity four-body channels $E_{2,\text{SRG}}^{(+/-)} = E_{3,\text{SRG}}^{(+/-)} = E_{4,\text{SRG}}^{(+)}$ and for negative-parity four-body channels $E_{2,\text{SRG}}^{(+/-)} = E_{3,\text{SRG}}^{(+/-)} = E_{4,\text{SRG}}^{(-)} = E_{4,\text{SRG}}^{(+)} + 1$.

This subtraction scheme ensures that there are no obvious contributions incorporated in the three-body SRG space that effectively do not contribute to the evolution in the four-body SRG space. But the two-body SRG space that is used for the subtraction to obtain the irreducible 3N parts still contains contributions that do not contribute to the evolution in the three- and four-body space. For instance, we consider a positive-parity four-body channel with even $E_{4,\text{SRG}}^{(+)}$. The negative-parity three-body channels are effectively evolved with an $E_{3,\text{SRG}}^{(-)} = E_{4,\text{SRG}}^{(+)} - 1$ truncation while the positive-parity two-body evolution used for the subtraction is performed for $E_{2,\text{SRG}}^{(+)} = E_{4,\text{SRG}}^{(+)}$ and not for $E_{2,\text{SRG}}^{(+)} = E_{4,\text{SRG}}^{(+)} - 2$. This means, there are obviously contributions in the two-body space, that do not appear in the three-body space. To account for these contributions as well we introduce the following scheme.

SubC: The SRG spaces are defined as for the SubB scheme with the exception of the two-body SRG spaces that are used for the subtraction to obtain the irreducible three-body parts of a channel, whose parity differs from the parity of the four-body channel. In this case the two-body SRG spaces with the same parity as the four-body channel are adjusted by reducing $E_{2,\text{SRG}}$ to the effective truncation used for three-body evolution, i.e., $E_{2,\text{SRG}}^{(+/-)} = E_{4,\text{SRG}} - 1$ or $E_{2,\text{SRG}}^{(+/-)} = E_{4,\text{SRG}} - 2$ for the two-body channels with a different or equal parity than the three-body channel, respectively.

To formulate a subtraction scheme fully consistent with the principle of not incorporating contributions for the subtraction that are not included for the actual evolution, there is still a non-trivial aspect missing. So far, we have considered all subtractions described in Fig. 4.1, besides the direct subtraction of the irreducible NN contributions in the four-body space. As already explained, we first convert the NN contributions to the three-body space and subsequently to the four-body space to perform the subtraction. Let us, for instance, again consider a positive-parity four-body channel using an even $E_{4,\text{SRG}}^{(+)}$. As evident from this procedure,

¹²The $E_{4,\text{SRG}}^{(-)}$ truncation is increased and not lowered by one for the negative-parity channels in order to have an equal number of contributing (E_{123}, E'_{123}) -blocks for positive and negative parities during the SRG evolution.

there are irreducible two-body parts with positive parity, evolved with $E_{2,\text{SRG}}^{(+)} = E_{4,\text{SRG}}^{(+)}$, that contribute to the four-body space via a negative-parity three-body channel. This three-body space on the other hand can only represent SRG spaces with an $E_{3,\text{SRG}}^{(-)} = E_{4,\text{SRG}}^{(+)} - 1$ and one can adjust the corresponding two-body SRG spaces to take care of this issue, which leads to the final subtraction scheme.

SubD: The SRG spaces are defined as for the SubC scheme, with the exception of the two-body SRG spaces used for the subtraction in the four-body space. The two-body SRG spaces are adjusted according to the parity of the three-body channel, which is used for the conversion to the four-body space. The adjustment is performed in the same manner as described in SubC for the intermediate three-body channels, that have a different parity than the targeted four-body channels. For instance we consider the two-body contributions used for the subtraction in a positive-parity four-body channel with even $E_{4,\text{SRG}}^{(+)}$. If the two-body parts contribute via a positive-parity three-body channel we use the same truncations as for SubC and SubB, i.e., $E_{2,\text{SRG}}^{(+)} = E_{4,\text{SRG}}^{(+)}$ and $E_{2,\text{SRG}}^{(-)} = E_{4,\text{SRG}}^{(+)}$ (note it is equivalent to use $E_{2,\text{SRG}}^{(-)} = E_{4,\text{SRG}}^{(+)} - 1$). If the two-parts contribute via a negative-parity three-body channel we use $E_{2,\text{SRG}}^{(+)} = E_{4,\text{SRG}}^{(+)} - 1$ and $E_{2,\text{SRG}}^{(-)} = E_{4,\text{SRG}}^{(+)} - 2$.

These four subtraction schemes exhibit a successively increased complexity and consistency with regard to the principle of not incorporating contributions for the subtraction that are not included in the actual evolution. We utilize these schemes to investigate the dependence of nuclear observables on the subtraction and, thus, test if the results are insensitive to the SRG-space truncation.

4.7.3 Frequency Conversion

Due to the large model-space dimensions in the four-body space, we are computationally limited to rather small E_{SRG} truncations compared to the two- and three-body space. To improve the convergence with respect to the SRG space, it is crucial to apply the frequency-conversion approach. The general idea has been discussed for the three-body case in Sec. 4.6.3 and we can proceed with the derivation of the frequency-conversion formula. Our goal are interaction matrix elements in the antisymmetric four-body Jacobi-HO representation $|E_{123}i_{123}J_{123}T_{123}\rangle_a$ defined with respect to the HO frequency $\hbar\Omega$, that is required in the many-body calculations. Therefore, we express these matrix elements by a superposition of interaction matrix elements in the Jacobi representation $|\tilde{E}_{123}\tilde{i}_{123}J_{123}T_{123}\rangle_a$ defined with respect to the HO frequency $\hbar\Omega_{\text{SRG}}$,

that is used for the SRG evolution

$$\begin{aligned}
 {}_a\langle E_{123}i_{123}J_{123}T_{123} | \mathbf{V}_\alpha | E'_{123}i'_{123}J_{123}T_{123} \rangle_a &= \sum_{\tilde{E}_{123}\tilde{E}'_{123}} \sum_{\tilde{i}_{123}\tilde{i}'_{123}}^{E_{4,\text{SRG}}} \\
 &\times {}_a\langle E_{123}i_{123}J_{123}T_{123} | \tilde{E}_{123}\tilde{i}_{123}J_{123}T_{123} \rangle_a {}_a\langle E'_{123}i'_{123}J_{123}T_{123} | \tilde{E}'_{123}\tilde{i}'_{123}J_{123}T_{123} \rangle_a \\
 &\times {}_a\langle \tilde{E}_{123}\tilde{i}_{123}J_{123}T_{123} | \mathbf{V}_\alpha | \tilde{E}'_{123}\tilde{i}'_{123}J_{123}T_{123} \rangle_a,
 \end{aligned} \tag{132}$$

As in the three-body case the interaction only connects bra and ket states with equal angular momentum and isospin, also for HO states defined with respect to different frequencies. The transformation formula is obtained by inserting unity operators in the Jacobi representation defined with respect to $\hbar\Omega_{\text{SRG}}$. The model space of the frequency conversion is limited by $E_{4,\text{SRG}}$ and corresponds to the SRG space. Eventually, we have to determine the overlaps of the Jacobi-HO states for the different HO frequencies. To derive the expression for the overlap we first use the relation (65), such that we have to calculate the overlap between the partial antisymmetric four-body state $|E_{12}i_{12}N_3; \alpha'_{123}\rangle_{a_{12}}$ for different HO frequencies. The decoupling of the angular momenta of this four-body state yields a product state of an antisymmetric three-body Jacobi state and a state that is defined with respect to the third Jacobi coordinate $|E_{12}i_{12}J_{12}\rangle_{a_{12}} \otimes |N_3(L_3\frac{1}{2})J_3\rangle$, where we have omitted the isospin part and the projection quantum numbers for brevity. Based on these states we apply an analogous procedure as in Sec. 4.6.3 for the three-body case, to derive the transformation formula for the overlap, yielding

$$\begin{aligned}
 {}_a\langle E_{123}i_{123}J_{123}T_{123} | \tilde{E}_{123}\tilde{i}_{123}J_{123}T_{123} \rangle_a &= \sum_{N_1N_2N_3} \sum_{\tilde{N}_1\tilde{N}_2\tilde{N}_3} \sum_{\alpha_{12}} \sum_{L_3J_3} \\
 &\times \delta_{E_{12}, 2N_1+L_1+2N_2+L_2} \int d\pi_1 \pi_1^2 R_{\tilde{N}_1L_1}^*(\pi_1) R_{\tilde{N}_1L_1}(\pi_1) \\
 &\times \delta_{\tilde{E}_{12}, 2\tilde{N}_1+L_1+2\tilde{N}_2+L_2} \int d\pi_2 \pi_2^2 R_{\tilde{N}_2L_2}^*(\pi_2) R_{\tilde{N}_2L_2}(\pi_2) \\
 &\times \delta_{E_{123}, E_{12}+2N_3+L_3} \delta_{\tilde{E}_{123}, \tilde{E}_{12}+2\tilde{N}_3+L_3} \int d\pi_3 \pi_3^2 R_{\tilde{N}_3L_3}^*(\pi_3) R_{\tilde{N}_3L_3}(\pi_3) \\
 &\times \sum_{i_{12}} C_{N_1N_2\alpha_{12}}^{i_{12}} \tilde{C}_{E_{12}N_3\alpha_{123}}^{i_{12}i_{123}} \sum_{\tilde{i}_{12}} C_{\tilde{N}_1\tilde{N}_2\alpha_{12}}^{\tilde{i}_{12}} \tilde{C}_{\tilde{E}_{12}\tilde{N}_3\alpha_{123}}^{\tilde{i}_{12}\tilde{i}_{123}},
 \end{aligned} \tag{133}$$

with the collective index $\alpha_{12} = \{L_1, S_1, J_1, L_2, J_2, J_{12}, T_1, T_{12}\}$ and $\alpha_{123} = \{J_{12}, L_3, J_3, J_{123}, T_{12}, T_{123}\}$. Formula (133) has a similar structure as for the corresponding overlap in the three-body case (131), but additionally involves components that are defined with respect to the third Jacobi coordinate. In particular the calculation of the overlap becomes more complex due to the additional sums over the indexes (i_{12}, \tilde{i}_{12}) and the appearance of the four-body CFPs that both originate from relation (65). The additional sums and quantities included in the four-body frequency-conversion formula as well as the sheer number of matrix elements that appear in the four-body model spaces are the reason that the frequency-conversion approach provides

a computational challenge. Careful pre-cachings and optimized loop evaluations, e.g., using BLAS routines, are mandatory to efficiently perform the frequency conversion in the four-body space.

5 Role of the SRG Model Space and Frequency Conversion

An important technical aspect of the SRG evolution concerns the model space used for the numerical evolution. In this section we introduce the model spaces used for the three-body SRG evolution and validate that the nuclear structure results are independent to the SRG-space truncation. Furthermore, we demonstrate the benefits of the frequency conversion. We start with the investigation with the SRG evolution used in nuclear structure calculations for p- and sd-shell nuclei (see Sec. 5.1). Further, we present results using the frequency conversion that is applied to improve the convergence with respect to the SRG space (see Sec. 5.2). Finally, we discuss the challenges in terms of the three-body SRG evolution that appear in applications to medium-mass and heavy nuclei.

The three-body SRG evolution is performed separately for the $(J_{12}^{\pi}T_{12})$ -channels in the antisymmetric Jacobi-HO representation (60) as described in Sec. 4.6. Generally, the model-space dimension increases rapidly with J_{12} , while contributions for large angular momenta are typically less important for the low-energy properties we are focusing on. Therefore, we use an angular-momentum dependent SRG-space truncation parameter $E_{3,\text{SRG}}(J_{12})$ that decreases with increasing J_{12} .

The SRG space for applications to p- and sd-shell nuclei is schematically illustrated in Fig. 5.1 by plotting the truncation parameter $E_{3,\text{SRG}}$ as function of the relative angular momentum J_{12} . For comparison we present this SRG space (blue solid line), which has been applied in several publications [20, 23–25, 29, 35, 36, 145], with the SRG space used by Jurgenson et al. (gray dashed line), e.g., in Refs. [158, 163, 165]. Our SRG space starts with an $E_{3,\text{SRG}} = 40$ for the lowest $J_{12} \leq \frac{5}{2}$ and ramps down linearly to $E_{3,\text{SRG}} = 24$ used for all $J_{12} \geq \frac{13}{2}$. We denote this model space as ramp \mathcal{A} in the following. This SRG space contains all possible $(J_{12}^{\pi}T_{12})$ -channels, with $J_{12} \leq \frac{51}{2}$ for an energy truncation of $E_{3,\text{SRG}} = 24$. Due to the large SRG-space dimensions for ramp \mathcal{A} we have developed an efficient implementation of the three-body SRG evolution. The model space for the $(J_{12}^{\pi}T_{12}) = (5/2^{+}1/2)$ -channel is the largest for the ramp \mathcal{A} truncation. For this particular channel one requires about 250 MB to store the interaction matrix elements in single precision utilizing the basic symmetries discussed in Sec. 3.2. Owing to the efficient implementation, we can evolve this channel in about six hours to a typical flow-parameter value $\alpha = 0.04 \text{ fm}^4$ on a standard computing node.

The SRG space used by Jurgenson et al. starts at $E_{3,\text{SRG}} = 40$ for $J_{12} = \frac{1}{2}$ as well, but directly ramps linearly down to $E_{3,\text{SRG}} = 20$, which is used for $J_{12} \geq \frac{21}{2}$. As is evident from Fig. 5.1 the SRG space applied in this work exceeds or agrees with the one used by Jurgenson et al. for

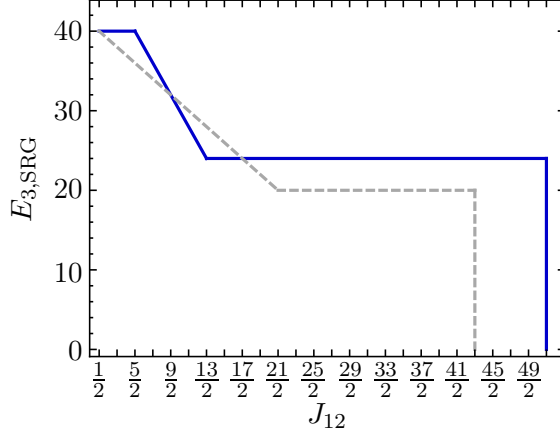


Figure 5.1 *Standard SRG space for p- and sd-shell nuclei*: Schematic representation of the $E_{3,\text{SRG}}$ truncation parameter as function of the relative angular momentum J_{12} that defines the standard SRG space used in this work for applications to p- and sd-shell nuclei (blue solid line). For comparison we plot the SRG space used by Jurgenson et. al (gray dashed line) [158, 163, 165].

all ($J_{12}^{\pi} T_{12}$)-channels except those from $J_{12} = \frac{11}{2}$ to $\frac{15}{2}$. For these particular channels they use a slightly larger $E_{3,\text{SRG}}$ than the ramp \mathcal{A} .

However, as we demonstrate in this section, our SRG space is sufficiently large and does not effect the energies for the p- and sd-shell nuclei investigated in this thesis. The results of these investigations are also summarized in Ref. [21]. Unfortunately, a similar validation for the SRG space used by Jurgenson et al. is not published, such that discrepancies observed for calculations with the two SRG spaces (see, e.g., [21] and [165]), need not necessarily originate from the truncations of the many-body approaches, but could be partially caused due to missing contributions in the SRG space of Ref. [165]. Therefore, we stress that a careful investigation of the truncations is crucial for reliable physical applications.

5.1 Sensitivity to the SRG Model Space

In the following we study the limitations of the standard three-body SRG space applied to nuclei up to the sd shell (denoted by ramp \mathcal{A}). For this purpose we introduce further SRG spaces that probe vital J_{12} sectors of the model space by variations of the $E_{3,\text{SRG}}(J_{12})$ truncation. The standard SRG space (blue solid line) as well as the additional SRG spaces are schematically illustrated in Fig. 5.2. The ramp \mathcal{B} (red dashed line) starts with $E_{3,\text{SRG}} = 40$ for $J_{12} \leq \frac{3}{2}$ and decreases linearly to $E_{3,\text{SRG}} = 24$ at $J_{12} = \frac{11}{2}$, wherefrom the truncation remains constant for the larger angular momenta. This SRG space is used to probe the sufficiency of the intermediate angular-momentum regime $\frac{5}{2} \leq J_{12} \leq \frac{11}{2}$, where it differs from ramp \mathcal{A} . Further, we introduce ramp \mathcal{C} (green dotted line) to probe the low angular-momentum regime, where we

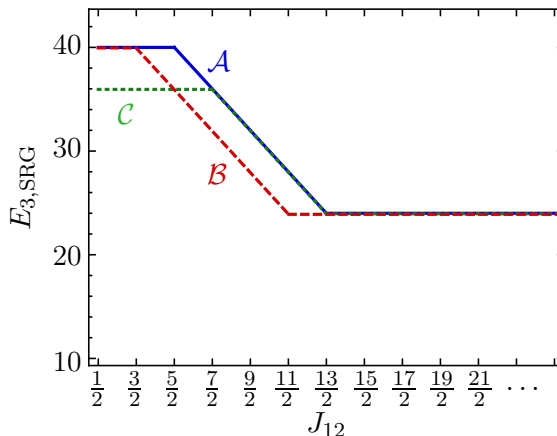


Figure 5.2 *SRG spaces for sensitivity analysis*: Illustrated is a schematic presentation of the $E_{3,\text{SRG}}$ truncation parameter as function of the relative angular momentum J_{12} , that defines the default SRG space used in this work for applications to p- and sd-shell nuclei, also called ramp \mathcal{A} (blue solid line), as well as ramp \mathcal{B} (red dashed line) and ramp \mathcal{C} (green dotted line) that are used for a sensitivity analysis.

use a truncation of $E_{3,\text{SRG}} = 36$ up to $J_{12} = \frac{7}{2}$. For the larger angular momenta this SRG space agrees with ramp \mathcal{A} .

To study the sensitivity to SRG-space truncation we perform IT-NCSM calculations with the $\text{NN}+3\text{N}_{\text{full}}$ Hamiltonian using the standard chiral $\text{NN}+3\text{N}$ interaction (see Sec. 1.3.3) SRG evolved in the different three-body model spaces illustrated in Fig. 5.2. We investigate the sensitivity of the nuclear many-body observables on the SRG-space truncation of ramp \mathcal{A} by comparing the results to those obtained with ramp \mathcal{B} and ramp \mathcal{C} . In Fig. 5.3 we show the ground-state energies of ${}^4\text{He}$ (left-hand panels) and ${}^{16}\text{O}$ (right-hand panels) using a HO frequency of $\hbar\Omega = 16$ MeV (upper panels) and 20 MeV (lower panels) as function of N_{max} . The three curves correspond to the results using the SRG spaces defined by ramp \mathcal{A} (blue circles), ramp \mathcal{B} (red diamonds) and ramp \mathcal{C} (green triangles).

For the larger frequency the ground-state energies of both nuclei agree for the different SRG spaces, indicating that for $\hbar\Omega = 20$ MeV the SRG spaces are sufficiently large to accurately describe these observables. In contrast, for $\hbar\Omega = 16$ MeV already the ${}^4\text{He}$ ground-state energy shows small deviations with ramp \mathcal{C} from the results with ramp \mathcal{A} and ramp \mathcal{B} . While the curves corresponding to ramp \mathcal{A} and ramp \mathcal{B} provide essentially the same result, ramp \mathcal{C} gives 0.4% less binding, indicating that the SRG space for $\hbar\Omega = 16$ MeV is not fully converged for the partial waves with low angular momenta. The dependence on the SRG-space truncation increases with particle number, such that for ${}^{16}\text{O}$ we observe a sizable discrepancy between the three curves of 1.5%.

A finite HO model space with a certain $E_{3,\text{SRG}}$ truncation incorporates a high momentum/energy

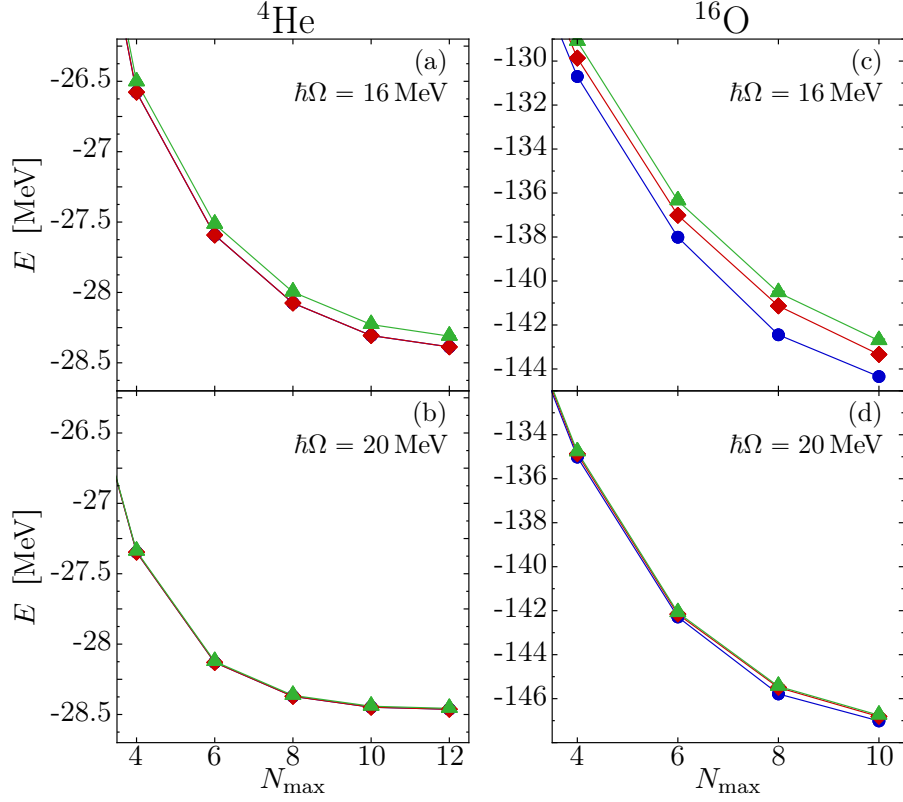


Figure 5.3 *Dependence of ground-state energies on the SRG space*: Plotted are the ground-state energies of ${}^4\text{He}$ (left-hand column) and ${}^{16}\text{O}$ (right-hand column) with the standard $\text{NN}+3\text{N}_{\text{full}}$ interaction obtained in IT-NCSM calculations as function of N_{max} , for $\hbar\Omega = 16$ MeV (upper row) and 20 MeV (lower row). The SRG evolutions are performed up to a flow parameter $\alpha = 0.08$ fm 4 using the SRG spaces defined by ramp \mathcal{A} (●), ramp \mathcal{B} (◆), and ramp \mathcal{C} (▲). The results are published in Ref. [21].

(so-called ultraviolet) truncation as well as a low momentum/energy (so-called infrared) truncation that both depended on the HO frequency. With decreasing HO frequency the ultraviolet truncation becomes significant while with decreasing HO frequency the infrared truncation becomes significant. From the results in Fig. 5.3 we can conclude that the ground-state energies, particularly for the heavier nuclei are predominantly affected by the ultraviolet truncation of the SRG space. Hence, the dependence on the SRG spaces increases with decreasing HO frequency, leading to spurious repulsion. The repulsive effect can be easily understood for an insufficient $E_{3,\text{SRG}}$ truncation used for a calculation of the triton binding energy, where the calculated energy corresponds to result of the bare Hamiltonian obtained in an $N_{\text{max}} = E_{3,\text{SRG}}$ model space. Due to the variational principle the missing contributions in SRG space increase the binding. For the heavier nuclei the spurious repulsion cannot be rigorously explained by such simple arguments, since the variational principle holds only for the truncations of the A -body space, but not for truncations of the three-body space (with $A > 3$). It is an interesting observation that the SRG space dependence has the naively-expected repulsive effect.

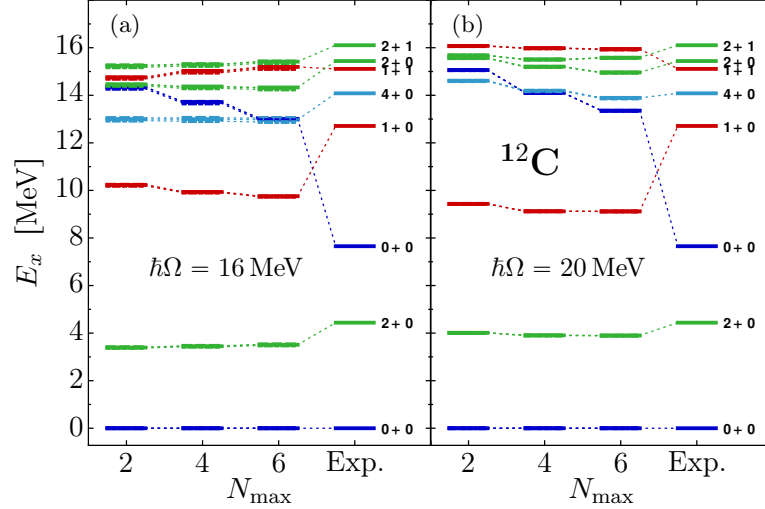


Figure 5.4 *Dependence of excitation energies on the SRG space*: Plotted is the excitation spectrum of ^{12}C with the standard $\text{NN}+3\text{N}_{\text{full}}$ interaction obtained with the IT-NCSM as function of N_{max} , for $\hbar\Omega = 16$ MeV (left-hand panel) and 20 MeV (right-hand panel). The SRG evolution are performed for $\alpha = 0.08 \text{ fm}^4$ using the SRG spaces defined by ramp \mathcal{A} (solid bars), ramp \mathcal{B} (dashed bars), and ramp \mathcal{C} (dotted bars). Note the excitation energies are almost on top of each other. The results are published in Ref. [21].

We can also investigate the sensitivity to the SRG space truncation in context of excitation energies as illustrated in Fig. 5.4, where the excitation spectrum of ^{12}C using $\hbar\Omega = 16$ (a) and 20 MeV (b) as function of N_{max} is shown. The excitation energies for the SRG spaces defined by ramp \mathcal{A} (solid bars), ramp \mathcal{B} (dashed bars), and ramp \mathcal{C} (dotted bars) are essentially on top of each other for both frequencies. This reveals, that the missing contributions of the SRG space for the lower frequency causes a similar repulsive effect for the ground state as well as for the excited states, such that the excitation energies are almost insensitive to the SRG space truncation.

In order to apply interactions SRG evolved in appropriately large SRG spaces to nuclear structure calculations, in particular, for lower HO frequencies that are required, e.g., investigate long-range properties of a nucleus, one could simply try to increase the SRG space. However, this would cause a tremendous increase of the computational efforts and becomes unfeasible for very low frequencies. Therefore, we apply the more sophisticated frequency conversion discussed in the next section.

5.2 The Frequency-Conversion Approach

The formal concept of the frequency-conversion approach in the three-body space is discussed in Sec. 4.6.3. In the following we illustrate the benefits of this approach revisiting the ^4He and

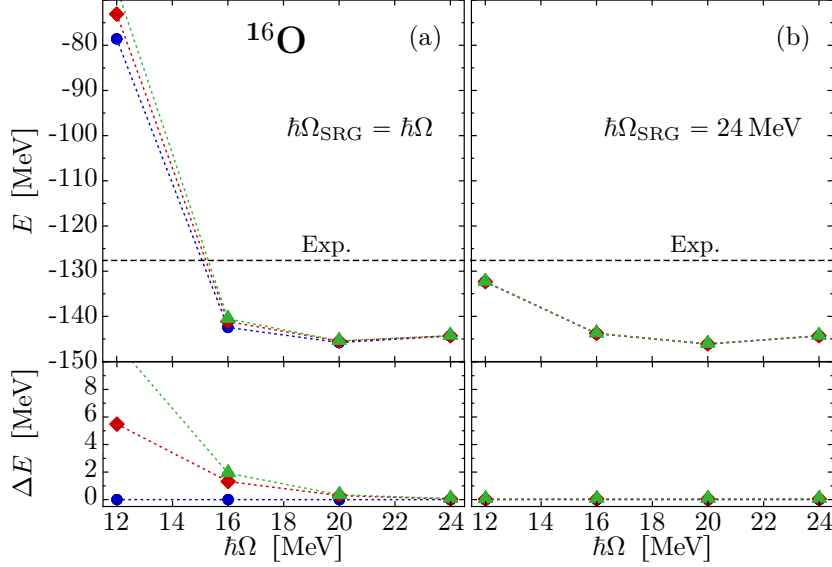


Figure 5.5 *Frequency conversion for ^{16}O ground-state energy*: Plotted is the ground-state energy of ^{16}O with the standard $\text{NN}+3\text{N}_{\text{full}}$ interaction as function of HO frequency $\hbar\Omega$ used in the IT-NCSM calculations for $N_{\text{max}} = 8$. We compare the standard SRG evolution, where the HO frequency $\hbar\Omega_{\text{SRG}}$ corresponds to the frequency $\hbar\Omega$ (left-hand column) with an SRG evolution at fixed $\hbar\Omega_{\text{SRG}} = 24$ MeV utilizing a subsequent frequency conversion of the interaction matrix elements to $\hbar\Omega$ (right-hand column). The SRG evolutions are performed with $\alpha = 0.08 \text{ fm}^4$ using to the SRG spaces defined by ramp \mathcal{A} (●), ramp \mathcal{B} (◆), and ramp \mathcal{C} (▲). The dashed line indicates the experimental value. The results are published in Ref. [21].

^{16}O ground-state energies. The results are plotted in Fig. 5.5 where we perform the IT-NCSM calculations for $N_{\text{max}} = 8$ and $\alpha = 0.08 \text{ fm}^4$, and a sequence of HO frequencies ranging from $\hbar\Omega = 24$ MeV down to 12 MeV. The results shown in the left-hand panels are obtained using the same HO frequency in the SRG evolution $\hbar\Omega_{\text{SRG}} = \hbar\Omega$ as for the many-body calculations. For the right-hand panels we use a fixed $\hbar\Omega_{\text{SRG}} = 24$ MeV for the three-body SRG evolution and subsequently convert the HO frequency to the $\hbar\Omega$ used for the many-body calculations. Note, that we apply the same model space for the frequency conversion as for the SRG evolution. The upper panels show the ground-state energies obtained for the SRG spaces defined by ramp \mathcal{A} (blue circles), ramp \mathcal{B} (red diamonds), and ramp \mathcal{C} (green triangles). To facilitate analysis the lower panels show the deviation of the ground-state energies from the ones obtained with the standard ramp \mathcal{A} .

The advantage of the frequency-conversion approach is obvious. Whereas the ground-state energies strongly deviate with decreasing frequency without using the frequency conversion the results with frequency conversion show no sensitivity to the SRG space truncation. This confirms that the model space used for the SRG evolution as well as for the frequency conversion are sufficiently large, such that the energies are not affected by the model space truncation.

The SRG evolution using $\hbar\Omega_{\text{SRG}} = \hbar\Omega$ leads to a substantial underbinding of the ground-state compared to the accurate result using the frequency-conversion approach. The relative deviations in the lower left-hand panel indicate that especially the insufficiency of the SRG space at the lowest angular momenta causes a sizable repulsion.

In summary, the frequency conversion is indispensable for nuclear structure calculations in the p shell using HO frequencies below $\hbar\Omega = 16$ MeV. Such low frequencies are relevant in the NCSM, e.g., to obtain convergence for observables that depend on long-range properties of the nucleus. Owing to the frequency conversion the prior disadvantage of the HO representation, i.e., the dependence of the model space on the HO frequency is turned into a practical tool to adapt the ultraviolet and infrared truncations to the requirements of the application. Besides the advantages that have been discussed above, the frequency conversion yields also a considerable gain in the computational efficiency. Without the frequency conversion the SRG evolution needs to be performed for each frequency used for the many-body investigations, while now one needs to evolve the Hamiltonian only for a single adequate frequency and can subsequently convert the matrix elements to the desired frequencies. The conversion is very robust with respect to the model space as illustrated in Fig. 5.5 (b) and due to the simple transformation discussed in Sec. 4.6.3 its computational demands are only a fraction of those for the SRG evolution.

5.3 SRG Space for Medium-Mass and Heavy Nuclei

The standard SRG space, denoted by $\text{ramp } \mathcal{A}$, is constructed to reliably SRG evolve interactions for nuclear calculations in the p shell and one needs to study if observables are still insensitive to this SRG-space truncation when increasing the mass number. In this section we focus on the three-body SRG evolution for medium-mass and heavy nuclei, which pose unforeseen challenges and requirements for a reliable evolution.

In our applications in the medium-mass regime [29, 35], using the coupled-cluster approach, we have observed that at low frequencies the sensitivity of ground-state energies to the SRG-space truncation increases with the mass number, such that in the $A \sim 50$ mass regime the adequate frequency range for the evolution is restricted to rather large HO frequencies. This behavior is illustrated in Fig. 5.6, where we present the ground-state energies per nucleon, obtained with the coupled-cluster method with single and doubles excitations (CCSD) for the closed-shell nuclei ^{40}Ca (a), ^{48}Ca (b), ^{56}Ni (c), and ^{68}Ni (d), using the $\text{NN}+3\text{N}_{\text{ind}}$ (red diamonds), and $\text{NN}+3\text{N}_{\text{full}}$ (green triangles) Hamiltonian. We compare the results obtained with the conventional SRG evolution without the frequency conversion, i.e., $\hbar\Omega_{\text{SRG}} = \hbar\Omega$ (open symbols) to those obtained by using $\hbar\Omega_{\text{SRG}} = 36$ MeV for the SRG evolution and a subsequent conversion to the frequency $\hbar\Omega$. The SRG evolution is performed up to $\alpha = 0.04 \text{ fm}^4$ using the model space defined by $\text{ramp } \mathcal{A}$. As initial interaction we use the standard NN and 3N interaction with a reduced three-body cutoff of $\Lambda_{3\text{N}} = 400 \text{ MeV}/c$ (see Sec. 1.3.3) in order to circumvent sizable induced

four-body contributions (see Sec. 6.2). All CCSD calculations are performed for a many-body model space truncated by the maximum single-particle energy quantum number $e_{\max} = 12$. The 3N contributions are included explicitly up to $E_{3,\max} = 14$.

Without the frequency conversion we observe a slight dependence on the SRG-space truncation at $\hbar\Omega = 24$ MeV for the ^{40}Ca ground-state energy, indicated by the deviation from the frequency-converted results. This dependence amplifies with increasing particle number, such that a description of the ^{68}Ni ground-state energy requires $\hbar\Omega_{\text{SRG}} \geq 32$ MeV. Interestingly, we observe the equivalent repulsive effect at small frequencies $\hbar\Omega_{\text{SRG}}$ using the $\text{NN}+3\text{N}_{\text{ind}}$ or $\text{NN}+3\text{N}_{\text{full}}$ Hamiltonians. This signifies that the sensitivity to the SRG space does originate from the three-body contributions that are induced by the initial NN interaction and not from the initial 3N interaction.

In conclusion, already for an application of the chiral NN interaction, we have to increase the HO frequency further with increasing particle number, in order to use appropriate ultraviolet truncations. This procedure cannot be applied to arbitrarily heavy systems using a certain $E_{3,\text{SRG}}$ truncation, because at too large frequencies the infrared truncation starts to affect the nuclear observables. In addition, the required model space for a reliable frequency conversion increases with the deviation of the initial frequency from the final one. Thus, we restrict the application range of the ramp \mathcal{A} SRG space to nuclei in the p and sd shell and define a new standard SRG space for heavier nuclei.

In Fig. 5.7 we illustrate the relevant SRG spaces applied in this section in order to verify the reliability of the evolution for heavy nuclear systems. Panel (a) compares the standard SRG space (ramp \mathcal{A}) of the previous section for lighter systems (thin blue line) to the new standard used for heavy nuclei (thick red line). The latter SRG space, denoted by ramp \mathcal{D} , is substantially larger compared to ramp \mathcal{A} , particularly for large angular momenta.

This extension can be motivated by the naive single-particle shell-model picture [166]. For heavy nuclei already the unperturbed HO Slater determinant occupies orbits with large single-particle angular momenta and there are several 3N configurations with large coupled angular momenta that contribute to the energy of this A -body state. Hence, the three-body channels with large angular momenta are expected to contribute considerably to ground-state energies of heavy nuclei and it is crucial to transform these channels as precise as those with low angular momenta.

For this purpose we employ a new SRG space denoted by ramp \mathcal{D} for the heavy nuclei using an $E_{3,\text{SRG}}$ truncation of 40 for $J_{12} \leq \frac{7}{2}$ and linear ramp down to $E_{3,\text{SRG}} = 36$, which is used for all $J_{12} \geq \frac{11}{2}$ (thick red line in Fig. 5.7). To confirm that this extended SRG space is appropriate over the complete angular-momentum domain we use ramp \mathcal{E} (orange dotted line) and ramp \mathcal{F} (dashed blue line) to resolve, in particular, the sensitivity to low angular momenta. Both SRG spaces are illustrated in Fig. 5.7 (b). Panel (c) shows the SRG spaces used to probe

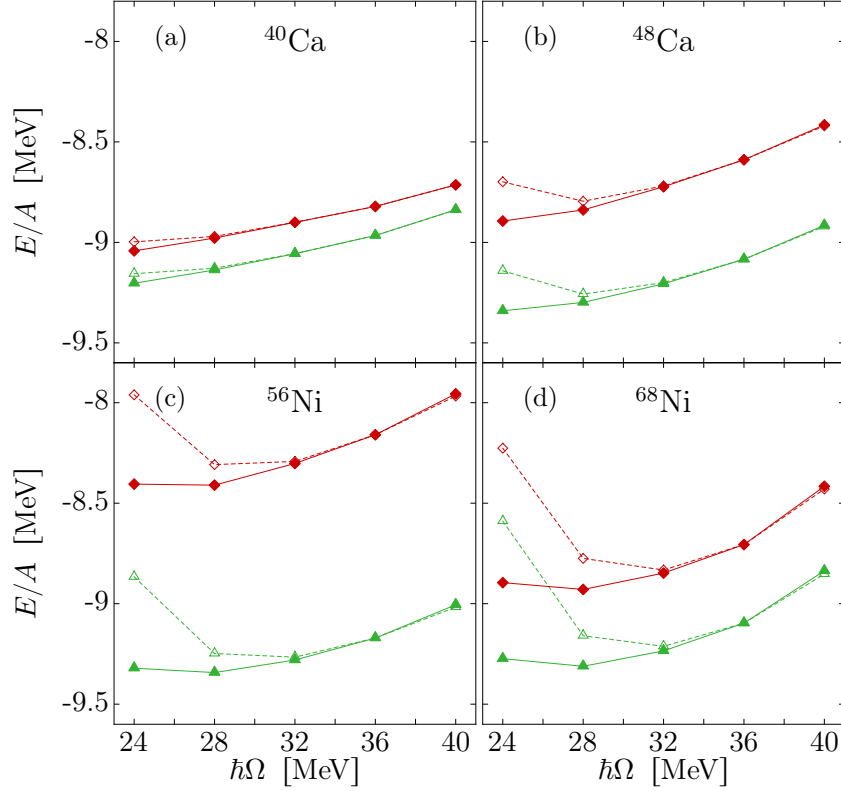


Figure 5.6 *Frequency conversion for medium-mass nuclei*: Plotted are the ground-state energies per nucleon of ^{40}Ca (a), ^{48}Ca (b), ^{56}Ni (c), and ^{68}Ni (d) with the $\text{NN}+3\text{N}_{\text{ind}}$ (\blacklozenge/\diamond) and $\text{NN}+3\text{N}_{\text{full}}$ (\blacktriangle/\triangle) interaction as function of the HO frequency $\hbar\Omega$ used in the CCSD calculations. We use the standard initial NN and 3N interaction with a reduced three-body cutoff of $\Lambda_{3\text{N}} = 400 \text{ MeV}/c$. Compared are the results for the conventional SRG evolution, where $\hbar\Omega_{\text{SRG}}$ corresponds to $\hbar\Omega$ (open symbols), with the results for an SRG evolution at fixed $\hbar\Omega_{\text{SRG}} = 36 \text{ MeV}$ utilizing a subsequent frequency conversion of the interaction matrix elements to $\hbar\Omega$ (solid symbols). The SRG evolutions are performed in the SRG space denoted by $\text{ramp } \mathcal{A}$ for $\alpha = 0.04 \text{ fm}^4$. The 3N contributions with $E_{3,\text{max}} = 14$ are included explicitly in all CCSD calculations using a model space defined by $e_{\text{max}} = 12$. The results are published in Ref. [30].

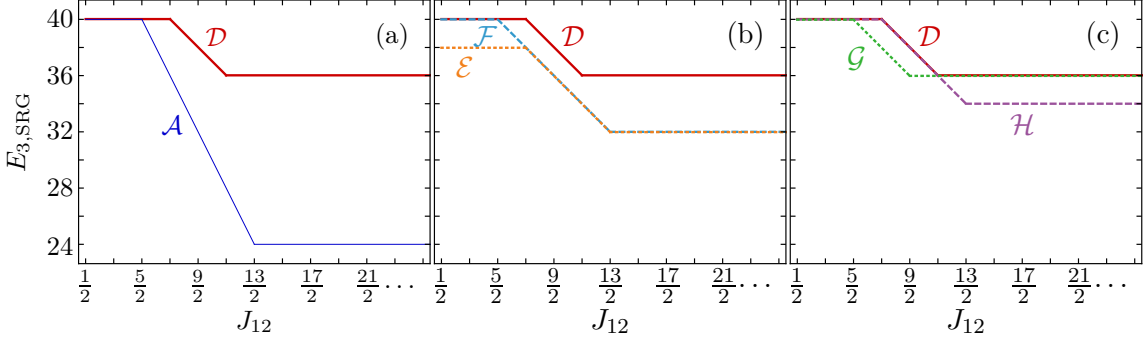


Figure 5.7 *SRG spaces for sensitivity analysis in the heavy nuclei regime*: Illustrated is a schematic representation of the $E_{3,\text{SRG}}$ truncation parameter as function of the relative angular momentum J_{12} . The standard SRG space for the heavy nuclei, denoted by ramp \mathcal{D} (thick solid red line) is compared with the default SRG space for p- and sd-shell nuclei, also called ramp \mathcal{A} (thin blue line) in panel (a), with ramp \mathcal{E} (orange dotted line) and ramp \mathcal{F} (dashed light blue line) in panel (b), as well as ramp \mathcal{G} (green dotted line) and ramp \mathcal{H} (violet dashed line) in panel (c).

the intermediate angular-momentum domain, denoted by ramp \mathcal{G} (green dotted line), as well as the large angular-momentum domain using ramp \mathcal{H} (violet dotted line).

We study the sensitivity to the SRG spaces, illustrated in Fig. 5.7, by means of CCSD calculations for the ground-state energy of several closed-shell nuclei in Fig. 5.8 for the same initial NN and NN+3N interactions as above. The interactions are SRG evolved up to $\alpha = 0.08 \text{ fm}^4$ for a frequency $\hbar\Omega_{\text{SRG}} = 36 \text{ MeV}$ using a subsequent frequency conversion to $\hbar\Omega = 24 \text{ MeV}$, which is an appropriate frequency for the CCSD calculations in this mass regime. Further, we use a many-body model space defined by $e_{\text{max}} = 12$ and explicitly include the 3N contributions up to $E_{3,\text{max}} = 14$.

Figure 5.8 (a) shows the corresponding ground-state energies per nucleon using the SRG spaces denoted by ramp \mathcal{A} (blue circles) and ramp \mathcal{D} (red diamonds). The black bars denote the data taken from Ref. [164]. Further, we show the deviations from the ramp \mathcal{D} results when using the SRG spaces denoted by ramp \mathcal{E} (orange stars) and ramp \mathcal{F} (light-blue triangles) in Fig. 5.8 (b), as well as ramp \mathcal{G} (green crosses) and ramp \mathcal{H} (violet squares) in Fig. 5.8 (c). Besides the NN+3N_{full} Hamiltonian (solid symbols) we additionally show results for the NN+3N_{ind} Hamiltonian (open symbols) in panel (c).

The comparison in panel (a) is striking: Even for the large frequency $\hbar\Omega_{\text{SRG}}$ the standard SRG-space truncation used in the p and sd shell (ramp \mathcal{A}) affects ^{56}Ni leading to an artificial repulsion that rapidly increases with the particle number. Compared to the ground-state energies obtained with ramp \mathcal{D} we observe a repulsion of about 6 MeV per nucleon in the tin isotopes when using ramp \mathcal{A} . We stress that the results illustrated in Fig. 5.8 serve for sensitivity analysis with respect to the SRG space, rather than for a quantitative comparisons to the experiment. Since there are several truncations concerning the many-body method, as well as

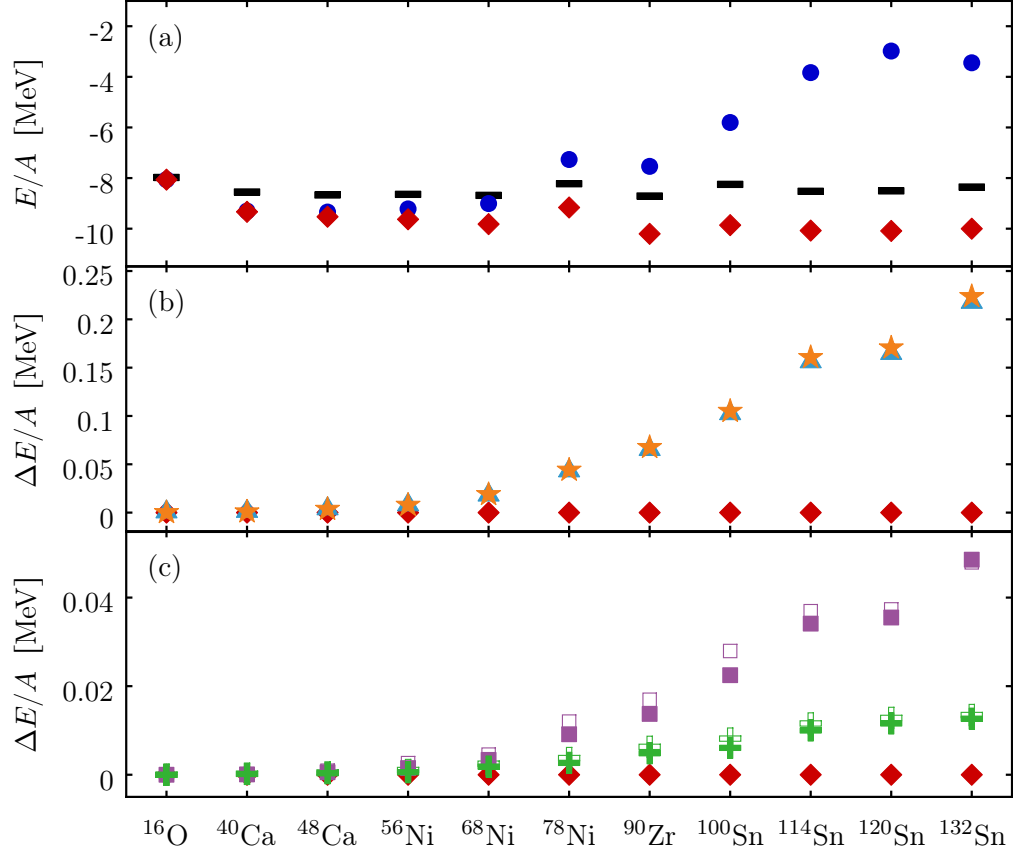


Figure 5.8 *SRG space dependence for heavy nuclei*: Panel (a) compares the ground-state energies per nucleon for several closed-shell nuclei from ^{16}O to ^{132}Sn using an SRG space denoted by ramp \mathcal{A} (●) and ramp \mathcal{D} (◆). The black bars denote the data taken from Ref. [164]. Panels (b) and (c) show the deviation of the ground-state energy per nucleon using ramp \mathcal{E} (★) and ramp \mathcal{F} (▲) as well as ramp \mathcal{G} (⊕) and ramp \mathcal{H} (■), respectively, from the results obtained with the largest SRG space, i.e., ramp \mathcal{D} . All calculations are performed with CCSD for the $\text{NN}+3\text{N}_{\text{ind}}$ (open symbols) and the $\text{NN}+3\text{N}_{\text{full}}$ Hamiltonian (solid symbols) using $\hbar\Omega_{\text{SRG}} = 36$ MeV, $\hbar\Omega = 24$ MeV and $\alpha = 0.08$ fm 4 . Further parameters as in Fig. 5.6. The results are published in Ref. [30].

the treatment of the interaction that need to be addressed first (see Sec. 7). A comprehensive investigation of the various truncations is published in Ref. [30].

As evident from Fig. 5.8 (b) the ground-state energies obtained for ramp \mathcal{E} and ramp \mathcal{F} , which both allow for considerably larger spaces in the large angular-momentum domain compared to ramp \mathcal{A} , show a strongly reduced but still noticeable deviation from the results with ramp \mathcal{D} . This difference increases from less than 8 keV for ^{56}Ni to more than 200 keV per nucleon for ^{132}Sn . However, more important is the deviation of the results from ramp \mathcal{E} to those from ramp \mathcal{F} , which is less than 10 keV per nucleon for all considered nuclei. This confirms the adequate size of the SRG spaces for the low angular-momentum domain, where ramp \mathcal{E} and ramp \mathcal{F} differ from each other. Eventually, we have to validate the medium and large angular-momentum domains of our standard SRG space for the heavy nuclei, which are probed in Fig. 5.8 (c). The discrepancies are below 50 keV per nucleon even for the heaviest nuclei and demonstrate the reliability of ramp \mathcal{D} .

As discussed above the inclusion of the initial 3N interaction has only a minor effect on the discrepancies identifying the induced 3N contributions of the initial NN interaction to be responsible for the high demands on the SRG space. Although the deviation we observe by probing the different domains of the SRG space are well below 1%, these deviations increase rapidly with the mass number, particularly due to large angular-momentum contributions, such that an application of an initial NN interaction beyond ^{132}Sn might require further extensions or novel developments regarding the SRG space. Note that we have explicitly probed the sensitivity of the energies to the frequency-conversion model space by reducing it for a fixed SRG space, observing a negligible sensitivity of the ground-state energies to frequency-conversion model space. Thus, the dependencies on the model-space truncation can be exclusively attributed to missing contributions during the SRG evolution.

For the applications in medium-mass and heavy nuclei the frequency conversion is an indispensable tool to reduce the computational demands that come along with the SRG evolution in the large model spaces and efficiently allows for an investigation of the HO frequency dependence in the many-body calculations.

6 SRG-Induced Many-Nucleon Contributions

In this section we discuss the treatment of many-body contributions that are induced during the SRG evolution. For this purpose we apply the standard NN and NN+3N interactions of Sec. 1.3.3 in nuclear structure calculations for p-shell nuclei using the IT-NCSM. In particular, we concentrate on the effect of the induced beyond-3N contributions. We study the appearance and origin of the induced many-nucleon contributions and present approaches to circumvent or suppress these contributions in Sec. 6.1- 6.3. Finally, we apply the four-body techniques that are discussed in this work to include these contributions explicitly to nuclear structure calculations in Sec. 6.4. We carefully investigate the truncations and limitations that accompany the large four-body model-space dimensions and present the first ab initio nuclear structure results for p-shell nuclei including 4N forces explicitly.

6.1 Ground-State and Excitation Energies up to the p Shell

We continue the discussion of SRG-induced contributions for the ${}^4\text{He}$ of Sec. 4.7.1, using the state-of-the-art interaction treatment discussed in the previous sections that enables us to employ the 3N interaction matrix elements in IT-NCSM calculations up to $N_{\text{max}} = 12$ for the heaviest p-shell nuclei.

In Fig. 6.1 we show the ground-state energies per nucleon of ${}^4\text{He}$ (upper panels), ${}^6\text{Li}$ (middle panels), and ${}^{16}\text{O}$ (lower panels) obtained with the NN_{only} , $\text{NN}+3\text{N}_{\text{ind}}$, and $\text{NN}+3\text{N}_{\text{full}}$ Hamiltonian (left to right) plotted as function of N_{max} . The SRG evolutions and IT-NCSM calculations are performed at $\hbar\Omega = 20$ MeV, which is close to the energy minimum in this mass regime [21]. The curves correspond to flow parameters between $\alpha = 0.04$ and 0.16 fm^4 . For all panels we clearly identify the major benefit of the SRG evolution. With increasing flow parameter the convergence of the many-body calculations with respect to the model space is accelerated. This is indispensable for reliable extrapolations of the energies to infinite many-body model spaces. Moreover, the regime of $N_{\text{max}} > 8$, which becomes applicable due to the use of the efficient three-body interaction-matrix treatment and the importance-truncation technique, is crucial to accurately extrapolate the ground-state energies (solid lines). The extrapolations use the $N_{\text{max}} = 6 - 12$ results to fit an exponential function (see [21] for a detailed discussion of different fit procedures).

The converged ${}^4\text{He}$ ground-state energies for the NN_{only} Hamiltonian in Fig. 6.1(a) show a strong dependence on the flow-parameter α , which indicates that the induced three- and many-

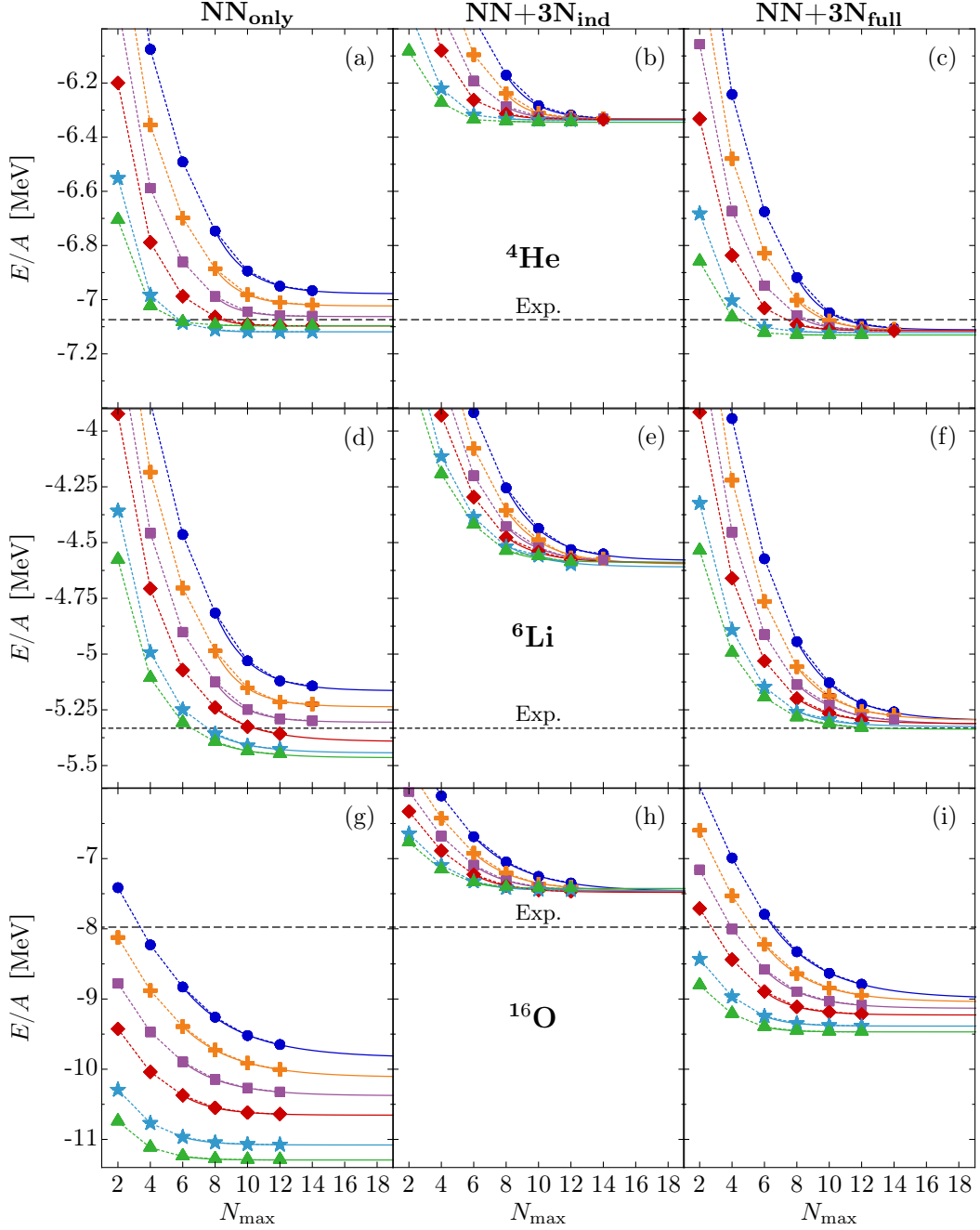


Figure 6.1 *Flow-parameter dependence of ground-state energies*: We show the ground-state energies of ${}^4\text{He}$ (upper row), ${}^6\text{Li}$ (middle row), and ${}^{16}\text{O}$ (lower row) obtained with the IT-NCSM as function of N_{max} , using the NN_{only} (left column), $\text{NN}+3\text{N}_{\text{ind}}$ (middle column), and $\text{NN}+3\text{N}_{\text{full}}$ (right column) Hamiltonian. We start with the standard initial NN and $\text{NN}+3\text{N}$ interactions and evolve them in the SRG space denoted by $\text{ramp}\mathcal{A}$ (see Fig. 5.2) up to $\alpha = 0.04 \text{ fm}^4$ (\bullet), 0.05 fm^4 ($+$), 0.0625 fm^4 (\blacksquare), 0.08 fm^4 (\blacklozenge), 0.12 fm^4 (\star), and 0.16 fm^4 (\blacktriangle) with $\hbar\Omega = \hbar\Omega_{\text{SRG}} = 20 \text{ MeV}$. The dashed horizontal lines indicate the experimental value [164]. The results are published in Ref. [20].

nucleon forces, which are omitted during the SRG evolution contribute significantly to the ground-state energy. The explicit inclusion of the induced 3N forces using the $\text{NN}+3\text{N}_{\text{ind}}$ Hamiltonian in Fig. 6.1 (b) leads to flow-parameter independent energies indicating that all relevant many-nucleon contributions are included. This means that the induced beyond-3N forces originating from the initial NN interaction have a negligible effect. A detailed discussion of the flow-parameter dependence for ${}^4\text{He}$ illustrated in Sec. 4.7.1 confirming that the energies of the $\text{NN}+3\text{N}_{\text{ind}}$ Hamiltonian indeed correspond to the ones of the bare Hamiltonian. The discrepancy between the $\alpha = 0.04 \text{ fm}^4$ and 0.16 fm^4 energies for the NN_{only} Hamiltonian of less than 120 keV per nucleon is rather small compared to the discrepancy of the more than 640 keV per nucleon between the $\alpha = 0.04 \text{ fm}^4$ and the bare energy. This reveals that an extrapolation from a sizable flow-parameter dependence to the bare energy is uncontrolled and we require flow-parameter independent energies for reliable predictions. In principle, sizable many-nucleon forces could be induced at the very beginning of the SRG evolution and affect the observable by a constant shift for the examined flow-parameter range. However, the investigations in Sec. 4.7.1 provide indications that sizable effects of the omitted induced contributions should be noticeable by a flow-parameter dependence in the α regime we use in practice.

The inclusion of the initial chiral 3N interactions at N^2LO shown in Fig. 6.1 (c) significantly improves the description of the experimental ${}^4\text{He}$ ground-state energy and retains the α independence. The attractive effect of the initial 3N interaction of about 780 keV per nucleon is of the same order as the repulsion from the induced 3N forces. A similar pattern as for ${}^4\text{He}$ can be observed for the ground-state energy of ${}^6\text{Li}$, such that the $\text{NN}+3\text{N}_{\text{ind}}$ Hamiltonian presented in Fig. 6.1 (e) underbinds the experimental value by more than 750 keV per nucleon, while the initial 3N interaction provides the missing attraction to significantly improve the experimental agreement illustrated in Fig. 6.1 (f). When increasing the mass number from the light to the heavy edge of the p shell, i.e., when going to ${}^{16}\text{O}$, a sizable flow-parameter dependence appears for the $\text{NN}+3\text{N}_{\text{full}}$ Hamiltonian in Fig. 6.1 (i), while for the $\text{NN}+3\text{N}_{\text{ind}}$ Hamiltonian in Fig. 6.1 (h) the ground-state energy remains flow-parameter independent. This leads to the conclusion that the induced beyond-3N contributions originating from the initial NN interaction are still negligible, while the beyond-3N contributions of the initial 3N interaction become strongly repulsive and should not be omitted. The $\text{NN}+3\text{N}_{\text{ind}}$ Hamiltonian underbinds the ${}^{16}\text{O}$ ground state by more than 0.5 MeV per nucleon, while the $\text{NN}+3\text{N}_{\text{full}}$ Hamiltonian overbinds the experimental ground-state energy, by 1 – 1.5 MeV per nucleon for the considered flow-parameter range. In contrast to ${}^4\text{He}$ and ${}^6\text{Li}$, where the NN_{only} Hamiltonian at $\alpha = 0.0625 \text{ fm}^4$ provides similar results as the $\text{NN}+3\text{N}_{\text{full}}$ Hamiltonian, this is not the case for ${}^{16}\text{O}$, emphasizing structural differences between the induced and initial 3N contributions. Thus, fitting the flow parameter for the NN_{only} Hamiltonian in order to account for missing initial 3N interactions, obviously does not work for different mass regions. We stress that because of the strong flow-parameter dependence with included initial 3N interactions one can not make reliable conclusion

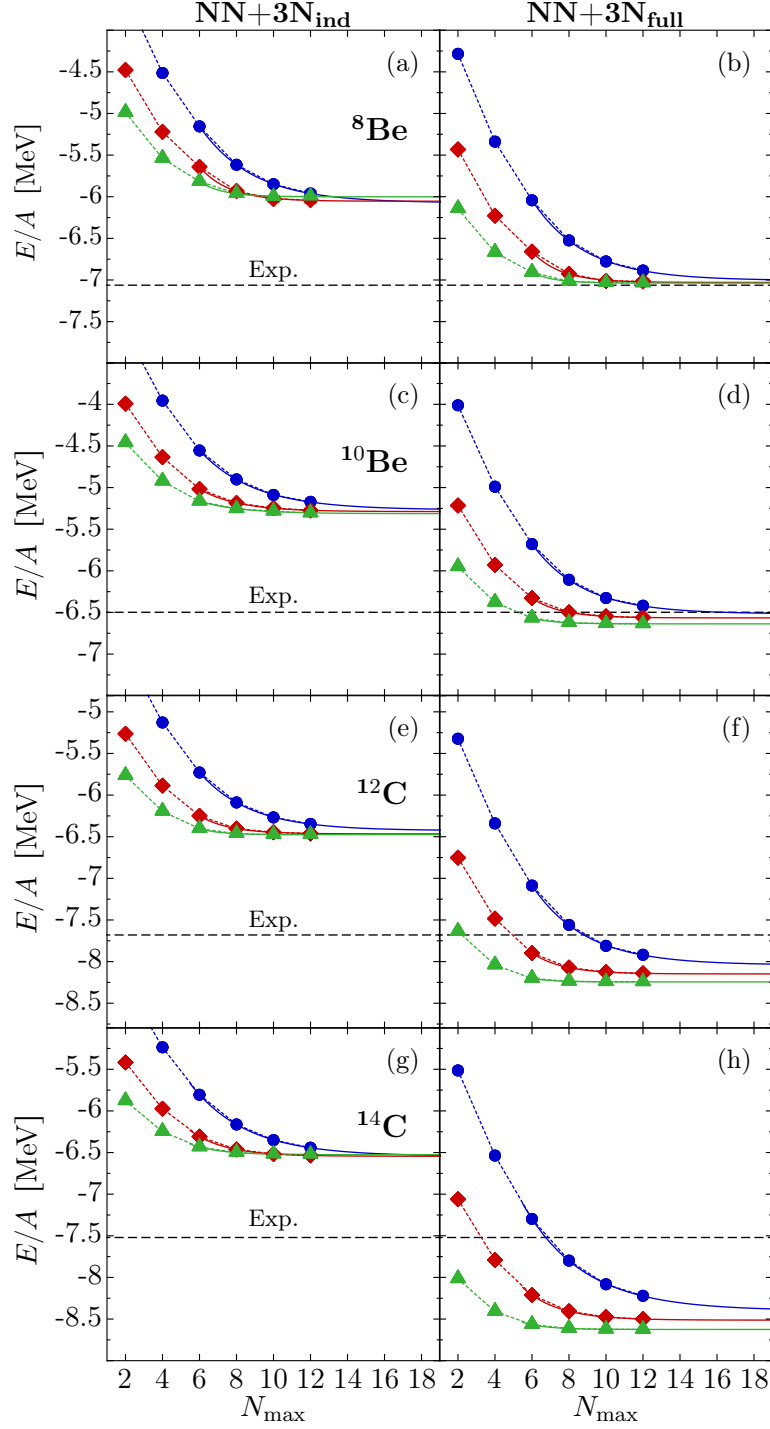


Figure 6.2 *Flow-parameter dependence of ground-state energies in the p shell*: We show the ground-state energies of ${}^8\text{Be}$, ${}^{10}\text{Be}$, ${}^{12}\text{C}$, and ${}^{14}\text{C}$ (top to bottom) obtained with the IT-NCSM as function of N_{max} , using the $\text{NN}+3\text{N}_{\text{ind}}$ (left column), and $\text{NN}+3\text{N}_{\text{full}}$ (right column) Hamiltonian for $\alpha = 0.04 \text{ fm}^4$ (\bullet), 0.08 fm^4 (\blacklozenge), and 0.16 fm^4 (\blacktriangle). Further parameters are chosen as in Fig. 6.1. The experimental data (dashed horizontal line) is taken from Ref. [164]. The results are published in Ref. [21].

on the ground-state energy for the bare Hamiltonian. Thus we cannot exclude that the bare NN+3N Hamiltonian describes the experimental energy appropriately as in the lighter systems. The induced many-body contributions provide a clear limitation to the application range of SRG-evolved chiral NN+3N interactions.

In Fig. 6.2 we show a systematic comparison of the NN+3N_{ind} and NN+3N_{full} ground-state energies per nucleon for selected even-even nuclei in the p shell: ⁸Be, ¹⁰Be, ¹²C, and ¹⁴C (from top to bottom). The calculations are performed for the same parameters as in Fig. 6.1 using a reduced number of flow-parameter values that span the same range from $\alpha = 0.04$ to 0.16 fm^4 . As before the flow-parameter independent energy obtained by using an initial NN interaction and including the induced 3N contributions underbinds the ground state by about 1 MeV per nucleon. In the lighter nuclei ⁸Be and ¹⁰Be the inclusion of the initial 3N interaction leads to a good agreement with the experimental value, while the dependence on the flow-parameter successively increases with mass such that ¹²C and ¹⁴C are systematically overbound, which might again be attributed to the missing repulsive beyond-3N contributions.

The induced beyond-3N contributions originating from the 3N force have a sizable impact on absolute ground-state energies for nuclei beyond the mid-p shell, but as demonstrated in Fig. 6.3 they have a minor influence on excitation energies. This figure shows the excitation spectrum for the lowest positive-parity eigenstates of ¹²C as function of N_{max} (a comprehensive spectroscopic investigation of this nucleus including negative-parity states with the NCSM and IT-NCSM is published in Ref. [22]). For the SRG evolution we use the model space defined by ramp \mathcal{A} (see Fig. 5.1) with $\alpha = 0.04 \text{ fm}^4$ (dashed bars) and 0.08 fm^4 (solid bars). The IT-NCSM calculations are performed at $\hbar\Omega = 16 \text{ MeV}$, where a good convergence with respect to the many-body model space is observed. The left panel shows the results using the NN_{only} Hamiltonian, with a noticeable but small flow-parameter dependence, which is reduced when including the induced 3N contributions in the middle panel.

The differences between the energies with the NN_{only} and the NN+3N_{ind} Hamiltonian indicate the effect of the repulsive induced 3N contributions increase the radius of the nucleus and leads to a compression of the spectrum. The additional inclusion of the initial 3N force shown in the right panel leads to an overall improved description of the experimental spectrum. The excitation energies of the rotational band, i.e., of the first 2⁺ and, in particular, of the first 4⁺ state are increased by the initial 3N interaction. The excitation energy of the first excited 1⁺ state declines, leading to an underestimation of the experimental excitation energy by more than 3 MeV. We further discuss the ¹²C spectrum in Sec. 8, where we analyze the sensitivity to the parameters of the initial 3N force and compare the spectrum to those computed with different present chiral interactions.

It is important to note that the omitted induced many-nucleon contributions for the NN+3N_{full} Hamiltonian do not affect the internal structure of the spectrum and lead to a rather constant shift of the absolute energies. The excitation energies show a negligible flow parameter depen-

NN+3N _{full}	c_1 [GeV ⁻¹]	c_3 [GeV ⁻¹]	c_4 [GeV ⁻¹]	c_D	c_E
standard	-0.81	-3.2	+5.4	-0.2	-0.205
$c_i = 0$	0	0	0	-0.2	+0.444
$c_D = 0$	-0.81	-3.2	+5.4	0	-0.205
$c_E = 0$	-0.81	-3.2	+5.4	+1.238	0.0
$c_1 = 0$	0	-3.2	+5.4	-0.2	-0.207
$c_3 = 0$	-0.81	0	+5.4	-0.2	-0.228
$c_4 = 0$	-0.81	-3.2	0	-0.2	+0.141

Table 6.1 *LECs for local chiral 3N interactions with excluded contributions*: In addition to the standard NN+3N interaction [77] the table summarize the LECs of the local 3N interaction using a cutoff of $\Lambda_{3N} = 500$ MeV/c for variations with excluded 3N contribution, while keeping the standard NN part at N³LO fixed.

and discussed in Sec. 1.3.2. To assess the impact of the individual terms we switch them off by setting the corresponding LECs to zero and refit c_E to the ⁴He ground-state energy of -28.30 MeV with an uncertainty below 10 keV. To reproduce the triton β -decay half-life we keep $c_D = -0.2$, with the exception of the $c_D = 0$ or $c_E = 0$ cases, where we exclusively reproduce the ⁴He ground-state energy by fitting c_E or c_D , respectively. The resulting LECs for the different Hamiltonians are summarized in Tab. 6.1.

Figure 6.4 shows the results obtained for the ground-state energy of ¹⁶O with the IT-NCSM using the modified Hamiltonians and compares them to the results obtained with the standard NN+3N interaction. The Hamiltonians are SRG evolved using $\alpha = 0.04$ fm⁴ (blue circles), 0.08 fm⁴ (red diamonds), and 0.16 fm⁴ (green triangles) treating the interaction matrix elements with the three-body HO machinery. The upper panels compare the standard NN+3N_{full} energies in Figure 6.4 (a) to those obtained from switching off the two-pion exchange term (b), the two-nucleon contact term (c), and the three-nucleon contact term (d). The latter two modifications have only minor effects on the still sizable flow-parameter dependence, while setting $c_1 = c_3 = c_4 = 0$ to eliminate the two-pion exchange term dramatically changes the picture. The flow-parameter dependence of the converged results vanishes completely. From these observations we can conclude that the induced beyond-3N forces almost exclusively originate from the long-range two-pion exchange terms.

We further study the impact of different operator structures in this term, by switching off the individual contributions that are proportional to c_1 , c_3 , and c_4 illustrated in Figure 6.4 (f), (g), and (h), respectively. The c_1 structure has only negligible impact, already indicated by the small change of the refitted c_E value to describe the ⁴He ground-state energy. The omitted c_4 contribution strongly affects the refitted c_E , but leads to minor changes of the ¹⁶O ground-state energy and the flow-parameter dependence. The omission of the operator structure proportional to c_3 apparently eliminates the flow-parameter dependence, identifying the c_3 term to be the

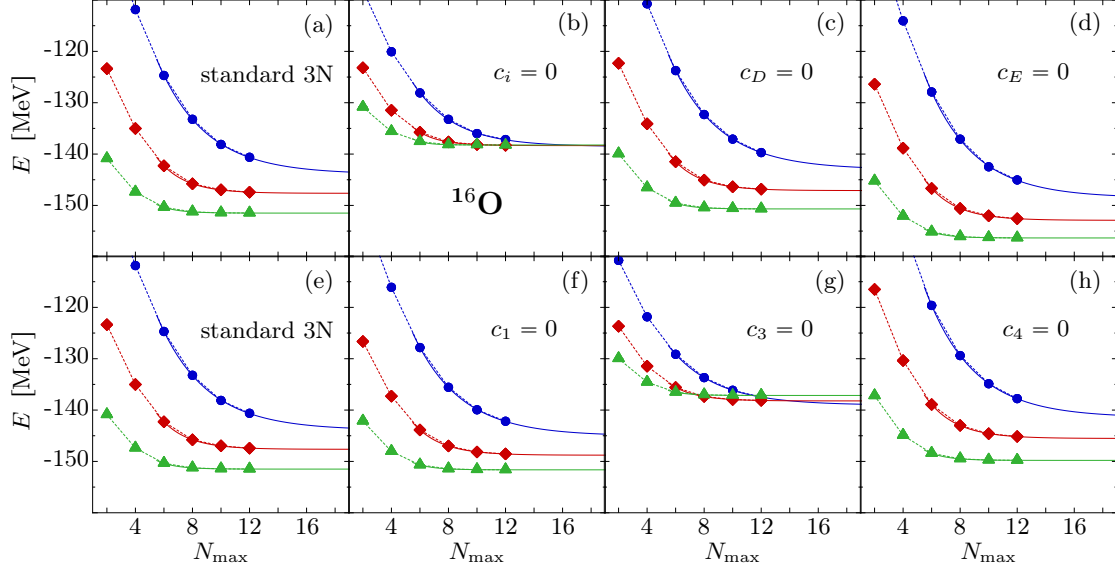


Figure 6.4 *Origin of induced $4N$ forces in initial $3N$ interaction*: Plotted is the ground-state energy of ^{16}O obtained with the $\text{NN}+3\text{N}_{\text{full}}$ Hamiltonian for $\alpha = 0.04 \text{ fm}^4$ (\bullet), 0.08 fm^4 (\blacklozenge), and 0.16 fm^4 (\blacktriangle) with $\hbar\Omega = 20 \text{ MeV}$ as function of N_{max} . The upper row compares the results obtained with the standard $3N$ interaction (a) with those for $c_i = 0$ (b), $c_D = 0$ (c), and $c_E = 0$ (d). The lower row compares the results obtained again with the standard $3N$ interaction (e) with those for $c_1 = 0$ (f), $c_3 = 0$ (g), and $c_4 = 0$ (h). The solid curves indicate the N_{max} -extrapolated results. See text for further details. The results are published in Ref. [21].

main driver of the SRG induced beyond- $3N$ contributions. From analogies to the NN interaction, where the tensor force represents an important source of induced $3N$ contributions [18], it is not surprising that the complicated operator structure of the two-pion exchange terms, including intermediate-range tensor- and spin-orbit-type interactions, is responsible for sizable induced beyond- $3N$ contributions. However, it is not obvious why the c_3 term is the dominant driver of the induced contributions, while the operator structures that correspond to c_4 have only a small effect on the flow-parameter dependence.

The identification of the long-range two-pion exchange terms as major source of induced many-nucleon contributions seems to be contradictory to the fact that the SRG evolution, in particular, acts on the high-momentum or high-energy contributions that typically corresponds to short-range physics. Despite the general characterization as long-range contribution the two-pion exchange topology also significantly contributes to the high energy regime. To study the impact of this regime, we lower the $3N$ cutoff Λ_{3N} and thus suppress the high energy contributions of the $3N$ interaction. We use an analogous procedure as for the variation of the LECs, i.e., we keep the standard NN interaction fixed and modify exclusively the cutoff in the momentum-transfer regulator of the initial $3N$ interaction. Since the three-body regularization has a small impact on the triton β -decay half-life [77] we keep $c_D = -0.2$ and refit c_E to the

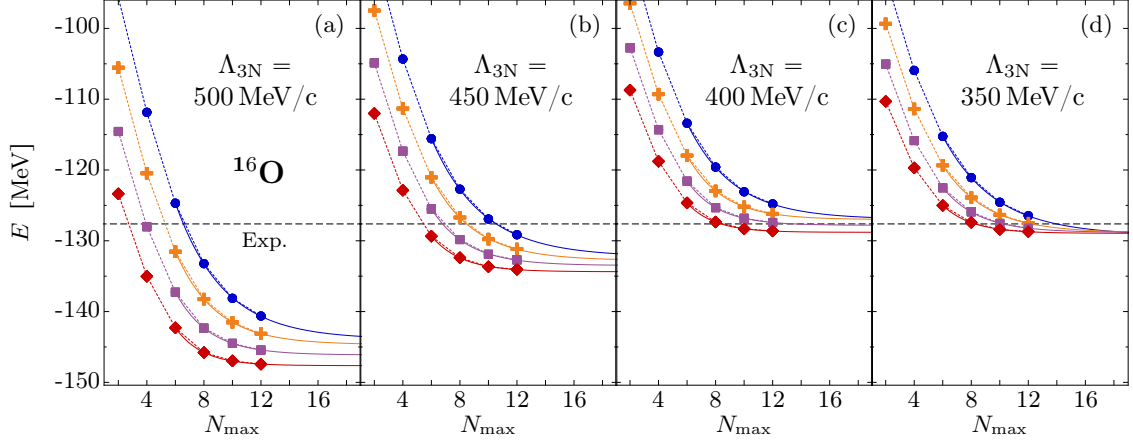


Figure 6.5 *Suppression of induced 4N forces by cutoff reduction*: Plotted is the ground-state energy of ^{16}O obtained with the $\text{NN}+3\text{N}_{\text{full}}$ Hamiltonian using the standard $\text{NN}+3\text{N}$ interaction with the three-body cutoff of $\Lambda_{3\text{N}} = 500 \text{ MeV}/c$ (a) as well as with $\Lambda_{3\text{N}} = 450 \text{ MeV}/c$ (b), $400 \text{ MeV}/c$ (c), and $350 \text{ MeV}/c$ (d). The curves correspond to the flow-parameters $\alpha = 0.04 \text{ fm}^4$ (\bullet), 0.05 fm^4 (\oplus), 0.0625 fm^4 (\blacksquare), and 0.08 fm^4 (\blacklozenge). Extrapolations are indicated by solid lines. The IT-NCSM calculations are performed at $\hbar\Omega = 20 \text{ MeV}$. The results are published in [21].

^4He ground-state energy. Note, the c_i values already appear in the NN interaction and are fixed by a fit to the NN system. The parameters of the 3N interactions for the standard $\text{NN}+3\text{N}$ interaction, as well as for those with a reduced three-body cutoff are summarized in Tab. 1.1 on page 18.

We show the ^{16}O ground-state energy obtained with the $\text{NN}+3\text{N}_{\text{full}}$ Hamiltonians using the standard cutoff $\Lambda_{3\text{N}} = 500 \text{ MeV}/c$ in Fig. 6.5 (a), as well as the reduced cutoffs $\Lambda_{3\text{N}} = 450 \text{ MeV}/c$ (b), $400 \text{ MeV}/c$ (c), and $350 \text{ MeV}/c$ (d). By reducing the cutoff the effects of induced contributions are indeed suppressed, such that the spread of the converged ground-state energies for the considered flow-parameter range of $\alpha = 0.04 - 0.08 \text{ fm}^4$ continuously narrows from more than 3.5 MeV for the standard cutoff to less than 0.5 MeV for $\Lambda_{3\text{N}} = 350 \text{ MeV}/c$. Even more important, the substantial overbinding reduces with decreasing cutoff, such that with the two lowest cutoffs that enable reliable predictions the experimental ground-state energy is well reproduced. This reveals the predictive power of the chiral interactions in such large systems.

At this point it is still not clear whether the bare Hamiltonians with larger cutoffs reproduce the experimental ground-state energy as well, since the regularization might impact the results and we come back to this issue when including the induced 4N contributions explicitly in Sec. 6.4. Of course, with decreasing cutoff one not only suppresses the induced many-body contributions as demonstrated in Fig. 6.5, but might also start to exclude physically relevant contributions. Therefore, we typically use the 3N interaction with the reduced $400 \text{ MeV}/c$ cutoff, when aiming at the description of absolute energies for nuclei beyond the p shell [23, 28–30, 33, 35, 36, 145].

In conclusion, the initial 3N contributions proportional to c_3 of the two-pion exchange term with high-momentum components beyond 400 MeV/c are responsible for the induced beyond-3N contributions, which have a sizable repulsive effect on the absolute energies for nuclei beyond the mid-p shell. These studies, which are published in Ref. [21], show a suppression of the induced beyond-3N contributions by reducing the cutoff of the 3N interaction, enabling reliable applications of the chiral NN+3N interaction beyond p-shell nuclei (see Sec. 7).

However, it is desirable to assess the theoretical uncertainties of the chiral EFT approach by a variation of the fundamental chiral parameters, i.e., the chiral perturbation order and the regularization. In this work we present a crucial step towards this fundamental uncertainty quantification for nuclear structure physics in Sec. 8 and 9, focusing on spectroscopy. In terms of absolute ground-state energies, studying the influence of the regularization by a cutoff variation, requires either to avoid the induced many-nucleon contributions from the outset, e.g., by using an alternative SRG generator or the inclusion of the relevant 4N contributions in the many-body calculations. Both approaches are investigated in the following.

6.3 Alternative SRG Generators

Motivated by the findings in the previous section, we discuss two fundamental ideas of modifying the canonical SRG generator

$$\boldsymbol{\eta}_\alpha = \left(2\frac{\mu}{\hbar^2}\right)^2 [\mathbf{T}_{\text{int}}, \mathbf{H}_\alpha] \quad (134)$$

in order to suppress the induced many-nucleon forces. Based on these ideas we design alternative SRG generators and probe their impact, regarding convergence acceleration and induced many-nucleon forces in nuclear structure calculations of ground-state energies.

6.3.1 Exclusion of Initial 3N Contributions

In the following we concentrate on the evolution of the initial NN+3N interaction in the three-body space leading to the NN+3N_{full} Hamiltonian $\mathbf{H}_{\text{NN}+3\text{N}_{\text{full}}}$. Considering the fact that sizable beyond-3N effects originate from the initial 3N contributions motivates attempts to reduce the effect of the SRG evolution on these contributions. In order to ensure the formal unitarity we exclude the initial 3N part from the applied generator, i.e., we solve the flow equation

$$\frac{d}{d\alpha} \mathbf{H}_{\text{NN}+3\text{N}_{\text{full}}} = [\boldsymbol{\eta}_\alpha^{\text{NN}}, \mathbf{H}_{\text{NN}+3\text{N}_{\text{full}}}], \quad (135)$$

where we replace the generator by

$$\boldsymbol{\eta}_\alpha^{\text{NN}} = \left(2\frac{\mu}{\hbar^2}\right)^2 [\mathbf{T}_{\text{int}}, \mathbf{H}_{\text{NN}+3\text{N}_{\text{ind}}}], \quad (136)$$

We have to simultaneously solve the flow equation for the initial NN interaction

$$\frac{d}{d\alpha} \mathbf{H}_{\text{NN}+3\text{N}_{\text{ind}}} = [\boldsymbol{\eta}_{\alpha}^{\text{NN}}, \mathbf{H}_{\text{NN}+3\text{N}_{\text{ind}}}], \quad (137)$$

to obtain the NN+3N_{ind} Hamiltonian $\mathbf{H}_{\text{NN}+3\text{N}_{\text{ind}}}$ that appears in the generator (136).

For these simultaneous evolutions we exclude the contributions of the initial 3N interaction in the generator, such that the unitary transformation is not optimized for the prediagonalization of the initial 3N contributions. Nevertheless, the initial 3N interaction is affected by the evolution in a different manner and we examine if the alternative SRG formulation sustains an appropriate convergence acceleration of the many-body calculations and at the same time prevents induced beyond-3N forces.

In Fig. 6.6 we compare the ground-state energies of ${}^4\text{He}$ (upper panels) and ${}^{16}\text{O}$ (lower panels) using the NN+3N_{full} Hamiltonian, that is obtained by using the canonical generator $\boldsymbol{\eta}_{\alpha}$ of Eq. (134) (left panels) and the alternative generator $\boldsymbol{\eta}_{\alpha}^{\text{NN}}$ of Eq. (136) (middle panels). While the ground-state energies with the standard evolution are well converged for the largest N_{max} in the flow-parameter range $\alpha = 0.04 - 0.16 \text{ fm}^4$, this is not the case for the alternative generator, where we observe an almost linear dependence of the ground-state energy with respect to N_{max} for the larger model spaces.

Even for an untypically large flow parameter $\alpha = 0.32 \text{ fm}^4$ that is used for ${}^{16}\text{O}$ in Fig. 6.6 (e) convergence is not achieved for the alternative generator. Moreover, the energies show an almost parallel shift compared to those with smaller flow parameters. This indicates that a longer evolution seems to produce attraction without improving the convergence. Unfortunately, the convergence pattern with the alternative generator $\boldsymbol{\eta}_{\alpha}^{\text{NN}}$ does not allow for a meaningful extrapolation to infinite model spaces and it is hardly possible to judge on a potential suppression of induced many-nucleon forces.

Instead of excluding the complete initial 3N part from the Hamiltonian in the generator one, e.g., can exclude only the two-pion exchange term by setting $c_1 = c_3 = c_4 = 0$ keeping c_E and c_D fixed. With such a generator one obtains almost the same ground-state energies as with the alternative generator $\boldsymbol{\eta}_{\alpha}^{\text{NN}}$, such that the curves mainly lie on top of those in Fig. 6.6 (b) and (e). This identifies the two-pion exchange term, which is responsible for the sizable induced beyond-3N effects, to be also required for the convergence acceleration in the many-body calculations.

If we assume the effects of the induced 4N forces to be small with the alternative generator one can think about a combination of the SRG generators. For instance, we start with the alternative evolution up to a certain α value, such that we have improved the convergence compared to the bare Hamiltonian, while assuming the induced 4N effect to be small. Based on this Hamiltonian we perform an additional evolution with the canonical generator for a rather small evolution period $\Delta\alpha$, in order to retain the substantial convergence acceleration, while avoiding sizable induced 4N effects due to small $\Delta\alpha$. The ${}^4\text{He}$ case (c) illustrates that the combined evolution

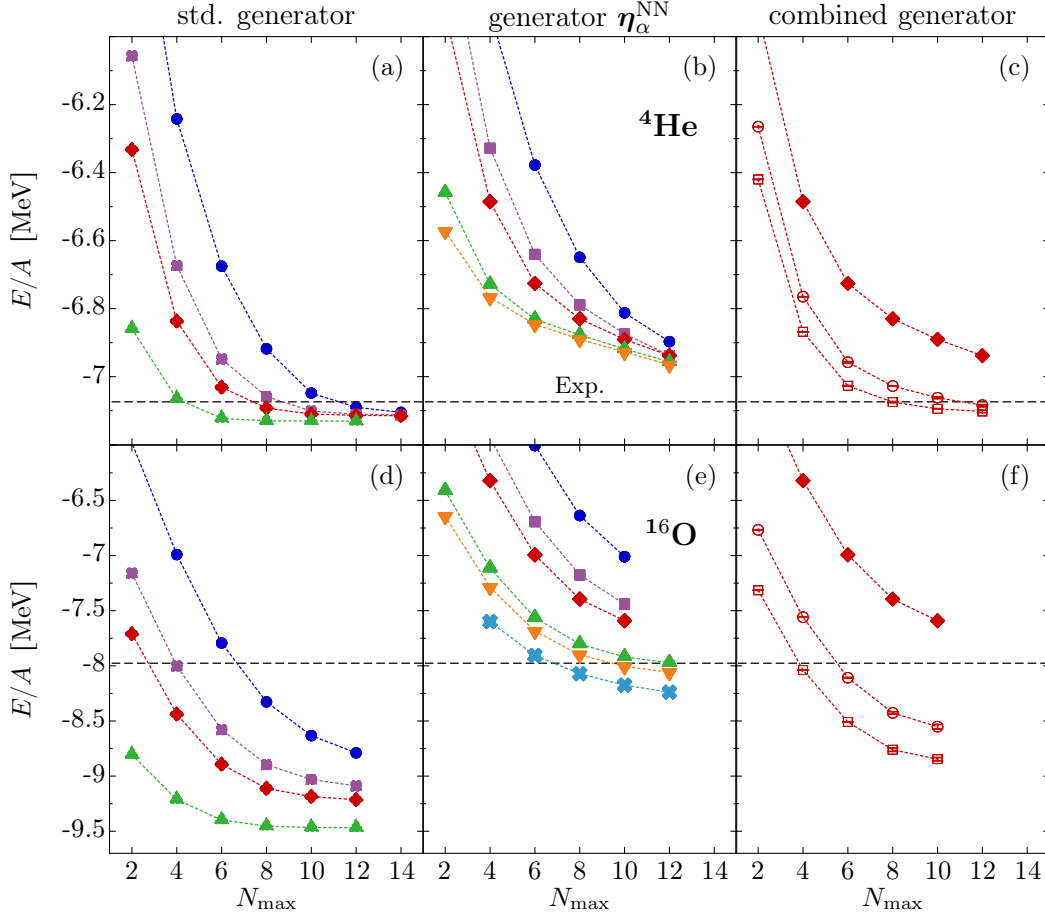


Figure 6.6 *Alternative SRG generators without initial 3N contributions*: Plotted are the ground-state energies of ${}^4\text{He}$ (upper panels) and ${}^{16}\text{O}$ (lower panels) obtained with the IT-NCSM at $\hbar\Omega = 20 \text{ MeV}$ as function of N_{max} . We start with the standard initial NN+3N interaction and perform the SRG evolution with the canonical generator (left column) and with the alternative generator η_α^{NN} (middle column) using the flow-parameter $\alpha = 0.04 \text{ fm}^4$ (\bullet), 0.0625 fm^4 (\blacksquare), 0.08 fm^4 (\blacklozenge), 0.16 fm^4 (\blacktriangle), 0.2 fm^4 (\blacktriangledown), and 0.32 fm^4 (\times). In the right column we show the results obtained by performing the SRG evolution with the alternative generator η_α^{NN} up to $\alpha = 0.08 \text{ fm}^4$ (\blacklozenge) and additionally evolve the obtained interaction further by 0.01 fm^4 (\circ), and 0.02 fm^4 (\square) using the canonical generator. See text for further details.

indeed improves the convergence, such that we recover the converged result of the standard evolution. Unfortunately, for the ^{16}O ground-state energy the convergence is still not sufficient to accurately extrapolate to infinite N_{max} . Moreover, the additional short evolutions with the canonical generator seem to induce sizable repulsive many-nucleon contributions, that cause a strong attractive shift of the energies with increasing $\Delta\alpha$. This indicates that the SRG evolution already induces sizable beyond-3N contributions at very small flow-parameter values. As before, the lack of convergence complicates an interpretation regarding the effect of induced many-nucleon forces and eliminates the alternative generators for applications to nuclear structure physics.

6.3.2 Restriction of Range

As shown in the previous section the high-momentum contributions of the long-range two-pion exchange term induce sizable many-nucleon contributions during the SRG evolution. Moreover, the two-pion exchange contributions in the generator are crucial to accelerate the convergence with respect to the many-body model space. Instead of omitting the complete two-pion exchange term we now aim at an exclusive suppression of the long-range components of the generator. Already from a naive picture, long-range transformations tend to effect more particles. Thus, it is not surprising that the long-range term of the initial 3N interaction is responsible for the induced contributions and we show that one observes a similar behavior for the NN interaction, which induces sizable beyond-NN contributions. We present an alternative generator that suppresses the induced contributions by restricting the range of the generator and leaves the long-range contributions mainly unaffected. In contrast to the approach of the previous section, which is adjusted to the particular operator structure of the chiral 3N interaction, the following concept is of general validity. We evolve the initial NN interaction at the two-body level (NN_{only}) aiming at the suppression of the sizable induced 3N and many-nucleon forces. We solve the evolution equation

$$\frac{d}{d\alpha}\mathbf{H}_\alpha = [\boldsymbol{\eta}_\alpha^r, \mathbf{H}_\alpha], \quad (138)$$

with the generator

$$\boldsymbol{\eta}_\alpha^r = \Theta_{(R,p)}^\dagger \boldsymbol{\eta}_\alpha \Theta_{(R,p)}. \quad (139)$$

The Hermitian operator $\Theta_{(R,p)}^\dagger$ suppresses the long-range contributions of the canonical generator by a Gaussian factor

$$\Theta_{(R,p)}^\dagger = \Theta_{(R,p)} = e^{-\left(\frac{r}{R}\right)^{2p}}, \quad (140)$$

where $\mathbf{r} = |\mathbf{r}_b - \mathbf{r}_a|$ is the absolute value of the relative distance operator of the two-nucleon system, R is the range parameter to adjust the range of the generator and p is a power that determines the suppression behavior. The special form of the operator Θ , designed in collaboration with Hans Feldmeier, is adjusted for the application to a two-body evolution, but in principle can be generalized to the three-body or four-body space by using the corresponding Jacobi coordinates.

To illustrate the effect of the restricted-range generator we investigate the deuteron S-wave functions in Fig. 6.7 obtained by solving the Schrödinger equation in momentum space, using the SRG-evolved NN_{only} Hamiltonians. The wave functions correspond to the bare Hamiltonian (dashed black line) and the flow-parameter values $\alpha = 0.08 \text{ fm}^4$ (red solid line), 0.16 fm^4 (green solid line), and 0.32 fm^4 (light-blue solid line). We compare the wave functions for the Hamiltonians that are evolved with the canonical generator in Fig. 6.7 (a) to those where we performed the restricted-range evolution for several parameter combinations. In almost every case the SRG evolution strongly affects the short-range correlations of the wave function, which is related to high-momentum contributions of the interaction, such that the repulsion at short-distances reduces. In Fig. 6.7 (b)-(d) we fix the range $R = 1.5 \text{ fm}$ and vary the power p from 1 to 3. As evident from the deuteron wave functions, with increasing power p the suppression by the operator Θ increases. For the largest p the generator is suppressed too strongly, such that the short-range repulsion is not completely eliminated. In Fig. 6.7 (e)-(f) we fix the power $p = 2$ and vary the range parameter $R = 1.0 - 2.0 \text{ fm}$. For small range parameters $R < 1.5 \text{ fm}$ we suppress too much of the generator, such that the deuteron S-wave function is almost unaffected by the evolution. The important difference between the standard and the restricted range SRG evolution is the effect on the wave function at about $r = 3 \text{ fm}$. While for the standard evolution the wave function is noticeably increased compared to the bare Hamiltonian, the restricted range evolution leaves these medium-range part ($r \gtrsim 2.5 \text{ fm}$) unchanged.

We anticipate that exactly these medium-range correlations induce sizable many-nucleon forces during the SRG evolution and we investigate this issue for the ground-state energy of ^4He in Fig. 6.8. We show the ground-state energy obtained in NCSM calculations at $\hbar\Omega = 20 \text{ MeV}$ plotted as function of N_{max} for the bare Hamiltonian (open circles) and the flow-parameter range $\alpha = 0.08 - 0.32 \text{ fm}^4$. We compare the energies for the canonical generator in Fig. 6.8 (a), with those obtained for the restricted-range generator for the same parameter combinations as in Fig. 6.7 using an equivalent arrangement of the panels. The dashed line indicates the experimental value and the thick black bar corresponds to the converged energy of the bare NN interaction.

The ground-state energies are in agreement with the interpretations for the deuteron wave functions. For too large powers p in Fig. 6.8 (d) and too small ranges R (e) one starts to suppress contributions of the generator that are relevant for the convergence acceleration, such that reliable N_{max} extrapolations are not possible. On the other hand, for too small powers

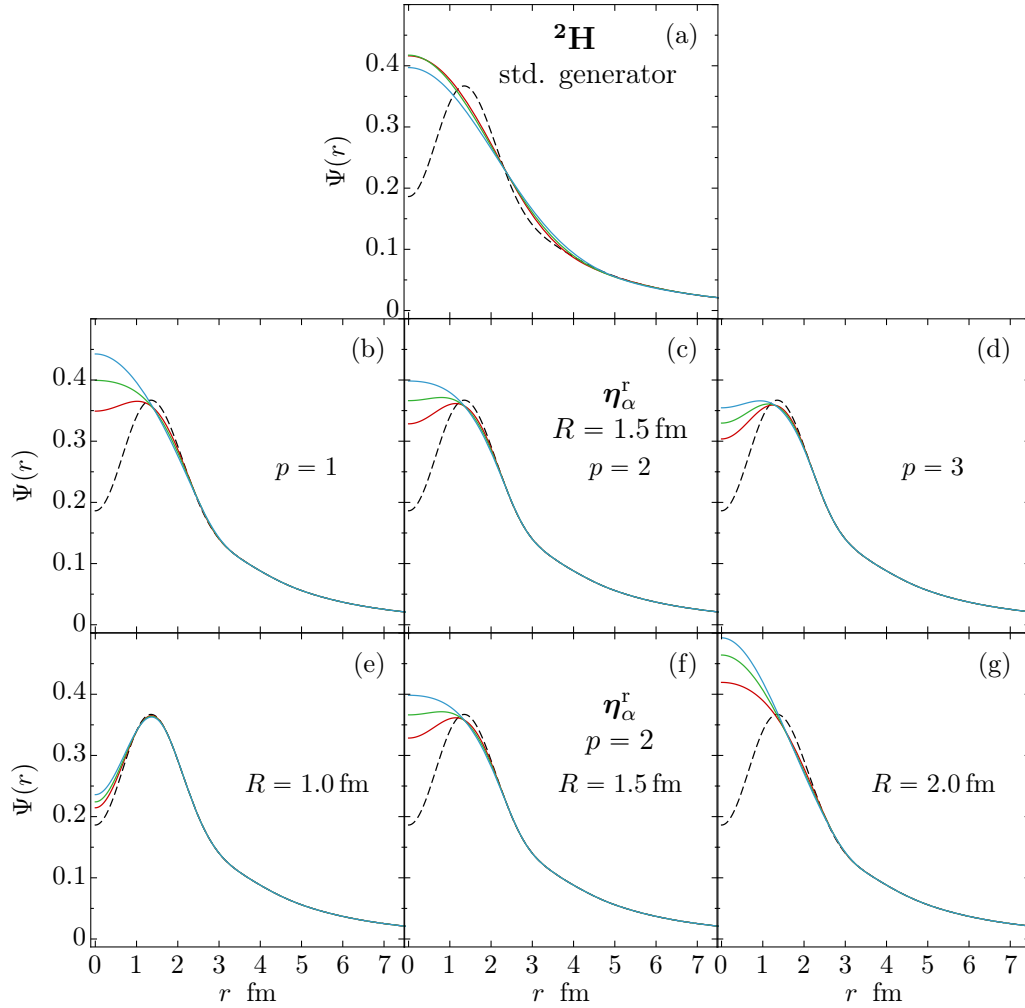


Figure 6.7 *Deuteron wave function with restricted range generator*: Plotted is the deuteron S-wave wave function over the relative distance of the two nucleons. We compare the results obtained for the SRG-evolved initial NN interaction in the two-body space (NN_{only}) with the canonical generator (a) and with the alternative generator η_{α}^r using a fixed range $R = 1.5$ fm and varying the power $p = 1, 2, 3$ (b,c,d) as well as for a fixed power $p = 2$ and a variation of the range $R = 1.0, 1.5, 2.0$ fm (e,f,g). The wave functions are obtained for the bare Hamiltonian (black dashed line) as well as for the flow-parameter values 0.08 fm^4 (red solid line), 0.16 fm^4 (green solid line) and 0.32 fm^4 (light-blue solid line). See text for further details.

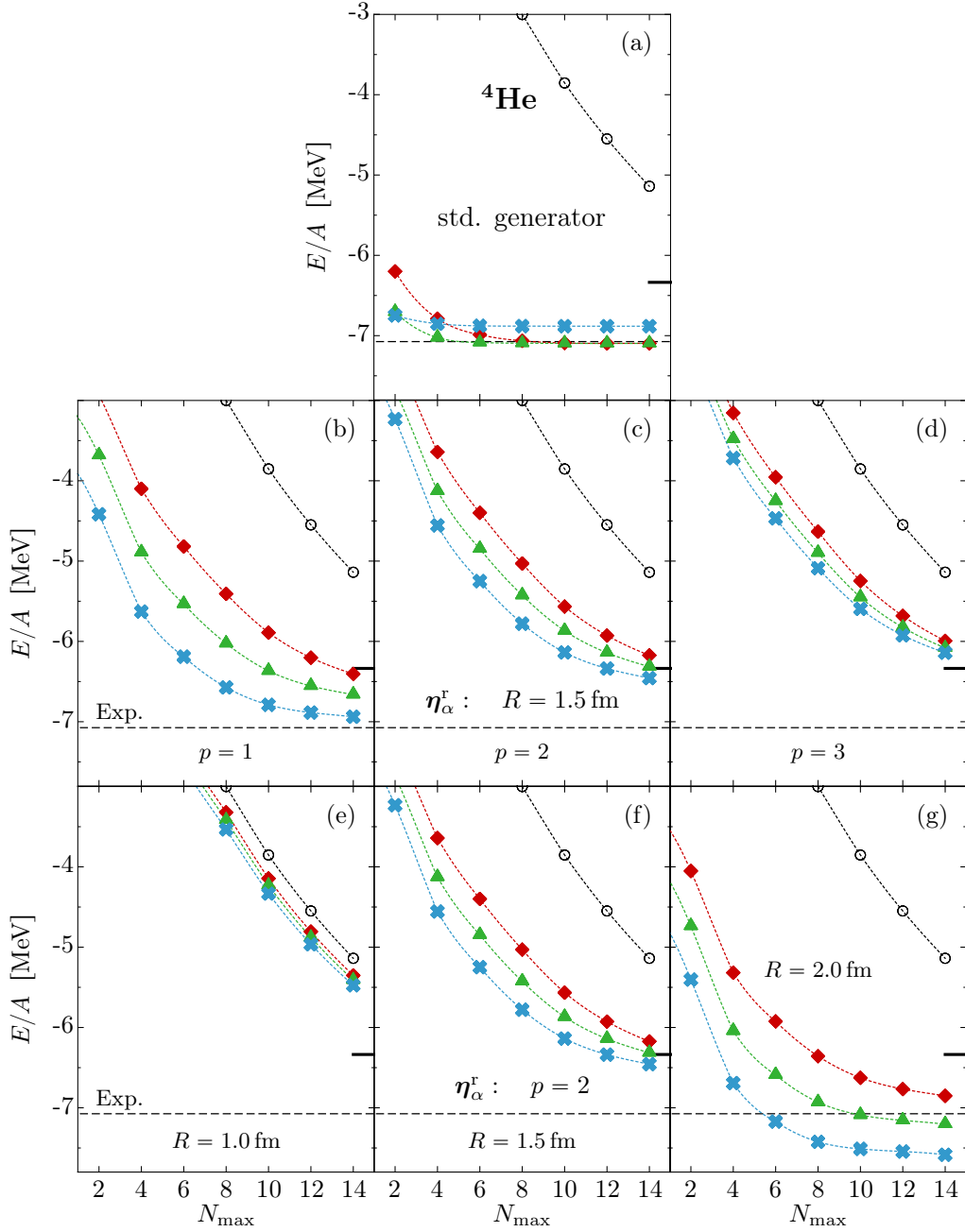


Figure 6.8 ${}^4\text{He}$ ground-state energy with restricted-range generator: Plotted is the ground-state energy of ${}^4\text{He}$ obtained with the NCSM at $\hbar\Omega = 20$ MeV as function of N_{\max} . We compare the results obtained for the SRG-evolved initial NN interaction in the two-body space (NN_{only}) with the canonical generator (a) and with the alternative generator η_α^r using a fixed range $R = 1.5$ fm and varying power $p = 1, 2, 3$ (b,c,d) as well as for a fixed power $p = 2$ and a variation of the range $R = 1.0, 1.5, 2.0$ fm (e,f,g). The curves correspond to the results obtained for flow parameters 0.08 fm^4 (\blacklozenge), 0.16 fm^4 (\blacktriangle) and 0.32 fm^4 (\blacktimes). For comparison of the convergence acceleration we also illustrate the results for the bare Hamiltonian (\circ). See text for further description.

p in Fig. 6.8(b) and too large ranges R (g), we retain the medium-range contributions that induce sizable 3N forces, such that we significantly overbind the converged energy of the bare Hamiltonian. Thus, we have to optimize these two parameters of the alternative generator to achieve an appropriate trade-off between the convergence acceleration and the suppression of induced many-body contributions. In Fig. 6.8(c), which is equivalent to (f), we illustrate a rather optimized parameter set. The curves for the larger flow-parameter values already tend to slightly overbind the bare result, indicating the appearance of repulsive induced 3N forces, while simultaneously the energies are not yet converged up to $N_{\max} = 14$.

The parameters of the restricted-range generator allow to control the trade-off between convergence and induced many-nucleon forces. With parameters for the generator that suppress the induced 3N contributions one cannot obtain converged energies with the IT-NCSM in tractable model spaces. Nevertheless, this generator could be useful for other ab initio methods, such as the CC approaches or the IM-SRG that can handle much larger model spaces. Moreover, we have studied the suppression of the induced 3N contributions with the restricted-range generator, while a suppression of the induced 4N contributions could be less critical. Therefore, a formulation of this alternative generator in the three-body space is an interesting subject for future investigations.

In conclusion, from the studies of the alternative generators, we achieve a deep insight in the SRG evolution for nuclear structure calculations, identifying the medium-range components of the NN interaction to be important for the convergence pattern and at the same time responsible for the sizable induced many-body effects. It seems that those parts of the interaction that need to be softened by the SRG evolution to accelerate the model-space convergence are also responsible for sizable induced many-nucleon contributions. Therefore, the search of alternative generators presumably concentrates on optimizations of a trade-off, such that the generator is adjusted to a specific observable, nucleus, and interaction and the findings of this work might be crucial for the development of future SRG generators. Keeping the results with the alternative generators in mind the SRG evolution up to the three-body level with the canonical generator already provides an appropriate compromise, allowing for successful applications of the chiral NN+3N interactions to a wide range of physics. In order to broaden the application range and, in particular, to study the nature of the induced many-nucleon contributions, we aim at the explicit inclusion of the induced 4N forces.

6.4 Inclusion of Induced 4N Forces

In the following, we discuss the successes and limitations regarding the inclusion of 4N contributions and point out that the presented techniques are directly capable to handle initial 4N forces as well. The chiral 4N force already appears at N³LO in the Weinberg power-counting scheme and is required for a fully consistent Hamiltonian at this order. Therefore, the present studies

are of particular interest for the continuation of current efforts of the LENPIC collaboration to employ consistent Hamiltonians at this chiral order.

To treat the 4N contributions, we start with an SRG evolution in the four-body Jacobi-HO basis truncated by the relative-energy quantum number $E_{4,\text{SRG}}$ as described in Sec. 4.7. During the evolution irreducible 4N contributions are induced that we separate from lower-particle rank contributions using the subtraction procedure presented in Fig. 4.1 on page 78. The irreducible 4N contributions in the Jacobi-HO representation are transformed into the single-particle basis, namely into the JT -coupled scheme (see Sec. 3.2.2). The resulting interaction matrix elements are truncated by the total energy quantum number $E_{4,\text{max}}$ and are explicitly included in the many-body calculations using the IT-NCSM. The many-body method is extended to treat the 4N interactions explicitly using an analogous on-the-fly decoupling procedure as for the 3N interactions. The irreducible NN and 3N forces are treated with the established two- and three-body techniques described in this work. For instance we use the three-body SRG space denoted by ramp \mathcal{A} , while the two-body evolution is performed in the momentum representation.

To include the 4N contributions to the many-body calculations we need to introduce the following truncations in the four-body space:

- We truncate the number of included partial waves, restricting ourselves to those with low angular momenta J_{123} .
- We are limited to a finite SRG space defined by the maximum relative-energy quantum number $E_{4,\text{SRG}}$.
- The four-body interaction matrix-element set in the JT -coupled scheme are truncated by the maximum total-energy quantum number $E_{4,\text{max}}$. This set is typically not large enough to provide all matrix elements that contribute to the many-body model space, such that $E_{4,\text{max}}$ poses an additional truncation.

In the following, we use the ^{16}O ground-state energy as prime example for studying induced 4N effects and analyzing their sensitivity to the four-body truncations. Based on these studies, we present the results for different Hamiltonians and nuclei including for the first time explicit 4N contributions with estimated uncertainties.

6.4.1 SRG-Space and Subtraction-Scheme Dependence

Due to the rapid growth of the model-space dimensions in the four-body Jacobi-HO basis with the energy quantum number and the angular momentum (see Fig. 3.1 on page 47), the SRG evolution is restricted to partial waves with low J_{123} in model spaces with rather small energy quantum numbers compared to the three-body space (see Sec. 5). In the following, we examine

PW	$(J_{123}^\pi T_{123})$ -channels
0	-
1	0^+0
2	$0^+0, 0^-0$
3	$0^+0, 0^-0, 0^+1$
4	$0^+0, 0^-0, 0^+1, 0^-1$
5	$0^+0, 0^-0, 0^+1, 0^-1, 0^+2$
6	$0^+0, 0^-0, 0^+1, 0^-1, 0^+2, 0^-2;$
7	$0^+0, 0^-0, 0^+1, 0^-1, 0^+2, 0^-2; \quad 1^+1$
8	$0^+0, 0^-0, 0^+1, 0^-1, 0^+2, 0^-2; \quad 1^+1, 1^-1$
\vdots	\vdots
12	$0^+0, 0^-0, 0^+1, 0^-1, 0^+2, 0^-2; \quad 1^+0, 1^-0, 1^+1, 1^-1, 1^+2, 1^-2;$
\vdots	\vdots
18	$0^+0, 0^-0, 0^+1, 0^-1, 0^+2, 0^-2; \quad 1^+0, 1^-0, 1^+1, 1^-1, 1^+2, 1^-2;$ $2^+0, 2^-0, 2^+1, 2^-1, 2^+2, 2^-2$

Table 6.2 *Definition of four-body partial waves:* In this table we define different 4N contributions. The partial-wave index $\text{PW} = \{0, \dots, 18\}$ enumerates the 4N contributions containing a successively increasing number of partial waves, i.e., $(J_{123}^\pi T_{123})$ -channels. An interaction corresponding to the partial-wave index $\text{PW} = 0$ does not contain 4N contributions. First we first add the positive- and then the negative-parity channels increasing initially the isospin $T_{123} = \{0, 1, 2\}$ and afterwards the angular momentum J_{123} . For $\text{PW} = 6, 12, 18$ the interaction contains all 4N contributions with $J_{123} \leq 0, 1, 2$, respectively.

if the computational tractable SRG spaces are sufficient to cover the relevant contributions of the induced 4N interactions.

In order to reduce the computational effort and to gain an impression of the SRG space we initially restrict our studies to NCSM calculations in a small $N_{\text{max}} = 2$ model space. For this many-body model space a truncation of $E_{4,\text{max}} = 6$ provides the complete set of required four-body matrix elements, such that we can focus exclusively on the sensitivity to the SRG space and the subtraction scheme (see Sec. 4.7.2). To disentangle the 4N effects of the different partial waves we define a number of Hamiltonians, for which we successively add four-body partial waves as illustrated in Tab. 6.2.

In Fig. 6.9 we illustrate the ^{16}O ground-state energy as function of the included four-body partial waves. The NCSM calculations are performed at a HO frequency of $\hbar\Omega = 24 \text{ MeV}$ with $\alpha = 0.08 \text{ fm}^4$. Note, that $\text{PW} = 0$ corresponds to the standard $\text{NN}+3\text{N}_{\text{full}}$ Hamiltonian. For the larger PW we successively add the 4N channels according to Tab. 6.2, i.e., we obtain several $\text{NN}+3\text{N}_{\text{full}}+4\text{N}_{\text{ind}}$ Hamiltonians with different partial-wave truncations. The 4N contributions result from an SRG evolution in a model space, truncated by $E_{4,\text{SRG}} = 15$ (blue circles), 17 (red diamonds), 19 (green triangles), and 21 (violet squares) using the subtraction scheme SubB (see

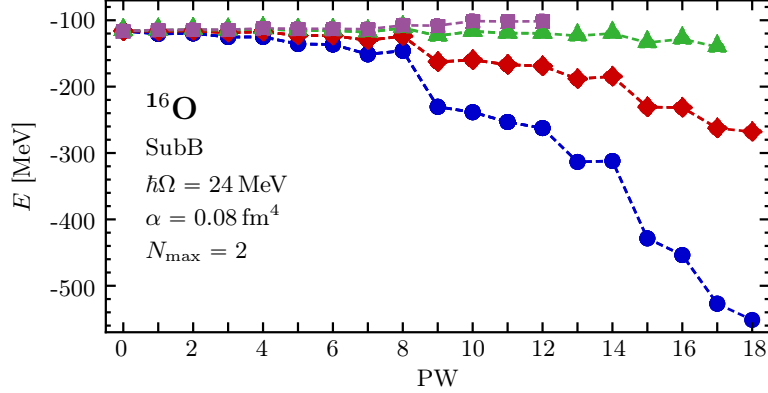


Figure 6.9 *SRG-space dependence of the ^{16}O ground-state energy*: Plotted is the ^{16}O ground-state energy as function of the included four-body partial waves. The energies are calculated with the NCSM in a small $N_{\text{max}} = 2$ model space at $\hbar\Omega = 24$ MeV. The standard NN+3N interaction is SRG evolved for $\alpha = 0.08$ fm 4 using the four-body SRG space $E_{4,\text{SRG}} = 15$ (\bullet), 17 (\blacklozenge), 19 (\blacktriangle), and 21 (\blacksquare) combined with the subtraction scheme SubB. See text further details.

Sec. 4.7.2 for the definition of the subtraction schemes).

The sensitivity of the ground-state energy to the SRG space increases with the number of included partial waves. In particular, when we include the $(J_{123}^\pi T_{123}) = (1^-1)$ and (2^-1) channels (corresponding to PW = 9 and PW = 15) the sensitivity increases dramatically. Unfortunately, the partial waves that are most sensitive to the SRG-space truncation have the largest model-space dimensions. The SRG evolutions of the $(J_{123}^\pi T_{123}) = (1^-1)$ and (2^-1) channels for $E_{4,\text{SRG}} = 21$ and 19, respectively, are computationally highly demanding and constitute the limit for the current implementation. The corresponding model-space dimensions are much larger than the ones for the three-body SRG evolution discussed in Sec. 5.3. To increase $E_{4,\text{SRG}}$ further, one needs to distribute the solution of the SRG flow equation (128) over several nodes, since memory and computing time simultaneously become an obstacle. Also the production of the CFPs limits the access to larger model spaces as discussed in Sec. 3.1.3 and needs to be improved. Due to the significant growth of the model-space dimensions the treatment of the 4N contributions rapidly starts to exceed the computational cost of the subsequent many-body calculations.

If we compare the energies for PW = 6, 12, 18 including all partial waves with $J_{123} \leq 0, 1, 2$, respectively, we observe a strong increase of the $E_{4,\text{SRG}}$ sensitivity with the angular momentum. For instance, the differences between the $E_{4,\text{SRG}} = 17$ and 19 results correspond to about 8, 50, and 127 MeV for these PW indices, respectively. Although, the deviations decrease rapidly with increasing $E_{4,\text{SRG}}$ the $J_{123} = 2$ contributions cannot be evolved in sufficiently large model spaces to resolve flow-parameter dependence below 10 MeV, which occurs without 4N contributions (see panel (a) of Fig. 6.5). Therefore, we have to restrict ourselves to the inclusion of the $J_{123} \leq 1$ contributions.

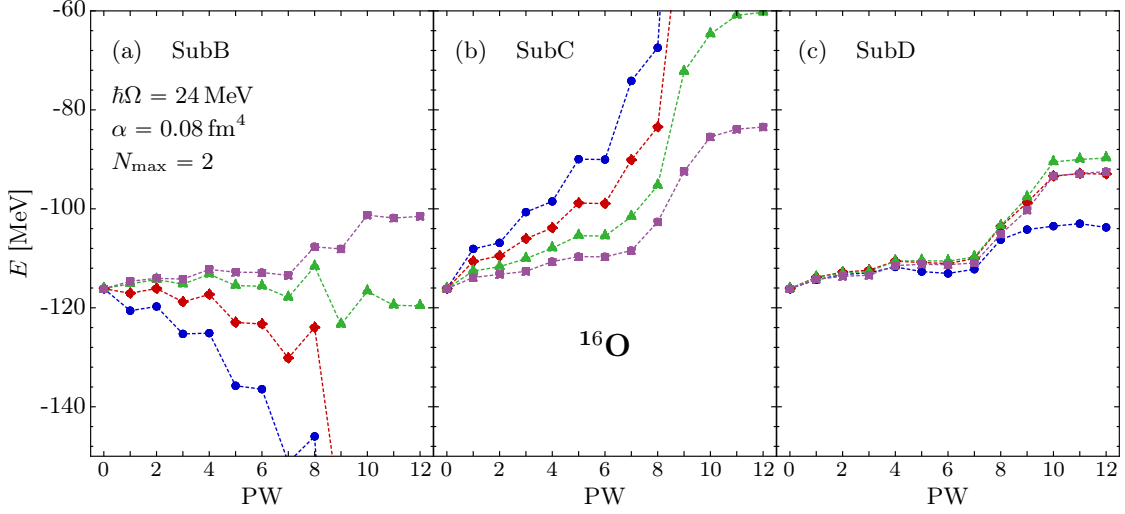


Figure 6.10 *SRG-space dependence of the ^{16}O ground-state energy*: Similar plot as in Fig. 6.9 using the subtraction scheme SubB (a), SubC (b), and SubD (c).

As explained in Sec. 4.4 the Jacobi-HO basis does not allow for a fully consistent model-space truncation in the two-, three-, and four-body space. Thus, the subtraction procedure is a potential source of error. For sufficiently large model spaces these errors become negligible. However, since we are limited to rather small maximum energy quantum numbers in the four-body space, the subtraction procedure can have sizable impact on the observables. To confirm that the SRG space is sufficiently large we need to demonstrate that the results do not depend on the subtraction scheme. In Fig. 6.10 (a) we show the same results as in Fig. 6.9, i.e., using subtraction scheme SubB. We include only $J_{123} \leq 1$ contributions and compare these results to the energies obtained with the subtraction schemes SubC in Fig. 6.10 (b) and SubD (c) (see Sec. 4.7.2). The dependence on the subtraction scheme is striking and indicates that the sensitivity to the SRG space is completely biased by the subtraction procedure. While the SubB and SubC schemes lead to opposite convergence patterns with respect to the SRG space, the SubD scheme seems to provide an averaged convergence pattern and the ground-state energy shows a strongly reduced sensitivity to the SRG space.¹⁴

The reduction of the SRG-space dependence with the SubD scheme seems to be very promising, but it turns out that the $E_{4,\text{SRG}}$ convergence pattern is rather uncontrolled. This is illustrated in Fig. 6.11 where we compare the ^{16}O ground-state energies obtained with the SubD subtraction scheme for the flow-parameter values $\alpha = 0.04$ fm 4 in Fig. 6.11 (a), 0.08 fm 4 (b), and 0.16 fm 4 (c). Remaining details of the many-body calculation and SRG evolution are as in the previous figures. Obviously, the $E_{4,\text{SRG}}$ convergence pattern changes with the flow parameter and shows some rather uncontrolled behavior. For instance the $E_{4,\text{SRG}}$ dependence is largest for the

¹⁴Indeed the SubD scheme is equivalent to an averaging of the subtracted contributions in the SubB and SubC scheme. A prove of this relation is straight-forward exercise and requires the consideration of the appearing factors for the conversion of a two- and three-body interaction matrix elements into the four-body space.

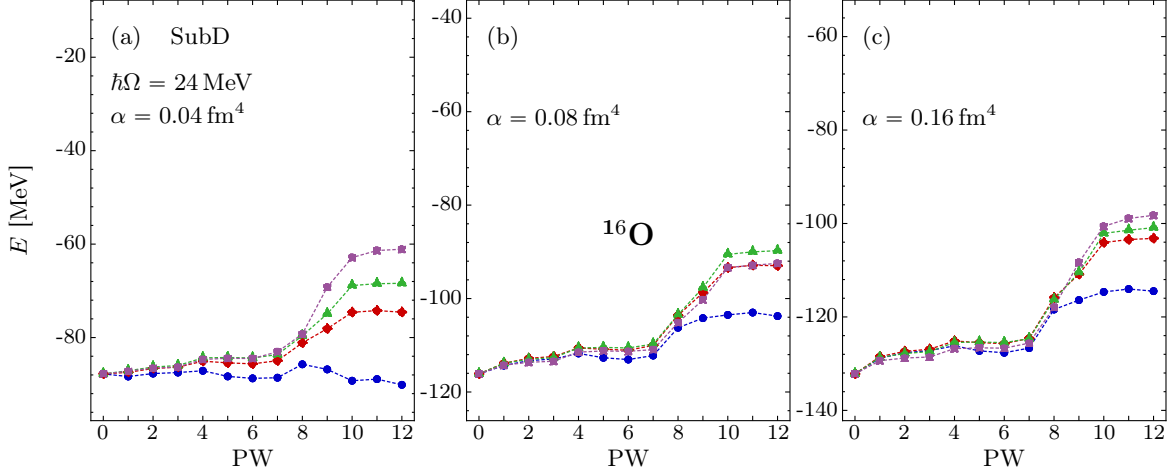


Figure 6.11 *SRG-space dependence of the ^{16}O ground-state energy*: Similar plot as in Fig. 6.9 using the subtraction scheme SubD and different flow-parameter values $\alpha = 0.04 \text{ fm}^4$ (a), 0.08 fm^4 (b), and $\alpha = 0.16 \text{ fm}^4$ (c).

smallest flow-parameter, which is counterintuitive, since with vanishing flow parameter also the $E_{4,\text{SRG}}$ dependence vanishes. Moreover, for $\alpha = 0.08 \text{ fm}^4$ the convergence pattern is reversed beyond $E_{4,\text{SRG}} = 19$, which can also happen for the other flow-parameter values.

Thus, in principle one could utilize the freedom of choosing the subtraction procedure to improve the $E_{4,\text{SRG}}$ convergence. But we point out that, as long as the results are sensitive to a change of the subtraction scheme, one cannot disentangle the spurious subtraction effects from the effects caused by missing induced 4N contributions and generalizations to the infinite SRG space are questionable. Therefore, we aim at a procedure that is not biased by the subtraction. The subtraction schemes SubB and SubC have caused the largest deviations in Fig. 6.10. Thus, we compare the results for these two schemes to validate the independence on the subtraction procedure.

To improve the convergence without further increasing the SRG spaces we take advantage of the experience from the three-body SRG evolution, where the ultraviolet truncation is the reason for sensitivities to the SRG space. Hence, one can increase the HO frequency to improve the $E_{4,\text{SRG}}$ convergence. In Fig. 6.12 we compare the ^{16}O ground-state energy as function of the included four-body partial waves for the subtraction scheme SubB (left panels) and SubC (right panels), as well as for different HO frequencies $\hbar\Omega = 24 \text{ MeV}$ (upper panels), 32 MeV (middle panels), and 40 MeV (lower panels). We stress that the absolute energies are meaningless for the NCSM calculations in a small $N_{\text{max}} = 2$ model space and, e.g., for the largest frequency the ground state is unbound. However, we use equivalent plot ranges for all frequencies, such that we can compare the deviations for the different partial waves and SRG spaces. With increasing frequency the results with the SubB scheme change the convergence pattern, such that the repulsive effect by increasing $E_{4,\text{SRG}}$ turns into an attractive effect. Further, we observe that

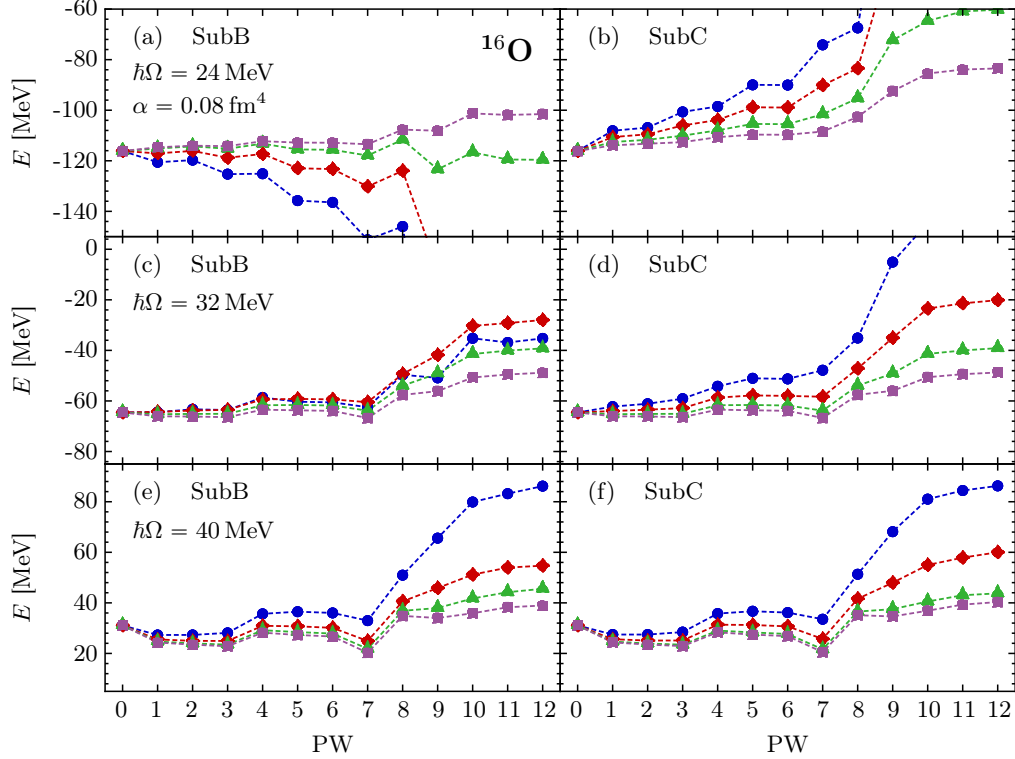


Figure 6.12 *Influence of the frequency on the SRG-space dependence:* We compare the ^{16}O ground-state energies for the subtraction scheme SubB (left panels) and SubC (right panels) at $\hbar\Omega = 24$ MeV (upper panels), 32 MeV (middle panels), and 40 MeV (lower panels). The results correspond to the four-body SRG spaces $E_{4,\text{SRG}} = 15$ (●), 17 (◆), 19 (▲), and 21 (■). Further parameter are chosen as in Fig. 6.10.

the convergence with respect to the SRG space is enhanced for both subtraction schemes if we increase the frequency. Even more important is that the ground-state energy for $\hbar\Omega = 40$ MeV becomes almost insensitive to the subtraction scheme, such that we can identify the effect of missing high-energy 4N contributions, while for the lowest frequency the convergence pattern is dominated by the subtraction procedure. At $\hbar\Omega = 40$ MeV the SRG-space convergence pattern is consistent with the observations in the three-body space, where insufficient SRG spaces cause an artificial repulsion (see Sec. 5).

6.4.2 The Frequency-Conversion Approach

From the previous discussion it becomes evident that the four-body SRG evolution has to be performed at large HO frequencies of about $\hbar\Omega = 40$ MeV to improve the $E_{4,\text{SRG}}$ convergence and to be insensitive to the subtraction procedure. But we require smaller frequencies for the subsequent IT-NCSM calculations to achieve convergence with respect to N_{max} . Therefore, we extend the frequency-conversion approach to the four-body space as discussed in Sec. 4.7.3. The ^{16}O ground-state energies in Fig. 6.13 are obtained from an NCSM calculation with $N_{\text{max}} = 2$.

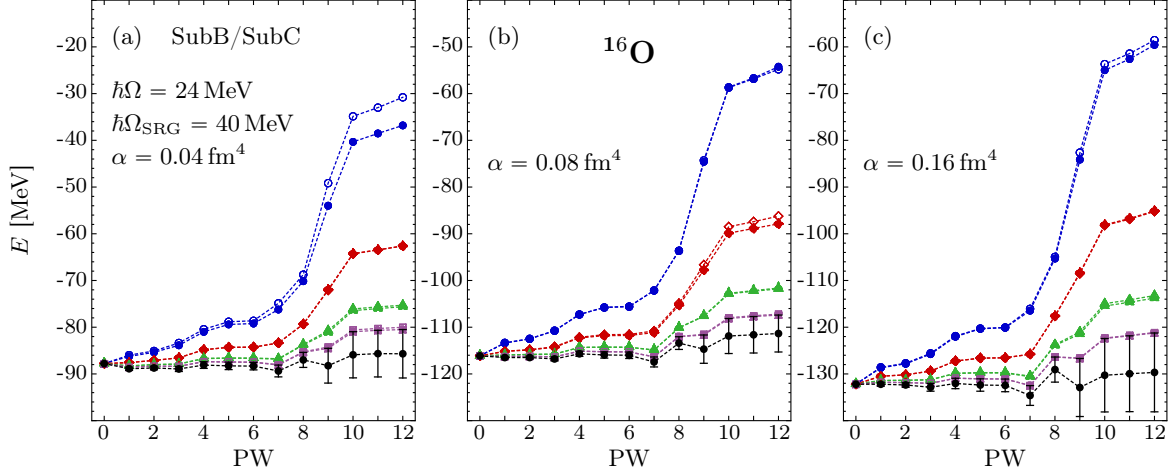


Figure 6.13 *Frequency-conversion and SRG-space dependence for the ^{16}O ground-state energy:* Illustrated is the SRG-space dependence of the ^{16}O ground-state energy for a four-body SRG evolution at $\hbar\Omega_{\text{SRG}} = 40 \text{ MeV}$ with $E_{4,\text{SRG}} = 15$ (\bullet), 17 (\blacklozenge), 19 (\blacktriangle), and 21 (\blacksquare) using a subsequent conversion of the frequency to $\hbar\Omega = 24 \text{ MeV}$, used in the $N_{\text{max}} = 2$ NCSM calculations. Independent of the used flow parameters $\alpha = 0.04 \text{ fm}^4$ (a), 0.08 fm^4 (b), and 0.16 fm^4 (c) the ground-state energies for subtraction scheme SubB (solid symbols) and SubC (open symbols) are almost on top of each other. The black circles correspond to the extrapolated energies to an infinite SRG space as described in the text.

The 3N contributions are obtained from an SRG evolution at $\hbar\Omega = 24 \text{ MeV}$ in a sufficiently large three-body space. The four-body SRG evolution, as well as the evolutions for the subtraction procedure, are performed at $\hbar\Omega_{\text{SRG}} = 40 \text{ MeV}$. We subsequently convert the frequency of the four-body interaction matrix elements to $\hbar\Omega = 24 \text{ MeV}$ that is used in the many-body calculation. We perform the four-body SRG evolutions in model spaces truncated by $E_{4,\text{SRG}} = 15$ (blue circles), 17 (red diamonds), 19 (green triangles), and 21 (violet squares) and compare the results for subtraction scheme SubB (solid symbols) and SubC (open symbols) for $\alpha = 0.04 \text{ fm}^4$ in Fig. 6.13(a), 0.08 fm^4 (b), and 0.16 fm^4 (c). The black circles correspond to the energies extrapolated to an infinite SRG space and we discuss this extrapolation later, but focus initially on the results obtained in finite SRG spaces.

The ground-state energies for the two subtraction schemes are almost on top of each other, in particular, for the larger $E_{4,\text{SRG}}$. This is remarkable especially in view of the large discrepancies observed without the frequency-conversion approach in Fig. 6.10. In accordance with intuition, the SRG-space dependence slightly increases with increasing flow parameter and shows a similar monotonic convergence pattern for all α values. Moreover, the $E_{4,\text{SRG}}$ convergence is strongly improved by the frequency-conversion approach. If we include only the $J_{123} = 0$ contributions, i.e., $PW = 1 - 6$, we achieve good convergence, where the $PW = 6$ results for $E_{4,\text{SRG}} = 19$ and 21 differ by about 1 MeV but rapidly decrease with increasing $E_{4,\text{SRG}}$. The 4N contributions up to $PW = 6$ seem to be too small to explain a flow-parameter dependence of about 10 MeV that appears for the N_{max} converged results when we omit all 4N contributions. This is interesting,

since for ^{16}O one might have assumed that the ^4He -channel provides the dominant contributions. The results in Fig. 6.10 indicate that it is important to include $J_{123} > 0$ contributions as well. Including the partial waves with $J_{123} = 1$ increases the SRG-space dependence considerably, such that for the two largest SRG spaces the deviation of the $\text{PW} = 12$ results are about 4 – 7.5 MeV, increasing with the flow parameter.

However, the SRG-space dependence rapidly and monotonically decreases with $E_{4,\text{SRG}}$, such that we can extrapolate the ground-state energies to an infinite SRG space (black circles). We use an exponential fit of the results of the three largest SRG spaces. The error is conservatively estimated by the deviation from the energies in the largest SRG space and reflects the quality of the SRG-space convergence. In particular, the inclusion of the $(J_{123}^\pi T_{123}) = (1^-1)$ channel (i.e., $\text{PW} = 9$) increases the extrapolation error. Interestingly, the $(J_{123}^\pi T_{123}) = (1^-0)$ channel (i.e., $\text{PW} = 8$) leads to a strong repulsive effect that increases with the flow parameter.

To make quantitative conclusions about the induced 4N effects it is advisable to increase the many-body model space, since the change of the ground-state structure has an impact on the 4N effects. Thus, we study the 4N effects as function of N_{max} in the next section.

6.4.3 Final Results

The frequency-conversion approach in combination with the extrapolation to infinite SRG spaces enables the access to the induced 4N contributions for all partial waves with $J_{123} \leq 1$. In the following, we study the effect of the induced 4N forces for different Hamiltonians and p-shell nuclei in IT-NCSM calculations as function of N_{max} . We also focus on the flow-parameter dependence, which is expected to be reduced or even vanish by including the induced 4N contributions.

We compare the ^{16}O ground-state energy obtained with the $\text{NN}+3\text{N}_{\text{full}}$ Hamiltonian in Fig. 6.14 (a) to those obtained with the $\text{NN}+3\text{N}_{\text{full}}+4\text{N}_{\text{ind}}$ Hamiltonians, where we included all 4N contributions with $J_{123} = 0$ in Fig. 6.14 (b) and $J_{123} \leq 1$ in Fig. 6.14 (c). We start with the standard $\text{NN}+3\text{N}$ interaction for $\Lambda_{3\text{N}} = 500 \text{ MeV}/c$ and evolve it in four-body space truncated by $E_{4,\text{SRG}} = 21$ at $\hbar\Omega_{\text{SRG}} = 40 \text{ MeV}$. Subsequently we use the frequency conversion to construct the interaction matrix elements at $\hbar\Omega = 24 \text{ MeV}$ that are applied in the many-body calculation up to $E_{4,\text{max}} = 6$. The results correspond to $\alpha = 0.04 \text{ fm}^4$ (blue circles), 0.08 fm^4 (red diamonds), and 0.16 fm^4 (green triangles). To confirm the insensitivity to the subtraction procedure we compare in panel in Fig. 6.14 (b) and (c) the results obtained by using the schemes SubB (solid symbols) and SubC (open symbols), which are essentially on top of each other.

As observed in the previous section, the 4N contributions with $J_{123} = 0$ in Fig. 6.14 (b) have an almost negligible effect. The repulsion to the converged result caused by these contributions corresponds to about 0.6, 1.0, and 1.6 MeV for the flow-parameter values $\alpha = 0.04, 0.08,$ and 0.16 fm^4 , respectively, leading to a slight reduction of the flow-parameter dependence. The

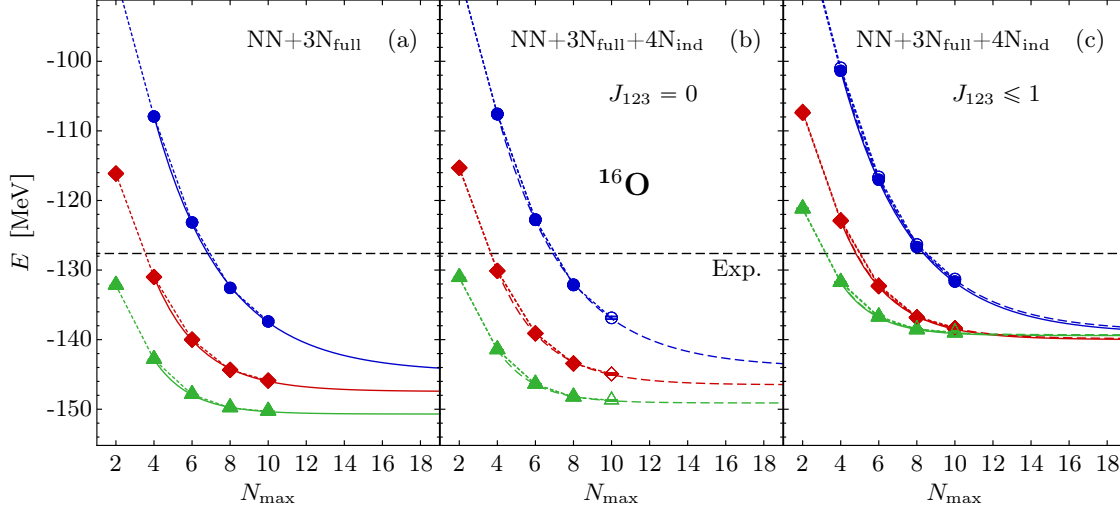


Figure 6.14 *Effect of the induced $4N$ contributions for the ^{16}O ground-state energy:* Illustrated is the ^{16}O ground-state energy calculated with the IT-NCSM at $\hbar\Omega = 24$ MeV as function of the N_{max} . We compare the results for the standard $\text{NN}+3\text{N}_{\text{full}}$ Hamiltonian (a) with those obtained for included $4N$ contributions of all partial waves with $J_{123} = 0$ (b) and $J_{123} \leq 1$ (c) using the flow parameters $\alpha = 0.04 \text{ fm}^4$ (\bullet/\circ), 0.08 fm^4 (\blacklozenge/\diamond), and 0.16 fm^4 (\blacktriangle/\triangle), as well as $E_{4,\text{max}} = 6$. The four-body SRG evolution is performed with $E_{4,\text{SRG}} = 21$ at $\hbar\Omega_{\text{SRG}} = 40$ MeV using the frequency-conversion approach and the subtraction scheme SubB (solid symbols) and SubC (open symbols). The solid and dashed curves correspond to the N_{max} -extrapolated results for the SubB and SubC scheme, respectively. See text for further information.

$J_{123} = 0$ contributions are rather well converged with respect to the SRG space. To conclude about the $E_{4,\text{SRG}}$ we also calculate the ground-state energies for $E_{4,\text{SRG}} = 19$. The converged results differ from those with $E_{4,\text{SRG}} = 21$ in the figure by about 0.5 MeV, such that the $J_{123} = 0$ contribution obtained in an infinite SRG space have a slightly smaller impact. Therefore, we focus on the induced $4N$ forces including also the $J_{123} = 1$ contributions (c). This inclusion leads to sizable repulsive effects that almost completely reduce the flow-parameter dependence from 6 MeV to less than 800 keV for the considered α regime.

Note that the $J_{123} = 1$ contributions are not fully converged with respect to the SRG space. We illustrate the lack of convergence in Fig. 6.15, where the ^{16}O ground-state energies of Fig. 6.14(c) for $\alpha = 0.08 \text{ fm}^4$, subtraction scheme SubB and $E_{4,\text{SRG}} = 21$ (violet squares) are compared to those obtained with $E_{4,\text{SRG}} = 19$ (green triangles). The discrepancy slightly increases with N_{max} from about 6 to 7.5 MeV. In principle, one can extrapolate the ground-state energy to an infinite SRG space by performing the IT-NCSM calculations for the smaller $E_{4,\text{SRG}}$ and use the results for an exponential fit to $E_{4,\text{SRG}} \rightarrow \infty$. Such an extrapolation procedure requires multiple many-body calculations for each parameter set. In order to obtain a first impression we perform an extrapolation exclusively for the $N_{\text{max}} = 2$ results, yielding an estimate for the ground-state energy shift from $E_{4,\text{SRG}} = 21$ to the infinite SRG space. Eventually, we add this shift to the

ground-state energies for the larger N_{\max} and use the energy shift as a conservative estimate of error from the extrapolation of the SRG space. The corresponding results for the infinite SRG spaces are indicated by the black circles in Fig. 6.15. Note that the discrepancy of the $E_{4,\text{SRG}} = 19$ and $E_{4,\text{SRG}} = 21$ ground-state energy is slightly dependent on N_{\max} . Therefore, a separate extrapolation for each N_{\max} is recommended when aiming at an improved estimate of the induced 4N-force effects.

After the elimination of the sensitivity to the subtraction procedure as well as the reduction and quantification of the uncertainty due to the remaining SRG-space dependence we are left with the $E_{4,\max}$ truncation. To provide all four-body matrix elements that appear in an N_{\max} many-body model space for ^{16}O one requires the 4N contributions up to $E_{4,\max} = N_{\max} + 4$. With increasing $E_{4,\max}$ the many-body Hamilton matrix becomes less sparse, such that the computational demands of the NCSM-type calculations increase [100]. In this section we typically use a four-body truncation of $E_{4,\max} = 6$. To validate this truncation Fig. 6.15 also shows ground-state energies obtained for $E_{4,\max} = 8$ for the largest SRG space. The $E_{4,\max} = 6$ (solid symbols) and $E_{4,\max} = 8$ (open symbols) are almost on top of each other indicating that this truncation causes negligible uncertainties compared to those of the SRG-space dependence. Nevertheless, the uncertainty of the $E_{4,\max}$ truncation increases with N_{\max} and for high-precision applications one needs to increase $E_{4,\max}$ further.¹⁵

To verify the four-body developments, from the SRG evolution in the Jacobi-HO representation over the frequency conversion to the transformation into the JT coupled scheme, we study initial interactions that are expected to induce 4N forces with minor or vanishing effects. In Fig. 6.16 we compare the ^{16}O ground-state energies obtained without 4N forces (left panels) to the results including all four-body partial waves with $J_{123} \leq 1$ (right panels). We start with the NN (upper panels) and NN+3N interactions for $\Lambda_{3\text{N}} = 400 \text{ MeV}/c$ (middle panel) and $500 \text{ MeV}/c$ (lower panels). Further parameters of the SRG evolution and IT-NCSM calculation are chosen as in Fig. 6.14 using exclusively subtraction scheme SubB.

The results for the NN+3N interaction for $\Lambda_{3\text{N}} = 500 \text{ MeV}/c$ in Fig. 6.16 (e,f) are identical to those shown in Fig. 6.14. In comparison to this initial interaction the other two interactions are expected to cause an almost vanishing induced 4N effect, indicated by the small flow-parameter dependence for the results without 4N contributions. Surprisingly, the included 4N forces obtained for $E_{4,\text{SRG}} = 21$ lead to a rather large repulsion that increases the flow-parameter dependence. To understand this observation it is important to note that also the NN and NN+3N interactions with $\Lambda_{3\text{N}} = 400 \text{ MeV}/c$ induce 4N contributions during the SRG, which have a small but not completely vanishing effect to the ^{16}O ground-state energy. For instance in Sec. 7 we show that these 4N contribution have a sizable impact for heavier nuclei. Therefore,

¹⁵With the current implementation the four-body matrix elements in the JT -coupled scheme can be produced up to $E_{4,\max} = 10$ on a single node. But to reduce the computational cost of the many-body calculations we typically include the four-body matrix elements only up to $E_{4,\max} = 6$.

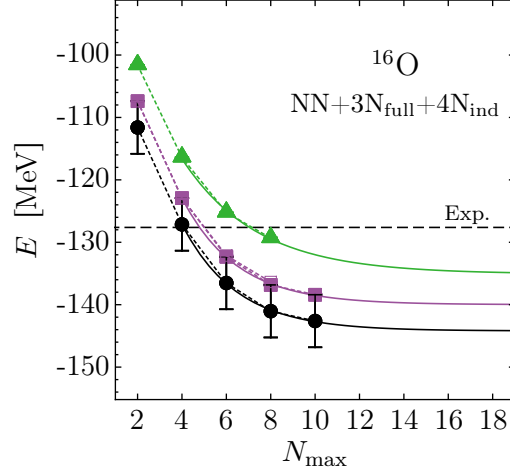


Figure 6.15 *Extrapolation to infinite SRG space*: Illustrated are the ^{16}O ground-state energies for the $\text{NN}+3\text{N}_{\text{full}}+4\text{N}_{\text{ind}}$ Hamiltonian, starting from the standard $\text{NN}+3\text{N}$ interaction and including all induced 4N contributions with $J_{123} \leq 1$. The four-body SRG evolution is performed in the SRG spaces $E_{4,\text{SRG}} = 19$ (\blacktriangle) and 21 (\blacksquare/\square) for $\alpha = 0.08 \text{ fm}^4$. The 4N contributions are included up to $E_{4,\text{max}} = 6$ (solid symbols) and $E_{4,\text{max}} = 8$ (open symbols). Further we used $\hbar\Omega_{\text{SRG}} = 40 \text{ MeV}$, $\hbar\Omega = 24 \text{ MeV}$ and subtraction scheme SubB. The black circles correspond to the results achieved by an extrapolation to infinite SRG space as described in the text. The solid curves corresponds to the N_{max} -extrapolated results.

the four-body SRG-space truncation might lead to an artificial repulsion as well. In fact, if one studies the convergence with respect to the SRG space, one finds a similar convergence pattern as in the previous sections for the standard $\text{NN}+3\text{N}$ interaction.

To account for this effect we perform a schematic extrapolation to infinite SRG spaces, as discussed above, and illustrate the corresponding results for all three interactions in Fig. 6.17. As expected the extrapolation to infinite four-body SRG space lowers the energy compared to the energies for $E_{4,\text{SRG}} = 21$ in Fig. 6.16. The ground-state energies for the initial NN interaction in Fig. 6.17 (a) and (b) agree within the error of the SRG-space extrapolation, which confirms that the 4N contributions are under control for the included four-body partial waves.

For the initial $\text{NN}+3\text{N}$ interactions the 4N forces are repulsive and lead to a reduction of the flow-parameter dependence, in particular, for the $\Lambda_{3\text{N}} = 500 \text{ MeV}/c$ case. It is important to note that by including the induced 4N contribution with $J_{123} \leq 1$ we achieve a flow-parameter independent result within the uncertainties for all initial interactions. This indicates that effects of omitted four-body partial waves with $J_{123} \geq 2$ and also higher many-nucleon contributions beyond the 4N level are smaller than the conservatively estimated errors of the SRG-space extrapolation.

Finally, we study the effect of induced 4N contribution for different p-shell nuclei. We compare

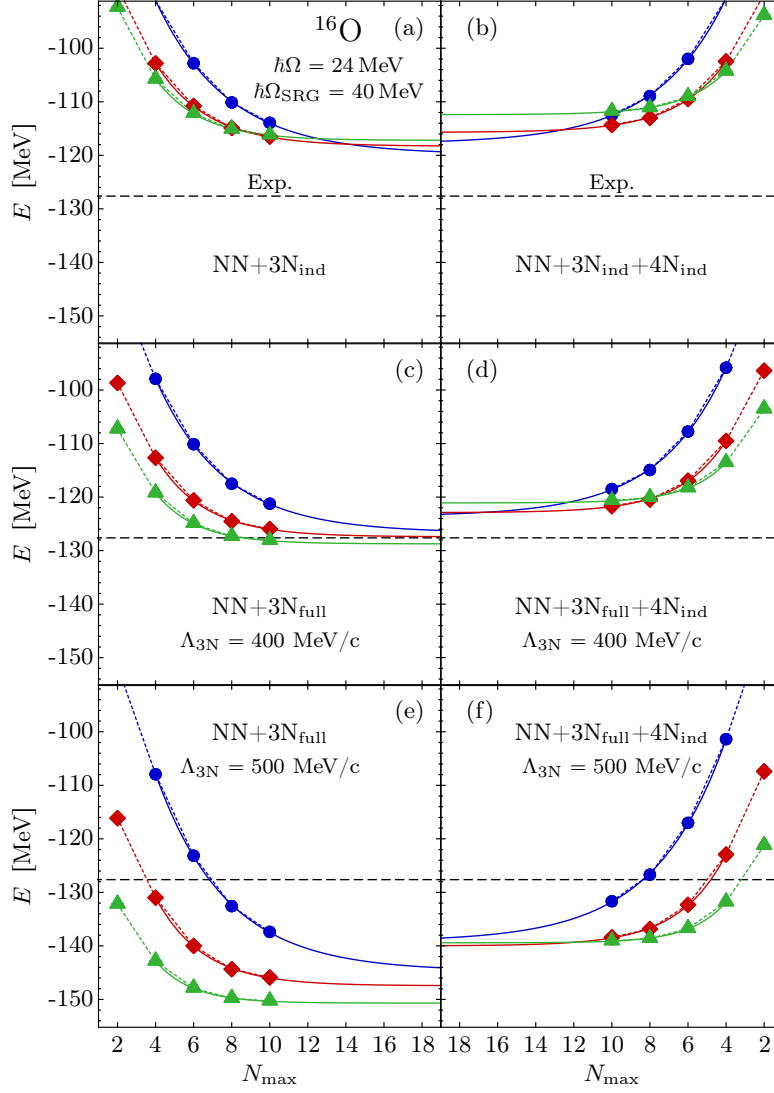


Figure 6.16 *Effect of the induced 4N contributions for the ^{16}O ground-state energy:* We compare the flow-parameter dependence (color code as in Fig. 6.14) of the ^{16}O ground-state energy performing the SRG evolution up to the three- (left panels) and four-body space (right panels) for the standard initial NN interaction (upper panels) as well as for the initial NN+3N interactions with $\Lambda_{3\text{N}} = 400 \text{ MeV}/c$ (middle panels) and $\Lambda_{3\text{N}} = 500 \text{ MeV}/c$ (lower panels). The IT-NCSM calculations are performed at $\hbar\Omega = 24 \text{ MeV}$. All four-body partial waves with $J_{123} \leq 1$ are included using $E_{4,\text{SRG}} = 21$, $\hbar\Omega_{\text{SRG}} = 40 \text{ MeV}$, $E_{4,\text{max}} = 6$ and subtraction scheme SubB.

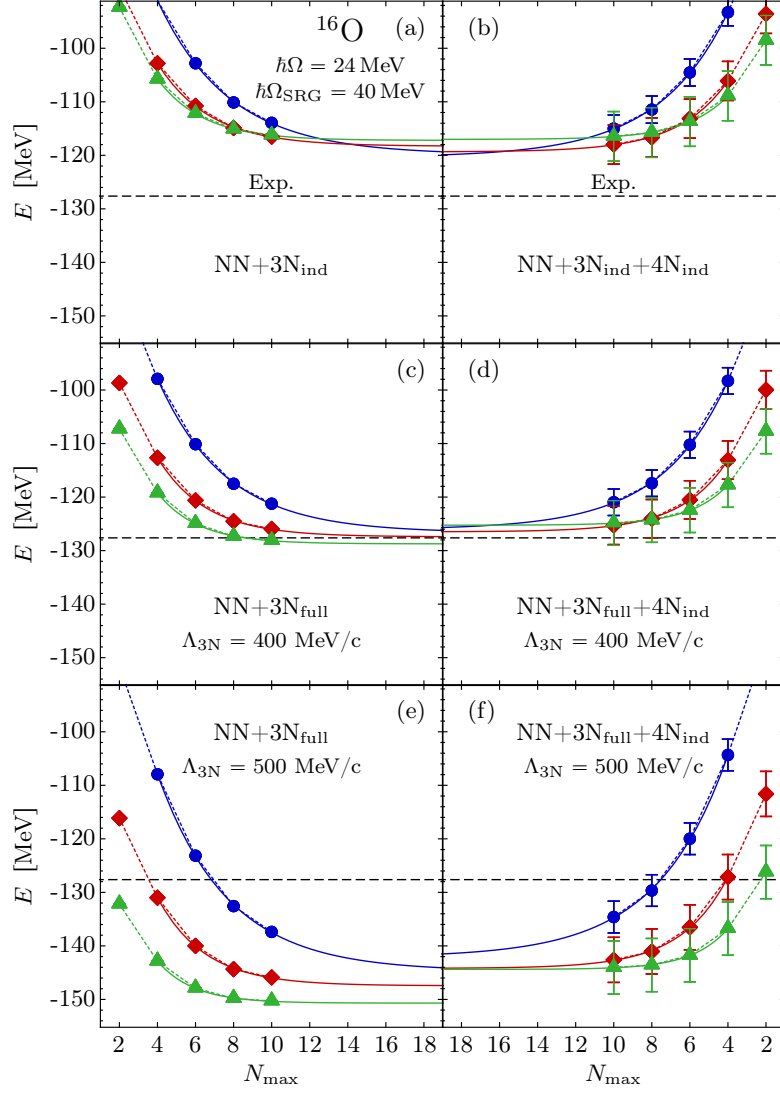


Figure 6.17 ^{16}O ground-state energies with extrapolated induced $4N$ contributions: We compare the flow-parameter dependence (color code as in Fig. 6.14) of the ^{16}O ground-state energy performing the SRG evolution up to the three- (left panels) and four-body space (right panels) for the standard NN interaction (upper panels) as well as for the NN+3N interactions with $\Lambda_{3N} = 400$ MeV/c (middle panels) and $\Lambda_{3N} = 500$ MeV/c (lower panels). The 4N contributions are included for all partial waves with $J_{123} \leq 1$ using the extrapolation to infinite SRG spaces. The solid curves correspond to the N_{\max} -extrapolated results. See text for more information.

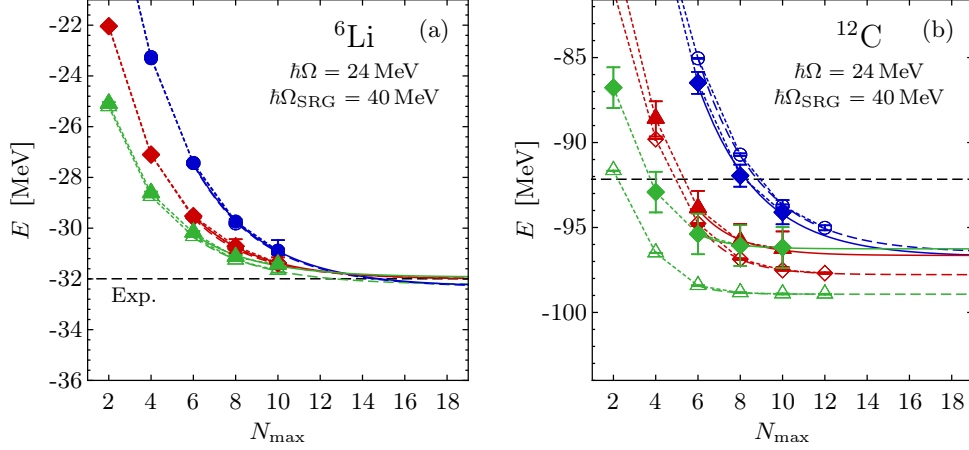


Figure 6.18 *Induced 4N contributions in ${}^6\text{Li}$ and ${}^{12}\text{C}$* : Plotted are the ground-state energies calculated with the IT-NCSM of ${}^6\text{Li}$ (a) and ${}^{12}\text{C}$ (b) for the standard NN+3N $_{\text{full}}$ Hamiltonian (open symbols) and the NN+3N $_{\text{full}}$ +4N $_{\text{ind}}$ Hamiltonian (solid symbols). The solid and dashed curves correspond to the N_{\max} -extrapolated results with and without induced 4N contributions, respectively. Further parameters are chosen as in Fig. 6.17.

the ground-state energies of ${}^6\text{Li}$ in Fig. 6.18 (a) and ${}^{12}\text{C}$ in Fig. 6.18 (b) for the NN+3N $_{\text{full}}$ (open symbols) and NN+3N $_{\text{full}}$ +4N $_{\text{ind}}$ (solid symbols) Hamiltonian, starting from the standard NN+3N interaction with $\Lambda_{3\text{N}} = 500$ MeV/ c . The IT-NCSM calculation and SRG evolution are performed with the same parameters as in Fig. 6.17, where the 4N contributions are extrapolated to infinite $E_{4,\text{SRG}}$. The results correspond to the flow-parameter values $\alpha = 0.04$ fm 4 (blue circles), 0.08 fm 4 (red diamonds), and 0.16 fm 4 (green triangles). The ${}^6\text{Li}$ ground-state energy is essentially not effected by the induced 4N forces and the converged results are independent of the flow parameter. As indicated by the small error bars for the NN+3N $_{\text{full}}$ +4N $_{\text{ind}}$ Hamiltonian the four-body SRG space for $E_{4,\text{SRG}} = 21$ is sufficiently large to cover the relevant contributions. The ${}^{12}\text{C}$ ground-state energy shows a noticeable flow-parameter dependence without the induced 4N contributions. Analogously to the ${}^{16}\text{O}$ the inclusion of the $J_{123} \leq 1$ 4N contributions leads to a repulsive effect that suppresses the flow-parameter dependence.

In summary, this work presents the first application of 4N forces in nuclear structure calculations and focuses on a prove of concept to lay the foundation for future calculations with induced as well as initial 4N forces. With the developed four-body machinery we are able to include all induced 4N contributions with $J_{123} \leq 1$ with controlled uncertainties and moderate computational costs. While the $J_{123} = 0$ contributions have only a minor effect, the inclusion of the $J_{123} = 1$ contributions yields approximately flow-parameter independent results, within the estimated uncertainties, for all initial interactions and p-shell nuclei that we have been considered in this section. This indicates that we can include the dominant induced 4N forces in ab initio nuclear structure calculations. The NN+3N $_{\text{full}}$ +4N $_{\text{ind}}$ results for the standard NN+3N interaction with $\Lambda_{3\text{N}} = 500$ MeV/ c have uncertainties of the order of the flow-parameter depen-

dence of the NN+3N_{full} results. Nevertheless, the inclusion of the induced 4N forces indicate that the initial Hamiltonian overbinds the experimental ground-state energy by about 4 MeV and 10 MeV for ¹²C and ¹⁶O, respectively.

Unfortunately, the uncertainties due to the SRG-space truncation do not allow to resolve the effect of the omitted $J_{123} \geq 2$ or possibly induced beyond-4N contributions. To reduce the uncertainties further one can increase the four-body SRG space as discussed above. Due to rapid convergence with respect to $E_{4,\text{SRG}}$ one should achieve sufficiently small extrapolation errors in feasible SRG spaces. If the $J_{123} \geq 2$ contributions become accessible by such a procedure remains questionable, in particular, because their effects in the p shell seem to be rather small and, thus, require a highly accurate treatment. Nevertheless, to estimate the contributions for the larger angular momenta one can aim at the inclusion of selected partial waves that do not significantly increase the SRG-space dependence.

7 NN+3N forces in Medium-Mass and Heavy Nuclei

The major obstacle for the use of chiral NN+3N interactions in ab initio nuclear structure calculations are the SRG-induced contributions beyond the three-body level that have a sizable effect beyond the mid-p shell. Hence, reliable predictions for ground-state energies using the standard NN+3N interaction with the cutoff $\Lambda_{3N} = 500 \text{ MeV}/c$ are restricted to p-shell nuclei. In the previous section we have discussed the emergence, origin, and treatment of SRG-induced 4N forces. The explicit inclusion of the 4N forces without an intermediate normal-ordering approximation is so far restricted to applications in the p shell using the IT-NCSM. While there will be exciting future developments in these directions, the suppression of the induced many-body forces by reducing the three-body cutoff to $\Lambda_{3N} = 400 \text{ MeV}/c$ extends the range of applicability to heavier nuclei and has led to several publications [23, 28–30, 35, 36, 145].

An important example is the systematic analysis of the oxygen isotopic chain [36], illustrated in Fig. 7.1, where we compare the ground-state energies of all even oxygen isotopes from the proton to the neutron drip line, obtained with different ab initio many-body methods. The details of the calculations can be found in the figure caption and in Ref. [36]. The application of the initial chiral NN interaction by using the NN+3N_{ind} Hamiltonian in Fig. 7.1 (a) leads to a systematic underbinding of the experimental values. Remarkably, the inclusion of the initial chiral 3N interaction with $\Lambda_{3N} = 400 \text{ MeV}/c$ in Fig. 7.1 (b) improves the description dramatically. Except for larger deviations in ^{12}O and ^{26}O , the experimental binding energies are reproduced within 2 – 3 MeV, revealing the predictive power of the chiral interactions and highlighting the importance of the chiral 3N forces. Even more impressive is that the different many-body methods provide a consistent description indicating that in terms of the many-body approaches this mass regime is well under control. By starting from the same Hamiltonian one can benchmark novel approaches such as the extension of the in-medium similarity renormalization group (IM-SRG) [34, 35], i.e., the multi-reference IM-SRG in the two-body normal ordering approximation (MR-IM-SRG(2)) [36], to established methods such as the IT-NCSM as well as the coupled cluster with singles and doubles (CCSD) and perturbative triples corrections ($\Lambda\text{CCSD(T)}$) [28–30, 93–95]. These calculations verify the reliability of the many-body methods, prove the ability of the chiral interactions to predict the neutron drip line in the oxygen isotopic chain and motivate the study of heavier nuclei.

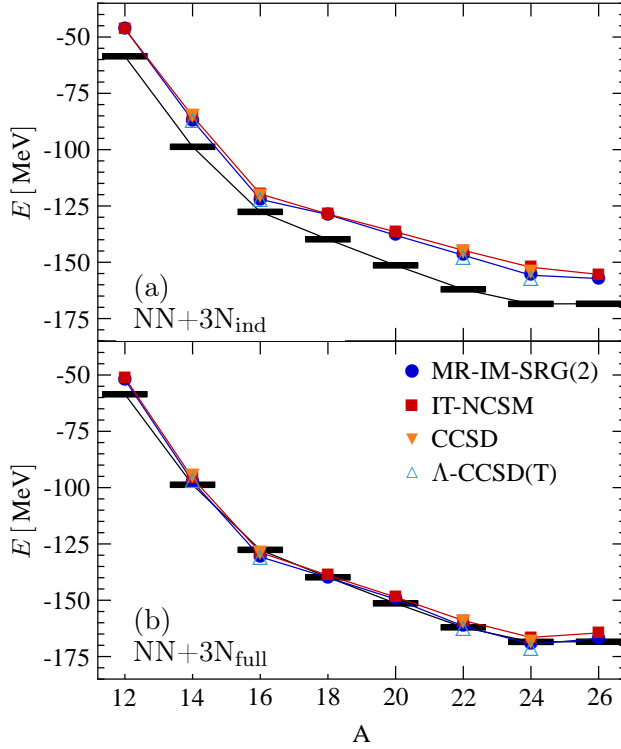


Figure 7.1 *Ground-state energies of the oxygen isotopic chain*: Plotted are the ground-state energies for the even oxygen isotopes with mass number $A = 12 - 26$, using the $NN+3N_{\text{ind}}$ (upper panel) and the $NN+3N_{\text{full}}$ Hamiltonian (lower panel) with $\Lambda_{3N} = 400 \text{ MeV}/c$. The Hamiltonians are SRG evolved using ramp \mathcal{A} up to $\alpha = 0.08 \text{ fm}^4$. The curves correspond to different ab initio many-body methods. The IT-NCSM energies are obtained by calculations up to $N_{\text{max}} = 12$ using a subsequent exponential extrapolation to infinite model space, the MR-IM-SRG(2), CCSD, and Λ CCSD(T) results, are obtained in a many-body model space truncated by $e_{\text{max}} = 14$. All calculations are performed at optimal HO frequencies. The black bars indicate the experimental values [170,171]. For further details see Ref. [36], where the results are published.

7.1 Normal-Ordering Approximation

The rapidly growing number of three-body interaction matrix elements with increasing $E_{3,\text{max}}$, presents a serious limitation for their explicit inclusion in large many-body model spaces. Moreover, the explicit inclusion of 3N interactions typically requires non-trivial formal extensions of the medium-mass methods. Thus, a crucial step towards the application of chiral 3N interactions beyond p- and sd-shell nuclei is the reduction of the 3N information to a lower particle-rank interaction. For this purpose we use the normal-ordering approximation discussed in Sec. 3.3 and study its quality.

In Fig. 7.2 we illustrate the expectation values of the 3N interaction with respect to the ground state of ${}^4\text{He}$, ${}^{16}\text{O}$, and ${}^{40}\text{Ca}$. The eigenstates are obtained in IT-NCSM calculations for a fixed

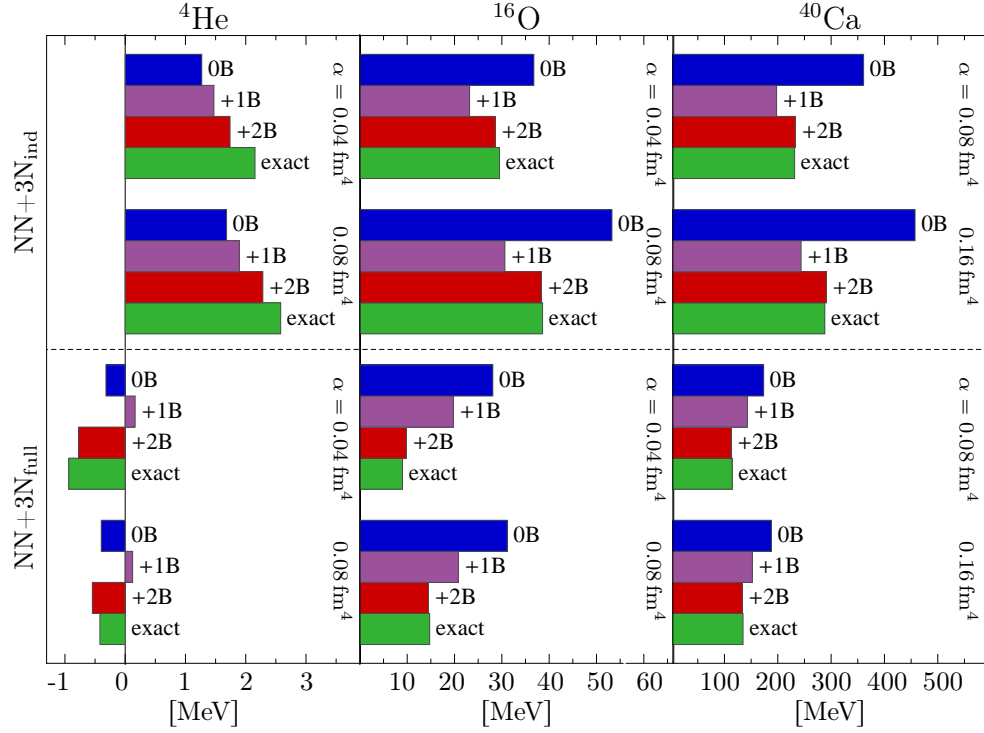


Figure 7.2 *Anatomy of the NOnB approximation*: Illustrated are the expectation values of the 3N interaction computed at different levels of the normal-ordering approximation, i.e., NO0B, NO1B, NO2B as well as using the exact 3N interaction. The eigenstates correspond to the ground states of ${}^4\text{He}$ and ${}^{16}\text{O}$ obtained in an IT-NCSM calculation using $N_{\text{max}} = 10$, as well as to ${}^{40}\text{Ca}$ using $N_{\text{max}} = 8$. We use $\hbar\Omega = 20$ MeV for all calculations. We investigate the anatomy of the 3N interaction using the $\text{NN}+3\text{N}_{\text{ind}}$ and $\text{NN}+3\text{N}_{\text{full}}$ Hamiltonian for two flow-parameter values (see labels). The interaction is normal-ordered regarding the unperturbed HO Slater determinant. The results are published in Ref. [145].

N_{max} at $\hbar\Omega = 20$ MeV using the $\text{NN}+3\text{N}_{\text{ind}}$ and $\text{NN}+3\text{N}_{\text{full}}$ Hamiltonians for two flow-parameter values and treating the 3N contributions explicitly. The 3N interactions used to evaluate the expectation value result from a normal-ordered n -body approximation (NOnB) with $n = \{0, 1, 2\}$ or are used without approximations, i.e., “exact”. The normal ordering is performed with respect to the unperturbed HO Slater determinant.

We discuss the anatomy of the expectation values with respect to the additional n -body (n B) terms that appear at NOnB. Note that the expectation values in Fig. 7.2 result for the sum of NO terms up to the n B level. For ${}^{16}\text{O}$ and ${}^{40}\text{Ca}$ the expectation values show a similar pattern, while the zero-body (0B) term provides the largest positive contribution, the one-body (1B) contribution is negative and reduces the expectation value. The absolute value and sign of the two-body (2B) contribution depend on the inclusion of the initial 3N interaction and have almost the same magnitude for the $\text{NN}+3\text{N}_{\text{full}}$ Hamiltonian. It is important to note that the additional three-body (3B) terms of the exact 3N treatment have only a minor effect, indicating the NO2B approximation to be accurate. The choice of the flow parameter slightly influences

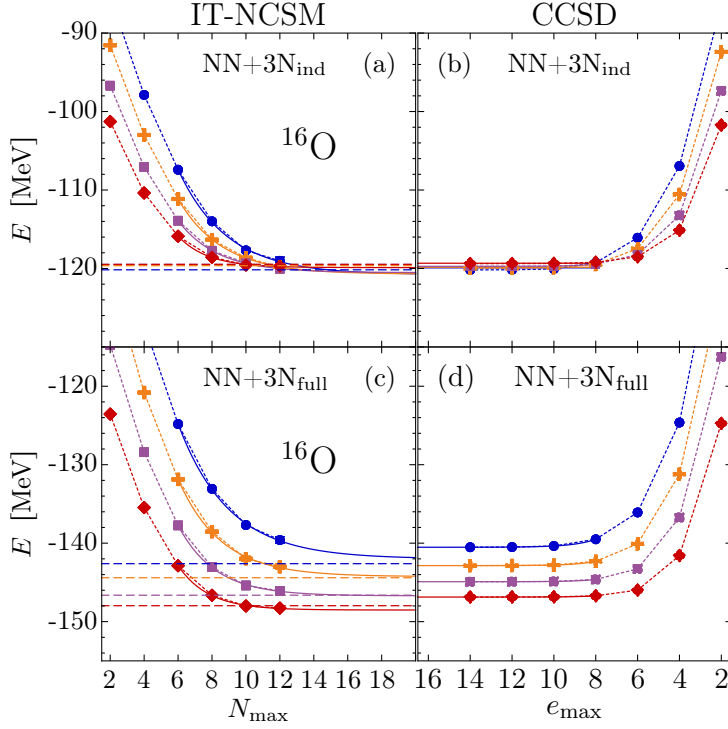


Figure 7.3 *Benchmark of CCSD with the IT-NCSM*: We compare the ground-state energies of ^{16}O obtained in IT-NCSM and CCSD calculations including 3N interactions in the NO2B approximation for the $\text{NN}+3\text{N}_{\text{ind}}$ and the $\text{NN}+3\text{N}_{\text{full}}$ Hamiltonians. The SRG evolution is performed for $\alpha = 0.04 \text{ fm}^4$ (\bullet), 0.05 fm^4 (\oplus), 0.0625 fm^4 (\blacksquare), and 0.08 fm^4 (\blacklozenge), starting from the standard initial NN or NN+3N interaction. The dashed horizontal lines correspond to the converged IT-NCSM results, treating the 3N contributions exactly (the flow-parameters are indicated by the same color coding as for the NO2B results). We use $E_{3,\text{max}} = 14$ and $\hbar\Omega = 20 \text{ MeV}$. Solid curves indicate the N_{max} -extrapolated results. The results are published in Ref. [145].

the deviation, but does not change the general trend.

The picture is different for the lightest nucleus, i.e., the ^4He ground-state expectation values. In particular the inclusion of the initial 3N interaction changes the pattern completely, such that the 0B term does not necessarily provide the largest contribution. This indicates that there is no universal hierarchy of the individual $\text{NO}n\text{B}$ contributions for this nucleus. Moreover, the deviation of the NO2B approximation from the exact 3N treatment is noticeable and depend on the Hamiltonian and the flow parameter. Nonetheless, these studies demonstrate that the NO2B approximation is very accurate beyond the lightest nuclei. We have published these investigations of the normal-ordering approximation in Ref. [145].

Since the IT-NCSM is typically limited to nuclei in the sd shell (see Sec. 2.2) we use the CC approach (see Sec. 2.3) for heavier nuclei. We demonstrate the agreement of the CC approach with the exact IT-NCSM in more detail in Fig. 7.3. Shown are the ^{16}O ground-state energies obtained with the IT-NCSM (left panels) and the CCSD (right panels) for the $\text{NN}+3\text{N}_{\text{ind}}$ (upper

panels) and $\text{NN}+3\text{N}_{\text{full}}$ Hamiltonian (lower panels). We use different flow-parameter values and include the 3N interaction in the NO2B approximation, where the normal ordering is performed with respect to the unperturbed HO Slater determinant.

In Fig. 7.3 (a) and (c) we compare the N_{max} -extrapolated results (solid curves) with the NO2B approximation to the converged IT-NCSM results obtained with the exact treatment of the 3N interaction (dashed horizontal lines). For the $\text{NN}+3\text{N}_{\text{ind}}$ Hamiltonian the NO2B approximation leads to an overestimation of the binding energy by less than 1 MeV for all flow parameters. For the $\text{NN}+3\text{N}_{\text{full}}$ Hamiltonian the NO2B approximation leads to an underestimation of the binding energy for the smallest flow parameter, which turns into an overestimation with increasing α . However, the deviations caused by the NO2B approximation are below 1% for the ^{16}O ground-state energy, confirming the reliability of this approximation.

The CCSD method in Fig. 7.3 (b,d) can access large model spaces and achieves an advanced convergence with respect to the model space compared to the IT-NCSM method in Fig. 7.3 (a,b) at substantially reduced computational costs. The CCSD predicts 1 – 2 MeV less binding energy than the IT-NCSM. This slight discrepancy results from missing triples and higher excitations as well as 3N contributions beyond $E_{3,\text{max}} = 14$, which are considered in the IT-NCSM calculations by an extrapolation to infinite model space (solid lines). These are the only additional truncations of the CCSD approach compared to the IT-NCSM calculations (see Refs. [28–30] and, in particular, Ref. [99] for further discussions regarding the CC truncations).

Having determined the errors from the NO2B approximation as well as the further truncations of the CCSD approach to be less than 2% for the ground-state energy of ^{16}O , we can increase the mass number beyond the sd shell and study the effect of the induced many-body contributions in analogy the p-shell investigation in Sec. 6.1. In Fig. 7.4 we illustrate the ground-state energies for ^{16}O , ^{24}O , ^{40}Ca , and ^{48}Ca as function of e_{max} using the NN_{only} , $\text{NN}+3\text{N}_{\text{ind}}$, and $\text{NN}+3\text{N}_{\text{full}}$ Hamiltonian for a set of flow-parameter values. As in the p shell when starting with the initial NN interaction the induced 3N contributions lead to a sizable repulsion and their inclusion ($\text{NN}+3\text{N}_{\text{ind}}$) provides flow-parameter independent results. Moreover, when we include the standard initial 3N interaction with $\Lambda_{3\text{N}} = 500 \text{ MeV}/c$ (solid symbols) the omitted induced beyond-3N contributions cause a strong flow-parameter dependence that is absent when using the initial 3N interaction with the reduced cutoff $\Lambda_{3\text{N}} = 400 \text{ MeV}/c$ (open symbols). With the exception of ^{48}Ca , where the $\text{NN}+3\text{N}_{\text{ind}}$ Hamiltonian already provides an accurate description of the ground-state energy, the attractive effect of the initial 3N interaction with the reduced cutoff improves the description of the experimental ground-state energy (dashed horizontal line).

It is important to note that the calculations contain truncations that need to be verified for applications beyond the p shell in order to make quantitative conclusions. In the next section we discuss and improve on these truncations. For instance, we show in the following that the almost perfect flow-parameter independence of the ground-state energies with the $\text{NN}+3\text{N}_{\text{ind}}$ Hamil-

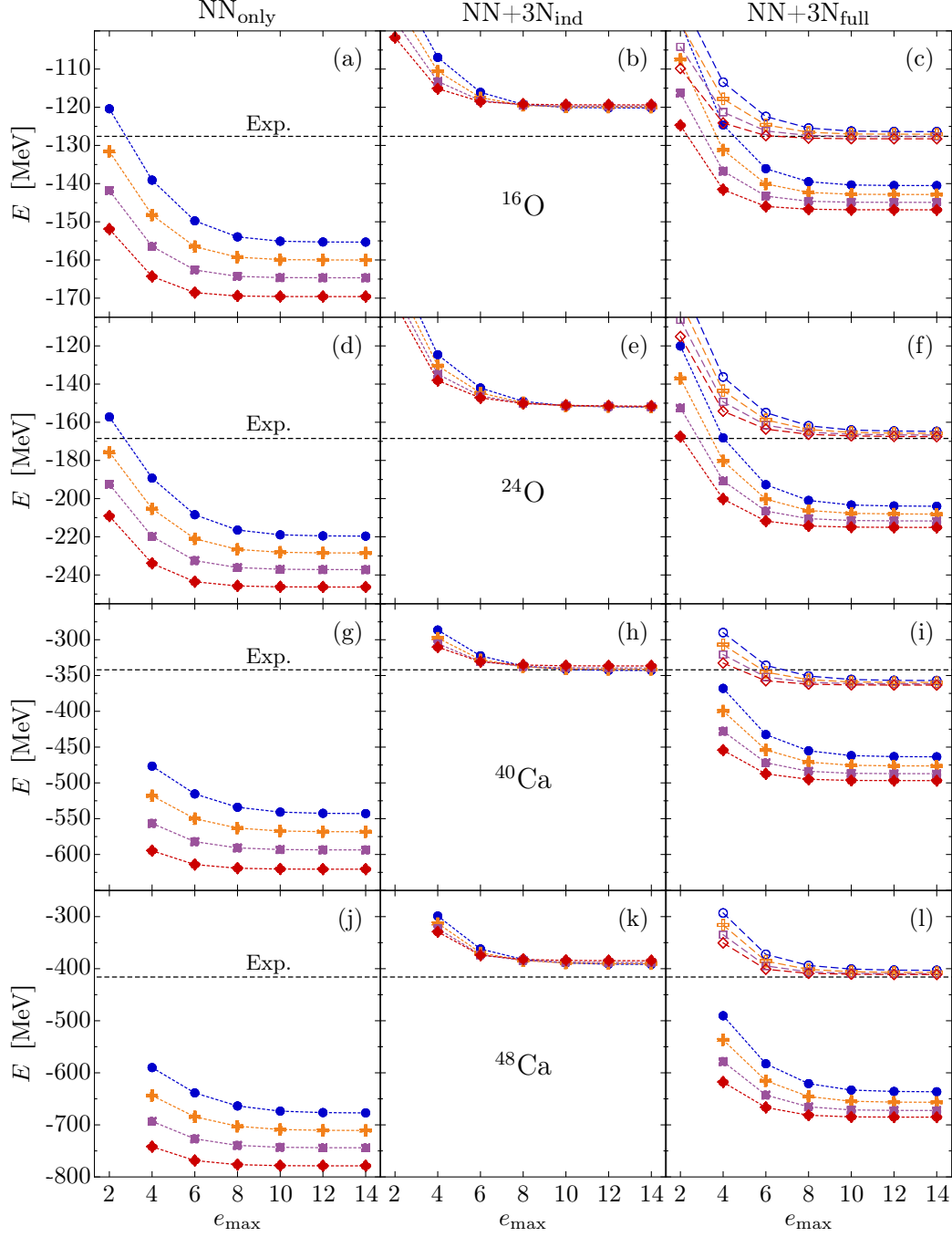


Figure 7.4 *Ground-state energies with CCSD beyond the p-shell nuclei:* We illustrate ground-state energies of ^{16}O , ^{24}O , ^{40}Ca , and ^{48}Ca using NN_{only} , $\text{NN}+3\text{N}_{\text{ind}}$, and $\text{NN}+3\text{N}_{\text{full}}$ Hamiltonians. The filled symbols for the $\text{NN}+3\text{N}_{\text{full}}$ Hamiltonian correspond to the chiral 3N interaction with cutoff 500 MeV/c, the open symbols to the 3N interaction with reduced cutoff 400 MeV/c. Further parameters of the CCSD calculations are chosen as in Fig. 7.3. The dashed horizontal line indicates the experimental value [164] and the results are published in Ref. [145].

tonian is due to a cancellation of different truncation effects, such that the induced beyond-3N forces, which become noticeable in the calcium isotopes, are concealed. Nevertheless, the results in Fig. 7.3 clearly emphasize that the SRG evolution in the three-body space is indispensable for applications of the chiral NN and NN+3N interactions and that the induced 3N contributions have a large impact. Moreover, the beyond-3N contributions that originate from the chiral 3N interaction with the reduced three-body cutoff are moderate over the considered mass range.

7.2 Towards Heavy Nuclei with Coupled Cluster

The NO2B approximation allows for the consideration of the relevant 3N contributions by treating the normal-ordered interaction up to the two-body level. The combination with the reduced three-body cutoff that suppresses the induced many-nucleon contributions enables the application to heavy nuclei. We briefly discuss the truncations in the coupled-cluster (CC) approach that need to be addressed when increasing the mass number and present the final state-of-the-art results for a mass-trend investigation up to heavy tin isotopes.

First of all, the challenges appearing with respect to the SRG evolution due to the increasing importance of three-body partial waves with large angular momenta are discussed in Sec. 5.3. As we have shown in this section calculations beyond the sd shell require a substantial increase of the SRG space. Thus, we use the SRG space denoted by ramp \mathcal{D} (see Fig. 5.7) for a sufficiently large HO frequency of $\hbar\Omega_{\text{SRG}} = 36 \text{ MeV}$, performing a subsequent frequency conversion to $\hbar\Omega = 24 \text{ MeV}$ that is used for the CC calculations. As demonstrated, the uncertainties that originate from the SRG space truncation are well below 1% for the mass regime up to the tin isotopes.

The model-space truncation of the CC calculations by the maximum single-particle energy e_{max} needs to be examined. While the ground-state energies converge rather fast with respect to e_{max} for the medium-mass regime the heavier nuclei require larger model spaces manifested in a slower convergence. For the model space truncations of $e_{\text{max}} = 12$ used in the following, the convergence uncertainties are at the order of 1% for the considered mass range up to ^{132}Sn [30]. The model space defined by $e_{\text{max}} = 12$ in principle contains 3N contributions up to $E_{3,\text{max}} = 36$, which is far beyond reach. It is crucial to study the impact of the $E_{3,\text{max}}$ truncation in the calculations. In order to increase $E_{3,\text{max}}$ as far as possible we perform the normal-ordering approach during the transformation to the single-particle scheme as described in Sec. 3.3. This procedure prevents explicit storage of the 3N interaction matrix elements for such large $E_{3,\text{max}}$ and reduces the number of computed 3N interaction matrix elements to those required for the normal-ordering approach.

Note that the reference state for the normal-ordering procedure follows from a Hartree-Fock calculation with $E_{3,\text{max}} = 14$, which provides an improved approximation of the ground state compared to the unperturbed Slater determinant. However, the reference state contains no

information of 3N contribution with $E_{3,\max} > 14$. Thus, we use the iterative normal-ordered JT -coupling as explained in Sec. 3.3 (see Refs. [99,116]). In order to further reduce the uncertainties related to the normal-ordering approximation the CC method is extended to explicitly include the 3N contributions up to $E_{3,\max} = 12$ [99] and combines them with 3N contributions for the larger energies up to $E_{3,\max} = 18$ in the NO2B approximation.

Finally, it is important to consider the cluster truncation of the CC method, i.e., the restriction to singles and doubles excitations with the CCSD method. Due to the pioneering work in Ref. [99] the 3N contributions in the NO2B approximation can be included to estimate the effect of the triples excitations via an a posteriori correction to the energy using the left-eigenstate completely renormalized coupled-cluster method with singles, doubles and non-iterative triples excitations [134, 135], CR-CC(2,3) for short, or the Λ CCSD(T) [28–30, 93–95] method. The energy contribution of the triples corrections allows to estimate the uncertainty due to the cluster truncation, e.g., by conservatively assuming the effect of higher excitations to be of the order of the triples corrections. An investigation of the uncertainties of the cluster truncation as well as of the normal-ordering approximation is published in Ref. [28].

By novel developments and substantial improvements regarding the interaction matrix elements treatment, i.e., the SRG evolution, the transformation to the JT -coupled scheme, and the normal-ordering approach, as well as regarding the CC method, a new physics regime becomes accessible to ab initio many-body methods with chiral NN+3N interactions. A comprehensive investigation of the listed truncations is published in Ref. [30] and the final results are illustrated in Fig. 7.5, where we plot the ground-state energies per nucleon for several closed-shell nuclei from ^{16}O to ^{132}Sn obtained from the CR-CC(2,3) method. From a careful analysis of all truncations that have been discussed above, the uncertainties are of the order of 2% and increase through the tin isotopes to about 4%. The cluster truncation, indicated by the triples corrections, leads to a rather constant energy contribution per nucleon [30]. This is in agreement with the size extensivity argument of the CC theory [172, 173]. The uncertainties of the remaining truncations grow with the mass number, particularly throughout the tin isotopes, such that ^{132}Sn is identified to be the current limit of ab initio calculations with the presented developments.

Eventually, we come to the interpretation of the results in Fig. 7.5. The boxes indicate the spread of the ground-state energies per nucleon for $\alpha = 0.04\text{ fm}^4$ to 0.08 fm^4 , where the tip points to the smaller flow-parameter value. Typically, the SRG evolution affects the impact of all employed truncations, such that a dependence on the flow parameter might have multiple reasons. However, the uncertainties of all employed truncations, besides the omission of SRG-induced beyond-3N forces, are determined to be of the order of 2 – 4%. Therefore, the flow-parameter dependence can be almost exclusively attributed to the omission of induced beyond-3N contributions. The CR-CC(2,3) calculations for the ground-state energies with the standard NN+3N_{ind} Hamiltonian (upper plot) depict a noticeable flow-parameter dependence already

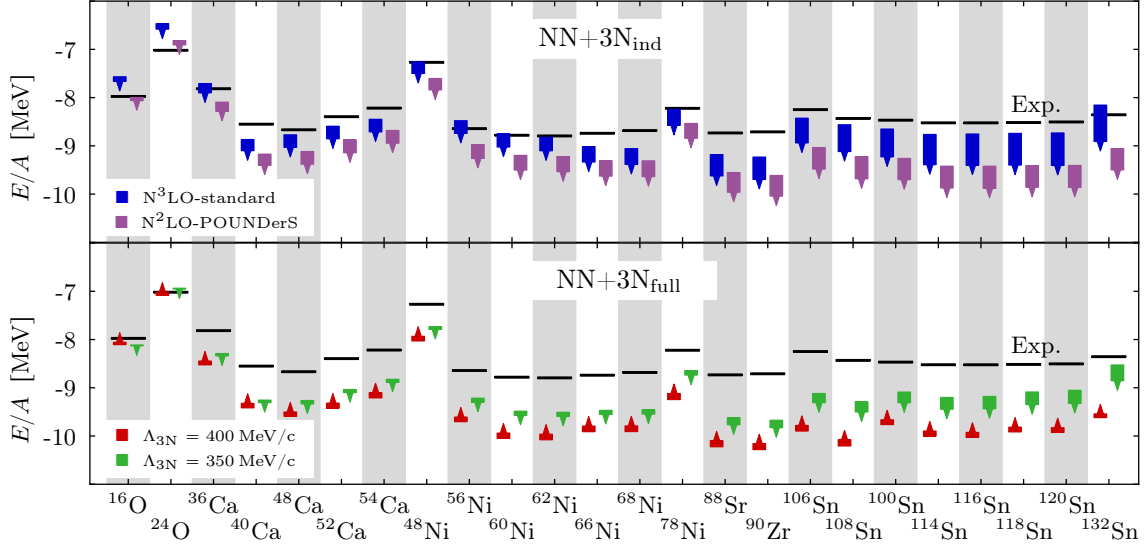


Figure 7.5 *Ground-state energies throughout the nuclear chart*: Illustrated are the ground-state energies per nucleon obtained with the CR-CC(2,3) method for the $\text{NN}+3\text{N}_{\text{ind}}$ Hamiltonian (upper plot) starting from the standard N^3LO and the POUNDerS N^2LO NN interaction and for the standard $\text{NN}+3\text{N}_{\text{full}}$ Hamiltonian (lower plot) with the reduced three-body cutoffs $\Lambda_{3\text{N}} = 400 \text{ MeV}/c$ and $350 \text{ MeV}/c$. The three-body SRG evolution is performed in the significantly larger model space ramp \mathcal{D} (see Fig. 5.7) for $\hbar\Omega_{\text{SRG}} = 36 \text{ MeV}$, subsequently converted to $\hbar\Omega = 24 \text{ MeV}$ that is used in the CC calculations. The boxes represent the spread of the results from $\alpha = 0.04 \text{ fm}^4$ to 0.08 fm^4 . The tip points into the direction of the smaller flow parameter. All results employ the 3N contributions up to $E_{3,\text{max}} = 18$ in NO2B approximation and explicit inclusion of the 3N interaction in CCSD up to $E_{3,\text{max}} = 12$. Black bars correspond to data taken from Ref. [164]. The results are published in Ref. [30].

for the calcium isotopes that increases with the mass number. For ^{132}Sn the deviation for the considered α regime is almost 1 MeV per nucleon. This indicates that the omitted induced beyond-3N contributions that originate from the initial NN interaction have a sizable impact beyond the sd shell and make a reliable prediction of the result for the bare Hamiltonian hardly feasible. In addition, to the standard NN interaction at N^3LO we also present the ground-state energies with the POUNDERs NN interaction at N^2LO , showing a similar pattern regarding the flow-parameter dependence. Therefore, the induced contributions are not a unique property of the standard NN interaction, and the operator structures that cause these contributions already appear in N^2LO . Provided that the impact of the beyond-3N contributions increases monotonously with the flow parameter up to $\alpha = 0.08 \text{ fm}^4$ they become strongly attractive with the mass number, such that the ground-state energies for the bare Hamiltonian considerably overbind the ground states compared to experiment.

The results obtained with the $\text{NN}+3\text{N}_{\text{full}}$ Hamiltonian including the initial reduced-cutoff 3N interactions with $\Lambda_{3\text{N}} = 350 \text{ MeV}/c$ and $400 \text{ MeV}/c$ are surprising. We observe a cancellation of the attractive and repulsive effects of the beyond-3N contributions that originate from the initial NN and 3N interaction, respectively, yielding a moderate dependence on the flow parameter throughout a wide mass range. Provided that the beyond-3N contributions increase with α the direction of the small flow-parameter dependence for $\Lambda_{3\text{N}} = 350 \text{ MeV}/c$ indicate that the net effect of the beyond-3N contributions is attractive, i.e., the induced beyond-3N contributions originating from initial NN interaction a slightly larger than those originating from the initial 3N interaction. In contrast, for $\Lambda_{3\text{N}} = 400 \text{ MeV}/c$ the repulsive beyond-3N contributions from the initial 3N interaction seem to be larger. This is in agreement with the assumption that a lower three-body cutoff suppresses the induced many-nucleon contributions that originate from the initial 3N interaction. This indicates that the beyond-3N contributions from the initial 3N interactions with a three-body cutoff between $\Lambda_{3\text{N}} = 350 \text{ MeV}/c$ and $400 \text{ MeV}/c$ cancel with the beyond-3N contributions from the initial NN interaction.

From the investigation in Sec. 4.7.1 regarding the flow-parameter dependence in ^4He we have observed that the effect of the induced 4N contributions does not necessarily behave monotonically, in particular, for large flow parameters. Of course the behavior can change with the mass number, and it could be that the chosen α range leads to a small flow-parameter dependence by coincidence. It is important to confirm that the flow-parameter dependence remains small also for larger α ranges. Unfortunately, a reduction of the flow parameter increases the uncertainties discussed above. Therefore, we increase the flow-parameter and study the beyond-3N contributions.

In Fig. 7.6 we show the mass trend obtained with the standard NN and $\text{NN}+3\text{N}$ interaction with $\Lambda_{3\text{N}} = 400 \text{ MeV}/c$ and compare the results of the flow-parameter regime of Fig. 7.5 $\alpha = 0.04 - 0.08 \text{ fm}^4$ to $\alpha = 0.08 - 0.16 \text{ fm}^4$. For the $\text{NN}+3\text{N}_{\text{ind}}$ Hamiltonian the induced many-nucleon contributions seem to have an attractive effect monotonously increasing with the flow

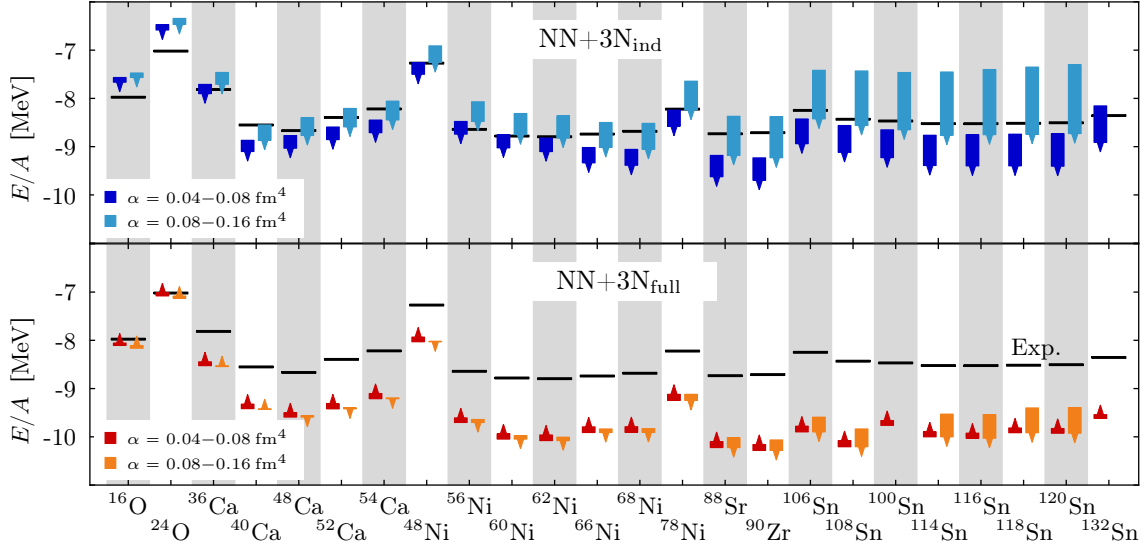


Figure 7.6 *Ground-state energies throughout the nuclear chart*: In addition to the results with the standard $\text{NN}+3\text{N}_{\text{ind}}$ and $\text{NN}+3\text{N}_{\text{full}}$ Hamiltonian using $\Lambda_{3\text{N}} = 400 \text{ MeV}/c$ with $\alpha = 0.04 - 0.08 \text{ fm}^4$ of Fig. 7.5, we show the corresponding ground-state energies per nucleon in the regime $\alpha = 0.08 - 0.16 \text{ fm}^4$. Data taken from [99].

parameter. For the $\text{NN}+3\text{N}_{\text{full}}$ Hamiltonian the additional effect of the induced many-nucleon contributions seems to be repulsive for $\alpha = 0.04 - 0.08 \text{ fm}^4$ with increasing flow parameter and attractive for $\alpha = 0.08 - 0.16 \text{ fm}^4$. This hints to a complex beyond-3N contribution to the ground-state energies that does not increase monotonously with the flow parameter.

Nevertheless, the observed flow-parameter dependence for the large α regime is still moderate. Moreover, the observed cancellation of the induced beyond-3N effects over the complete mass range is a strong indication that we can reliably predict on the chiral $\text{NN}+3\text{N}$ interactions.

The effects caused by the omission of induced many-nucleon forces are indicated by the dependence on the flow parameter. However, the boxes for the $\text{NN}+3\text{N}_{\text{ind}}$ results in Fig. 7.5 and 7.6 cannot be interpreted as typical error bars, since an extrapolation to the energies of the bare Hamiltonian is uncontrolled. Furthermore, fundamental uncertainties of the chiral 3N interaction can be estimated by the three-body cutoff variation. Within these uncertainties, we observe a rather accurate description of the oxygen masses, that turns into an almost constant overbinding of around 1 MeV per nucleon for the heavier systems. It is remarkable that the quantitative systematics of the binding energies can be reproduced with ab initio calculations, starting from chiral $\text{NN}+3\text{N}$ interactions that are constrained in $A \leq 4$ systems.

The results confirm the predictive power of the chiral interaction and in addition raise the question, whether initial 4N interactions that appear at N^3LO might become relevant for such heavy systems. This question is supported by the fact that the effect of the initial 4N force

in ${}^4\text{He}$ is estimated to be of the order of a few hundred keV [174] while for the considered flow-parameter range the induced 4N forces have an even smaller impact of about 50 keV (see Sec. 4.7.1), but rapidly increase with the mass number. Thus, the techniques developed within this work for the inclusion of the 4N contributions will be relevant in the future for the accurate description of medium-mass and heavy nuclei including initial and induced 4N effects.

8 Sensitivity Analysis and Spectroscopy with Chiral Interactions

We dedicate the first part of this section to the investigation of nuclear spectra in the p shell utilizing the IT-NCSM. In particular, we study the sensitivity of excitation energies to variations of the standard local 3N interaction. In the second part we focus on a comparison of nuclear ground-state and excitation energies obtained with a variety of currently available chiral NN+3N interactions introduced in Sec. 1.3.3. These investigations provide important information about the structure of the eigenstates and mark a first step towards a systematic determination of the uncertainties caused by the LECs fit, the regularization and the truncation to a certain chiral order. Moreover, these studies provide hints to the few-body community for the construction of future chiral potentials.

8.1 Sensitivity Analysis of Local 3N Interaction

The local 3N interaction at N²LO that we have introduced as standard 3N interaction consists of the short-range three-nucleon contact term proportional to c_E , the medium-range two-nucleon contact one pion-exchange term proportional to c_D and the long-range two-pion exchange term that depends on $c_i = \{c_1, c_3, c_4\}$ (see Sec. 1.3.2). In the following, we study the sensitivity of nuclear spectra to variations of the 3N parameters, i.e., the LECs and the cutoff. In Tab. 8.1 we summarize the 3N parameters of the standard NN+3N interaction and of the interactions employed for the sensitivity analysis. For the latter interactions the c_E value is refitted to the ⁴He ground-state energy, while for the interactions where we do not explicitly vary the parameter c_D we use $c_D = -0.2$ to reproduce the triton beta-decay half-life [77].

There are several reasons for such investigations. First of all, identifying sensitivities to variations of certain parameters determines the dominant operator structures affecting the relevant observables. This allows to draw conclusions about the underlying structure of the nuclear eigenstate. Furthermore, the LECs are not unique but depend on the fit procedure and the observables utilized for the fit. There are various sets of the $c_i = \{c_1, c_3, c_4\}$ values in the literature from different fits to nucleon-nucleon and pion-nucleon data [8, 10, 62, 175–179] (see Ref. [180] for a recent summary of the fits). From these fits one obtains a large spread for the LECs of the two-pion exchange term $c_1 = (-0.8, \dots, -1.2 \text{ GeV}^{-1})$, $c_3 = (-3.2, \dots, -5.9 \text{ GeV}^{-1})$, and $c_4 = (+3.4, \dots, +5.4 \text{ GeV}^{-1})$. Moreover, there are subleading 3N contributions of the two-pion exchange topology, that can be partially absorbed via a shift of the c_i values as proposed in

NN+3N _{full}	Λ_{3N} [MeV/c]	c_1 [GeV ⁻¹]	c_3 [GeV ⁻¹]	c_4 [GeV ⁻¹]	c_D	c_E
standard	500	-0.81	-3.2	+5.4	-0.2	-0.205
c_i shifted	500	-0.94	-2.3	+4.5	-0.2	-0.085
c_1 shifted	500	-0.94	-3.2	+5.4	-0.2	-0.247
c_3 shifted	500	-0.81	-2.3	+5.4	-0.2	-0.200
c_4 shifted	500	-0.81	-3.2	+4.5	-0.2	-0.130
$c_3 = 0$	500	-0.81	0	+5.4	-0.2	-0.228
$c_D = -1$	500	0	-3.2	+5.4	-1.0	-0.207
$c_D = +1$	500	-0.81	0	+5.4	+1.0	-0.228
$\Lambda_{3N} = 450$ MeV/c	450	-0.81	-3.2	+5.4	-0.2	+0.098
$\Lambda_{3N} = 400$ MeV/c	400	-0.81	-3.2	+5.4	-0.2	-0.016

Table 8.1 *LECs for local chiral 3N interactions with excluded contributions*: Besides the standard NN+3N interaction [77] the table summarize the LECs of the local 3N interaction for variations of the LECs and the three-body cutoff, keeping the standard NN interaction at N³LO fixed.

Refs. [75, 83, 85]. The “ c_i shifted” parameters in Tab. 8.1 uses exactly these shifts. Thus, the variations we perform in the following provide additional constraints for the LEC fit and, in addition, allow to estimate partial effects from subleading 3N contributions. Finally, we vary the cutoff to examine the impact of the regularization and to perform a first step towards a systematic quantification of the theoretical uncertainties of the chiral EFT approach.

Before we start the sensitivity analysis we briefly reconsider the results of the ¹²C excitation spectrum of Fig. 6.3 on page 114. While the SRG-induced beyond-3N forces considerably affect the absolute energies beyond the mid-p shell, the excitation spectra are essentially independent of the flow parameter. Furthermore, the excitation energies rapidly converge with respect to N_{\max} , such that the typically applied IT-NCSM model spaces of $N_{\max} = 8$ at $\hbar\Omega = 16$ MeV are sufficient to obtain well converged results. The SRG evolutions are performed using the SRG space corresponding to ramp \mathcal{A} (see Fig. 5.1) up to $\alpha = 0.08$ fm⁴.

In Figs. 8.1 and 8.2 we show the excitation spectra of ¹²C obtained with the initial NN interactions (NN+3N_{ind}), as well as with the initial NN+3N interactions (NN+3N_{full}) defined in Tab. 8.1. From a comparison of the NN+3N_{ind} spectrum to the one obtained with the standard NN+3N_{full} Hamiltonian in Fig. 8.1, we observe that the initial 3N interaction has a strong impact on the excitation energies of the first excited 0⁺, 1⁺ and 4⁺ state. As discussed in Sec. 6.1 the first excited 0⁺ state is known to exhibit a complicated cluster structure that requires too large model spaces for an adequate description in the HO representation. Thus, the excitation energy of this state is not yet converged for $N_{\max} = 8$ and substantiated conclusions on the 3N effects cannot be drawn. Interestingly, the initial 3N force reduces the first 1⁺ excitation energy by about 2.5 MeV, which worsens the rather good agreement with the experimental value we find with the initial NN interaction. Simultaneously, the increase of the 4⁺ excitation energy by more than 2 MeV improves the experimental agreement. The remaining excitation energies

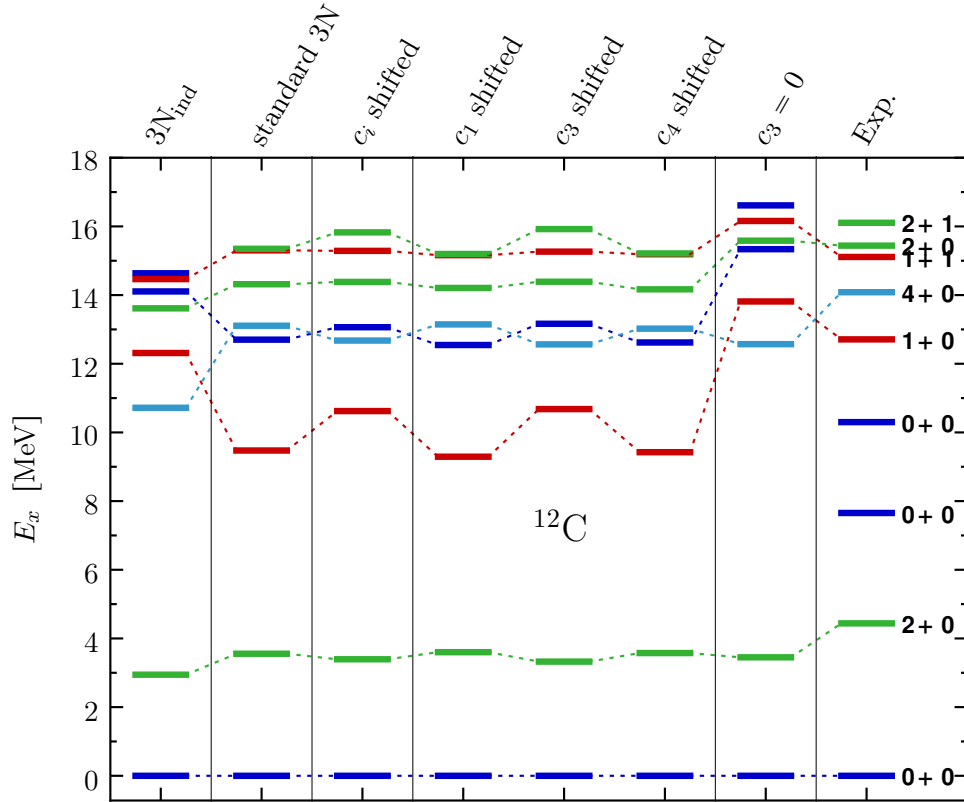


Figure 8.1 *Sensitivity analysis in ^{12}C spectrum:* Excitation spectra of ^{12}C for the standard $\text{NN}+3N_{\text{ind}}$ and $\text{NN}+3N_{\text{full}}$ Hamiltonians, as well as for the Hamiltonians with varied LECs of the two-pion exchange term according to Tab. 8.1. The results are obtained with the IT-NCSM at $\hbar\Omega = 16$ MeV in an $N_{\text{max}} = 8$ model space. The SRG evolution is performed using $\text{ramp}\mathcal{A}$ up to $\alpha = 0.08 \text{ fm}^4$. Experimental data taken from Ref. [167].

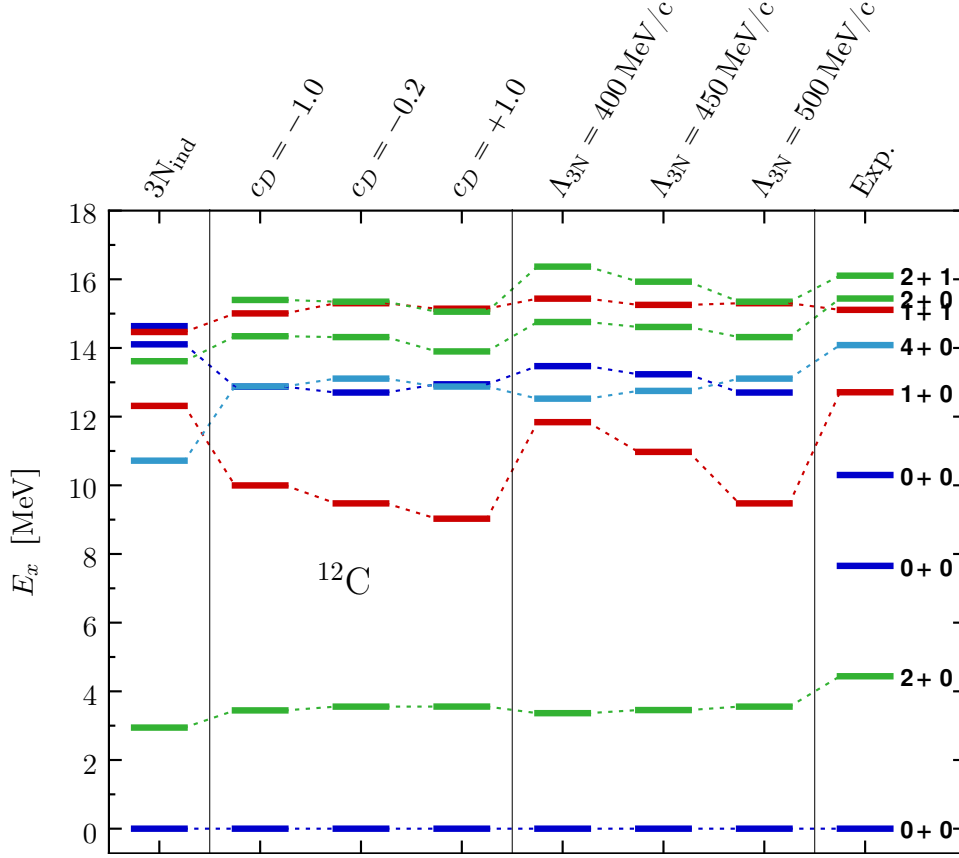


Figure 8.2 *Sensitivity analysis in ^{12}C spectrum*: Excitation spectra of ^{12}C obtained with the $\text{NN}+3\text{N}_{\text{ind}}$ and the $\text{NN}+3\text{N}_{\text{full}}$ Hamiltonians for different values of c_D and the three-body cutoff $\Lambda_{3\text{N}}$. Remaining parameters are identical to Fig. 8.1.

are slightly increased leading to an overall improved description of the experimental spectrum.

In the following, we concentrate on the excitation energies of the first excited 1^+ and 4^+ states, when changing the parameters of the initial 3N interaction. The ^{12}C spectrum is rather insensitive to the shifts of the two-pion exchange LECs. The only exception is the first 1^+ excitation energy that is increased by about 1 MeV towards experiment. When performing the c_i -shifts separately, we identify the operator structures proportional to c_3 to be responsible for this pronounced sensitivity. If we neglect this term by setting $c_3 = 0$ almost all excitation energies are noticeably increased, in particular, the one of the first 1^+ state. The exceptions are the excitation energies of the 2^+ and 4^+ states that show almost no sensitivity to the long-range two-pion exchange contributions.

A similar strong sensitivity of the first 1^+ excitation energy can be observed in Fig. 8.2 for variations of c_D and $\Lambda_{3\text{N}}$ while the remaining spectrum shows a comparatively small dependence. With decreasing $\Lambda_{3\text{N}}$ cutoff the 1^+ excitation energy seems to rapidly approach the

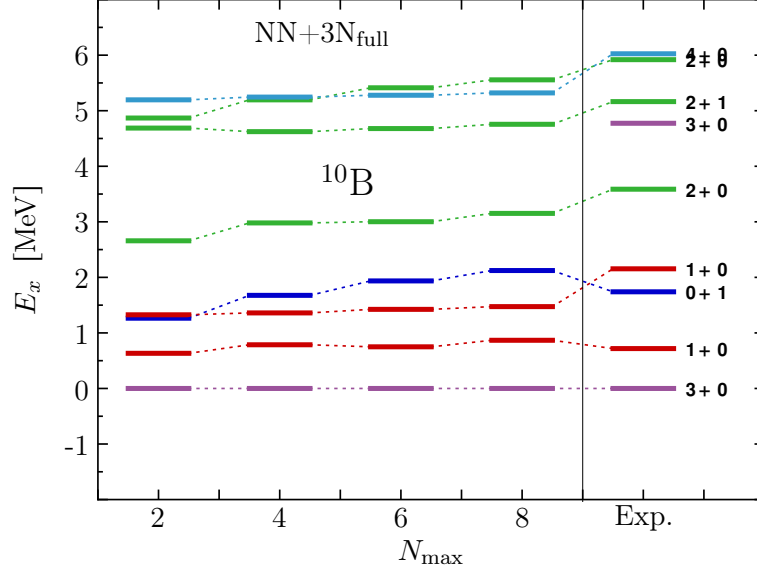


Figure 8.3 *Convergence of ^{10}B spectrum*: Excitation spectrum of ^{10}B for the standard $\text{NN}+3\text{N}_{\text{full}}$ Hamiltonian as function of N_{max} . Remaining parameters are identical to Fig. 8.1. Experimental data taken from Ref. [181].

value obtained for the $\text{NN}+3\text{N}_{\text{ind}}$ Hamiltonian. This might indicate that the complex structure of this state is mostly effected by the high-energy components of the initial 3N force. The 4^+ excitation energy does not show a strong sensitivity to the parameter changes, indicating that its improved description by the initial 3N interaction is caused by all 3N terms simultaneously. See also Ref. [22] for a recent investigation of the ^{12}C spectrum with the NCSM and IT-NCSM, including also negative parity states.

An even more interesting case to study the 3N-force effects is the ^{10}B excitation spectrum. As demonstrated in Fig. 8.3 we obtain an appropriate convergence with respect to N_{max} for the HO frequency of $\hbar\Omega = 16$ MeV, and in the following we perform the analogous sensitivity analysis with respect to the 3N parameters as illustrated in Fig. 8.4 and 8.5.

As known from calculations with the Argonne V18 and CD-Bonn potentials the initial NN forces typically predict the wrong ground state [4] and one requires an initial 3N force to predict the 3^+ state to be the energetically lowest eigenstate, rather than the 1^+ state. The same applies to the standard chiral NN and $\text{NN}+3\text{N}$ interaction used in the first two panels of Fig. 8.4. While the excitation energy of the second 1^+ with respect to the 3^+ state is almost insensitive to the 3N force, the remaining excitation energies increase. In general, the initial 3N force improves the agreement with experiment, although the order of the first 0^+ and second 1^+ state is reversed. Furthermore, the second 3^+ excitation energy is strongly increased by the initial 3N interaction, such that the state is not anymore within the computed eight lowest eigenstates and has an excitation energy large than 5.5 MeV.

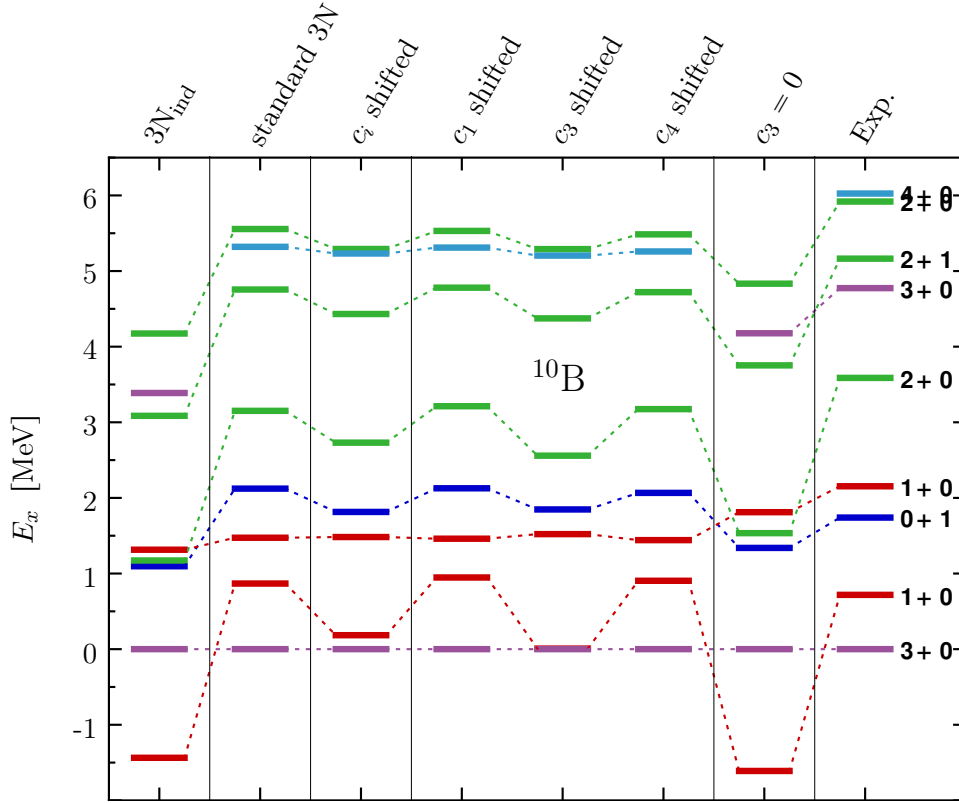


Figure 8.4 *Sensitivity analysis in ^{10}B spectrum*: Calculations performed as in Fig. 8.1.

By considering the results obtained for variations of the two-pion exchange term LECs in columns 3 – 5 we again observe a substantial sensitivity of the first 1^+ excitation energy originating from the operator structures proportional to c_3 . In comparison to the ^{12}C spectrum the c_3 contributions improve the agreement with experiment and we reconsider this correlation later on. A striking impact on the spectrum occurs when setting $c_3 = 0$. Besides small variations, the spectrum shows the same ordering and essentially an equivalent result as with initial NN interaction, identifying the c_3 term to have the major impact on the changes caused by the 3N force.

This is also consistent with the results obtained for the c_D and cutoff variation in Fig. 8.5. The variation of c_D generates minor changes in the spectrum and, in particular, no changes of the level ordering. For the reduction of the three-body cutoff, which has an impact on all 3N force terms, the spectrum seems to approach the results for the initial NN interaction. The strong impact of the cutoff variation indicates the sensitivity of the excitation spectrum to high-momentum components. Moreover, we have identified the c_3 term to dominate the 3N effects. Thus, the 3N contributions that are responsible for sizable induced beyond-3N forces (see Sec. 6), i.e., the high-momentum components of the c_3 term, have also a strong impact on

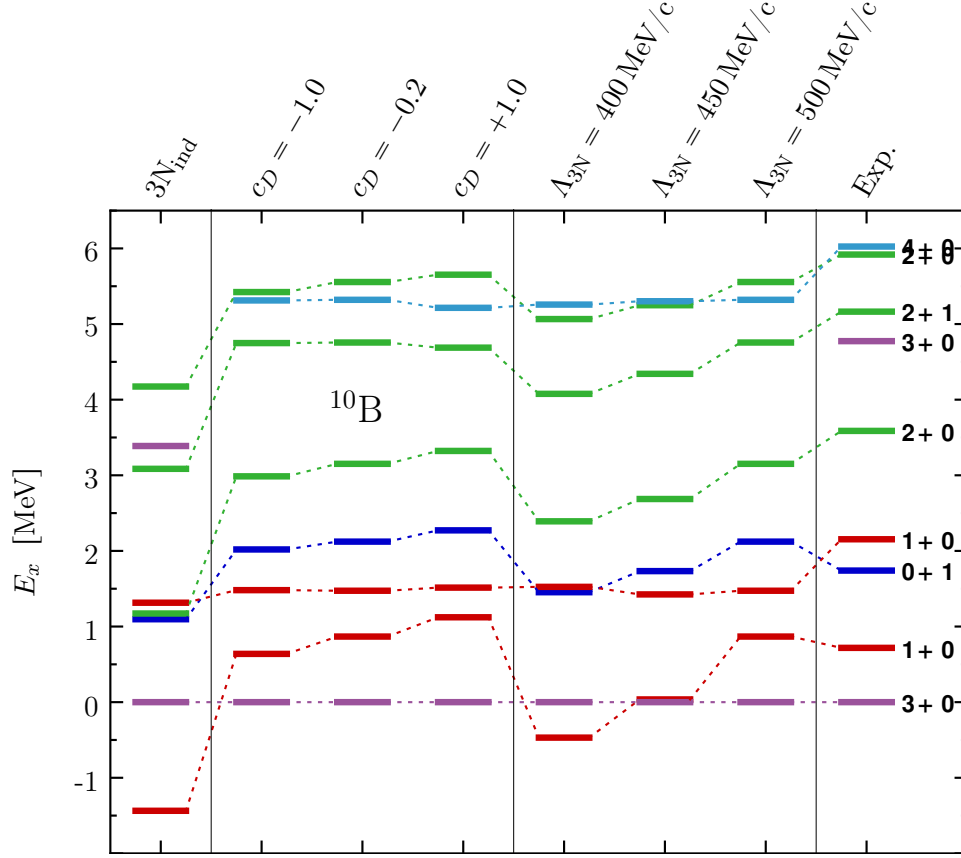


Figure 8.5 Sensitivity analysis in ^{10}B spectrum: Calculations performed as in Fig. 8.2.

the details of the ^{10}B spectrum.

From the variation of the three-body cutoff a further interesting property of the ^{10}B spectrum can be observed. For the larger $\Lambda_{3\text{N}}$ of 500 MeV/c the order of the 3^+ ground state with respect to the first 1^+ state agrees with experiment while the order of the 0^+ and second 1^+ state is reversed compared to experiment. When reducing the cutoff this is inverted. It seems that we cannot describe both orderings simultaneously. In other words, although the 3N force generally improves the description of the spectra, there are still discrepancies for certain excitation energies, which cannot be resolved by adjusting the parameters of the 3N interaction. These excitation energies can be used as benchmark cases for future interactions.

Moreover, one can identify to types of states that show similar changes of the energy under variations of the 3N interaction. The one type of states are the first 3^+ and second 1^+ states, which keep an almost constant energy distance. The remaining excitation energies belong to the other type of states and show similar qualitative changes. In particular, the 3N impact to the energies of the 2^+ states is almost the same.

Finally we concentrate on the strong sensitivity of the first 1^+ excitation energies of ^{12}C and

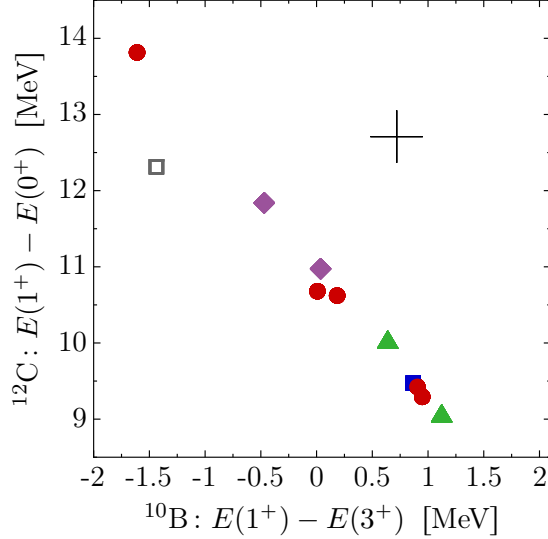


Figure 8.6 *Correlation of the 1^+ excitation energies of ^{10}B and ^{12}C* : Plotted is the excitation energy of the first 1^+ with respect to 0^+ ground state in ^{12}C , as function of the excitation energy of the first 1^+ with respect to the first 3^+ in ^{10}B . The parameters of the IT-NCSM calculations are identical to Fig. 8.1 using the standard $\text{NN}+3\text{N}_{\text{ind}}$ (\square) and $\text{NN}+3\text{N}_{\text{full}}$ (\blacksquare) Hamiltonian, as well as those obtained from the c_i (\bullet), c_D (\blacktriangle), and $\Lambda_{3\text{N}}$ (\blacklozenge) variations. The thin cross indicates the experimental value.

^{10}B and illustrate their correlation in Fig. 8.6 by plotting the corresponding excitation energy for ^{12}C as function of the one for ^{10}B , obtained for the $\text{NN}+3\text{N}_{\text{ind}}$, as well as the Hamiltonians introduced in Tab. 8.1. The result is surprising: The data point for the initial NN interaction (gray open box) leads to a rather accurate description of the 1^+ excitation energy for ^{12}C , but is almost 2.5 MeV too low for the 1^+ excitation energy for ^{10}B . By including the 3N forces with the parameter variations, the results lie on a line in the correlation plot that does not intersect with the experimental data point (thin cross). Obviously, we cannot describe both excitation energies correctly by variations of the three-body parameters. Thus, these results either hint to an insufficiency of the NN force, or a lack of operator structure in the 3N force that, e.g., could be found at N^3LO .

In summary, spectra of p-shell nuclei constitute a powerful testbed for chiral NN and 3N forces and we have observed a general improvement of the spectra by including the standard chiral 3N interaction. In addition, we have identified certain excitation energies that cannot be described properly and require changes in the Hamiltonian beyond the adjustment of 3N parameters. These observables can be consulted to examine the reliability of future chiral interactions.

8.2 Comparison of Present Chiral NN+3N Interactions

We now focus on a comparison of the standard interaction, i.e., the NN at N³LO by Entem & Machleidt and the local 3N interaction at N²LO, to the consistent N²LO NN+3N interactions introduced in Sec. 1.3.3. For this purpose we apply the N²LO NN+3N interactions to nuclear spectra in the p shell. Finally, we examine the ground-state energy of ¹⁶O to conclude about the effects of the initial 3N interactions and the SRG-induced beyond-3N contributions.

The starting point for the POUNDerS and Epelbaum NN forces are interaction matrix elements in the two-body partial-wave momentum representation. The corresponding matrix elements are SRG evolved and transformed to the two-body Jacobi-HO representation. We refer to Ref. [182] for an investigation of the Epelbaum NN interaction at N²LO and at N³LO for the ground state of the deuteron and ⁴He. There, one can find illustrations of the NN potentials in the momentum and HO representation for the partial-wave channels that contribute to the deuteron. From these studies one finds that, in particular, the Epelbaum NN interaction at N³LO for the largest cutoffs show striking properties, e.g., a sign change of the deuteron S-wave function at short distances or untypical large amplitudes of the of the interaction matrix elements in the momentum and HO representation for the S-wave channel. Apart from that, the remaining Epelbaum interactions at N²LO and N³LO show a rather consistent picture compared to the standard NN interaction at N³LO, e.g., the form of the potential, the resulting deuteron wave function, or the ⁴He ground-state energies are comparable. In particular, after softening the interactions by the SRG the universality property, i.e., the independence of the high-momentum details in the initial potential, becomes obvious (see Ref. [159] for an detailed overview). For instance, one observes similar deuteron S-wave functions that exhibit only minor discrepancies at short distances.

However, in the following we focus on the impact of the initial 3N force to nuclear energies in the p shell. The POUNDerS NN interaction is combined with the standard local 3N interaction, such that the resulting Hamiltonian can be treated as the standard NN+3N Hamiltonian.

In case of the non-local Epelbaum 3N interaction at N²LO, the procedure is different. The starting point are matrix elements in the partial-wave decomposed momentum representation, that are unregularized and, in general, only partially antisymmetrized. These matrix elements result from the automatized partial-wave decomposition (aPWD) developed by Skibiński et. al [75]. The procedure does not account for the locality of the interaction.¹⁶ Thus, the calculation of the interaction matrix elements is computationally demanding and the model space needs to be reduced compared to the one used for the local 3N interaction. This reduction is typically achieved by introducing additional physical motivated truncations of the angular momenta. In the following, the applied non-local 3N interaction matrix is calculated on a four-dimensional

¹⁶The fundamental operator structure of the 3N force at N²LO is local in coordinate space, but the applied regularization for the Epelbaum interactions causes non-local contributions.

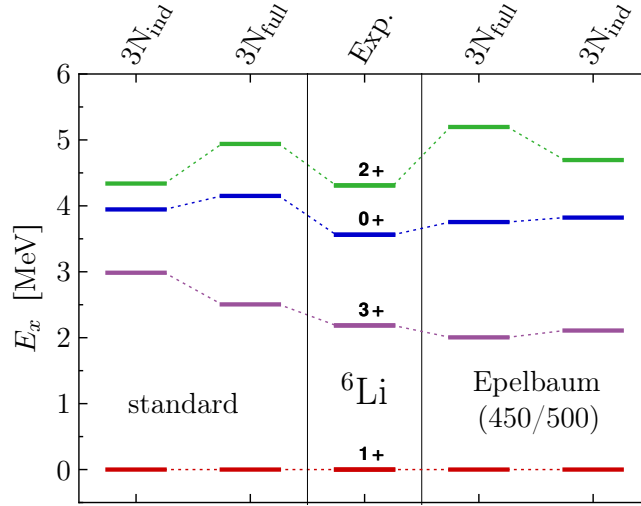


Figure 8.7 *Excitation spectra for ${}^6\text{Li}$* : Excitation spectrum of ${}^6\text{Li}$ for the $\text{NN}+3\text{N}_{\text{ind}}$ and $\text{NN}+3\text{N}_{\text{full}}$ Hamiltonians using the standard interaction (left-hand side) and the Epelbaum interaction for the (450/500) MeV/c cutoff combination (right-hand side). The IT-NCSM calculations are carried out for $N_{\text{max}} = 12$ at $\hbar\Omega = 20$ MeV and the SRG evolution is performed up to $\alpha = 0.08 \text{ fm}^4$ for the SRG space corresponding to $\text{ramp}\mathcal{A}$. In the middle we show the experimental values [183].

momentum grid using 8 – 14 grid points for each dimension, which is sufficient for a reliable interpolation. The coupled relative angular momentum is typically truncated to $J_{12} \leq \frac{7}{2}$ and the angular momentum corresponding to the first Jacobi coordinate is truncated to $J_1 \leq 7$ for $J_{12} = \frac{1}{2}$ and $J_1 \leq 6$ for the remaining partial waves. In order to apply these 3N interactions to nuclear structure calculations, we perform the regularization, antisymmetrization and transformation to the Jacobi-HO representation as discussed in Sec. 3.5. From thereon we can treat the non-local 3N interactions in the same manner as the standard 3N interaction with the three-body HO framework. Thus, all novel techniques regarding the matrix-element treatment in the HO representation are directly applicable to the non-local 3N interactions.

8.2.1 Spectroscopy of p-Shell Nuclei

We examine the spectroscopy for p-shell nuclei and compare the results to those obtained from the standard interactions. While the POUNDERs interaction has been applied recently to nuclear structure calculations for oxygen and calcium isotopes [11] the Epelbaum interactions are rather untested in nuclear structure calculations. We begin with a simple case, the excitation spectrum of ${}^6\text{Li}$, to provide a proof of concept for the inclusion of the Epelbaum 3N forces to the HO framework and to verify the principal applicability of the Epelbaum interactions to nuclear structure calculations.

The corresponding results for the Epelbaum interaction with $(\Lambda/\hat{\Lambda}) = (450/500)$ MeV/c are

shown in Fig. 8.7 and are compared to the results for the standard interaction. The calculations are carried out with the IT-NCSM at $N_{\max} = 12$ and $\hbar\Omega = 20$ MeV, such that an adequate convergence with respect to N_{\max} is reached. The interactions are SRG evolved at the three-body level up to $\alpha = 0.08$ fm⁴. While for the standard interaction the initial 3N force considerably improves the description of the 3^+ excitation energy, the Epelbaum NN interaction already provides a good description that is only slightly affected by the 3N force. Also the 0^+ excitation energy is in slightly better agreement with experiment for the Epelbaum interaction. For the 2^+ excitation energy the 3N force worsens the agreement with experiment for both interactions leading to an overestimation of the excitation energy. In total, both interactions provide reasonable results for the ⁶Li spectrum and we proceed to the ¹²C and ¹⁰B spectra.

We concentrate on a comparison of the spectra for the standard interaction to several NN+3N interactions at N²LO, i.e., the POUNDerS interaction with $(\Lambda/\hat{\Lambda}) = (450/700)$ MeV/c and four Epelbaum interactions with cutoff combinations $(\Lambda/\hat{\Lambda}) = (450/500), (600/500), (550/600),$ and $(450/700)$ MeV/c. Note, that we omit the fifth available Epelbaum with $(\Lambda/\hat{\Lambda}) = (600/700)$ MeV/c, since it has a rather large cutoff already close to the critical value where spurious bound states violate the naturalness of the LECs [42] and only differs from the other $\Lambda = 600$ MeV/c interaction by the spectral-function regularization (SFR). However, we use both $\Lambda = 450$ MeV/c interactions to study the impact of the SFR cutoff. The calculations are performed with the IT-NCSM at $N_{\max} = 8$ and $\hbar\Omega = 20$ MeV for the POUNDerS interaction and at $\hbar\Omega = 16$ MeV for the remaining interactions. The SRG evolution is carried out for the model space ramp \mathcal{A} up to $\alpha = 0.08$ fm⁴.

In Fig. 8.8 we show a comparison for the ¹²C excitation spectrum. The left-hand spectra for each interaction are obtained with the NN+3N_{ind} Hamiltonians including exclusively the initial NN force while the right-hand spectra correspond to the NN+3N_{full} Hamiltonians including the initial NN+3N force. We first focus on the effect of the initial 3N force. The excitation energy of the first 1^+ state that has been identified to be highly sensitive to the initial 3N force decreases for all interactions owing to the initial 3N interaction. Furthermore, except for the Epelbaum interaction with $(\Lambda/\hat{\Lambda}) = (450/700)$ MeV/c the initial 3N force increases the excitation energy of the rotational 2^+ and 4^+ states, indicating an enhancement of the momentum of inertia. The exceptional behavior with this Epelbaum interaction is surprising since the regularization only differs by the SFR cutoff from the first Epelbaum interaction with $(\Lambda/\hat{\Lambda}) = (450/500)$ MeV/c. The distinct differences of the 3N-force effects for these two interactions reveal the importance of changes in the NN force that have a strong impact on nuclear structure observables.

The standard and POUNDerS interactions provide a rather consistent description of the lowest excited eigenstates regarding the 3N-force effect and the level ordering with and without initial 3N interactions. There is work in progress to produce additional POUNDerS interactions for further cutoff combinations and it will be interesting to investigate if the spectroscopy changes for these interactions.

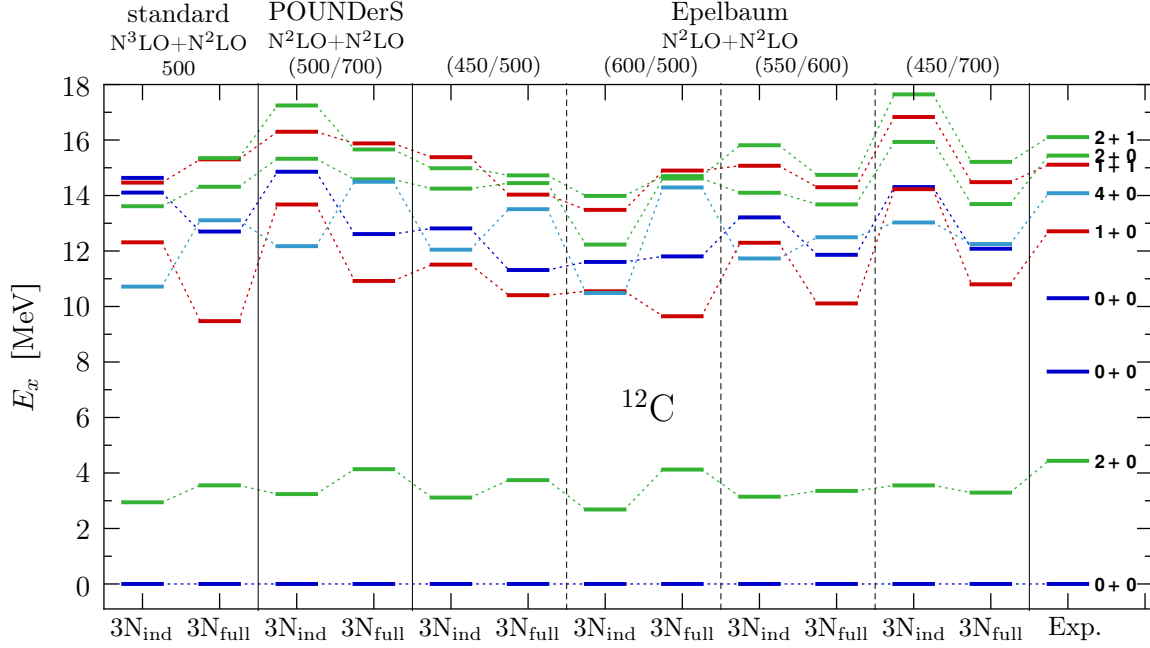


Figure 8.8 *Excitation spectra for ^{12}C with different chiral interactions*: Excitation spectra of ^{12}C for the NN+ 3N_{ind} and NN+ 3N_{full} Hamiltonians using the standard interaction with $\Lambda = 500$ MeV/c, the POUNDerS interaction with $(\Lambda/\hat{\Lambda}) = (450/700)$ MeV/c and four different Epelbaum interactions with the cutoff combinations $(\Lambda/\hat{\Lambda}) = (450/500)$, $(600/500)$, $(550/600)$, and $(450/700)$ MeV/c (left to right). The calculations are performed with the IT-NCSM at $\hbar\Omega = 20$ MeV for the POUNDerS interaction and at $\hbar\Omega = 16$ MeV for the remaining interactions. Further, we use $N_{\text{max}} = 8$ and $\alpha = 0.08$ fm⁴.

The spectra for the Epelbaum NN+ 3N_{ind} Hamiltonians show a strong dependence on the cutoff, such that the level ordering and agreement with experiment changes. Moreover, it is hardly possible to identify a certain systematic trend with respect to the cutoff variation, as it has been the case for an exclusive three-body cutoff variation in Sec. 8.1. In particular, the fourth interaction with $(\Lambda/\hat{\Lambda}) = (450/700)$ MeV/c predicts a spectrum that differs from those of the remaining Epelbaum NN+ 3N_{ind} interactions. It is questionable if the large variations for the Epelbaum NN+ 3N_{ind} Hamiltonians reflect the theoretical uncertainty of the chiral interaction at this order or if the spectra are biased by an insufficient LEC-fit procedure.

If we concentrate on the spectra with the Epelbaum NN+ 3N_{full} Hamiltonians we observe a rather consistent description. It seems that the adjustment of the 3N-force LECs c_D and c_E accounts for the changes in the NN sector and leads to a rather consistent description that, in addition, agrees with the results with the standard NN+ 3N_{full} Hamiltonian. This indicates that the 3N force is not a small correction to the NN force, but an essential ingredient required to stabilize the chiral N²LO force regarding variations of the cutoff. However, further studies along these lines are mandatory, including variations of the NN force combined with an improved fit

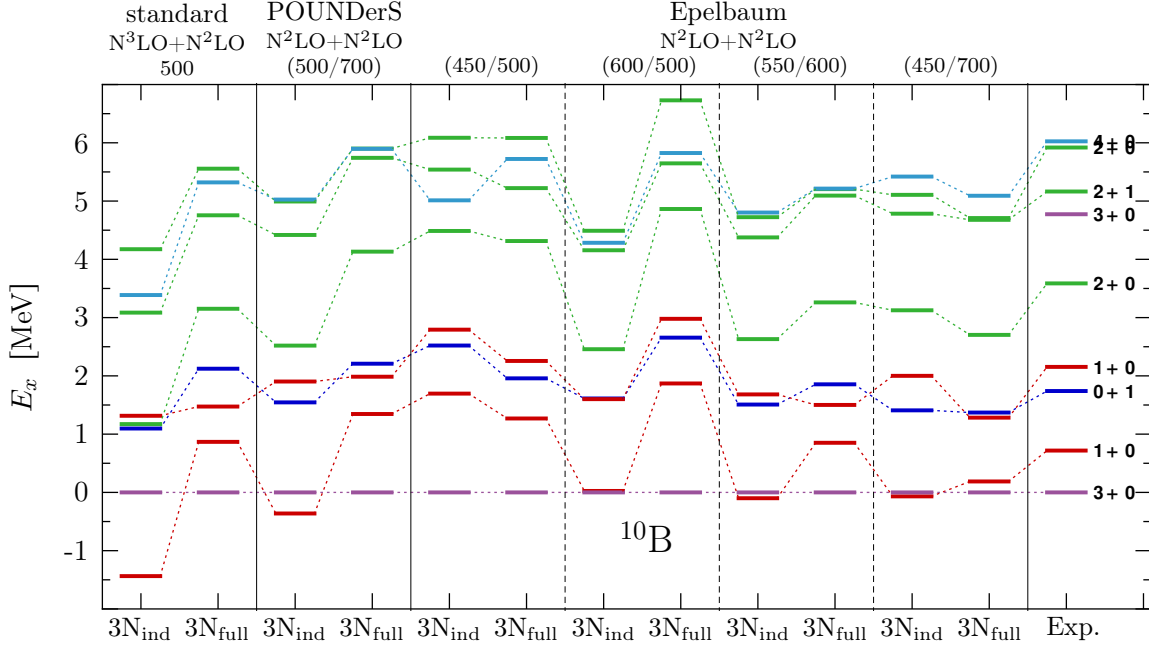


Figure 8.9 Excitation spectra for ^{10}B with different chiral interactions: Calculations performed as in Fig. 8.8.

procedure.

To extend the examinations of the NN+3N interactions at N^2LO we consider the analogous calculations for the ^{10}B spectra in Fig. 8.9. As expected from the previous discussions the Epelbaum NN+3N_{ind} results strongly depend on the cutoff. While the majority of the interactions predict an almost degenerate ground state, the $(\Lambda/\hat{\Lambda}) = (450/500)$ MeV/c interaction distinctly predicts the correct ground state without an initial 3N force. In contrast to the ^{12}C nucleus the consistency of the spectra is not substantially improved when including the initial 3N force. For instance, the Epelbaum NN+3N interaction with $(\Lambda/\hat{\Lambda}) = (600/500)$ MeV/c predicts rather large excitation energies compared to the other interactions. Further, the ordering of the second 1^+ state with respect to the 0^+ state changes for the different cutoff values. As for ^{12}C , systematics regarding the cutoff variation are not recognizable.

Note that the Epelbaum 3N interaction contains a truncation regarding the angular momenta and their convergence behavior with respect to N_{max} might be different compared to the standard interaction, in particular, for the ^{10}B spectrum (see Fig. 8.3). To confirm the reliability of the presented calculations we study the convergence of the spectra with respect to the IT-NCSM model space and the applied angular-momentum truncation of the 3N interaction. In Fig. 8.10 we exemplarily illustrate the ^{10}B excitation spectrum for the Epelbaum interactions with $(\Lambda/\hat{\Lambda}) = (450/500)$ MeV/c (upper panel) and $(\Lambda/\hat{\Lambda}) = (450/700)$ MeV/c (lower panel). In

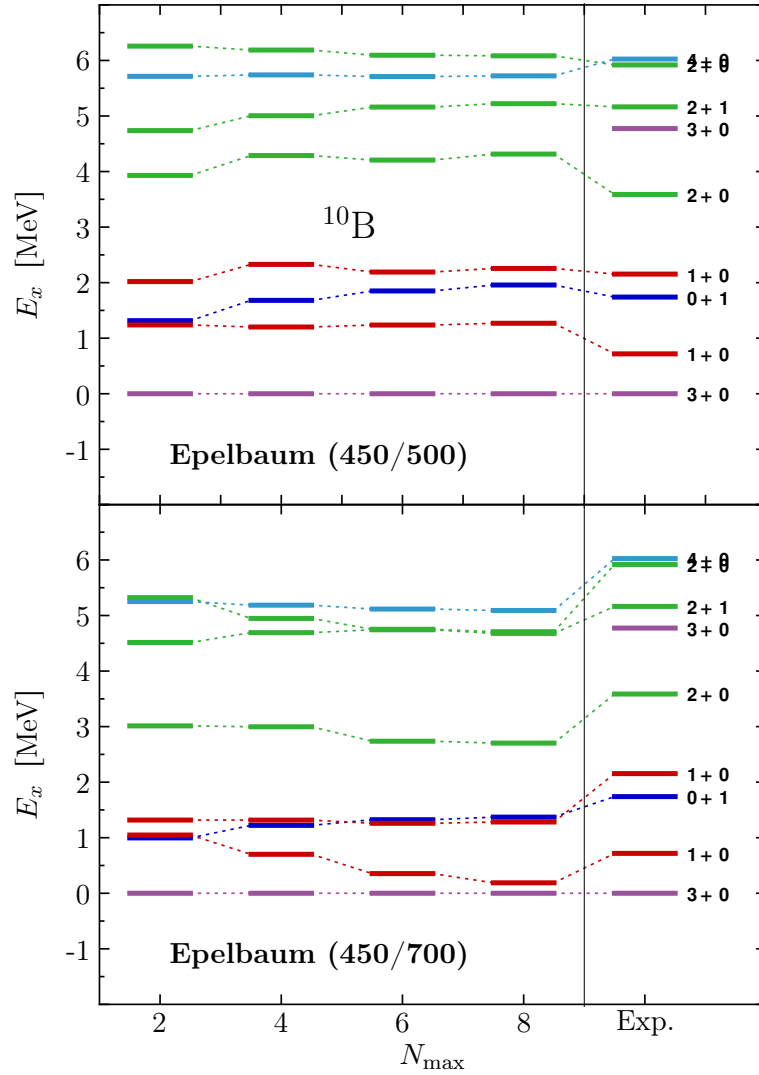


Figure 8.10 *Convergence of ^{10}B spectrum*: Excitation spectra of ^{10}B for the Epelbaum $\text{NN}+3\text{N}_{\text{full}}$ Hamiltonians with $(\Lambda/\hat{\Lambda}) = (450/500)\text{MeV}/c$ (upper panel) and $(450/700)\text{MeV}/c$ (lower panel) as function of N_{\max} . The calculations are performed with the same parameters as in Fig. 8.8.

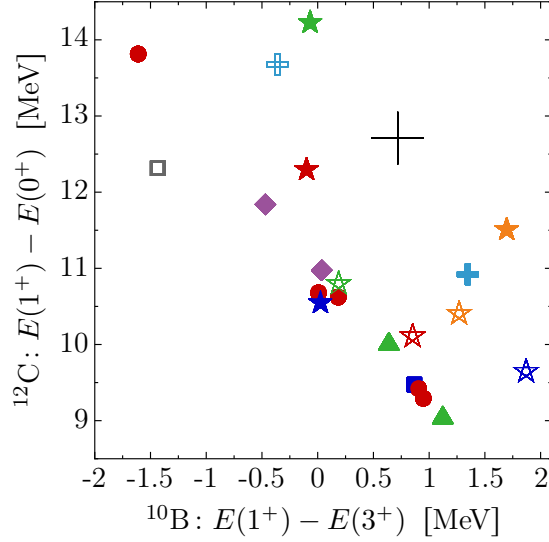


Figure 8.11 *Correlation of the 1^+ excitation energies of ^{10}B and ^{12}C* : Same plot as in Fig. 8.6 including the results for the POUNDerS interaction (light-blue crosses) as well as for the Epelbaum interactions (stars) with $(\Lambda/\hat{\Lambda}) = (450/500)$ MeV/c (orange), $(600/500)$ MeV/c (blue), $(550/600)$ MeV/c (red), and $(450/700)$ MeV/c (green). The open symbols correspond to $\text{NN}+3\text{N}_{\text{ind}}$ Hamiltonians and the solid symbols to $\text{NN}+3\text{N}_{\text{full}}$ Hamiltonians.

general, the ^{10}B excitation spectra at $N_{\text{max}} = 8$ are reasonably well converged with respect to N_{max} (also for the remaining interactions) and the ordering of the eigenstates is not expected to change for larger model spaces. An exception is the first excited 1^+ state for the Epelbaum $\text{NN}+3\text{N}_{\text{full}}$ interaction with the cutoff combination $(450/700)$ MeV/c that shows a surprisingly slow convergence. For an infinite model space this particular interaction seems to predict the wrong ground state of ^{10}B with the initial 3N force.

To benchmark the validity of the J_{12} truncation we compare the results with $J_{12} \leq \frac{5}{2}$ to those with $J_{12} \leq \frac{7}{2}$ for the ^{10}B spectrum using exemplarily the Epelbaum $\text{NN}+3\text{N}_{\text{full}}$ interaction with the $(450/500)$ MeV/c cutoff combination. We find discrepancies below 350 keV for the absolute energies and about 150 keV for the excitation energies. Therefore, the omitted angular-momentum contributions of the 3N force are expected to cause minor changes of the presented results and the general conclusions are not affected.

Finally, we reconsider the correlation of the first 1^+ excitation energies in ^{12}C and ^{10}B that has been identified for the parameter variations of the standard 3N force in Sec. 8.1. Figure 8.11 shows the similar correlation plot as in Fig. 8.6 including the results obtained with the POUNDerS and Epelbaum interactions at N^2LO . The variation of the 3N-force parameters of the standard interaction yields only data points on a line that does not intersect with the experimental data point (thin cross). The POUNDerS (light-blue cross) and Epelbaum (stars) results are typically located to the upper right of this line, i.e., on the side where experiment

can be found. Obviously, the different initial NN interactions provide an opportunity to leave this line, even though none of the investigated NN+3N_{ind} (open symbols) or NN+3N_{full} (open symbols) Hamiltonians provide results close to the experiment.

The analogous sensitivity analysis to the 3N-force parameters, as in Sec. 8.1 for the standard interaction, can be performed for the NN+3N interactions at N²LO. Although such studies are important to identify the impact of certain 3N-force contributions, presently the NN forces of the Epelbaum interactions are not fully satisfying. These N²LO forces show a rather large χ^2/datum for the description of the NN data compared to the standard NN interaction at N³LO and we observe a strong dependence of the 3N-force effects on the NN interaction.

The agreement of the results with the POUNDerS and the standard NN and NN+3N interactions is remarkable, revealing accurate spectroscopic predictions even without NN contributions at N³LO. However, an investigation of further interactions constructed in the same manner as the POUNDerS interaction for different cutoff combinations is required to assess the uncertainties. The variations in the excitation spectra obtained with the Epelbaum interactions for the different cutoff combinations can be interpreted as the actual uncertainties of these interactions at N²LO. Although, the resulting error bands are rather large the experimental energies typical can be reproduced within these uncertainties. It will be interesting to study if improvements of the LEC-fit procedure or inclusions of the N³LO contributions can decrease the uncertainties and retain the agreement with experiment.

8.2.2 Ground-State Energies and Induced Many-Nucleon Force

After discussing nuclear spectroscopy in the p shell we study the POUNDerS and Epelbaum interactions with respect to the description of the ¹⁶O ground-state energy. For instance, the POUNDerS interaction has shown success in the description of the oxygen isotopic chain without an initial 3N force [11], and we investigate if the experimental agreement persists when the initial 3N contributions at N²LO are included. Moreover, we study the effect of SRG-induced many-nucleon contributions beyond the three-body level indicated by the flow-parameter dependence of the converged ground-state energies.

In Fig. 8.12 we show the ground-state energies of ¹⁶O computed with the standard (left-hand panels), POUNDerS (middle panels) and Epelbaum (right-hand panels) interactions as function of N_{max} . We exemplarily use the Epelbaum interaction with the cutoff combination (450/500) MeV/c. The IT-NCSM calculations are performed at $\hbar\Omega = 20$ MeV and we use an SRG evolution up to $\alpha = 0.04$ fm⁴ (blue circles), 0.08 fm⁴ (red diamonds), and 0.16 fm⁴ (green triangles). For all three NN+3N_{ind} Hamiltonians we observe an almost negligible flow-parameter dependence. This reveals the small impact on the ¹⁶O ground-state energy of the omitted induced beyond-3N contributions originating from the initial NN force. While the standard NN interaction in Fig. 8.12 (a) considerably underbinds by about 10 MeV, the POUNDerS

interaction in Fig. 8.12 (b) already reproduces the experiment without an initial 3N force, as observed in Ref. [11]. The Epelbaum NN interaction in Fig. 8.12 (c) leads to a large overbinding of the ground state by about 30 MeV.

In the lower panels of Fig. 8.12 we depict the energies for the initial NN+3N interactions (NN+3N_{full}). We add the local 3N force with $\Lambda_{3N} = 500$ MeV/c (solid symbols) and 400 MeV/c (open symbols) to the standard (c) and POUNDerS (d) NN interactions. The Epelbaum interaction is combined with the corresponding non-local 3N force with $\Lambda_{3N} = 450$ MeV/c. As observed in Sec. 6 the standard NN+3N interaction with $\Lambda_{3N} = 500$ MeV/c induced beyond-3N forces that have a sizable repulsive effect. For the $\Lambda_{3N} = 400$ MeV/c interaction the many-nucleon effects are successfully suppressed and one achieves an accurate description of the ground-state energy. A similar pattern regarding the flow-parameter dependence is also observed for the POUNDerS interactions. The effects of the omitted induced many-nucleon forces are slightly smaller but also repulsive and get suppressed by reducing the three-body cutoff. The similar flow-parameter dependence for the Epelbaum and standard NN+3N interaction with $\Lambda_{3N} = 500$ MeV/c indicates that both 3N forces induce repulsive many-nucleon effects of the same order.

However, in contrast to the standard interaction, the NN+3N_{full} Hamiltonians of the other interactions lead to an underbinding of the experimental ground-state energy. The omitted induced beyond-3N forces have a repulsive effect, such that the results for the standard interaction with $\Lambda_{3N} = 500$ MeV/c is shifted towards the experimental value (see Sec.6.4.3). This is not the case for the POUNDerS interaction with $\Lambda_{3N} = 500$ MeV/c and the Epelbaum interaction, where the bare result is expected to be even less bound.

In summary, the present NN+3N interactions at N²LO induce beyond-3N contributions with a sizable repulsive effect and the investigations and developments, regarding their suppression or the inclusion of 4N contributions in Sec. 6 are relevant for these chiral forces as well. Moreover, we have identified a fundamental problem when combining the POUNDerS NN interaction with an initial 3N interaction. The repulsion of the initial 3N force destroys the experimental agreement of the ¹⁶O ground-state energy. In view of heavy nuclei this observation might become interesting. As we have shown in Sec. 7.2 the standard NN+3N interactions with the reduced three-body cutoff provide an accurate description of the oxygen binding energies, but systematically overbind the heavier nuclei by about 1 MeV per nucleon. The repulsive effect of the 3N force for the POUNDerS interaction could correct for this overbinding, yielding a better agreement with experiment. Finally, we have illustrated that the applied Epelbaum NN or NN+3N interaction over- or underbinds the absolute ground-state energy, respectively. These deviation might be due to the large uncertainties of the actual Epelbaum interactions at N²LO and there is work in progress [79] to revisit the LEC-fit procedure to improve these interactions.

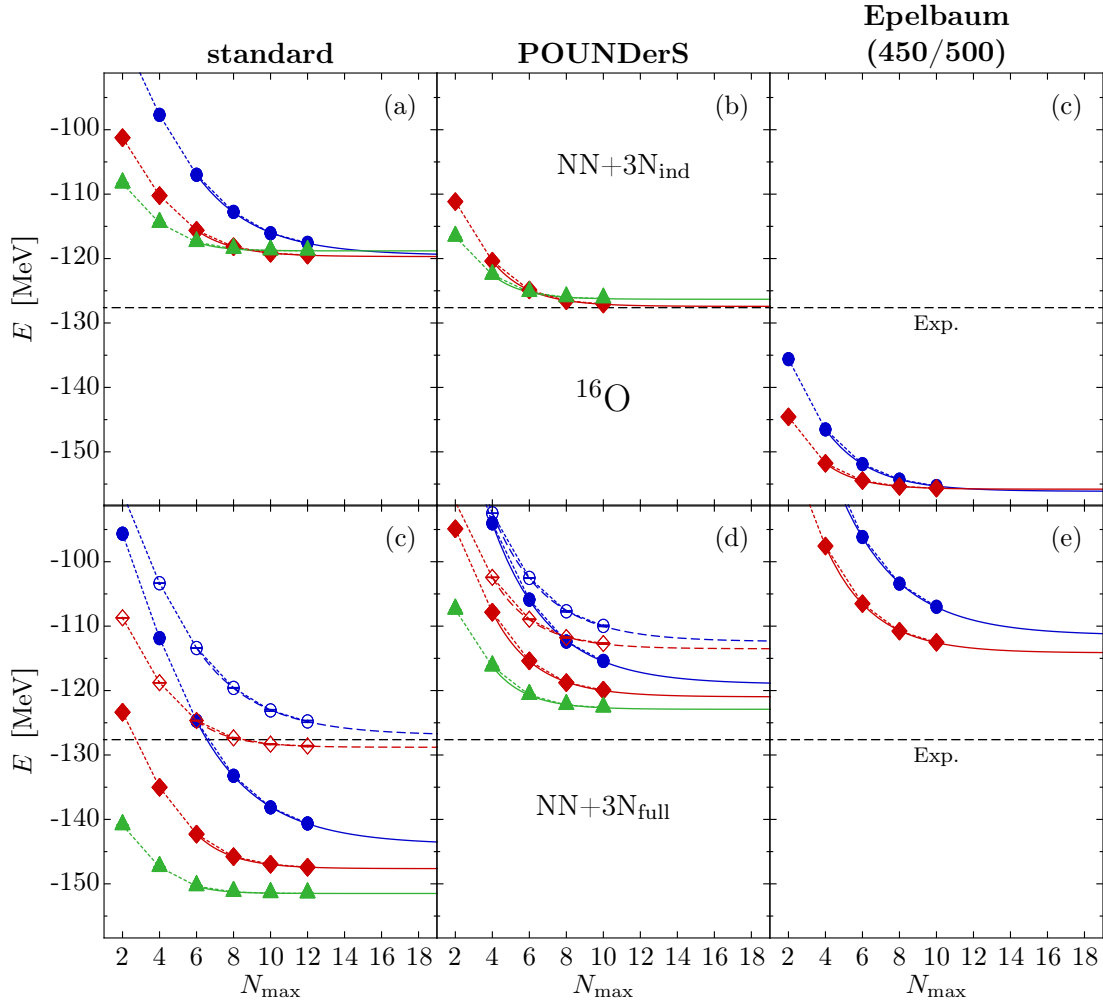


Figure 8.12 *Ground-state energy for ^{16}O* : Ground-state energies of ^{16}O computed with the IT-NCSM at $\hbar\Omega = 20$ MeV as function of N_{\max} using the flow parameters $\alpha = 0.04$ fm 4 (\bullet), 0.08 fm 4 (\blacklozenge), and 0.16 fm 4 (\blacktriangle). We show results with the NN+ $3N_{\text{ind}}$ (upper row) and NN+ $3N_{\text{full}}$ (lower row) Hamiltonians using the standard (left panels) and POUNDERs (middle panels) interaction with $\Lambda_{3\text{N}} = 500$ MeV/c (solid symbols) and 400 MeV/c (open symbols), as well as the Epelbaum interaction with $(\Lambda/\hat{\Lambda}) = (450/500)$ MeV/c (right panels). The solid and dashed curves indicate the N_{\max} -extrapolated results.

9 Next-Generation Chiral Interactions

In the following, we show first ab initio nuclear structure results with next-generation chiral interactions, i.e., we employ the NN and 3N contributions consistently at N³LO (see Sec. 1.4). The Epelbaum NN+3N interaction at N³LO allows to study the numerous operator structures that appear at this chiral order. In particular, the 3N contributions at N³LO have never been studied in nuclear structure calculations beyond the s shell. Moreover, this next-generation interaction enables to extend the uncertainty quantification for the Epelbaum interactions. In Sec. 8.2.1 we have studied the chiral uncertainty at N²LO via a cutoff variation. For a complete uncertainty quantification we need to study the impact of the truncation with respect to the chiral order, which we present in this section.

The non-local 3N contributions at N³LO are produced within the LENPIC collaboration [76], and are available in the partial-wave decomposed Jacobi-momentum representation. We treat these matrix elements with the same techniques and truncations as before for the application of the non-local 3N interactions at N²LO (see Sec. 8.2). This means, we truncate the angular momenta of the 3N interactions to $J_{12} \leq \frac{7}{2}$ and $J_1 \leq 6$ or 7 and perform the transformation to the Jacobi-HO representation as discussed in Sec. 3.5. Subsequently, we utilize the HO three-body machinery to apply the interaction in nuclear structure calculations.

We concentrate on the Epelbaum interaction with $(\Lambda/\hat{\Lambda}) = (450/500)$ MeV/c and compare the p-shell spectra obtained from the Epelbaum interactions at N²LO (see Sec. 1.3.3) and N³LO (see Sec. 1.4) to those for the standard interaction. In Fig. 9.1 we show the ⁶Li excitation spectra for these three NN+3N Hamiltonians. The IT-NCSM calculations are performed at $N_{\max} = 12$ and $\hbar\Omega = 16$ MeV using $\alpha = 0.08$ fm⁴. All three Hamiltonians provide reasonable predictions for the excitation spectrum and can reproduce the level ordering of the investigated states. However, a noteworthy general improvement compared to experiment cannot be achieved when increasing the chiral order for the Epelbaum interactions. Moreover, we observe large changes of about 1 MeV for the 3⁺ and 2⁺ excitation energies when we compare the N²LO and N³LO results. It is interesting to observe that the variations of the excitation energies with the Epelbaum interactions at both chiral orders include the experimental energies as well as the energies obtained with the standard NN+3N interaction.

We proceed to the ¹²C excitation spectrum depicted in Fig. 9.2. In addition to the NN+3N energies (NN+3N_{full}) of the three interactions we also quote the energies for the corresponding initial NN interactions (NN+3N_{ind}). The parameters of the calculations are identical to those in Fig. 9.1 using a smaller IT-NCSM model space truncated at $N_{\max} = 8$. The depicted spectra

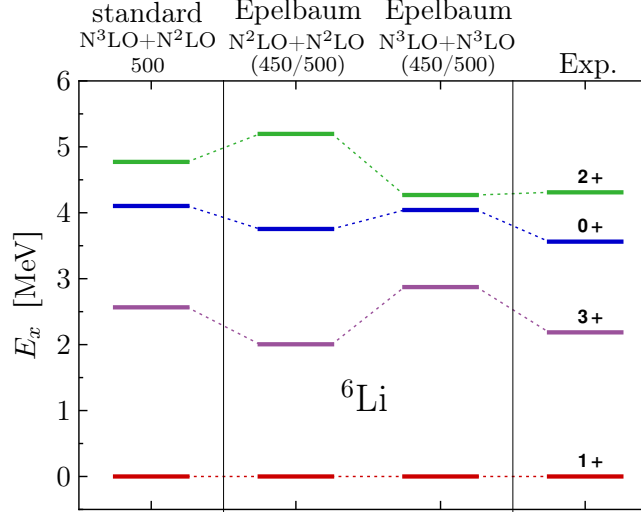


Figure 9.1 *Excitation spectra of ${}^6\text{Li}$ with present and next-generation chiral interactions:* Excitation spectra of ${}^6\text{Li}$ obtained with the $\text{NN}+3\text{N}_{\text{full}}$ Hamiltonians using the standard interaction with $\Lambda_{3\text{N}} = 500 \text{ MeV}/c$ and the Epelbaum interaction with $(\Lambda/L\text{m}SFR) = (450/500) \text{ MeV}/c$ at N^2LO and N^3LO . The IT-NCSM calculations are carried out at $N_{\text{max}} = 12$ and $\hbar\Omega = 16 \text{ MeV}$ using $\alpha = 0.08 \text{ fm}^4$. In the right-hand column we show the experimental values [183].

show a similar effect when including the initial 3N force. For instance, the excitation energies of the rotational band (first 2^+ and 4^+ state) increase and the excitation energy of the first 1^+ state decreases. The Epelbaum $\text{NN}+3\text{N}$ interaction at N^3LO predicts a rather large 0^+ excitation energy and small excitation energies of the rotational band, in particular, of the 4^+ state compared to the other $\text{NN}+3\text{N}$ interactions and to experiment. Note that the observed deviations for the N^2LO and N^3LO interactions already appear for the results of the initial NN interactions, which seem to be the origin of the discrepancies. However, again we observe large discrepancies when we compare the spectra for the Epelbaum $\text{NN}+3\text{N}$ interaction at N^2LO and N^3LO . Also the absolute ground-state energies deviate by more than 10 MeV.

Finally, we consider the ${}^{10}\text{B}$ excitation spectrum in Fig. 9.3 that constitutes an excellent benchmark case for chiral interactions. The results are striking: While the standard interaction and the Epelbaum interaction at N^2LO provide comparable predictions when the initial 3N forces are included, the spectrum for the N^3LO interaction is quite different. The excitation energies with respect to the 3^+ state are generally underestimated compared to experiment or to the other $\text{NN}+3\text{N}$ interactions. In particular, the first and second 2^+ as well as the first 1^+ excitation energies are too small, such that the level ordering is not well reproduced and the ground state is predicted to be a 1^+ state.

However, the effect caused by the inclusion of the chiral 3N force at N^3LO seems to be reasonable and generally improves the agreement with experimental. The observed deviations due to the increase of the chiral order for the ${}^{12}\text{C}$ and, in particular, for the ${}^{10}\text{B}$ spectrum seem to

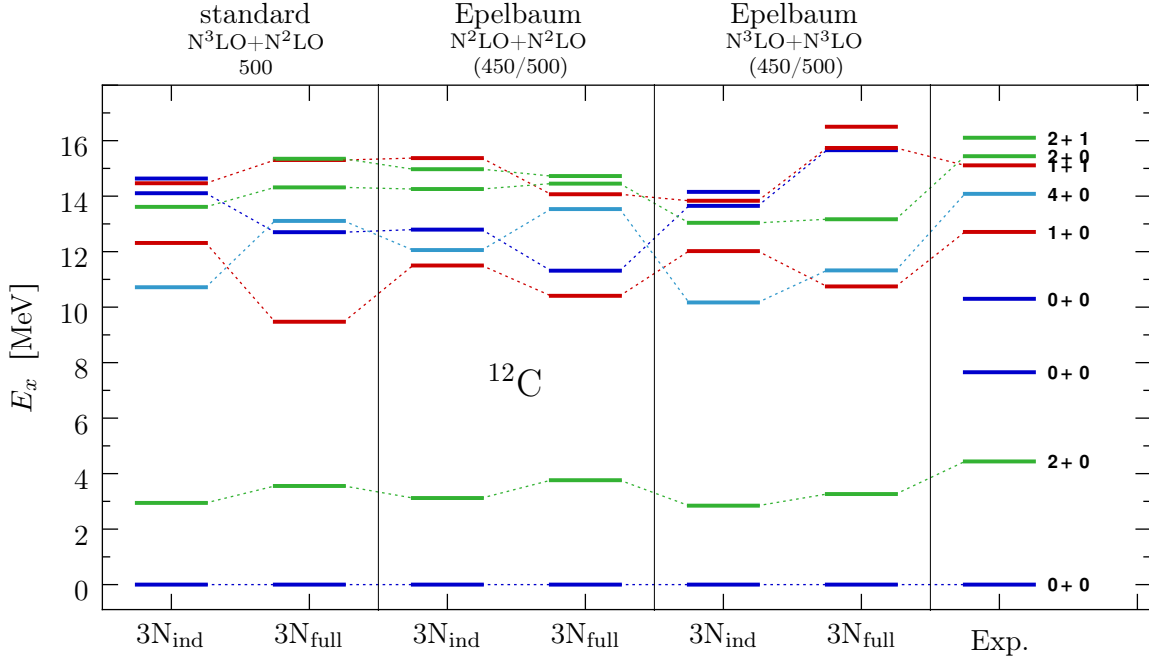


Figure 9.2 *Excitation spectra for ^{12}C with the next-generation chiral interactions:* Similar plot as in Fig. 8.8 comparing the excitation spectrum for the standard interaction to those for the Epelbaum interactions with $(\Lambda/\hat{\Lambda}) = (450/500)$ MeV/c at N^2LO and N^3LO . Experimental data taken from Ref. [167].

originate from the initial NN interaction. As mentioned in Sec. 8.2 one should revisit the LEC-fit procedure to improve the NN forces, which could be the reason for the unsatisfying results with the consistent NN+3N interaction at N^3LO . An indication for problems with the fit procedure of the N^3LO interaction is the unnaturally large c_D value. One can interpret this large value as the requirement of a strong 3N correction to account for the ill defined NN interactions and to describe the $A = 3$ systems properly.

In summary, with the developments of this work we have the ability to apply the present and also the next-generation chiral NN+3N interactions to ab initio nuclear structure calculations. From a comparison of the p-shell spectra one can draw conclusions about the uncertainties of the studied chiral NN+3N interactions. From these observations we conclude that the Epelbaum NN interactions seem to be the origin for the strong variations in the studied spectra when we increase the chiral order from N^2LO to N^3LO . For future applications one needs to study the error bands caused by a cutoff variation at both chiral orders and should try to reduce these error bands by improving the LEC-fit procedure. An exciting question is whether the next-generation chiral interactions can reproduce the experimental results within the error bands and whether the uncertainties shrink with increasing chiral order,

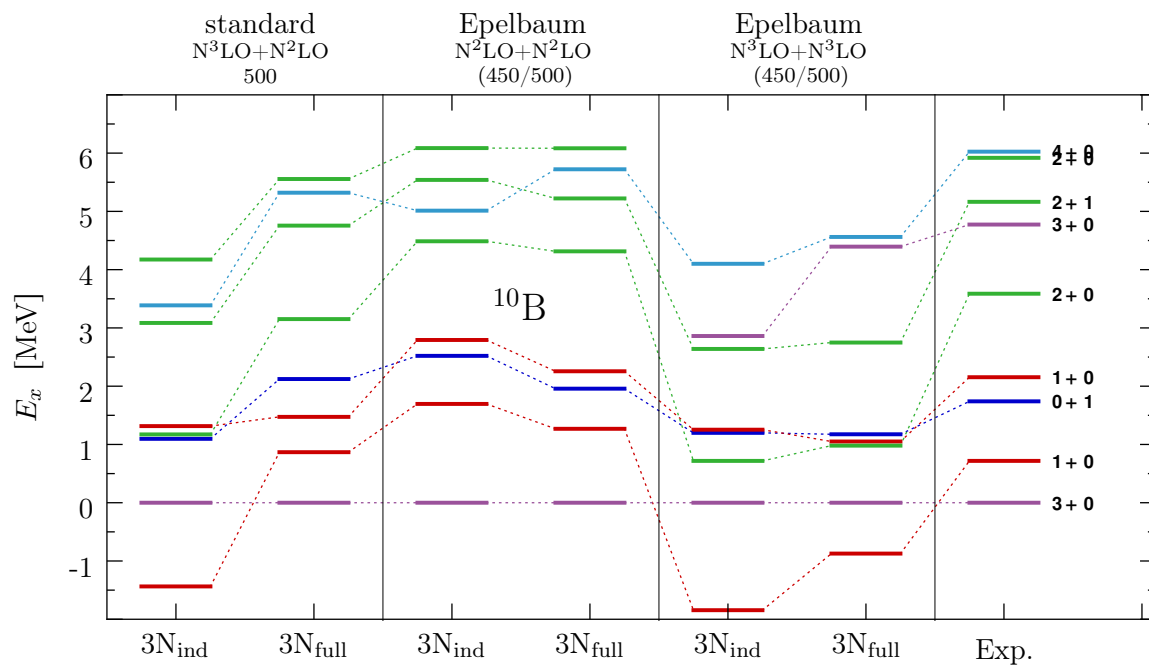


Figure 9.3 *Excitation spectra for ^{10}B with the next-generation chiral interactions:* Similar plot as in Fig. 9.2 for the excitation spectra of ^{10}B . Experimental data taken from Ref. [181].

10 Conclusion and Outlook

Starting from interaction matrix elements in the Jacobi-momentum or harmonic-oscillator (HO) representation we have developed a complete toolchain to efficiently employ present and future chiral nucleon-nucleon (NN), three-nucleon (3N), and four-nucleon (4N) interactions in nuclear structure calculations. This toolchain includes the consistent similarity renormalization group (SRG) evolution, the frequency-conversion approach, and the Talmi-Moshinsky transformation in the three- and four-body space.

The SRG is an important ingredient for many practical computations in nuclear structure theory. By softening the interaction with the SRG the convergence of the many-body calculations with respect to the model space is accelerated and the impact of further truncations, e.g., regarding the inclusion of 3N matrix elements or the truncations in the many-body method is reduced. However, during the evolution the SRG induces many-nucleon forces that generally cannot be fully included in the calculations and, thus, pose a great challenge for reliable applications.

Initially we have focused on the standard NN+3N interaction to study the effects of truncations in three-body space and of the induced many-body forces. The induced 3N contributions originating from the initial NN interactions generally have sizable repulsive effects on the ground-state energies and need to be included in order to allow for quantitative predictions. Moreover, the two-pion exchange contributions in the initial 3N force, mainly the c_3 terms, have been identified as main source of induced beyond-3N forces that have sizable repulsive contributions to the ground-state energies for nuclei beyond the mid-p shell. This limits the range of applicability of the standard NN+3N interaction. To address this issue we have presented a way to suppress the impact of induced many-nucleon forces by reducing the three-body cutoff Λ_{3N} to enable applications beyond the p and sd shell.

It is important to carefully study the impact of truncations when entering a new physical regime, such as the regime of heavy nuclei. While the truncations of the ab initio coupled-cluster approach are rather well under control, the treatment of the 3N matrix elements poses some unexpected challenges. In particular, the SRG-induced 3N contributions with large angular momenta originating from the initial NN force become significant for the description of the ground-state energies and require a substantial extension of the SRG space. The frequency conversion has proven to be a useful tool to accelerate the convergence with respect to the SRG space and to reduce the computational demands when targeting at calculations for multiple frequencies.

Beyond the sd shell also induced 4N and many-nucleon forces originating from the initial NN interaction become significant for ground-state energies and we have verified this observation for the POUNDerS NN interaction as well. For a three-body cutoff between 350 MeV/c and 400 MeV/c we have found a cancellation of the induced beyond-3N contributions that originate from the standard initial NN and 3N interactions. This cancellation enables us to study the nuclear ground-state energies up to the tin isotopes using the chiral NN+3N interactions with reduced three-body cutoff. The ground states beyond the sd shell are overbound by an almost constant energy shift of about 1 MeV per nucleon, such that the systematic mass trend can be reproduced. In consideration of the fact that the parameters of the chiral interactions have been fixed in $A \leq 4$ systems, this constitutes an impressive demonstration of the predictive power of the chiral interactions. Nevertheless, the cancellation of the induced beyond-3N contributions does not appear for all three-body cutoffs.

In order to prevent the induced many-body forces from the outset we have introduced physically motivated alternatives to the canonical SRG generator, which exclude the initial 3N forces or restrict the range in coordinate space. We have observed that a reduction of the induced many-body forces and, typically, worsens the convergence acceleration of the many-body calculations with respect to the model space. These studies provide a deeper insight in the nature and origin of the induced many-nucleon forces and indicate that induced many-nucleon contributions of the initial NN interaction primarily originate from medium-range components that need to be softened by the SRG to accelerate the convergence in the many-body calculations. The findings of this work might be crucial for the development of future SRG generators.

To include the dominant induced many-nucleon forces explicitly we have extended the three-body developments to the four-body space. This extension is of particular importance since it enables us to include SRG-induced as well as initial 4N forces. We have discussed the truncations in four-body space and have studied their impact on the ^{16}O ground-state energy. The model-space dimensions in the four-body space rapidly increase with the maximum energy quantum number and the SRG-space truncation constitutes the major limitation for the inclusion of 4N contributions. Therefore, the frequency conversion is indispensable to reduce the dependence on the SRG space truncation. We have presented first ab initio nuclear structure results obtained with the importance-truncated no-core shell model (IT-NCSM) for ground-state energies in the p shell explicitly including 4N contributions for the lowest angular momenta. The inclusion of the 4N contributions reduces the impact omitted induced contributions and decreases the flow-parameter dependence. Due to the rather large uncertainties of the approach the impact of missing 4N contributions with larger angular momenta as well as higher particle-rank contributions cannot be assessed.

However, the studies indicate that a further increase of the SRG space will strongly reduce the actual uncertainties, such that missing contributions can be estimated by the remaining flow-parameter dependence. The four-body techniques developed in this work are the basis

for future employments of induced as well as initial 4N forces. Through a straight-forward extension of the normal-ordering (NO) approach the 4N contributions can be included in a variety of many-body methods. In particular, for increasing mass number the sensitivity to the SRG space is expected to become critical, such that careful studies and further improvements regarding the SRG space are required.

While the ground-state energies show a strong sensitivity to the induced many-nucleon forces, excitation spectra are only weakly affected and the chiral NN+3N forces can be used without restrictions to lower three-body cutoffs. We have studied the significance of local 3N contributions at N²LO in a comprehensive sensitivity analysis for excitation spectra in the p shell. The components of the two-pion exchange term proportional to c_3 have a strong impact on the excitation spectrum and dominate the total effect of the 3N forces. Moreover, the excitation energies of the first 1⁺ state of ¹²C and ¹⁰B are highly sensitive to the 3N force and we have identified a correlation between these two excitation energies that prevent a simultaneous description of the experimental values by adjusting the parameters of the 3N force at N²LO. This observation indicates the need for additional 3N operator structures that emerge, e.g., in the subleading 3N force or in a Δ -full formulation of the chiral EFT, but might also hint at deficiencies of the NN sector. Thus, it is important to construct a whole family of consistent NN+3N interactions with varying cutoff and chiral order to assess the uncertainties of the chiral interaction.

As a first step towards a systematic uncertainty quantification we have investigated different sets of presently available chiral NN+3N interactions obtained at N²LO. While the POUNDerS NN interaction currently exist for a single cutoff combination and has been augmented by local 3N forces, there is a whole set of Epelbaum NN+3N interactions for different cutoff combinations. The inclusion of the initial 3N force generally improves the agreement of the excitation spectra with experiment for the considered interactions. However, we have found large discrepancies in the excitation energies obtained with the different Epelbaum interactions that originate from the NN force. This indicates deficiencies in the NN sector of the Epelbaum interactions that also influence the effect of the 3N forces and we stress that the parameter fit of these NN interactions needs to be revisited for reliable nuclear structure applications.

In addition, we also have compared the ground-state energy of ¹⁶O for the standard interaction to the results obtained with the POUNDerS and Epelbaum interactions. The standard NN interaction typically underbinds the ground-state energies in the p shell and the attractive effect of the initial 3N force substantially improves the experimental agreement. The POUNDerS NN interaction already predicts the ¹⁶O ground-state energy in agreement with experiment, but the inclusion of the local 3N interaction worsens the agreement and its repulsive effect leads to a strong underbinding. The Epelbaum NN and NN+3N interactions strongly over- or underbind the ground state, respectively, once again indicating fundamental problems with these forces. An important aspect are the SRG-induced beyond-3N forces that have become sizable also

for the Epelbaum and POUNDerS interactions, such that the investigations and developments regarding the suppression or inclusion of the induced many-nucleon forces are of general interest for the present and, without much doubt, also future chiral interactions.

Finally, we have presented the first nuclear structure results for p-shell nuclei using the next-generation Epelbaum NN+3N interaction at N³LO that has been constructed within the LENPIC collaboration. This interaction enables us to study the impact of the chiral-order truncation by comparing to results with the Epelbaum interaction at N²LO. The discrepancies observed in the excitation spectra for the different chiral orders are very large and again seem to originate from the NN sector. Besides, the ¹⁰B excitation spectrum obtained with the NN+3N interaction at N³LO shows large deviations from the experimental values, e.g., the ground state is predicted to be a 1⁺ state instead of a 3⁺ state found in experiments.

In conclusion, we have presented the developed techniques to efficiently include the currently available and future chiral NN+3N+4N interactions in a variety of ab initio nuclear structure and also reaction calculations. The construction of interaction matrix elements for chiral NN+3N forces at N³LO within the LENPIC collaboration will have a significant impact on the nuclear structure community. Nevertheless, the studies of this work reveal the necessity for systematic and accurate refits of the NN parameters at N²LO and N³LO.

The presented nuclear structure results provide constraints for the fit of the LECs. In particular, the c_3 parameter has a strong influence on spectroscopic observables and its accurate and appropriate determination is recommended. Finally, we stress the importance of constructing the chiral interactions for several cutoffs at different chiral orders to enable a systematic quantification of the uncertainties.

A Notation and Conventions

Acronyms

1PE	one-pion exchange
2PE	two-pion exchange
3N	three-nucleon
4N	four-nucleon
ACCS(D)(T)	coupled-cluster method with singles, doubles, and perturbative triples corrections
aPWD	automatized partial-wave decomposition
CC	coupled-cluster
CCSD	coupled-cluster method with singles and doubles excitations
CCSDT	coupled-cluster method with singles, doubles, and triples excitations
CFP	coefficient of fractional parentage
ChPT	chiral perturbation theory
CI	configuration interaction
CR-CC(2,3)	left-eigenstate completely renormalized coupled-cluster method with singles, doubles and non-iterative triples excitations
ct	three-nucleon contact
EFT	effective field theory
GFMC	Green's function Monte Carlo
HO	harmonic oscillator
HOB	harmonic-oscillator bracket
IM-SRG	in-medium similarity renormalization group
IT	importance truncation
IT-NCSM	importance truncated no-core shell model
LEC	low-energy constant
LENPIC	low-energy nuclear physics international collaboration

LO	leading order
MFDn	many-fermion dynamics for nuclei
MR-IM-SRG	multi-reference in-medium similarity renormalization group
MR-IM-SRG(2)	multi-reference in-medium similarity renormalization group in the normal-ordered two-body approximation
N ² LO	next-to-next-to-leading order
N ³ LO	next-to-next-to-next-to-leading order
NCSM	no-core shell model
NCSMC	no-core shell model combined with continuum
NCSM/RGM	no-core shell model combined with the resonating group method
NLO	next-to-leading order
NN	nucleon-nucleon
NO	normal ordering
NO _n B	normal-ordered n -body approximation
POUNDerS	practical optimization using no derivatives (for squares) algorithm
QCD	quantum chromodynamics
SFR	spectral-function regularization
SRG	similarity renormalization group
UCOM	unitary correlation operator method

Short-Hand Notations

Throughout this work we introduce some short-hands to denote different Hamiltonians, model spaces, or procedures that are used in the interaction toolchain.

Chiral NN+3N interactions (see Tab. 1.1 on page 18)	
standard	NN interaction at N ³ LO by Entem and Machleidt combined with local 3N force at N ² LO
Epelbaum	NN+3N interaction by Epelbaum et. al at N ² LO and N ³ LO using a non-local 3N force
POUNDERs	NN interaction at N ² LO fitted with POUNDERs algorithm combined with local 3N force at N ² LO
SRG-evolved Hamiltonians (see Tab. 4.1 on page 75)	
NN _{only}	NN interaction evolved at the two-body level
NN+3N _{ind}	NN interaction evolved at the three-body level
NN+3N _{full}	NN+3N interaction evolved at the three-body level
NN+3N _{ind} +4N _{ind}	NN interaction evolved at the four-body level
NN+3N _{full} +4N _{ind}	NN+3N interaction evolved at the four-body level
SRG model spaces	
ramp $\mathcal{A} - \mathcal{C}$	SRG spaces applied in the p shell (see Fig. 5.2 on page 99)
ramp $\mathcal{D} - \mathcal{H}$	SRG spaces applied beyond the p and sd shell (see Fig. 5.7 on page 106)
Subtraction procedures in the four-body space	
SubA - D	Subtraction schemes increasing in complexity (see Sec. 4.7.2)

B Publications

The developments and results that have been work out throughout this thesis led to multiple publications listed in the following:

1. H. D. Potter, S. Fischer, P. Maris, J. P. Vary, S. Binder, A. Calci, J. Langhammer, R. Roth
“Ab Initio study of neutron drops with chiral Hamiltonians”
arXiv:1406.1160 (submitted to Phys. Lett. B)
2. P. Maris, J. P. Vary, R. Roth, A. Calci, J. Langhammer, S. Binder
“ $^{12}\text{-C}$ Properties with Evolved Chiral Three-Nucleon Interactions”
arXiv:1405.1331 (submitted to Phys. Rev. C)
3. R. Wirth, D. Gazda, P. Navrátil, A. Calci, J. Langhammer, R. Roth
“Ab Initio Description of p -Shell Hypernuclei”
arXiv:1403.3067 (submitted to Phys. Rev. Lett.)
4. S. K. Bogner, H. Hergert, J. D. Holt, A. Schwenk, S. Binder, A. Calci, J. Langhammer, R. Roth
“Nonperturbative shell-model interactions from the in-medium similarity renormalization group”
arXiv:1402.1407 (submitted to Phys. Rev. Lett.)
5. S. Binder, J. Langhammer, A. Calci, R. Roth
“Ab Initio Path to Heavy Nuclei”
arXiv:1312.5685 (submitted to Phys. Lett. B)
6. R. Roth, A. Calci, J. Langhammer, S. Binder
“Evolved Chiral $NN+3N$ Hamiltonians for Ab Initio Nuclear Structure Calculations”
arXiv:1311.3563 (submitted to Phys. Rev. C)
7. S. Binder, P. Piecuch, A. Calci, J. Langhammer, P. Navrátil, R. Roth
“Extension of coupled-cluster theory with a non-iterative treatment of connected triply excited clusters to three-body Hamiltonians”
Phys. Rev. C 88, 054319 (2013)
8. G. Hupin, J. Langhammer, P. Navrátil, S. Quaglioni, A. Calci, R. Roth
“Ab initio many-body calculations of nucleon- ^4He scattering with three-nucleon forces ”
Phys. Rev. C 88, 054622 (2013)

-
9. H. Hergert, S. Binder, A. Calci, J. Langhammer, R. Roth
“Ab Initio Calculations of Even Oxygen Isotopes with Chiral Two- Plus Three-Nucleon Interactions”
Phys. Rev. Lett. 110, 242501 (2013)
 10. H. Hergert, S. K. Bogner, S. Binder, A. Calci, J. Langhammer, R. Roth, A. Schwenk
“In-Medium Similarity Renormalization Group with Chiral Two- Plus Three-Nucleon Interactions”
Phys. Rev. C 87, 034307 (2013)
 11. S. Binder, J. Langhammer, A. Calci, P. Navrátil, R. Roth
“Ab Initio Calculations of Medium-Mass Nuclei with Explicit Chiral 3N Interactions”
Phys. Rev. C 87, 021303(R) (2013) - Editors’ Suggestion
 12. R. Roth, A. Calci, J. Langhammer, S. Binder
“Ab Initio Nuclear Structure Theory: From Few to Many”
Proceedings of the 22nd European Conference on Few-Body Problems in Physics (EFB22),
September 9-13, 2013, Krakow, Poland
 13. R. Roth, A. Calci, J. Langhammer, S. Binder
“Towards New Horizons in Ab Initio Nuclear Structure Theory”
Proceedings of the 25th International Nuclear Physics Conference 2013 (INPC2013), June
2 - 7, 2013, Firenze, Italy
 14. P. Maris, H. M. Aktulga, S. Binder, A. Calci, Ü. V. Çatalyürek, J. Langhammer, E. Ng,
E. Saule, R. Roth, J. P. Vary, C. Yang
“No Core CI calculations for light nuclei with chiral 2- and 3-body forces”
J. Phys. Conf. Ser. 454, 012063 (2012)
Proceedings of the 24th IUPAP Conference on Computational Physics (IUPAP-CCP
2012), October 14 - 18, 2012, Kobe, Japan
 15. R. Roth, J. Langhammer, A. Calci, S. Binder,
“From Chiral EFT Interactions to Ab Initio Nuclear Structure”
PoS(CD12) 015 (2013)
Proceedings of the 7th International Workshop on Chiral Dynamics, August 6 - 10, 2012,
Jefferson Lab, Newport News, VA, USA

-
16. R. Roth, S. Binder, K. Vobig, A. Calci, J. Langhammer, P. Navrátil
“Ab Initio Calculations of Medium-Mass Nuclei with Normal-Ordered Chiral NN+3N Interactions”
Phys. Rev. Lett. 109, 052501 (2012)
 17. R. Roth, J. Langhammer, S. Binder, A. Calci
“New Horizons in Ab Initio Nuclear Structure Theory”
J. Phys.: Conf. Ser. 403, 012020 (2012)
Proceedings of the Conference on Horizons of Innovative Theories, Experiments, and Supercomputing in Nuclear Physics (HITES 2012), June 4 - 7, 2012, New Orleans, USA
 18. R. Roth, J. Langhammer, A. Calci, S. Binder, P. Navrátil
“Ab Initio Nuclear Structure Theory with Chiral NN+3N Interactions”
Prog. Theor. Suppl. 196, 131 (2012)
Proceedings of the YKIS2011 Symposium on Frontier Issues in Physics of Exotic Nuclei, October 11 - 15, 2011, Yukawa Institute for Theoretical Physics, Kyoto, Japan
 19. R. Roth, J. Langhammer, A. Calci, S. Binder, P. Navrátil
“Similarity-Transformed Chiral NN+3N Interactions for the Ab Initio Description of 12-C and 16-O”
Phys. Rev. Lett. 107, 072501 (2011)

References

- [1] H. Yukawa; *On the Interaction of Elementary Particles. I*; Proc. Phys.-Math. Soc. Jpn. **17** (1935) 48.
- [2] R. B. Wiringa, V. G. J. Stoks, R. Schiavilla; *An Accurate Nucleon–Nucleon Potential with Charge–Independence Breaking*; Phys. Rev. C **51** (1995) 38.
- [3] R. Machleidt; *High-precision, charge-dependent Bonn nucleon-nucleon potential*; Phys. Rev. C **63** (2001) 024001.
- [4] E. Caurier, P. Navrátil, W. E. Ormand, J. P. Vary; *Ab initio shell model for $A = 10$ nuclei*; Phys. Rev. C **66** (2002) 024314.
- [5] P. Navrátil, W. E. Ormand; *Ab Initio Shell Model Calculations with Three-Body Effective Interactions for p -Shell Nuclei*; Phys. Rev. Lett. **88** (2002) 152502.
- [6] S. C. Pieper, K. Varga, R. B. Wiringa; *Quantum Monte Carlo calculations of $A = 9, 10$ nuclei*; Phys. Rev. C **66** (2002) 044310.
- [7] S. Weinberg; *Phenomenological Lagrangians*; Physica A: Statistical Mechanics and its Applications **96** (1979) 327.
- [8] D. R. Entem, R. Machleidt; *Accurate charge-dependent nucleon-nucleon potential at fourth order of chiral perturbation theory*; Phys. Rev. C **68** (2003) 041001(R).
- [9] E. Epelbaum, W. Glöckle, U.-G. Meißner; *Improving the convergence of the chiral expansion for nuclear forces - II: Low phases and the deuteron*; Eur. Phys. J. A **19** (2004) 401.
- [10] E. Epelbaum, W. Glöckle, U.-G. Meißner; *The two-nucleon system at next-to-next-to-next-to-leading order*; Nucl. Phys. A **747** (2005) 362.
- [11] A. Ekström, G. Baardsen, C. Forssén, *et al.*; *Optimized Chiral Nucleon-Nucleon Interaction at Next-to-Next-to-Leading Order*; Phys. Rev. Lett. **110** (2013) 192502.
- [12] E. Epelbaum, A. Nogga, W. Glöckle, *et al.*; *Three-nucleon forces from chiral effective field theory*; Phys. Rev. C **66** (2002) 064001.
- [13] P. Navrátil; *Local three-nucleon interaction from chiral effective field theory*; Few Body Syst. **41** (2007) 117.
- [14] R. Skibiński, J. Golak, K. Topolnicki, *et al.*; *3H at Next-to-Next-to-Next-to Leading Order of the Chiral Expansion*; Few-Body Systems **54** (2013) 1315.

-
- [15] F. Wegner; *Flow Equations for Hamiltonians*; Ann. Phys. (Leipzig) **3** (1994) 77.
- [16] F. J. Wegner; *Flow Equations for Hamiltonians*; Nucl. Phys. B Proc. Suppl. **90** (2000) 141.
- [17] S. Szpigel, R. J. Perry; *The Similarity Renormalization Group*; in A. N. Mitra (editor), *Quantum Field Theory. A 20th Century Profile*; Hindustan Publishing Co., New Delhi (2000).
- [18] R. Roth, T. Neff, H. Feldmeier; *Nuclear Structure in the Framework of the Unitary Correlation Operator Method*; Prog. Part. Nucl. Phys. **65** (2010) 50.
- [19] S. K. Bogner, R. J. Furnstahl, R. J. Perry; *Similarity renormalization group for nucleon-nucleon interactions*; Phys. Rev. C **75** (2007) 061001(R).
- [20] R. Roth, J. Langhammer, A. Calci, *et al.*; *Similarity-Transformed Chiral NN+3N Interactions for the Ab Initio Description of ^{12}C and ^{16}O* ; Phys. Rev. Lett. **107** (2011) 072501.
- [21] R. Roth, A. Calci, J. Langhammer, S. Binder; *Evolved Chiral NN+3N Hamiltonians for Ab Initio Nuclear Structure Calculations*; arXiv:1311.3563 [nucl-th] (2013).
- [22] P. Maris, J. P. Vary, A. Calci, *et al.*; *^{12}C properties with evolved chiral three-nucleon interactions*; arxiv:1405.1331 [nucl-th] (2014).
- [23] S. K. Bogner, H. Hergert, J. D. Holt, *et al.*; *Nonperturbative shell-model interactions from the in-medium similarity renormalization group*; arxiv:1402.1407 [nucl-th] (2014).
- [24] G. Hupin, J. Langhammer, P. Navrátil, *et al.*; *Ab initio many-body calculations of nucleon- ^4He scattering with three-nucleon forces*; Phys. Rev. C **88** (2013) 054622.
- [25] R. Wirth, D. Gazda, P. Navrátil, *et al.*; *Ab Initio Description of p-Shell Hypernuclei*; arxiv:1403.3067 [nucl-th] (2014).
- [26] H. D. Potter, S. Fischer, P. Maris, *et al.*; *Ab Initio study of neutron drops with chiral Hamiltonians*; arxiv:1406.1160 [nucl-th] (2014).
- [27] G. Hagen, M. Hjorth-Jensen, G. R. Jansen, *et al.*; *Continuum Effects and Three-Nucleon Forces in Neutron-Rich Oxygen Isotopes*; Phys. Rev. Lett. **108** (2012) 242501.
- [28] S. Binder, P. Piecuch, A. Calci, *et al.*; *Extension of coupled-cluster theory with a non-iterative treatment of connected triply excited clusters to three-body Hamiltonians*; Phys. Rev. C **88** (2013) 054319.
- [29] S. Binder, J. Langhammer, A. Calci, *et al.*; *Ab initio calculations of medium-mass nuclei with explicit chiral 3N interactions*; Phys. Rev. C **87** (2013) 021303(R).
-

-
- [30] S. Binder, J. Langhammer, A. Calci, R. Roth; *Ab Initio Path to Heavy Nuclei*; arXiv:1312.5685 [nucl-th] (2013).
- [31] V. Somà, T. Duguet, C. Barbieri; *Ab initio self-consistent Gorkov-Green's function calculations of semimagic nuclei: Formalism at second order with a two-nucleon interaction*; Phys. Rev. C **84** (2011) 064317.
- [32] A. Cipollone, C. Barbieri, P. Navrátil; *Isotopic Chains Around Oxygen from Evolved Chiral Two- and Three-Nucleon Interactions*; Phys. Rev. Lett. **111** (2013) 062501.
- [33] V. Somà, A. Cipollone, C. Barbieri, *et al.*; *Leading chiral three-nucleon forces along isotope chains in the calcium region*; arXiv:1312.2068 [nucl-th] (2013).
- [34] K. Tsukiyama, S. K. Bogner, A. Schwenk; *In-Medium Similarity Renormalization Group For Nuclei*; Phys. Rev. Lett. **106** (2011) 222502.
- [35] H. Hergert, S. K. Bogner, S. Binder, *et al.*; *In-medium similarity renormalization group with chiral two- plus three-nucleon interactions*; Phys. Rev. C **87** (2013) 034307.
- [36] H. Hergert, S. Binder, A. Calci, *et al.*; *Ab Initio Calculations of Even Oxygen Isotopes with Chiral Two-Plus-Three-Nucleon Interactions*; Phys. Rev. Lett. **110** (2013) 242501.
- [37] H. Krebs, E. Epelbaum, U.-G. Meißner; *Nuclear forces with Δ excitations up to next-to-next-to-leading order, part I: Peripheral nucleon-nucleon waves*; The European Physical Journal A **32** (2007) 127.
- [38] N. Ishii, S. Aoki, T. Hatsuda; *Nuclear Force from Lattice QCD*; Phys. Rev. Lett. **99** (2007) 022001.
- [39] W. Weise; *The QCD vacuum and its hadronic excitations*; arXiv:0504087 [nucl-th] (2005).
- [40] K. Nakamura *et al.*, (Particle Data Group); *Review of Particle Physics*; J. Phys. G: Nucl. Part. Phys. **37** (2010) 075021.
- [41] A. Pich; *Effective Field Theory*; arXiv:hep-ph/9806303 (1998).
- [42] Evgeny E.; *Few-nucleon forces and systems in chiral effective field theory*; Progress in Particle and Nuclear Physics **57** (2006) 654.
- [43] J. Goldstone; *Field theories with Superconductor solutions*; Nuovo Cim. **19** (1961) 154.
- [44] J. Goldstone, A. Salam, S. Weinberg; *Broken Symmetries*; Phys. Rev. **127** (1962) 965.
- [45] E. Epelbaum, H.-W. Hammer, U.-G. Meißner; *Modern theory of nuclear forces*; Rev. Mod. Phys. **81** (2009) 1773.
-

-
- [46] E. Epelbaum; *Nuclear forces from chiral effective field theory: A primer*; arXiv:1001.3229 [nucl-th] (2010).
- [47] R. Machleidt, D. R. Entem; *Chiral effective field theory and nuclear forces*; Phys. Rep. **503** (2011) 1.
- [48] D. Lindley; *Nobel Focus: Limited Freedom for Quarks*; Phys. Rev. Focus **14** (2004) 15.
- [49] R. Machleidt; *Origin and properties of strong inter-nucleon interactions*; arXiv:1308.0103 (2013).
- [50] J. Beringer, J. F. Arguin, R. M. Barnett, *et al.*; *Review of Particle Physics*; Phys. Rev. D **86** (2012) 010001.
- [51] S. Weinberg; *Effective chiral lagrangians for nucleon-pion interactions and nuclear forces*; Nucl. Phys. B **363** (1991) 3.
- [52] S. Weinberg; *Nuclear forces from chiral lagrangians*; Phys. Lett. B **251** (1990) 288.
- [53] S. Weinberg; *Three-body interactions among nucleons and pions*; Phys. Lett. B **295** (1992) 114.
- [54] N. Kalantar-Nayestanaki, E. Epelbaum, J. G. Messchendorp, A. Nogga; *Signatures of three-nucleon interactions in few-nucleon systems*; Reports on Progress in Physics **75** (2012) 016301.
- [55] A. Nogga, R. G. E. Timmermans, U. van Kolck; *Renormalization of one-pion exchange and power counting*; Phys. Rev. C **72** (2005) 054006.
- [56] M. Pavón Valderrama, E. Ruiz Arriola; *Erratum: Renormalization of the NN interaction with a chiral two-pion exchange potential. II. Noncentral phases [Phys. Rev. C **74**, 064004 (2006)]*; Phys. Rev. C **75** (2007) 059905.
- [57] D. R. Entem, E. Ruiz Arriola, M. Pavón Valderrama, R. Machleidt; *Renormalization of chiral two-pion exchange NN interactions: Momentum space versus coordinate space*; Phys. Rev. C **77** (2008) 044006.
- [58] C.-J. Yang, C. Elster, D. R. Phillips; *Subtractive renormalization of the NN scattering amplitude at leading order in chiral effective theory*; Phys. Rev. C **77** (2008) 014002.
- [59] M. Pavón Valderrama; *Perturbative renormalizability of chiral two-pion exchange in nucleon-nucleon scattering*; Phys. Rev. C **83** (2011) 024003.
- [60] P. Lepage; *How to Renormalize the Schrödinger Equation*; arXiv: nucl-th/9706029 (1997).

-
- [61] S. Aoki; *Nucleon-nucleon interactions via Lattice QCD: Methodology*; The European Physical Journal A **49** (2013) 1.
- [62] P. Büttiker, U.-G. Meißner; *Pion-nucleon scattering inside the Mandelstam triangle*; Nucl. Phys. A **668** (2000) 97.
- [63] N. Fettes, U.-G. Meißner, S. Steininger; *Pion-nucleon scattering in chiral perturbation theory (I): Isospin-symmetric case*; Nuclear Physics A **640** (1998) 199.
- [64] E. Epelbaum, W. Glöckle, U.-G. Meißner; *Improving the convergence of the chiral expansion for nuclear forces - I: Peripheral phases*; Eur. Phys. J. A **19** (2003) 125.
- [65] M. Kortelainen, T. Lesinski, J. Moré, *et al.*; *Nuclear energy density optimization*; Phys. Rev. C **82** (2010) 024313.
- [66] V. G. J. Stoks, R. A. M. Klomp, M. C. M. Rentmeester, J. J. de Swart; *Partial-wave analysis of all nucleon-nucleon scattering data below 350 MeV*; Phys. Rev. C **48** (1993) 792.
- [67] U. van Kolck; *Few-nucleon forces from chiral Lagrangians*; Phys. Rev. C **49** (1994) 2932.
- [68] J. Fujita, H. Miyazawa; *Pion Theory of Three-Body Forces*; Progress of Theoretical Physics **17** (1957) 360.
- [69] J. L. Friar, D. Hüber, U. van Kolck; *Chiral symmetry and three-nucleon forces*; Phys. Rev. C **59** (1999) 53.
- [70] P. Navrátil, G. P. Kamuntavicius, B. R. Barrett; *Few-nucleon systems in a translationally invariant harmonic oscillator basis*; Phys. Rev. C **61** (2000) 044001.
- [71] K. Hebeler, R. J. Furnstahl; *Neutron matter based on consistently evolved chiral three-nucleon interactions*; Phys. Rev. C **87** (2013) 031302.
- [72] I. Tews, T. Krüger, K. Hebeler, A. Schwenk; *Neutron Matter at Next-to-Next-to-Next-to-Leading Order in Chiral Effective Field Theory*; Phys. Rev. Lett. **110** (2013) 032504.
- [73] T. Krüger, I. Tews, K. Hebeler, A. Schwenk; *Neutron matter from chiral effective field theory interactions*; Phys. Rev. C **88** (2013) 025802.
- [74] E. Epelbaum, U.-G. Meißner; *Chiral Dynamics of Few- and Many-Nucleon Systems*; Annual Review of Nuclear and Particle Science **62** (2012) 159.
- [75] R. Skibiński, J. Golak, K. Topolnicki, *et al.*; *Triton with long-range chiral N³LO three-nucleon forces*; Phys. Rev. C **84** (2011) 054005.

-
- [76] *Low-Energy Nuclear Physics International Collaboration (LENPIC)*, see <http://www.lenpic.org>.
- [77] D. Gazit, S. Quaglioni, P. Navrátil; *Three-Nucleon Low-Energy Constants from the Consistency of Interactions and Currents in Chiral Effective Field Theory*; Phys. Rev. Lett. **103** (2009) 102502.
- [78] P. Navrátil, S. Quaglioni; *private communication* .
- [79] E. Epelbaum; *private communication* .
- [80] A. Nogga, P. Navrátil, B. R. Barrett, Vary J. P.; *Spectra and binding energy predictions of chiral interactions for ${}^7\text{Li}$* ; Phys. Rev. C **73** (2006) 064002.
- [81] P. Navrátil, V. G. Gueorguiev, J. P. Vary, *et al.*; *Structure of $A1013$ nuclei with two- plus three-nucleon interactions from chiral field theory*; Phys. Rev. Lett. **99** (2007) 042501.
- [82] K. Hebel; *private communication*.
- [83] V. Bernard, E. Epelbaum, H. Krebs, U.-G. Meißner; *Subleading contributions to the chiral three-nucleon force: Long-range terms*; Phys. Rev. C **77** (2008) 064004.
- [84] V. Bernard, E. Epelbaum, H. Krebs, U.-G. Meißner; *Subleading contributions to the chiral three-nucleon force II: Short-range terms and relativistic corrections*; Phys.Rev. **C84** (2011) 054001.
- [85] S. Ishikawa, M. R. Robilotta; *Two-pion exchange three-nucleon potential: $O(q^4)$ chiral expansion*; Phys. Rev. C **76** (2007) 014006.
- [86] P. Navrátil, J. P. Vary, B. R. Barrett; *Properties of ${}^{12}\text{C}$ in the *Ab Initio* Nuclear Shell Model*; Phys. Rev. Lett. **84** (2000) 5728.
- [87] P. Navrátil, J. P. Vary, B. R. Barrett; *Large-basis *ab initio* no-core shell model and its application to ${}^{12}\text{C}$* ; Phys. Rev. C **62** (2000) 054311.
- [88] P. Navrátil, S. Quaglioni, I. Stetcu, B. Barrett; *Recent developments in no-core shell-model calculations*; J. Phys. G: Nucl. Part. Phys. **36** (2009) 083101.
- [89] B. R. Barrett, P. Navrátil, J. P. Vary; *Ab initio no core shell model*; Progress in Particle and Nuclear Physics **69** (2013) 131.
- [90] S. C. Pieper, R. B. Wiringa; *Quantum Monte Carlo Calculations of Light Nuclei*; Ann. Rev. Nucl. Part. Sci. **51** (2001) 53.
- [91] R. B. Wiringa, S. C. Pieper; *Evolution of Nuclear Spectra with Nuclear Forces*; Phys. Rev. Lett. **89** (2002) 182501.
-

-
- [92] S. C. Pieper, R. B. Wiringa, J. Carlson; *Quantum Monte Carlo calculations of excited states in $A = 6-8$ nuclei*; Phys. Rev. C **70** (2004) 054325.
- [93] A. G. Taube, R. J. Bartlett; *Improving upon CCSD(T): Lambda CCSD(T). I. Potential energy surfaces*; The Journal of Chemical Physics **128** (2008) 044110.
- [94] R. J. Bartlett I. Shavitt; *Many-Body Methods in Chemistry and Physics: MBPT and Coupled-Cluster Theory*; Cambridge Molecular Science (2009).
- [95] G. Hagen, T. Papenbrock, D. J. Dean, M. Hjorth-Jensen; *Ab initio coupled-cluster approach to nuclear structure with modern nucleon-nucleon interactions*; Phys. Rev. **C82** (2010) 034330.
- [96] P. Ring, P. Schuck; *The Nuclear Many-Body Problem*; Springer Verlag, New York (1980).
- [97] D. H. Gloeckner, R. D. Lawson; *Spurious center of mass motion*; Phys. Lett. **53B** (1974) 313.
- [98] G. Hagen, T. Papenbrock, D. J. Dean, *et al.*; *Coupled-cluster theory for three-body Hamiltonians*; Phys. Rev. C **76** (2007) 034302.
- [99] S. Binder; *Coupled-Cluster Theory for Nuclear Structure*; Ph.D. thesis; TU Darmstadt (2014).
- [100] J. P. Vary, P. Maris, E. Ng, *et al.*; *Ab initio nuclear structure - the large sparse matrix eigenvalue problem*; Journal of Physics: Conference Series **180** (2009) 012083.
- [101] P. Maris, H. M. Aktulga, S. Binder, *et al.*; *No Core CI calculations for light nuclei with chiral 2- and 3-body forces*; Journal of Physics: Conference Series **454** (2013) 012063.
- [102] I. Mayer; *Simple Theorems, Proofs, and Derivations in Quantum Chemistry*; Kluwer Academic (2003).
- [103] J. C. Slater; *The Theory of Complex Spectra*; Phys. Rev. **34** (1929) 1293.
- [104] D. Oryspayev, H. Potter, P. Maris, *et al.*; *Leveraging GPUs in Ab Initio Nuclear Physics Calculations*; in *Proceedings of the 2013 IEEE 27th International Symposium on Parallel and Distributed Processing Workshops & PhD Forum (IPDPSW), 20-24 May 2013, Cambridge, MA, USA* (2013).
- [105] T. Neff; *Clusters and halos in light nuclei*; Journal of Physics: Conference Series **403** (2012) 012028.
- [106] B. D. Keister, W. N. Polyzoou; *Useful Bases for Problems in Nuclear and Particle Physics*; Journal of Computational Physics **134** (1997) 231.
-

-
- [107] M. A. Caprio, P. Maris, J. P. Vary; *Coulomb-Sturmian basis for the nuclear many-body problem*; Phys. Rev. C **86** (2012) 034312.
- [108] M. A. Caprio, P. Maris, J. P. Vary; *The no-core shell model with general radial bases*; Phys. Conf. Ser. **403** (2012) 012014.
- [109] D. J. Rowe; *An algebraic approach to problems with polynomial Hamiltonians on Euclidean spaces*; Journal of Physics A: Mathematical and General **38** (2005) 10181.
- [110] P. Isserstedt; *Generalisierte Oszillatorbasen für ab initio Kernstrukturrechnungen*; B.Sc. thesis (2013).
- [111] M. Schmidt; *Ab initio No-Core-Schalenmodell mit generalisierten Oszillatorbasen*; B.Sc. thesis (2013).
- [112] S. Quaglioni, P. Navrátil; *Ab Initio Many-Body Calculations of n - ^3H , n - ^4He , p - $^3,4\text{He}$, and n - ^{10}Be Scattering*; Phys. Rev. Lett. **101** (2008) 092501.
- [113] S. Quaglioni, P. Navrátil; *Ab initio many-body calculations of nucleon-nucleus scattering*; Phys. Rev. C **79** (2009) 044606.
- [114] S. Baroni, P. Navrátil, S. Quaglioni; *Ab Initio Description of the Exotic Unbound ^7He Nucleus*; Phys. Rev. Lett. **110** (2013) 022505.
- [115] S. Baroni, P. Navrátil, S. Quaglioni; *Unified ab initio approach to bound and unbound states: No-core shell model with continuum and its application to ^7He* ; Phys. Rev. C **87** (2013) 034326.
- [116] J. Langhammer; *Chiral Three-Nucleon Interactions in Ab-Initio Nuclear Structure and Reactions*; Ph.D. thesis; TU Darmstadt (2014).
- [117] R. Roth, P. Navrátil; *Ab Initio Study of ^{40}Ca with an Importance-Truncated No-Core Shell Model*; Phys. Rev. Lett. **99** (2007) 092501.
- [118] R. Roth; *Importance Truncation for Large-Scale Configuration Interaction Approaches*; Phys. Rev. C **79** (2009) 064324.
- [119] M. K. G. Kruse, E. D. Jurgenson, P. Navrátil, *et al.*; *Extrapolation uncertainties in the importance-truncated no-core shell model*; Phys. Rev. C **87** (2013) 044301.
- [120] J. L. Whitten, M. Hackmeyer; *Configuration Interaction Studies of Ground and Excited States of Polyatomic Molecules. I. The CI Formulation and Studies of Formaldehyde*; The Journal of Chemical Physics **51** (1969) 5584.

-
- [121] M. Hackmeyer, J. L. Whitten; *Configuration Interaction Studies of Ground and Excited States of Polyatomic Molecules II. The Electronic States and Spectrum of Pyrazine*; The Journal of Chemical Physics **54** (1971) 3739.
- [122] C. Stumpf; *Importance-Truncated Large-Scale Shell Model*; Master's thesis; TU Darmstadt (2013).
- [123] E. Caurier, F. Nowacki; *Present Status of Shell Model Techniques*; Acta Phys. Pol. B **30** (1999) 705.
- [124] M. D. Schuster, S. Quaglioni, C. W. Johnson, *et al.*; *Operator evolution for ab initio nuclear theory*; arXiv:1402.7106 [nucl-th] (2014).
- [125] S. Reinhardt; *Unitary Transformations for Nuclear Structure Calculations*; Ph.D. thesis; TU Darmstadt (2014).
- [126] F. Coester; *Bound states of a many-particle system*; Nuclear Physics **7** (1958) 421.
- [127] F. Coester, H. Kümmel; *Short-range correlations in nuclear wave functions*; Nuclear Physics **17** (1960) 477.
- [128] R. Roth, P. Papakonstantinou, N. Paar, *et al.*; *Hartree-Fock and Many-Body Perturbation Theory with Correlated Realistic NN-Interactions*; Phys. Rev. C **73** (2006) 044312.
- [129] D. J. Thouless; *Stability conditions and nuclear rotations in the Hartree-Fock theory*; Nuclear Physics **21** (1960) 225.
- [130] J. Čížek; *On the Correlation Problem in Atomic and Molecular Systems. Calculation of Wavefunction Components in Ursell-Type Expansion Using Quantum-Field Theoretical Methods*; The Journal of Chemical Physics **45** (1966) 4256.
- [131] J. Čížek; *On the Use of the Cluster Expansion and the Technique of Diagrams in Calculations of Correlation Effects in Atoms and Molecules*; Adv. Chem. Phys. **14** (1969) 35.
- [132] G. D. Purvis III, R. J. Bartlett; *A full coupled-cluster singles and doubles model: The inclusion of disconnected triples*; J. Chem. Phys. **76** (1982) 1910.
- [133] R. Roth, J. R. Gour, P. Piecuch; *Ab initio coupled-cluster and configuration interaction calculations for ^{16}O using the V_{UCOM} interaction*; Phys. Rev. C **79** (2009) 054325.
- [134] P. Piecuch, M. Włoch; *Renormalized coupled-cluster methods exploiting left eigenstates of the similarity-transformed Hamiltonian*; The Journal of Chemical Physics **123** (2005) 224105.
-

-
- [135] P. Piecuch, J. R. Gour, M. Włoch; *Left-eigenstate completely renormalized equation-of-motion coupled-cluster methods: Review of key concepts, extension to excited states of open-shell systems, and comparison with electron-attached and ionized approaches*; International Journal of Quantum Chemistry **109** (2009) 3268.
- [136] I. Talmi; *Nuclear Spectroscopy with Harmonic Oscillator Wave-Functions*; Helv. Phys. Acta **25** (1952) 185.
- [137] M. Moshinsky; *Transformation brackets for harmonic oscillator functions*; Nucl. Phys. **13** (1959) 104.
- [138] A. Calci; *Ab initio nuclear structure with SRG-transformed chiral NN plus NNN interactions*; Master's thesis; TU Darmstadt (2010).
- [139] S. Binder; *Angular Momentum Projection and Three-Body Forces in the No-Core Shell Model*; Master's thesis; TU Darmstadt (2010).
- [140] G. P. Kamuntavicius, R. K. Kalinauskas, B. R. Barrett, *et al.*; *The general harmonic-oscillator brackets: compact expression, symmetries, sums and Fortran code*; Nucl. Phys. **A695** (2001) 191.
- [141] B. Buck, A. C. Merchant; *A simple expression for the general oscillator bracket*; Nucl. Phys. **A600** (1996) 387.
- [142] L. Trlifaj; *Simple Formula for the General Oscillator Brackets*; Phys. Rev. C **5** (1972) 1534.
- [143] P. Navrátil, B. R. Barrett; *Four-nucleon shell-model calculations in a Faddeev-like approach*; Phys. Rev. C **59** (1999) 1906.
- [144] S. Schulz; *SRG-Induced Four-Body Forces in Ab Initio Nuclear Structure*; Master's thesis; TU Darmstadt (2013).
- [145] R. Roth, S. Binder, K. Vobig, *et al.*; *Medium-Mass Nuclei with Normal-Ordered Chiral NN+3N Interactions*; Phys. Rev. Lett. **109** (2012) 052501.
- [146] E. Gebrerufael; *Multi-Reference Normal Ordering for 3N Interactions*; Master's thesis; TU Darmstadt (2013).
- [147] K. Vobig; *Normalgeordnete chirale Drei-Nukleonen-Wechselwirkung*; B.Sc. thesis (2001).
- [148] W. Glöckle; *The Quantum Mechanical Few-Body Problem*; Springer (1983).
- [149] K. Hebeler; *Momentum-space evolution of chiral three-nucleon forces*; Phys. Rev. C **85** (2012) 021002.

-
- [150] G. Engeln-Müllges, K. Niederdrenk, R. Wodicka; *Akima- und Renner-Subsplines*; in *Numerik-Algorithmen*; 469–496; Springer Berlin Heidelberg (2011).
- [151] C. Drischler, V. Somà, A. Schwenk; *Microscopic calculations and energy expansions for neutron-rich matter*; Phys.Rev. **C89** (2014) 025806.
- [152] S. K. Bogner, T. T. S. Kuo, A. Schwenk; *Model-independent low momentum nucleon interaction from phase shift equivalence*; Phys. Rep. **386** (2003) 1.
- [153] S. K. Bogner, T. T. S. Kuo, A. Schwenk, *et al.*; *Towards a model-independent low momentum nucleon-nucleon interaction*; Phys. Lett. **B576** (2003) 265.
- [154] S. K. Bogner, R. J. Furnstahl, P. Maris, *et al.*; *Convergence in the no-core shell model with low-momentum two-nucleon interactions*; Nucl. Phys. A **801** (2008) 21.
- [155] K. Suzuki, S. Y. Lee; *Convergent Theory for Effective Interaction in Nuclei*; Prog. Theo. Phys. **64** (1980) 2091.
- [156] Susumu Ôkubo; *Diagonalization of Hamiltonian and Tamm-Dancoff Equation*; Progress of Theoretical Physics **12** (1954) 603.
- [157] R. J. Furnstahl, K. Hebeler; *New applications of renormalization group methods in nuclear physics*; Reports on Progress in Physics **76** (2013) 126301.
- [158] E. D. Jurgenson, P. Navrátil, R. J. Furnstahl; *Evolution of Nuclear Many-Body Forces with the Similarity Renormalization Group*; Phys. Rev. Lett. **103** (2009) 082501.
- [159] S. K. Bogner, R. J. Furnstahl, A. Schwenk; *From low-momentum interactions to nuclear structure*; Prog. Part. Nucl. Phys. **65** (2010) 94.
- [160] S. Kehrein; *The Flow Equation Approach to Many-Particle Systems*; vol. 217 of *Springer Tracts in Modern Physics*; Springer, Berlin (2006).
- [161] H. Feldmeier, T. Neff, R. Roth, J. Schnack; *A Unitary Correlation Operator Method*; Nucl. Phys. **A632** (1998) 61.
- [162] K. A. Wendt; *Similarity renormalization group evolution of three-nucleon forces in a hyperspherical momentum representation*; Phys. Rev. C **87** (2013) 061001.
- [163] E. D. Jurgenson, P. Navrátil, R. J. Furnstahl; *Evolving Nuclear Many-Body Forces with the Similarity Renormalization Group*; Phys. Rev. C **83** (2011) 034301.
- [164] M. Wang, G. Audi, A. H. Wapstra, *et al.*; *The Ame2012 atomic mass evaluation*; Chinese Physics C **36** (2012) 1603.
-

-
- [165] E. D. Jurgenson, P. Maris, R. J. Furnstahl, *et al.*; *Structure of p-shell nuclei using three-nucleon interactions evolved with the similarity renormalization group*; Phys. Rev. C **87** (2013) 054312.
- [166] A. Bohr, B. Mottelson; *Struktur der Atomkerne*; Carl Hanser Verlag (1979).
- [167] F. Ajzenberg-Selove; *Energy levels of light nuclei A = 11-12*; Nuclear Physics A **506** (1990) 1.
- [168] E. Epelbaum, H. Krebs, D. Lee, U.-G. Meißner; *Ab initio calculation of the Hoyle state*; Phys. Rev. Lett. **106** (2011) 192501.
- [169] E. Epelbaum, H. Krebs, T. A. Lähde, *et al.*; *Structure and Rotations of the Hoyle State*; Phys. Rev. Lett. **109** (2012) 252501.
- [170] G Audi, AH Wapstra, C Thibault; *The AME2003 atomic mass evaluation (II). Tables, graphs and references*; Nucl. Phys. **A729** (2003) 337.
- [171] C. R. Hoffman, T. Baumann, D. Bazin, *et al.*; *Determination of the N = 16 Shell Closure at the Oxygen Drip Line*; Phys. Rev. Lett. **100** (2008) 152502.
- [172] J. W. Negele, H. Orland; *Quantum Many-Particle Systems*; Advanced Book Classics; Westview Press (1998).
- [173] R. J. Bartlett, M. Musiał; *Coupled-cluster theory in quantum chemistry*; Rev. Mod. Phys. **79** (2007) 291.
- [174] D. Rozpedzik, J. Golak, R. Skibiński, *et al.*; *A First Estimation of Chiral Four-Nucleon Force Effects in ^4He* ; Acta Phys. Polon. B **37** (2006) 2889.
- [175] N. Fettes, U.-G. Meißner, S. Steininger; *Pion-nucleon scattering in chiral perturbation theory (I): Isospin-symmetric case*; Nuclear Physics A **640** (1998) 199.
- [176] U.-G. Meißner; *On the low-energy constants of the chiral effective pion-nucleon Lagrangian*; in *Proceedings of the Workshop on "Three-Nucleon Interactions from Few- to Many-Body Systems"*, TRIUMF, Vancouver, Canada (2007).
- [177] M. C. M. Rentmeester, R. G. E. Timmermans, J. J. de Swart; *Determination of the chiral coupling constants c_3 and c_4 in new pp and np partial-wave analyses*; Phys. Rev. C **67** (2003) 044001.
- [178] D. R. Entem, R. Machleidt; *Chiral 2π exchange at fourth order and peripheral NN scattering*; Phys. Rev. C **66** (2002) 014002.
- [179] V. Bernard, N. Kaiser, U.-G. Meißner; *Aspects of chiral pion-nucleon physics*; Nuclear Physics A **615** (1997) 483.
-

- [180] H.-W. Hammer, A. Nogga, A. Schwenk; *Colloquium: Three-body forces: From cold atoms to nuclei*; Rev. Mod. Phys. **85** (2013) 197.
- [181] F. Ajzenberg-Selove; *Energy levels of light nuclei $A = 5-10$* ; Nuclear Physics A **490** (1988) 1.
- [182] T. Hütter; *Charakterisierung chiraler N^2LO & N^3LO Wechselwirkungen*; B.Sc. thesis (2012).
- [183] D. R. Tilley, C. M. Cheves, J. L. Godwin, *et al.*; *Energy levels of light nuclei $A=5, 6, 7$* ; Nuclear Physics A **708** (2002) 3.

Acknowledgements

First of all I would like to thank Prof. Robert Roth for providing me this interesting topic and giving me the opportunity to work in his group.

I want to thank Prof. Jochen Wambach for agreeing to be the second reviewer of this thesis.

Special thanks should be given to my collaborators. I would like to express my appreciation to Prof. Petr Navrátil for providing his Manyeff code and the long-lasting support regarding the four-body project. Helpful discussions with Prof. Hans Feldmeier about the SRG-generator developments were greatly appreciated. I am grateful for the collaboration with Kai Hebeler to produce and treat the interaction matrix elements in the momentum representation.

My special thanks are extended to the theory department and, in particular, to my group and office mates for the pleasant atmosphere as well as physical and non-physical conversations. Many thanks go to Sven Binder and Joachim Langhammer for commenting and proofreading this work.

Finally, I would like to thank Marion for her patience and continuous support.

Lebenslauf

Zur Person

Name: Angelo Calci
Geburtsdatum: 16. August 1984
Geburtsort: Kassel
Staatsangehörigkeit: deutsch
Eltern: Fiorino Calci
Elisabeth Calci, geb. Döring
Familienstand: ledig

Bildungsweg

1991 - 1995 Besuch der Grundschule am Warteberg in Kassel
1995 - 2001 Besuch der Gesamtschule Hegelsberg in Kassel
2001 - 2004 Besuch der Herderschule Kassel (Oberstufengymnasium)
2004 - 2005 Zivildienst in der Diakoniestation Kassel-Nord
2005 - 2008 Bachelorstudium Physik an der TU Darmstadt
Bachelor of Science, Gesamtnote: Sehr gut mit Auszeichnung
Thesis: *Investigation of the ground-state bands of the actinoids using the CBS Rotor Model*
2008 - 2010 Masterstudium Physik an der TU Darmstadt
Master of Science, Gesamtnote: Sehr gut
Thesis: *Ab initio nuclear structure with SRG-transformed chiral NN plus NNN interactions*
seit 2010 Promotionsstudium an der TU Darmstadt und Anfertigung der Dissertation

Erklärung zur Dissertation

Hiermit versichere ich, die vorliegende Dissertation ohne Hilfe Dritter nur mit den angegebenen Quellen und Hilfsmitteln angefertigt zu haben. Alle Stellen, die aus Quellen entnommen wurden, sind als solche kenntlich gemacht. Diese Arbeit hat in gleicher oder ähnlicher Form noch keiner Prüfungsbehörde vorgelegen.

Darmstadt, 17. Juni 2014

Angelo Calci